Magnetoelectric Coupling in $BaTiO_3$-$BiFeO_3$ Multilayers: Growth Optimization and Characterization

Von der Fakultät für Physik und Geowissenschaften
der Universität Leipzig
genehmigte

DISSERTATION

zur Erlangung des akademischen Grades
Doctor rerum naturalium
Dr. rer. nat.,

vorgelegt
von M. Sc. Stefan Hohenberger
geboren am 28.02.1987 in München

Gutachter: Prof. Dr. Michael Lorenz (Universität Leipzig)
Prof. Dr. Kathrin Dörr (Universität Halle-Wittenberg)

eingereicht am:	01.09.2020
Tag der Verleihung:	25.01.2021

“It’s the questions we can’t answer that teach us the most.
They teach us how to think.
If you give a man an answer, all he gains is a little fact.
But give him a question and he’ll look for his own answers.”

— *Patrick Rothfuss, The Wise Man’s Fear*

“With magic, you can turn a frog into a prince.
With science, you can turn a frog into a Ph.D
and you still have the frog you started with.”

— *Terry Pratchett, The Science of Discworld*

Bibliographische Beschreibung

Hohenberger, Stefan:
Magnetoelectric Coupling in $BaTiO_3$*-*$BiFeO_3$ *Multilayers:*
Growth Optimization and Characterization
Universität Leipzig, Dissertation
204 Seiten, 238 Zitate, 97 Grafiken, 15 Tabellen

Referat:

Die vorliegende Arbeit befasst sich mit der magnetoelektrischen (ME) Kopplung in multiferroischen Dünnfilm-Multilagen aus $BaTiO_3$ (BTO) und $BiFeO_3$ (BFO). Multiferroika besitzen mehr als einen ferroischen Ordnungsparameter, in diesem Fall Ferroelektrizität und Antiferromagnetismus. Eine Kreuzkopplung dieser anderweitig separaten Ordnungsparameter birgt großes Potential für die Anwendung in Multistate-Speichermedien, Spintronics und sogar dem medizinischen Bereich. Die erste Hürde dieses Forschungsbereichs ist die Rarität von Multiferroika. Eine zweite besteht darin, dass viele Multiferroika, sowohl intrinsicher als auch extrinsischer Natur, nur geringe magnetoelektrische Kopplungs-Konstanten aufweisen. In vorangegangenen Studien wurde eine Erhöhung des ME Kopplungs-Koeffizienten α_{ME} in BTO-BFO Multilagen, hergestellt mittels gepulster Laser-Deposition (PLD), um eine Größenordnung gegenüber Einzellagen des intrinsischen Multiferroikums BFO festgestellt. Jedoch ist der ME Kopplungs-Mechanismus in derartigen Heterostrukturen bisher noch kaum erforscht. In dieser Arbeit haben wir mit Hilfe einer Auswahl von strukturellen, chemischen, elektrischen und magnetischen Charakterisierungsmethoden versucht, den α_{ME}-Koeffizienten zu maximieren und ein tieferes Verständnis dieser verstärkten ME Kopplung zu gewinnen.

Im Vergleich von BTO-BFO Multilagen und Einzellagen zeigten sich nicht nur verbesserte ME-Kopplung, sondern auch verringerte Mosaizität, Rauigkeit und Leckstrom-Dichte in Multilagen. In Anschluss an eine parametrische Proben-Optimierung wurden durch die Einführung einer Schattenmaske im PLD Prozess atomar glatte Grenzflächen und drastisch verbesserte ferroelektrische Eigenschaften erzielt. Der höchste α_{ME}-Koeffizient wurde mit 480 $\mathrm{Vcm^{-1}Oe^{-1}}$ für eine Multilagen-Probe mit nur 4.6 nm Doppellagen-Dicke gemessen, was eine Verstärkung um zwei Größenordnungen gegenüber dem Wert von 4 $\mathrm{Vcm^{-1}Oe^{-1}}$ für eine $BiFeO_3$ Einzellage entspricht. Wir haben eine inverse Korrelation von α_{ME} mit der Doppellagen-Dicke d_{dl} aufgezeigt. Der Einfluss von Prozessgas-Druck und Verhältnis von BTO-BFO auf α_{ME} erwies sich als vernachlässigbar im Vergleich zu dem Einfluss von d_{dl}. Im Vergleich zu BFO Einzellagen zeichnen BTO-BFO Multilagen charakteristische Veräufe von α_{ME} mit dem externen Magnetfeld und der Messtemperatur ab. Wir schlussfolgern aus diesen Tatsachen die Präsenz eines Grenzflächen-Effektes als Grund für den verstärkten ME Effekt in BTO-BFO Multilagen.

Bibliographic Record

Hohenberger, Stefan:
Magnetoelectric Coupling in $BaTiO_3$-$BiFeO_3$ Multilayers:
Growth Optimization and Characterization
Universität Leipzig, Dissertation
204 Pages, 238 Citations, 97 Figures, 15 Tables

Abstract:

The presented thesis explores the magnetoelectric (ME) coupling in multiferroic thin film multilayers of $BaTiO_3$ (BTO) and $BiFeO_3$ (BFO). Multiferroics possess more than one ferroic order parameter, in this case ferroelectricity and anti-ferromagnetism. Cross-coupling between these otherwise separate order parameters promises great advantages in the fields of multistate memory, spintronics and even medical applications. The first major challenge in this field of study is the rarity of multiferroics. Second, most known multiferroics, both intrinsic and extrinsic in nature, possess very low ME coupling coefficients. In previous studies conducted by our group, BTO-BFO multilayers deposited by pulsed laser deposition (PLD) showed a ME coupling coefficient α_{ME} enhanced by one order of magnitude, when compared to single-layers of the intrinsic multiferroic BFO. However, the mechanism of ME coupling in such heterostructures is poorly understood until now. In this thesis, we used a selection of structural, chemical, electrical and magnetic measurements to maximize the α_{ME}-coefficient and shed light on the origin of this enhanced ME effect.

The comparison of BTO-BFO multilayers over single-layers revealed not only enhanced ME-coupling, but also reduced mosaicity, roughness and leakage current density in multilayers. Following a parametric sample optimization, we achieved an atomically smooth interface roughness and vast improvements in the ferroelectric properties by introducing a shadow mask in the PLD process. We measured the highest α_{ME}-value so far of 480 $\mathrm{Vcm^{-1}Oe^{-1}}$ for a multilayer with a double-layer thickness of only 4.6 nm, two orders of magnitude larger than the coefficient of 4 $\mathrm{Vcm^{-1}Oe^{-1}}$ measured for BFO single-layers. The α_{ME}-coefficient in these multilayers stands in an inverse correlation with the double-layer thickness d_{dl}. The influence of oxygen pressure during growth and BTO-BFO ratio on α_{ME} was shown to be neglible in comparison to that of d_{dl}. From the characteristic dependencies of α_{ME} on magnetic bias field, temperature and d_{dl}, we concluded the existence of an interface-driven coupling mechanism in BTO-BFO multilayers.

Contents

List of Figures

List of Tables

List of Abbreviations

aFM	anti-ferromagnetic
AFM	atomic force microscope
BFO	bismuth ferrite, $BiFeO_3$
BGFO	gadolinium substituted bismuth ferrite, $Bi_{0.95}Gd_{0.05}FeO_3$
BTO	barium titanate, $BaTiO_3$
DHM	dynamic hysteresis measurement
EDX	energy-dispersive X-ray spectroscopy
FE	ferroelectric
FFT	fast-*Fourier*-transformation
FWHM	full width at half maximum
HAADF	high-angle annular dark-field imaging
HR-TEM	high-resolution transmission electron microscopy
IP	in-plane
LSM	laser scanning microscope
ME	magnetoelectric
NSTO	niobium-doped strontium titanate, $SrTiO_3$:Nb
OOP	out-of-plane
OOT	oxygen octahedral tilt
PLD	pulsed laser deposition
PNR	polarized neutron reflectometry
PPMS	*Physical Property Measurement System*
RSM	reciprocal space map
STEM	scanning transmission electron microscopy

STO	strontium titanate, $SrTiO_3$
ToF-SIMS	time-of-flight secondary ion mass spectrometry
TEM	transmission electron microscope
VSM	vibrating sample magnetometer
XRR	X-ray reflectometry
XRD	X-ray diffraction

List of Symbols

A	area
$a,\ b,\ c$	lattice constants
$a^*b^*c^*$	*Glazer* notation for oxygen octahedral tilt systems
$\boldsymbol{B}$	magnetic flux density
C	capacitance
$\boldsymbol{D}$	dielectric displacement
d_{hkl}	distance between lattice planes
d_{dl}	double-layer thickness
d_{tot}	total film thickness
$\boldsymbol{E}$	electric field
$\boldsymbol{E}_{\mathbf{coer}}$	electric coercive field
E_{imprint}	imprint field
f	frequency
F	free energy
f.u.	formula unit
$\boldsymbol{H}$	magnetic field strength
$\boldsymbol{H}_{\mathrm{coer}}$	magnetic coercive field strength
$h,\ k,\ l$	Miller indices
(hkl)	specific plane specified by hkl
$\{hkl\}$	set of equivalent planes specified by hkl
$[hkl]$	specific direction specified by hkl
$\langle hkl\rangle$	set of equivalent directions specified by hkl
I	electric current
j	current density
L	lens-chamber distance
$\boldsymbol{m}$	magnetic moment
$\boldsymbol{M}$	magnetic polarization, magnetization
$\boldsymbol{M}_{\mathbf{rem}}$	remanent magnetization
$\boldsymbol{M}_{\mathbf{S}}$	spontaneous magnetic polarization, magnetization

$\boldsymbol{M}_{\mathbf{sat}}$	saturation magnetization
o_{lat}	lateral offset value
p	pressure
$\boldsymbol{p}$	electric dipole moment
$\boldsymbol{P}$	electric polarization
$p_{\mathrm{O_2}}$	oxygen partial pressure
$\boldsymbol{P}_{\mathbf{E}}$	field dependent electric polarization
$\boldsymbol{P}_{\mathbf{rem}}$	remanent electric polarization
$\boldsymbol{P}_{\mathbf{S}}$	spontaneous electric polarization
$\boldsymbol{P}_{\mathbf{max}}$	maximal measured electric polarization
Q	electric charge
QM	lateral offset setting
R	electrical resistance
R_{rms}	root mean squared roughness
t	time
T	temperature
T_{Curie}	*Curie* temperature
$T_{\mathrm{Néel}}$	*Néel* temperature
T_{p}	process temperature
U	voltage
U_{ME}	induced magentoelectric voltage
V	volume
$x,\ y,\ z$	spacial directions

$\alpha,\ \beta,\ \gamma$	crystal lattice angles
α_{ME}	linear magnetoelectric voltage coefficient
ϵ_0	vacuum permittivity, 8.854×10^{-12} $\mathrm{Fm^{-1}}$
ϵ_{r}	relative permittivity
θ	diffracted angle
λ	wavelength
μ_0	vacuum permeability, $4\pi \times 10^{-7}$ $VSA^{-1}m^{-1}$
μ_{B}	Bohr magneton, 9.247×10^{-24} $\mathrm{J \cdot T^{-1}}$
μ_{r}	relative permeability
ρ	resistivity
ρ_{f}	density of free charges
ρ_{L}	laser energy density
φ	in-plane rotational angle

χ	goniometer angle
χ_{el}	electric susceptibility
χ_{m}	magnetic susceptibility
ω	incident angle

Chapter 1

Introduction

A great deal of progress in the field of miniaturized electronics is driven by the discovery and advancement of novel materials and physical phenomena. In this context, research of multifunctional materials is gaining a lot of interest in the scientific community. One particular class of materials has shifted into the focus of attention over the last two decades: magnetoelectrically coupled multiferroics.

Multiferroics are materials with more than one ferroic order parameter. Generally, the two most relevant ferroic properties combined in multiferroics, which can be intrinsic or extrinsic in nature, are ferroelectricity and ferromagnetism. Magnetoelectric (ME) coupling in such materials allows the exertion of influence over one order parameter via the associated field of the other, e.g. the manipulation of electrical polarization by a magnetic field, called the direct magnetoelectric effect. Realizing a robust room temperature multiferroic, which additionally shows a sufficiently large magnetoelectric coupling, would open up a number of fascinating application options. One of the greatest goals of multiferroics research is the implementation of volatile magnetic memory devices that are switched by voltage pulses, which promises to lower the power consumption by an order of magnitude relative to devices based on the giant magnetoresistance effect [1, 2]. Multiferroics also find application in the field of spintronics [3] and in novel high precision magnetic sensor devices [4, 5]. Generally the largest ME effects, in particular in the field of sensor devices, have been reported for laminate composite multiferroics operated at electromechanical resonance frequencies [6]. Off-resonance, however, the ME effect is typically fairly weak. This poses a problem for a number of potential applications. For example, ME devices are being targeted for the use in therapeutic, highly miniaturized neural stimulation devices [7], which use a magnetic AC signal to generate an electric pulse via an implanted magnetoelectric microchip. Such a technique, however, requires the operation at low frequencies in the order of 100 Hz, far lower than the typical electromechanic resonance frequencies ranging from several kHz to MHz.

One of the most fundamental challenges of multiferroics research remains the rarity of intrinsic room temperature multiferroics. The underlying physics responsible for the formation of a ferroelectric and magnetic order in a material are substantially at odds with one another [8]. A brief outline of the theory of multiferroics and magnetoelectric coupling is provided in Chapter 2. Consequently, the discovery of a significant ME effect in thin films of one of the few single-phase room temperature multiferroics, $BiFeO_3$ (BFO), was incremental in sparking the current boom of research in this field [9]. Extrinsic multiferroics, i.e. heterostructures that gain their multiferroicity from either compounding individual ferroic materials, or by exploiting interface effects, provide a more far-reaching playground for exploration [10]. The semiconductor physics group at the *Univertsity of Leipzig* has been investigating epitaxial heterostructures of the ferroelectric $BatiO_3$ (BTO) and multiferroic BFO since 2014. Both solid solutions and multilayers of these two materials were shown to possess enhanced ME coupling coefficients by up to an order of magnitude, relative single layers of BFO [11]. Of the two, multilayers of BTO-BFO, depicted schematically in Fig. 1.1, have more malleable properties and allow a more direct manipulation of design parameters. This thesis focuses on the advancement of the understanding of their structural, ferroic and magnetoelectric properties. In Chapter 3, we elaborate on the fundamental properties of the constituent materials and the state of research into related heterostructures.

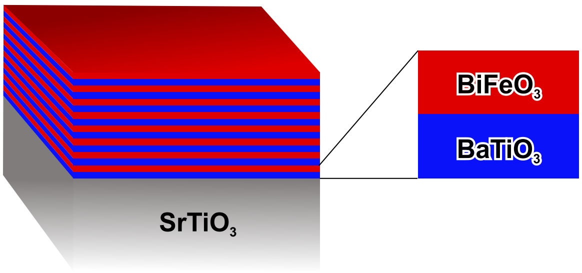

Figure 1.1: Schematic depiction of a thin film multilayer structure consisting of $BaTiO_3$ and $BiFeO_3$ on a $SrTiO_3$ substrate.

Despite excessive research in the field of magnetoelectrics in recent years, the microscopic origins of the ME coupling effect in both intrinsic and extrinsic multiferroics are currently still poorly understood. In this thesis, we take a largely phenomenological approach to explore the differences between ME coupling in BFO single layers and BTO-BFO multilayers. We used the physical vapor deposition technique of pulsed laser deposition (PLD) to deposit said multilayers and an array of structural (XRD, AFM, TEM), chemical (EDX, ToF-SIMS) and ferroic property characterization (DHM, VSM) techniques to investigate the sample properties in combination with measurements of the ME coupling coefficient α_{ME}. The mentioned experimental techniques are explained in Chapter 4.

The purpose of this thesis is to complement, clarify, and expand upon the known body of work on BTO-BFO multilayers. The crystalline structure of single-layers and multilayers has been previously optimized, yet the exact influence of temperature and oxygen pressure during growth on the ferroic and ME properties requires further research. Furthermore, a lack of controlled interface roughness, high droplet density and low breakdown field strength of multilayer samples necessitates appropriate countermeasures. To that effect, we studied the impact of laser fluence, lateral offset and eclipse-PLD on the sample properties. This work also provides an insight into the implications of various multilayer design aspects. Previously conducted studies were restricted to the variation of the BFO sub-layer thickness, which we augment by the explicit variation of the double-layer thickness and relative thickness ratio. Ultimately, this thesis tries to define the key parameters of design and growth conditions, which amplify the ME coupling in BTO-BFO multilayers and sets them apart from BFO single-layers.

The experimental results we have obtained through variation of the deposition conditions and design parameters are presented in Chapter 5. In addition, we have explored the advantages of the advanced deposition technique eclipse-PLD and advanced measurement techniques, such as polarized neutron reflectometry (PNR). Finally, we provide a summary of the main insights gained throughout this thesis and provide an outlook on potential future work in Chapter 6.

The experimental work cited in this work was conducted in the Semiconductor Physics group at the *University of Leipzig*, in the context of the collaborative research center *SFB 762: Functionality of Oxide Interfaces* and in cooperation with the Quantum Solid State Physics group at the *KU Leuven* in Belgium. Key parts of the results have been published in Refs. H1-H4 and a review of the work conducted in the framework of the project *SFB 762*, including the presented thesis, was published in Ref. H5.

Chapter 2

Theory of Multiferroic Magnetoelectrics

This chapter provides the foundation for a general understanding of ferroicity, multiferroics and magnetoelectricity. In Sec. 2.1 we define the concept of generalized ferroic order, discuss the microscopic origins of ferroelectricity and ferromagnetism, and the rarity of multiferroics. The theory of magnetoelectric coupling and the definition of the direct linear ME coefficient α_{ME} are introduced in Sec. 2.2.

2.1 Primary Ferroic Properties

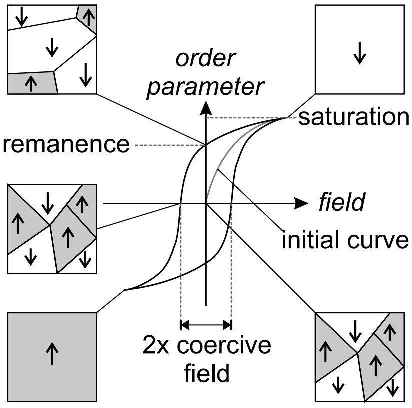

Figure 2.1: Generalized hysteresis curve of the order parameter of a ferroic material in the related field.

Ferroic materials are characterized by a broken inversion symmetry (spacial or temporal), which gives rise to a long-range order parameter that can be influenced by a corresponding field [12]. Cycling of said field gives rise to a hysteretic (from Greek, meaning “lagging behind”) behavior, as depicted in Fig. 2.1. Macroscopic regions in space that have a defined orientation of the order parameter are called domains. The order parameter has at least two opposing orientations and switching of the overall macroscopic order is achieved by field induced growth of the domains (see Fig. 2.1). All ferroic materials possess a critical temperature, above which the long range order does not persist. Today, four types of ferroicity are generally recognized [1,12]:

- Ferroelectricity: materials with spontaneous polarization $\boldsymbol{P}$ that can be switched by an electric field $\boldsymbol{E}$,
- Ferromagnetism: materials with spontaneous magnetization $\boldsymbol{M}$ that can be switched by a magnetic field $\boldsymbol{H}$,
- Ferroelasticity: materials with spontaneous deformation $\boldsymbol{\epsilon}$ that can be switched by stress $\boldsymbol{\sigma}$,
- Ferrotoroidicity: materials with spontaneous order of the nature of the curl of local magnetization or polarization, switchable by simultaneous application of $\boldsymbol{H}$ and $\boldsymbol{E}$. Ferrotoroidicity is expected by analogy to the former three, but has yet to be proven experimentally [1].

The term ferroic was coined due to the similarity of the other phenomena to ferromagnetism (lat. *ferro-*, referring to iron), which was discovered long before the others.

2.1.1 Ferroelectricity

The order parameter in ferroelectrics is the electrical polarization $\boldsymbol{P}$. It is linked to the dielectric displacement $\boldsymbol{D}$ and the electric field $\boldsymbol{E}$ by the equation:

$$\boldsymbol{D} = \epsilon_0 \boldsymbol{E} + \boldsymbol{P}\,, \tag{2.1}$$

where $\boldsymbol{D}$ is defined by the density of free charges ρ_f as

$$\mathrm{div}\;\boldsymbol{D} = \rho_\mathrm{f} \tag{2.2}$$

and ϵ_0 is the vacuum permittivity ($\epsilon_0 = 8.854 \times 10^{-12}\,\mathrm{F\,m^{-1}}$). The total polarization in a ferroelectric material is the product of a field dependent component $\boldsymbol{P}_\mathbf{E}$ and the spontaneous polarization $\boldsymbol{P}_\mathbf{S}$, which is present also at zero field. By introducing the electric susceptibility χ_el and the relative permittivity $\epsilon_\mathrm{r} = 1 + \chi_\mathrm{el}$, we can express $\boldsymbol{P}_\mathbf{E}$ as:

$$\boldsymbol{P}_\mathbf{E} = \epsilon_0 \chi_\mathrm{el} \boldsymbol{E}\,, \tag{2.3}$$

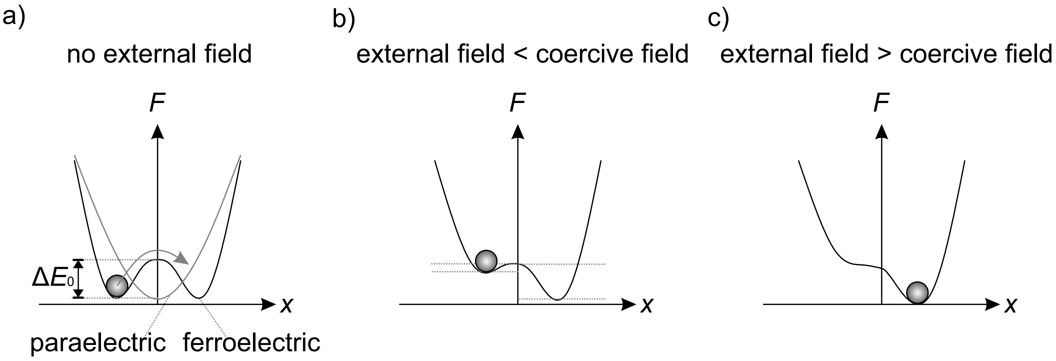

Figure 2.2: Ferroelectric double-well potential under the influence of an electric field.

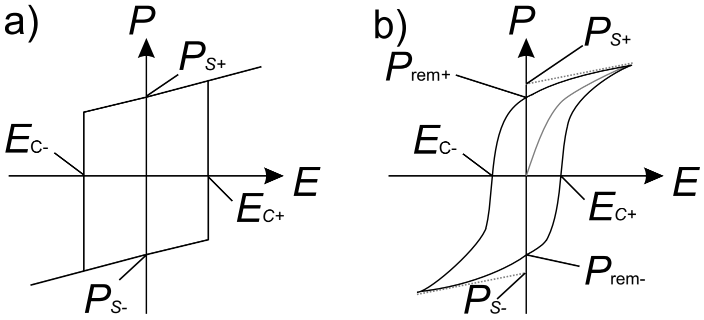

Figure 2.3: Ferroelectric hysteresis curve of an **(a)** ideal, mono-domain ferroelectric and **(b)** a real, polycrystalline/polydomain ferroelectric.

and further

$$\boldsymbol{D} = \epsilon_0 \epsilon_\mathrm{r} \boldsymbol{E} + \boldsymbol{P}_\mathbf{S} \,. \tag{2.4}$$

The simplest cause of a spontaneous polarization in a solid is the dipole moment created by ionic displacement in a structure with broken centrosymmetric symmetry, like in the model ferroelectric $\mathrm{BaTiO_3}$. In the case of a paraelectric material, the free energy relative to the displacement of an ion in a centrosymmetric lattice takes the form of a parabola, as depicted in Fig. 2.2 a). In a (tetragonal) ferroelectric, the free energy landscape is a double-well potential with two semi-stable ionic displacement positions, i.e. two opposing polarization orientations, also depicted in Fig. 2.2 a). Transferring the ion from one position to the other requires energy. Application of an external electrical field will shift the double well potential as depicted in Fig. 2.2 b) and c). Above the coercive field $\boldsymbol{E}_\mathbf{coer}$ the polarization is switched from one state to the other.

In an ideal single crystalline, single-domain ferroelectric, the field dependent polarization takes the form of the curve depicted in Fig. 2.3 a). In accordance with Eq. 2.4, there is a linear field dependent component and a non-zero spontaneous component at zero field $\boldsymbol{P}_\mathbf{S}$. In a polycrystalline, poly-domain ferroelectric, switching occurs not sharply at $\boldsymbol{E}_\mathbf{coer}$, but within a distribution around $\boldsymbol{E}_\mathbf{coer}$, reflecting the imperfections of a real ferroelectric. As a result, the remanent polarization $\boldsymbol{P}_{\mathbf{rem}}$ is smaller than $\boldsymbol{P}_{\mathbf{S}}$, though $\boldsymbol{P}_{\mathbf{S}}$ can be estimated by extrapolation from the saturated portion of the curve (see Fig. 2.3 b)). The mixed-domain remanent state of a partially polarization-reversed ferroic is depicted in Fig. 2.1. The critical temperature, above which the ferroelectric (FE) long range order disappears, is called the *Curie* temperature T_{Curie}.

2.1.2 Ferromagnetism and Anti-ferromagnetism

The order parameter in ferromagnet is the magnetic polarization, or magnetization $\boldsymbol{M}$. It is linked to the magnetic flux density $\boldsymbol{B}$ and the magnetic field strength $\boldsymbol{H}$ by the relation:

$$\boldsymbol{B} = \mu_0 \left(\boldsymbol{H} + \boldsymbol{M}\right) , \tag{2.5}$$

where $\boldsymbol{M}$ is defined as the density of magnetic moment $\boldsymbol{m}$ per volume V:

$$\boldsymbol{M} = \frac{\mathrm{d}\boldsymbol{m}}{\mathrm{d}V} \tag{2.6}$$

and μ_0 is the vacuum permeability ($\mu_0 = 4\pi \times 10^{-7}\,\mathrm{V\,s\,A^{-1}m^{-1}}$). Analogous to ferroelectricity, one defines the magnetic susceptibility χ_{m} and relative permeability μ_{r} $=1+\chi_{\mathrm{m}}$ such that:

$$\boldsymbol{M} = \chi_{\mathrm{m}}\boldsymbol{H} \tag{2.7}$$

and

$$\boldsymbol{B} = \mu_0\mu_{\mathrm{r}}\boldsymbol{H} = \mu_0 \left(1 + \chi_{\mathrm{m}}\right) \boldsymbol{H} . \tag{2.8}$$

In the case of materials without magnetic order, leading to a spontaneous magnetization $\boldsymbol{M}_{\mathbf{S}}$, χ_{m} is linear. Diamagnetism ($\chi_{\mathrm{m}} < 0$) occurs in all materials as a response of paired electrons to an external magnetic field. Materials with unpaired spins, i.e. atomic magnetic moment, exhibit paramagnetism ($\chi_{\mathrm{m}} > 0$). In ferromagnets, χ_{m} is non-linear due to hysteretic behavior. The magnetic ordering in ferromagnets is due to strong exchange interaction (direct, super- or double-exchange) between atoms with uncompensated spins. In addition to ferromagnetism, two related phenomena with anti-parallel coupling are known: anti-ferromagnetism and ferrimagnetism. In the case of anti-ferromagnetism, the coupled spins are of the same magnitude and hence cancel each other out on an unit-cell and macroscopic level. In ferrimagnets, the coupled spins are unequal and do not cancel each other out completely. The critical temperature, above which the magnetic long range order disappears, is called the *Curie* temperature T_{Curie} in the case of ferro- and ferrimagnets and the *Néel* temperature $T_{\mathrm{Néel}}$ in the case of anti-ferromagnets.

2.1.3 Multiferroicity

A multiferroic material is one that exhibits at least two of the ferroic order parameters. Most ferroelectrics are inherently also ferroelastic [13]. However, it is a widespread practice to imply the presence of ferromagnetism - or any kind of magnetic order [14] - alongside ferroelectricity when using the term. One makes a distinction between intrinsic multiferroics, which exhibit multiferroicity within a single phase, and extrinsic multiferroics, for which multiferroicity is the product of combining two or more materials. Intrinsic multiferroics can be further categorized as split-order and joint-order multiferroics [15]. In split-order multiferroics, ferroelectricity and magnetism arise individually. In joint-order multiferroics, one ferroic property arises as a result of the other. Principally, joint-order multiferroics would be expected to show a stronger ME coupling than split-order multiferroics. Practically they typically show vastly smaller polarizations and critical temperatures far below room temperature [15], which is highly disadvantageous for any generic application.

Intrinsic multiferroics are exceedingly rare, in particular when adding the restraint of room temperature stability. In part, this can be explained by the restrictions that symmetry aspects of the occurrence of ferroic properties impose on a material, leaving only a small number of symmetry point groups that favor multiferroicity in a crystalline material [12]. Another approach is to consider the origins of magnetism and ferroelectricity [8, 16]. Most known ferroelectrics are insulating transition metal oxides. Generally speaking, the source of magnetism in insulating oxides is the exchange coupling of uncompensated electrons from the partially filled d or f orbitals of the transition metals. On the other hand, most conventional ferroelectrics such as the $\mathrm{ABO_3}$ type perovskites BTO and $\mathrm{Pb(Zr,Ti)O_3}$ gain their electric polarizability from the off-centering of the B-site cation, which requires an empty d-orbital [8, 16]. Unconventional ferroelectrics, like the lone-pair multiferroic BFO, see Sec. 3.4, seemingly circumvent these generalized restrictions. In BFO, the magnetic order is inherent to the A-site $d5$ $\mathrm{Fe^{3+}}$ sub-lattice and the ferroelectricity originates not from the geometrical off-centering of the B-site cation, but from the stereo-chemically active $6s^2$ $\mathrm{Bi^{3+}}$ electrons. Closely related is $\mathrm{BiMnO_3}$, which exhibits both ferroelectricity below 550 K and ferromagnetism, but only below a transition temperature of 105 K [17]. A handful of other mechanisms exist that allow multiferroicity, such as ferroelectricity through geometric constraint and spin driven mechanisms, see Ref. 15. However, BFO has so far persisted as the only robust room temperature multiferroic.

2.2 Magnetoelectric Coupling

When considering a material with long range ferroelectric, magnetic and strain ordering, a number of possible cross-coupling interactions arise. The linear or quadratic coupling between strain and polarization is called piezoelectricity or electrostriction, and likewise the coupling of strain and magnetism is known as piezomagnetism or magnetostriction, respectively [1]. The coupling of polarization and magnetism is called linear (quadratic) magnetoelectricity. ME coupling is defined as the change of polarization in response to a magnetic field, converse ME coupling describes the change of magnetization in response to an electric field.

2.2.1 Theory of Magnetoelectric Coupling

Using the *Einstein* summation convention, one can express the free energy F in a material that possesses both magnetic and dielectric moments as [1, 18, 19]:

$$\begin{aligned} F(\boldsymbol{E},\boldsymbol{H}) = & F_0 - P_i^S E_i - M_i^S H_i - \frac{1}{2}\epsilon_0\epsilon_{ij}E_iE_j - \frac{1}{2}\mu_O\mu_{ij}H_iH_j - \alpha_{ij}E_iH_j \\ & - \frac{1}{2}\beta_{ijk}E_iH_jH_k - \frac{1}{2}\gamma_{ijk}H_iE_jE_k - \cdots \end{aligned} \tag{2.9}$$

The second and third terms denote the field dependent spontaneous polarization and magnetization. The fourth and fifth terms describe the linear response of polarization to an electric field and the response of magnetization to a magnetic field. The sixth term refers to linear ME coupling, the seventh and eighth to quadratic ME coupling, and so on. α_{ij}, β_{ijk} and γ_{ijk} are the respective ME coupling coefficients. The formalism for the ME effect is obtained by differentiation of Eq. 2.9 with respect to E_i to obtain:

$$\begin{aligned} P_i(\boldsymbol{E},\boldsymbol{H}) = & \frac{\partial F}{\partial E_i} = P_i^S + \epsilon_0\epsilon_{ij}E_j + \alpha_{ij}H_j \\ & + \frac{1}{2}\beta_{ijk}H_jH_k + \gamma_{ijk}H_iE_j - \cdots \end{aligned} \tag{2.10}$$

and the converse ME effect by differentiation of Eq. 2.9 with respect to H_i:

$$\begin{aligned} \mu_0 M_i(\boldsymbol{E},\boldsymbol{H}) = & \frac{\partial F}{\partial H_i} = M_i^S + \mu_0\mu_{ij}H_j + \alpha_{ji}E_i \\ & + \beta_{ijk}E_iH_j + \frac{1}{2}\gamma_{ijk}E_jE_k - \cdots \end{aligned} \tag{2.11}$$

In this thesis, the longitudinal linear ME coupling voltage coefficient α_{ME}, from now on simply referred to as the ME coefficient, is defined in terms of the induced voltage U_{ME}

and the capacitor thickness t using the expression for the ME tensor α_{ij} in Eq. 2.10, ignoring the higher order terms, as:

$$\alpha_{ij} = \frac{\partial P_i}{\partial H_j} = \epsilon_0 \epsilon_{ii} \frac{\partial E_i}{\partial H_j} = \epsilon_0 \epsilon_{ii} \frac{\partial U_{\mathrm{ME}}}{t\, \partial H_j} = \epsilon_0 \epsilon_r \alpha_{\mathrm{ME}} \,. \tag{2.12}$$

A relation for the upper bound to the ME tensor α_{ij} can be found by demanding the sum of first three terms in Eq. 2.9 be greater zero [20]. Omitting the higher order terms, the expression simplifies to:

$$\alpha_{ij}^2 \leq \epsilon_0 \mu_0 \epsilon_{ii} \mu_{jj} \,. \tag{2.13}$$

Hence, materials with both high permittivity ϵ_{r} and permeability μ_{r} are expected to exhibit the largest ME effects. While ferroelectrics (ferromagnets) generally tend to show large permittivity (permeability), it is not necessarily a prerequisite for ferroelectricity (ferromagnetism) and typically not the case for intrinsic multiferroics [1]. In practice, α_{ij} is much smaller than this upper limit [13]. The ME effect is further limited by the small values of $\boldsymbol{M}_{\mathbf{S}}$ in intrinsic room temperature multiferroics, almost all of which are weak canted anti-ferromagnets [13].

2.2.2 Magnetoelectric Multiferroic Heterostructures

The restrictions of Eq. 2.13, as well as the constraints for multiferroicity can be overcome by including composite materials in the considerations. Multiferroic ME composite materials can consist of any number of combinations of ferroelectric, magnetic, multiferroic, piezolectric, magnetostrictive, etc. components. One way to characterize composite materials is by the components' approximate dimensionality using the *Newnham* notation: for example, 0-3 would refer to nano-particles embedded in a 3D matrix or a solid solution and 2-2 to a bi- or multilayer thin film structure [21]. In such composites, the ME effect may either be a sum property, a scaling property or a product property [18, 22]. A sum property is the combined effect of both materials, a scaling property is an enhancement of both materials' individual effects and a product property denotes an emerging effect that is absent in both individual materials. The indirect coupling of a piezoelectric and a magnetostrictive phase mediated by strain is an example of such a product property. A side note on nomenclature: the term heterostructure applies to all structures that combine at least two distinct materials, such as substrate and film. A multilayer consists of a repeated stacking sequence of at least two distinct materials, typically, but not necessarily in a periodic fashion. Su-

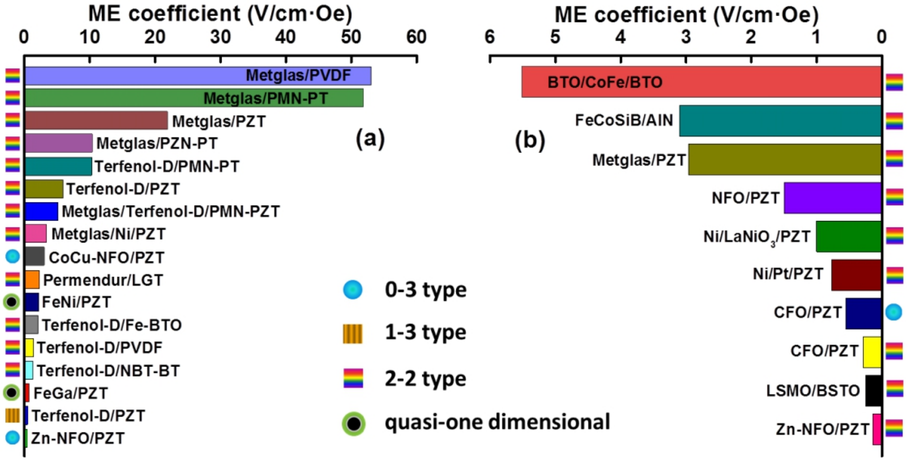

Figure 2.4: Reported α_{ME}-values measured out of resonance for *left*: bulk composite structures and *right*: thin film composite structures. Connectivity scheme in *Newnham* notation as color-coded. The image is directly adapted from Ref. 23.

perlattices are well ordered periodic multilayers and are generally referred to as such if the individual layers consist of countable monolayer units.

Bulk particulate composites were primarily investigated in the earlier stages of magnetoelectrics research, but they generally show small ME effects and suffer from high leakage currents [5]. Instead, most current research focuses on laminated bulk composites or thin film heterostructures [23]. Of these two, thin film heterostructures offer greater freedom in design and control over the fabrication process, as well as more direct mechanical and chemical bonding. In particular the engineering of interface structures via strain and layer thickness, as well as control over crystalline quality, structure and orientation led to stronger coupling of the constituent components [2, 23, 24]. A comparison of the magnetoelectric coupling coefficients of various such material systems is presented in Fig. 2.4. A similar comprehensive comparison can be found in Ref. 25.

The ME effect in purely strain-coupled composites is found to be highly dependent on the relative proportions of the constituent piezoelectric and a magnetostrictive phases [5, 10]. The α_{ME} vs. composition curve can be described as a skewed upside down parabola, α_{ME} tending towards zero for pure compounds and reaching a maximum for intermediate compositions, which is constituent with the theoretical model of a product property [26, 27]. Typical choices for the ferroelectric phase are BTO, $(\mathrm{Pb,Zr})\mathrm{TiO_3}$ (PZT), $\mathrm{Pb(Mg_{1/3}Nb_{2/3})O_3}$–$\mathrm{PbTiO_3}$ (PMN-PT), or polyvinyl-difluride. Magnetostrictive components are either metals like Ni or Co, alloys such as Metglas or Terfenol-D, or oxides like $\mathrm{La_{0.7}Sr_{0.3}MnO_3}$ (LSMO) or $\mathrm{CoFe_2O_4}$ [23] (see also Fig. 2.4). An ME effect can even be measured in commercially available $\mathrm{BaTiO_3}$-Ni multilayer capacitors [28, 29]. These kind of composites typically show α_{ME}-coefficients of a few

$\mathrm{V\,cm^{-1}\,Oe^{-1}}$ at most frequencies and up to two orders of magnitude enhanced values when measured at electromechanical or ferromagnetic resonance [2, 23]. However, the ME effect is mostly negligible, if no bias magnetic field H_{bias} is applied, or if H_{bias} is larger than a few 100 Oe [5, 24]. Measured at optimized H_{bias}, some macroscopic composites of Metglas or Terfenol-D with ferroelectric materials show α_{ME}-values in the order of several tens of $\mathrm{V\,cm^{-1}\,Oe^{-1}}$, as shown in Fig. 2.4. These material systems are hence currently the cutting-edge forerunners for application purposes, against which other magnetoelectrics are to be compared.

A number of other, interface-driven ME coupling effects have been identified over the past two decades. Charge-mediated coupling is based on the sensitivity of the magnetism in strongly correlated oxides on the charge carrier density [25]. ME coupling at PZT-LSMO interfaces can reach similar magnitudes as in strain-coupled heterostructures [10, 30]. There are also reports of strain and charge co-mediated coupling, for example in PMN-PT-$\mathrm{Ni_{0.79}Fe_{0.21}}$ [31] and BTO-LSMO [32] heterostructures. Other ME coupling mechanisms like interface orbital reconstruction [33,34] and charge ordering [34] have attracted academical interest, but have not yet shown to produce sizable α_{ME}-values. Exchange bias coupling makes use of one of the weaknesses of intrinsic multiferroics like BFO, $\mathrm{Cr_2O_3}$ and $\mathrm{YMnO_3}$, which is their anti-ferromagnetic ordering. In contact with a ferromagnet such as FeCo or NiFe, interface-spin coupling produces a horizontal shift of the $M(H)$-curve, called exchange bias. Controlling magnetism via exchange coupling is however limited to very thin layers of ~10 nm of the ferromagnetic component [25].

Another emerging factor to be considered in particular in perovskitic metal oxide heterostructures is the tilting of oxygen octahedra (see Sec. 3.1, [35-37]). The rotation of oxygen octahedra in perovskite oxides plays a crucial role in determining many of the materials' properties, as especially magnetism and ferroelectricity are highly sensitive to variations in bond angles [37]. Hence, the interfaces of materials with differing systems of oxygen octahedral tilt (OOT) are discontinuities with the potential for substantial novel effects. Disruption of an OOT system through geometric constraints can be blocked by just one monolayer of a tilt-free material [38], or in other cases propagate several nm from the interfaces [35-37]. The concept of OOT is outlined further in the following chapter.

Chapter 3

Materials

This chapter gives an overview over the materials used in this thesis. All materials used are perovskite oxides with closely matched lattice constants, which is advantageous for hetero-epitaxy. A brief summary of publications concerning heterostructures based on BFO and in greater detail BTO-BFO heterostructures is presented.

3.1 The General Structure of Perovskites ABX_3

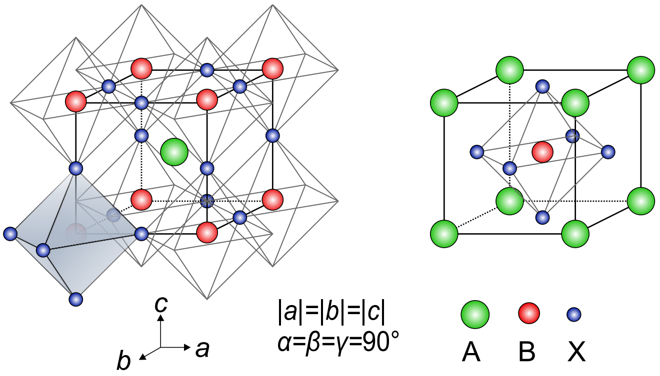

Figure 3.1: Generalized perovskite structure ABX_3 in two equivalent settings.

Perovskites are widely considered to be a particular versatile and technologically relevant crystal system [39, 40]. Named after the titular mineral *Perovskite* $CaTiO_3$, this class with the generalized sum formula ABX_3 includes insulators such as $SrTiO_3$ [39], metallic conductors like $SrRuO_3$ [41], high-capacity ferroelectrics like $BaTiO_3$ [42], multiferroic $BiFeO_3$, high temperature superconductors like $YBa_2Cu_3O_{7-x}$ [39], and a promising novel type of solar cell materials [43]. As complex metal oxides, they can accommodate a wide range of crystal defects [44]. In the extreme, ordered defects are the source of exceptional material properties, such as the superconductivity in certain cuprates [45]. The archetypical cubic ABX_3 perovskite structure is depicted in Fig. 3.1.

A and B form two nested cubic lattices with X in the center between adjacent B atoms, forming corner-sharing BX_6 octahedra.

The ideal perovskite is cubic with $Pm\bar{3}m$ symmetry, from which a large number of lower symmetry structures is derived. The crystal lattice angles $\alpha,\ \beta,\ \gamma$ are all equal to 90° and the lattice constants $a,\ b,\ c$ are all of the same length. Depending on factors like cation size ratio and temperature, three types of distortions of the ideal cubic structure can occur: distortion of the BX_6 octahedra, B cation displacement and BX_6 octahedral tilting [46, 47]. In fact, the perovskite structure can so easily adapt these predominantly subtle distortions that the ideal centrosymmetric cubic symmetry is only rarely found, such as in $SrTiO_3$ at room temperature. In fact, even the archetypical $CaTiO_3$ crystallizes in a monoclinically distorted structure. Some distortions, such as the distortion of the TiO_6 octahedra and displacement of Ti^{4+} in $P4mm$ symmetric $BaTiO_3$ retain the fourfold rotation axis and do not allow octahedral tilting [46,47]. In the case of oxide perovskites, one speaks of oxygen octahedral tilt (OOT). Octahedral tilting systems are typically classified using the notation introduced by *Glazer* [46,48] with the symbols $a^*b^*c^*$. Here, $a,\ b,\ c$ denote tilting toward the three spacial directions $x,\ y,\ z$ about which tilting of the BX_6 octahedra can occur, the repetition of a letter, such as in $a^*a^*a^*$ indicates equal tilt magnitude. The asterisk $*$ can take the values $+$, $-$ and 0, referring to in-phase $(+)$, out-of-phase $(-)$ and no tilting (0) of alternating octahedra. Thus cubic $Pm\bar{3}m$ perovskite would be denoted as $a^0a^0a^0$.

Both components of the multilayers discussed in this thesis, $BaTiO_3$ and $BiFeO_3$, as well as the substrate $SrTiO_3$ are oxide perovskite materials. The choice is deliberate, since it is advantageous for hetero-epitaxy to combine materials of similar structure and with low lattice misfit. Hence also the choice of $SrTiO_3$ as a substrate material for the thin film grown in the framework of this thesis.

3.2 Strontium Titanate $SrTiO_3$

Strontium titanate ($SrTiO_3$, STO) is a cubic perovskite. The lattice parameter a is 3.905 Å [49], Sr^{2+} and Ti^{4+} occupy the positions A and B, as depicted in Fig. 3.2. STO is insulating (resistivity $>10^7\,\Omega\,\mathrm{m}$), paraelectric due to its centrosymmetric structure and diamagnetic [49]. It has gained popularity in the past as growth substrate for $YBa_2Cu_3O_{7-x}$ superconductors [49] and is widely used as an inexpensive growth substrate for perovskite oxides. A prevalent preparatory method in thin film growth is etching with buffered HF and subsequent annealing of STO single crystalline substrates, which establishes a well defined surface [50, 51]. STO consists of alternating layers of SrO and TiO_2. In aqueous solution, hydrophilic SrO groups are hydroxyl-

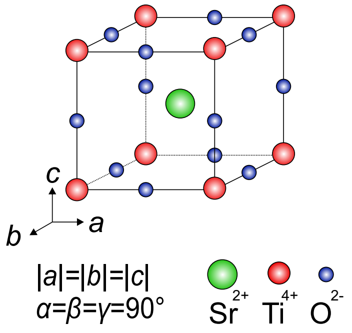

Figure 3.2: Representation of the structure of $SrTiO_3$. Along the {100} directions, $SrTiO_3$ can be represented as alternating layers of net stoichiometries SrO and TiO_2.

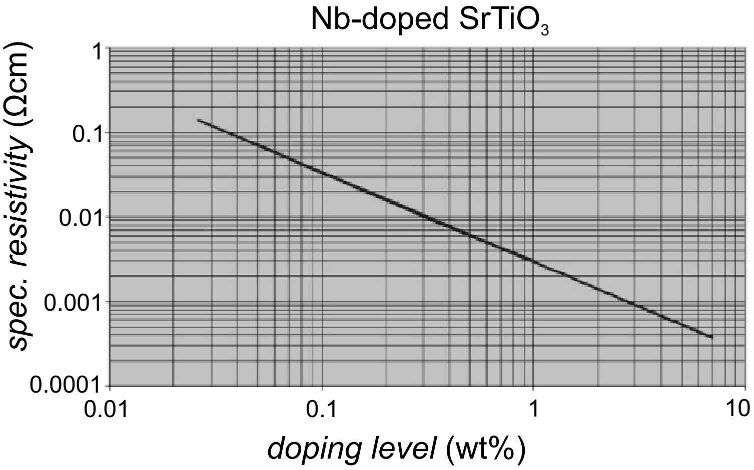

Figure 3.3: Specific resistivity of Nb doped $SrTiO_3$ in dependence of the Nb doping concentration in wt%. Graph adapted from Ref. 52.

ized and preferentially etched by HF. The annealing step leads to the formation of an unit-cell stepped, TiO_2-terminated surface structure.

STO can be doped with Nb to induce conductivity [52], the resistivity in $SrTiO_3$:Nb (NSTO) depends on the doping concentration (see Fig. 3.3). The specific resistivity of the predominantly used 0.1 wt% Nb doped STO is approximately $0.025\,\Omega\,\mathrm{cm}^{-1}$, hence any contact resistance between two electrodes on the typical 5 mm × 5 mm substrates will be negligible with respect to the typical $\sim 1 \times 10^6\,\Omega$ measured for the multilayer capacitors of BTO-BFO. Though perfect bulk STO is diamagnetic, weak ferromagnetic signals are often measured on STO [53,54] and NSTO [55] substrates. Impurities in the ppm range and surface defects at unpolished surfaces have been suggested at the origin of this effect, as well as contamination from Fe and Ni containing tools and sample holders [53, 56, 57]. The existence of intrinsic defect-induced magnetism in STO has been theorized, though this is still debated.

3.3 Barium Titanate $BaTiO_3$

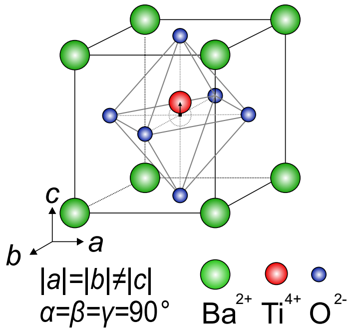

Figure 3.4: Representation of the structure of $BaTiO_3$. The lattice parameters a and b are equal, c is elongated. The tetragonal distortion and cation displacement are exaggerated for clarity.

Barium titanate ($BaTiO_3$, BTO) was the first oxide ceramic with ferroelectric properties discovered in the 1940's [42]. It was initially valued as dielectric material with high permittivity, which has been reported to be as large as 800 to 1600 [58], for its use in capacitors. While lead zirconate titanate (PZT) has largely replaced BTO for electromechanical actuator purposes due to PZT's superior ferroelectric properties, BTO-based ceramics have gained renewed popularity in recent years as a lead-free alternative [59]. BTO remains one of the most widely used ferroelectric ceramics, in particular for multilayer capacitors [59]. Room temperature resistivity can vary from 10^7 to $10^{10}\,\Omega\,\mathrm{m}$ [60].

BTO is cubic above the ferroelectric T_{Curie} of 393 K. Below 393 K, the tetragonal phase with $P4mm$ symmetry, depicted in Fig. 3.4, forms, succeeded by an orthorombic phase below 278 K and a rhombohedral phase below 183 K [61,62]. The tetragonal room temperature phase has the bulk lattice parameters $a = 3.991$ Å and $c = 4.035$ Å [62], with a lattice mismatch of 2.3 % of a relative to STO. The transition from cubic to tetragonal introduces the asymmetric displacement of the Ti^{4+} cations that give rise to the material's ferroelectricity. According to the geometrical constraints imposed by the tetragonal, orthorombic and rhombohedral phases, the resulting spontaneous polarization $\boldsymbol{P}_{\mathbf{S}}$ can point parallel to the pseudo-cubic $[001]_{\mathrm{pc}}$, $[011]_{\mathrm{pc}}$, or $[111]_{\mathrm{pc}}$ directions, respectively [61, 62]. The transition from cubic to tetragonal can create three distinct domains relative to a specific cubic $[001]_{\mathrm{c}}$ direction: c-domains where $\pm\boldsymbol{P}_{\mathbf{S}} \parallel [001]_{\mathrm{c}}$, a_1-domains where $\pm\boldsymbol{P}_{\mathbf{S}} \parallel [010]_{\mathrm{c}}$ and a_2-domains where $\pm\boldsymbol{P}_{\mathbf{S}} \parallel [100]_{\mathrm{c}}$. Here, $[001]_{\mathrm{c}}$ refers to the substrate out-of-plane direction. Deposition parameters can determine whether mixed, purely a-oriented or c-oriented films are grown in hetero-epitaxy [63].

As mentioned in Section 3.1, the $P4mm$ symmetry forbids OOT. In fact, a single monolayer of BTO has been shown to be sufficient to block the propagation of OOT from a layer with pronounced OOT, such as $GdScO_3$, into a layer that is highly susceptible to distortion via OOT, such as $SrRuO_3$ [38].

In this work, BTO is used mainly for its ferroelectric properties. BTO is also far less conductive than BFO and can reduce the inherent leakage current of BFO, when layered (see Sec. 5.1.4). While BTO is not ferromagnetic in bulk, there are reports on defect-induced ferromagnetism. Theoretical calculations predict the emergence of ferromagnetism in BTO due to oxygen vacancies [64]. Furthermore, nano-particles of BTO exhibit ferromagnetism due to uncompensated spins of sub-coordinated surface Ti^{2+} and Ti^{3+} [65]. Both effects can per se also occur in thin films and at the interfaces in multilayers.

3.4 Bismuth Ferrite $BiFeO_3$

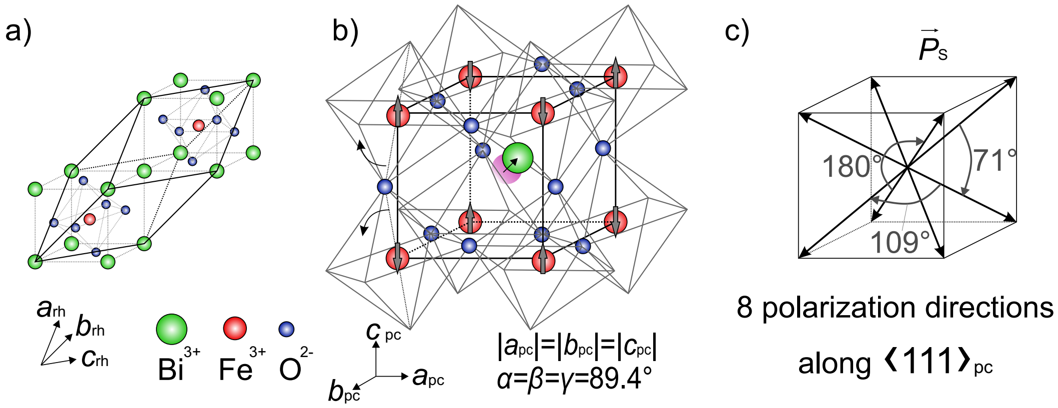

Figure 3.5: **(a)** Representation of the structure of $BiFeO_3$ in rhombohedral setting; **(b)** pseudo-cubic setting with oxygen octahedra tilted in alternating fashion in all three pseudo-cubic directions ($a^-a^-a^-$ in *Glazer* notation [48]). The Bi $6s^2$ lone pair electrons (indicated by the magenta cloud), not contributing to any chemical bond, are the source of the local dipole moment in the BFO unit cell. The gray arrows indicate the G-type anti-ferromagnetic ordering of the Fe^{3+} spins. **(c)** The resulting polarization can be directed along the four body diagonal directions, creating eight possible polarization directions along $\langle 111\rangle_{pc}$. The resulting domain wall angles of 71°, 109° and 180° are indicated.

At room temperature, bismuth ferrite ($BiFeO_3$, BFO) is an intrinsic magnetoelectric multiferroic with both ferroelectric and anti-ferromagnetic order. The ferroelectric T_{Curie} is 1100 K [66] and the anti-ferromagnetic $T_{\mathrm{Néel}}$ is 643 K [67]. Since it was first synthesized in 1957 [68], it has attracted significant interest from the multiferroics community. One publication in particular by *Wang et al.* in 2003 [9], reporting $\alpha_{\mathrm{ME}} = 3\,\mathrm{V\,cm^{-1}\,Oe^{-1}}$ in 0 T and claiming a magnetization of 1 μ_B/f.u. (f.u.: formula unit) and spontaneous polarization of up to 60 µC cm^{-2}, has prompted a veritable explosion of investigations in the last two decades. The impact BFO has had on the field of magnetoelectrics has been compared to that of $YBa_2Cu_3O_{7-x}$ on the field of superconductivity [69].

BFO is a rhombohedrally distorted perovskite with $R3c$ symmetry. Fig. 3.5 a) schematically depicts the rhombohedral structure. An alternative and commonly used description of the BFO structure uses a distorted pseudo-cubic setting, depicted in Fig. 3.5 b). In pseudo-cubic notation, the lattice parameter of BFO is $a_{\mathrm{pc}} = 3.965\,\text{Å}$ (lattice mismatch to STO: 1.5 %), with a 89.4° lattice angle [69, 70]. In hexagonal notation, the lattice parameters are $a_{\mathrm{hex}} = 5.58\,\text{Å}$ and $c_{\mathrm{hex}} = 13.90\,\text{Å}$ where $\langle 111\rangle_{\mathrm{pc}} \parallel \langle 001\rangle_{\mathrm{hex}}$. The ferroelectricity is driven by the stereochemically active Bi^{3+} $6s^2$ lone pair [71, 72]. The resulting broken cubic symmetry is accommodated in the rhombohedral structure by OOT around all $\langle 111\rangle_{\mathrm{pc}}$ directions ($a^-a^-a^-$ in *Glazer* notation [48]) with large tilt angles of approximately 11° to 14° [69]. The ferroelectric polarization can point toward any of the $\langle 111\rangle_{\mathrm{pc}}$ directions, leading to 8 possible polarization domains, as depicted in Fig. 3.5 c). Accordingly, there are 4 possible ferroelastic domains, corresponding to the 4 space diagonals, with possible domain wall angles of 71°, 109° and 180°. Though *Teague et al.* initially reported a bulk polarization of only 6 µC cm^{-2} [73], the true polarization was later found to be closer to the values reported by *Wang et al.*: 60 µC cm^{-2} along $\langle 001\rangle_{\mathrm{pc}}$, which is the projection of the polarization of 100 µC cm^{-2} along $\langle 111\rangle_{\mathrm{pc}}$ [69]. BFO has a permittivity of $\epsilon_{\mathrm{r}} = 53$, a relatively small value as compared to that of BTO [74].

BFO is a G-type anti-ferromagnet, meaning that the Fe^{3+} spins are coupled through the Fe−O−Fe bonds through super-exchange, leading to an anti-parallel arrangement in all pseudo-cubic x, y, z directions, as indicated in Fig. 3.5 b). The rhombohedral distortion due to the symmetry-breaking lone pair leads to a Fe−O−Fe bond angle of ∼155°. As a result, spin canting due to *Dzyaloshinsky-Moriya* interactions [75, 76] - an antisymmetric contribution to the super-exchange between Fe^{3+} ions - leads to the emergence of a non-zero net magnetic moment of the BFO unit cell [77, 78]. Though ferroelectricity and anti-ferromagnetism in itself have separate origins, this structural-magnetic relation is thought to be at the core of ME effect in BFO [77,79]. *Popkov et al.* used a *Ginzburg-Landau* symmetry approach to demonstrate that anti-ferrodistortion, i.e. anti-phase oxygen octahedra rotation is likely responsible for ME coupling in BFO [79]. However, in addition to this canting, the magnetic moment is arranged in a spin spiral along the $[1\bar{1}0]_{\mathrm{pc}}$ direction with periodicity of ∼62 nm, which is incommensurate with the crystal lattice and cancels out the net magnetization macroscopically [80]. As a result, the bulk ME effect is generally thought to be connected with γ-Fe_2O_3

impurities, with α_{ME}-values as low as $7\,\mathrm{mV\,cm^{-1}\,Oe^{-1}}$ [81]. It has been found that the spin spiral can be destroyed by large magnetic fields [82, 83], doping [84-87, H3] and epitaxial constraint [88], leading to a small net magnetization of 0.02 μ_{B}/f.u. [69].

Growth of phase pure BFO thin films by PLD is reportedly possible only in a small parameter range. *Bea et al.* found a narrow range close to 580 °C and 10^{-2} mbar O_2 pressure and likewise *Jiang et al.* report a temperature range of 600 to 730 °C [89]; above and below these ranges, formation of either Bi_2O_3, γ-Fe_2O_3, or Fe_3O_4 can occur. Bi_2O_3 is highly conductive and can act as a short circuit in a film. Both iron oxides are ferromagnetic and assumed to be at the root of many reports of substantial magnetization of BFO films substantially exceeding 0.02 μ_{B}/f.u. [69, 90, 91]. Eclipse PLD is known to improve both film roughness and increase FE remanent polarization [92]. Epitaxial constraint is also a powerful tool to stabilize a number of related phases of $BiFeO_3$ [93], including a monoclinic phase with a large aspect ratio of $c/a = 1.23$ [94]. Different miscut angles can furthermore restrict the number of possible domains [93,95], which can be readily identified in reciprocal space maps (RSMs) [96].

One of the major drawbacks of BFO concerning applications and complicating experimental characterization is the typically large leakage current [97, 98]. Oxygen vacancies are thought to play a fundamental role in the leakage mechanism and a great deal of effort has gone into alleviating this problem via doping [99-105] and adjusting the content of volatile Bi by using over-stoichiometric targets [106, 107]. Charge injection and disparate barrier heights of asymmetric metallic electrodes further complicate the issue [95,97,98,108]. Additionally, it has also been found that certain domain walls in BFO show conductivity up to 6 orders of magnitude larger than mono-domain bulk material [109, 110].

Another experimental complication is the electrically induced breakdown of BFO into Bi_2O_3 and Fe_3O_4 in fields higher than $700\,\mathrm{kV\,cm^{-1}}$ [111]. While bulk BFO has coercive fields of $\sim$$100\,\mathrm{kV\,cm^{-1}}$, thin films typically have much larger coercive fields, with values in the range of 300 to $500\,\mathrm{kV\,cm^{-1}}$ and larger not being uncommon [111, 112]. Hence, recording full FE hysteresis curves requires the application of fields of 1 to $2\,\mathrm{MV\,cm^{-1}}$. Self-poling and imprint effects, which can for example be induced by temperature gradients in bulk [113] and thin films [114] or asymmetric electrode structures [95, 98, 108], can further increase the fields required for FE measurements.

3.5 Heterostructures Based on $BiFeO_3$

As the most studied intrinsic multiferroic, a large number of heterostructures have been created using BFO as one of the constituent phases. A comprehensive review on this topic by *Wu et al.* can be found in Ref. 115. While for many ferromagnet-ferroelectric heterostructures research efforts commonly take the route of macroscopic ceramic composites [10], the vast majority of publications concerning BFO emphasize thin films and nano-structures [115]. The reason for this trend lies amongst others in the possibilities of strain tuning, through which a number of derived $BiFeO_3$ structural phases can be stabilized [115]. *Wu et al.* further point to the malleability of ferroic properties by means of doping and surface- and interface-design in nano-structures [115].

3.5.1 Doping of $BiFeO_3$

Doping with foreign ions is a common technique in materials science that can affect material properties profoundly by introducing micro-strain and affecting the electronic structure. In an effort to improve on the magnetic and electric shortcomings of BFO, the effects of doping with a broad range of different elements have been reported. For example, a profound reduction of the leakage current in BFO films was reported by doping with various elements, such as Nd^{3+} [116], Cr^{3+} [101] and La^{3+} [117]. Improvements of the weak ferromagnetic properties of BFO can be achieved via doping with hetero-valent atoms, such as Ca^{2+}, Sr^{2+}, Pb^{2+}, Ba^{2+} [118], or homo-valent elements, like Nd^{3+} [119] and Co^{3+} [120]. A comprehensive review of doped BFO materials can be found in the recent review on BFO-based heterostructures by *Wu et al.* 115. In cooperation with our group, *Lazenka et al.* have reported on the effect of substitution of Bi^{3+} with homo-valent rare-earth atoms of La^{3+}, Nd^{3+}, and Gd^{3+} in thin films [87]. In analogy to their former study on bulk BFO-samples [121], they found an enhanced magnetization with increasing doping percentage, with the most profound effect produced by doping with Gd^{3+}. They also found a reduction of surface roughness and higher grade of preferential poling in atomic force microscope (AFM) and piezo-force microscopy. In Ref. H3, we explored the impact of Gd-doping on BTO-BFO multilayers, following the previous work of *Lazenka et al.* [87].

3.5.2 Composite 2-2 Heterostructures with $BiFeO_3$

Most publications concerning ME coupling in BFO-based heterostructures explore exchange-bias effects using either transition metal or metal oxide ferromagnets layered on BFO thin films [115, 122]. Heterostructures of BFO and LSMO are a popular model system of a multiferroic coupled to an metal oxide ferromagnet [122-125]. The interface magnetism and exchange-bias coupling in this system are being studied extensively [124]. *Guo et al.* used PNR to locally resolve the magnetization in BFO-LSMO superlattices and found a magnetization of $1.86\,\mu_B$/Fe atom [125]. They "exclude charge transfer, intermixing, epitaxial strain, and octahedral rotations/tilts as dominating mechanisms for the large net magnetization" and instead suggest strong orbital reconstruction between Fe and Mn across the interfaces as the origin. Similarly orbital reconstruction was reported to occur at the interfaces in BTO-LSMO heterostructures [33]. Few reports on strain coupling based ME interactions in BFO based heterostructures exist. One such example are CoF_2O_4 nano-pillars embedded in a BFO thin film, for which a transverse α_{ME} of $60\,mV\,cm^{-1}\,Oe^{-1}$ at 6 kOe was obtained [126]. In a rare example of a multiferroic-multiferroic heterostructure, short period BFO-$BiMnO_3$ superlattices push the ferromagnetic transition temperature to 410 K [17].

3.5.3 $BaTiO_3$–$BiFeO_3$ and Related Heterostructures

Composites of BFO and a ferroelectric component, typically of the ABO_3 perovskite type, generally aim to mitigate the detrimental effects of leakage in bare BFO devices. Among the common oxide ferroelectrics, BTO has proven to additionally lead to ME coupling [11, H5]. This section will give a brief overview over the limited amount of publications which report on the explicit material combination of BTO and BFO and closely related systems outside our group. A large portion of these publications concern macroscopic solid-solution ceramics [127-132] and solid-solution thin films [133, 134]. In recent years, a few reports on polycrystalline BTO-BFO thin film heterostructures have been published [135-139]. And lastly, some closely related epitaxial heterostructure systems will be covered [140-145]. The α_{ME}-coefficients of these systems, where available, are listed in Table 3.1.

The first report on BTO-BFO solid-solution ceramics including ME measurements goes back to *Ismailzade et al.* in 1981 [127]. They investigated the systems BFO-BTO and BFO-$PbTiO_3$, which demonstrated bias field dependent ME coupling and multiferroicity. *Yang et al.* found magnetoelectricity in $BTO_{(1\text{-}x)}$-BFO_x solid-solution ceramics only in a limited range of $x = 0.71$ to 0.8 [128]. The largest value of α_{ME} with $0.87\,mV\,cm^{-1}\,Oe^{-1}$ was measured for a sample with $x = 0.725$, which is still an order of magnitude lower than the value reported for bulk BFO samples by *Caicedo et al.* [81]. A vastly stronger effect was measured when laminating the BTO-BFO ceramic with magnetostrictive Ni [128], resulting in α_{ME} of $75.4\,mV\,cm^{-1}\,Oe^{-1}$ at H_{bias} of 100 Oe with remanent α_{ME} of $13.6\,mV\,cm^{-1}\,Oe^{-1}$ at zero H_{bias}. *Priya et al.* were able

Table 3.1: Overview of ME coupling coefficients α_{ME} measured for BFO, BTO-BFO systems and related material combinations, as reported in the literature. †: measured at resonance frequency; ‡: measured in the $\boldsymbol{H}_{\mathrm{DC}}$ field resulting in the maximum α_{ME}-value.

material system	structure	f (kHz)	$\boldsymbol{H}_{\mathrm{DC}}$ (Oe)	α_{ME} ($\mathrm{V\,cm^{-1}\,Oe^{-1}}$)	Ref.
BFO	thin film	quasistatic	0	3	[9]
BFO	bulk	7	120‡	0.007	[81]
BTO-BFO:(Sc, MnO_2)	solid solution	257†	0	0.43	[131]
$BTO_{0.275}$–$BFO_{0.725}$	solid solution	1	2000‡	0.87	[128]
$BTO_{0.275}$–$BFO_{0.725}$/Ni	laminate	1	100‡	0.0754	[128]
$BTO_{0.2}$–$BFO_{0.8}$	solid solution	1	8000‡	0.0023	[146]
BTO-BFO:(Dy, Cu)	solid solution	n.a.	n.a.	3.2×10^{-6}	[132]
BFO–$CoFe_2O_4$	3-1 thin film	n.a.	6‡	0.06	[126]
BFO/BTO	thin film	0.999	500‡	0.061	[138]
BTO/BFO/BTO	thin film	0.999	4000‡	0.515	[139]
BFO-PZT	3-3 thin film	1	5100‡	0.3	[142]

to improve the saturation magnetization of $BTO_{0.15}$-$BFO_{0.85}$ phase pure ceramics by co-doping with Dy and Cu from ~0.01 to 0.1 μ_B/f.u., but only measured a α_{ME}-value of maximum 0.003 $\mathrm{mV\,cm^{-1}\,Oe^{-1}}$ [132]. *Wei et al.* found that BTO in BFO greatly increases resistivity, though an excessive amount of BTO reduces P_{rem} [130]. Similarly, *Guo et al.* reported a reduction of two orders of magnitude in the leakage current in $BiFe_{0.96}Sc_{0.04}O_3-BaTiO_3$ ceramics when modified with MnO_2 [131]. They further reported an enhanced magnetization and a - for bulk ceramics - considerable α_{ME}-coefficient of 429.6 $\mathrm{mV\,cm^{-1}\,Oe^{-1}}$ at resonance for 2.0 at% Mn ion doping. A review on symmetry transformations and ferroic properties in solid-solutions of BFO with BTO, $PbTiO_3$ and $PbZrO_3$ has been published by *Freitas et al.* [129]. A comprehensive review of BFO-ABO_3 solid solution ceramics can be found in Ref. 115.

Ueda et al. first reported on reduced leakage current in epitaxial BTO-BFO solid-solution thin films deposited on NSTO by PLD [133]. However, their films showed very low polarization ($P_{\mathrm{rem}} = 2.5\,\mathrm{\mu C\,cm^{-2}}$) and magnetization values of ~0.01 μ_B/f.u.. *Murugavel et al.* expanded on this research by creating similar epitaxial films across the entire composition range [134]. They obtained more reasonable polarization values of 24 $\mathrm{\mu C\,cm^{-2}}$ for an intermediate composition, with magnetization values up to 0.05 μ_B/f.u.. For comparison, our group found polarization values up to 75 $\mathrm{\mu C\,cm^{-2}}$ in BTO_{67}-BFO_{33} films [11]. No measurements of α_{ME}-coefficients of BTO-BFO solid-solution films are known aside from our own research [11, 147].

Sharma et al. published a series of articles on polycrystalline BTO-BFO multilayers on Pt/SiO_2/Si derived by PLD [135, 137] and spin-coating [136]. They reported enhanced ferroic properties for four-layer PLD-films of BFO/BTO/BFO/BTO with P_{sat}

of 50.49 µC cm^{-2} M_{sat} of $\sim$0.4 μ_{B}/f.u. [135] and a reduced leakage current relative to bare BFO films [136]. *Gupta et al.* reported on the ME coupling in sputtered polycrystalline bi- and tri-layers of BTO and BFO [138, 139]. They measured α_{ME}-values of 61 mV cm^{-1} Oe^{-1} and 515 mV cm^{-1} Oe^{-1}, respectively, and the highest value found in a sample with 20 nm BFO thickness, which they attributed to bonding of interfacial Fe and Ti atoms. These α_{ME}-values are still an order of magnitude lower than the values obtained by *Wang et al.* [9] and two orders of magnitude lower than our own.

Toupet et al. found that the magnetization in BTO-BFO multilayers with varied periodicity scales inversely with the periodicity [143]. They suggested a number of interface effects as the possible origin of this effect: a ME proximity effect that could occur, given the presence of ferroelectric self-poling the local breaking of magnetic anisotropy by adjacent Ba^{2+} and Fe^{3+} ions at the interfaces and the occurrence of so called “loose spins”. Further reports include $BaSrTiO_3$-$BiNdFeO_3$ multilayers with $\sim$0.4 μ_{B}/f.u. magnetization [144] and BFO-PZT core-shell composite films derived by sol-gel method with an α_{ME}-value of 300 mV cm^{-1} Oe^{-1} [142]. Reduced leakage current density was also achieved for STO-BFO superlattices [140, 141]. The existence of a 2D electron gas at a Ti-diffused STO-BFO interface was reported by *Chen et al.* [145].

To conclude: a great effort has been made by various groups over the last few decades to improve the ferroic and magnetoelectric properties of $BiFeO_3$-based bulk and thin film compounds. This research has lead to a great many discoveries of novel phenomena and a deepened insight into the base workings of magnetoelectric multiferroics. However, aside from the sources cited above and in Table 3.1, very few tangible, explicit measurements of α_{ME} on BFO-based thin films can be found. And among these, there exist only few that reach, or even improve on, the values published in the pertinent paper published by *Wang et al.* [9]. In light of these facts, the results gained on epitaxial BTO-BFO heterostructures by our group can be fairly deemed exceptional, as will be detailed in the following section.

3.5.4 Previous Results on $BaTiO_3$–$BiFeO_3$ Heterostructures

Over the last eight years, our group has worked on BTO- and BFO-based ME heterostructures within the collaborative research center *SFB 762: Functionality of Oxide Interfaces.* We recently published the cumulative results of the research performed from 2012 to 2019 in Ref. H5. The following is an excerpt from publication H4, giving an overview of the progress in understanding of the topic prior to the work on this thesis:

“In 2014 we first reported on the enhanced ME coupling in thin film $BaTiO_3$-$BiFeO_3$ (BTO-BFO) composites with 2:1 and 1:2 composition ratios and 15×(BTO-BFO) multilayers [11]. The intrinsic multiferroic BFO and the ferroelectric BTO both possess perovskitic unit cells with closely matched lattice constants [11]. We measured an enhanced α_{ME}-value of $21\,\mathrm{V\,cm^{-1}\,Oe^{-1}}$ for a composite film with a 2:1 BTO-BFO composition ratio relative to the $4.2\,\mathrm{V\,cm^{-1}\,Oe^{-1}}$ measured for a BFO single layer. Further experiments showed that while the enhanced ME effect was larger in composites than in multilayers, it proved far more malleable in multilayers. We also reported for the first time the characteristic dependencies of α_{ME} on an external DC bias magnetic field H_{bias} for these composites and multilayers [11]. While the BFO single layers and composite films show a maximum and subsequent decrease in α_{ME} when H_{bias} is increased from 0 T to 6 T, similar to the behavior of bulk samples [121], multilayers show a saturating behavior [11]. This field dependency was observed for all BTO-BFO multilayer samples since [148-152, H3]. By variation of the $p_{\mathrm{O_2}}$ pressure during growth we found an increase of oxygen octahedral tilt [148] and micro-strain [149] with lowered $p_{\mathrm{O_2}}$ that correlated with a decrease of the respective α_{ME}-values. Note, however, that the pulse numbers were kept constant for these experiments, yielding increasingly larger d_{dl}-values with decreasing $p_{\mathrm{O_2}}$. A decrease of the BFO sublayer thickness with constant BTO thickness leads to a significant increase of the measured α_{ME}-value [152, H1, H3]. *Jochum et al.* showed that lowering d_{BFO} from 50 nm to 5 nm led to an increase of α_{ME} from $11\,\mathrm{V\,cm^{-1}\,Oe^{-1}}$ to $56\,\mathrm{V\,cm^{-1}\,Oe^{-1}}$, which was accompanied by an increasing asymmetry of the hyperfine field distribution [152]. Simultaneously the temperature dependence of α_{ME} changed from monotonically falling to monotonically rising, indicating a change of the dominant coupling mechanism [152]. The variation of the volume fraction of the ferroelectric and magnetostrictive phases in artificial magnetoelectric multiferroic composites is expected to have a strong influence on the magnetoelectric coupling in purely strain mediated heterostructures according to theoretic calculations [26, 27]. This has often been confirmed in experiments, for reviews detailing such examples, we refer to [10] and [5]. It is debatable however, whether this theory should be applicable in this case, as a) the combination BTO-BFO is ferroelectric-multiferroic rather than just ferroelectric-ferromagnetic (and strictly speaking bulk BFO is anti-ferromagnetic, not ferromagnetic), b) the BTO-BFO ratio variation based on BFO thickness variation leads to an overall thickness variation, and c) it is not entirely clear, if a purely strain mediated coupling effect lies at the core of the observed enhanced ME coupling. Through Mössbauer spectroscopy, we found a tilt of the preferential magnetic orientation from in-plane for single layer BFO films to out-of-plane for multilayers [150]. The number of double-layer repetitions in a sample enhances this effect and also leads to an increase of α_{ME} [151]."

Chapter 4

Experimental Section

> Why think? Why not try the experiment?
>
> John Hunter 1728–1793

In this chapter, the experimental techniques employed in the framework of this thesis are presented. The thin film deposition techniques used to create multilayer samples are presented first. Subsequently, structural analysis by X-ray diffraction, microscopy techniques and chemical profiling methods are discussed. Concluding, the ferroelectric, magnetic and magnetoelectric measurement techniques are explained.

4.1 Thin Film Fabrication

As in all fields of experimental solid state physics and materials science, a crucial factor in the particular field of thin film physics is the preparation of apt samples. Pulsed laser deposition is a reliable technique to create high quality epitaxial thin films [153], suited in particular for the deposition of metal oxides [154]. Another technique, known as magnetron sputtering, was used to create metallic contacts on the deposited thin films.

4.1.1 Pulsed Laser Deposition (PLD)

The technique known as pulsed laser deposition (PLD) is a physical vapor deposition process, i.e. the film is deposited onto a substrate by condensation of material from the gas phase. The general process of thin film deposition by PLD is depicted schematically in Fig. 4.1. A high energetic laser pulse is focused onto a polycrystalline target in a vacuum chamber (typically $p \leq 1\,\mathrm{mbar}$). The absorption of the laser pulse leads to

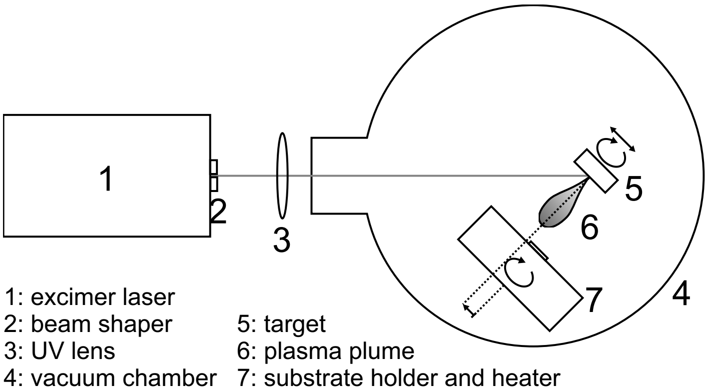

Figure 4.1: Schematic depiction of the key components involved in the PLD process.

the evaporation of material from the target surface and subsequent plasma formation [155,156], given that the pulse energy is above the target material's ablation threshold [157]. A number of ablation species of varying energy are formed, such as atoms, ions, electrons, and clusters. The angular spread of different species relative to the target surface is not necessarily uniform and transport to the substrate may vary due to different scattering probabilities, depending on target-substrate distance and ambient pressure [158]. Unfortunately, some processes such as subsurface heating [157,159] may cause the ejection of larger particles, called droplets, from the target surface. These droplets may reach sizes in the micron range and are thus often larger than the typical film thickness of a sample [159].

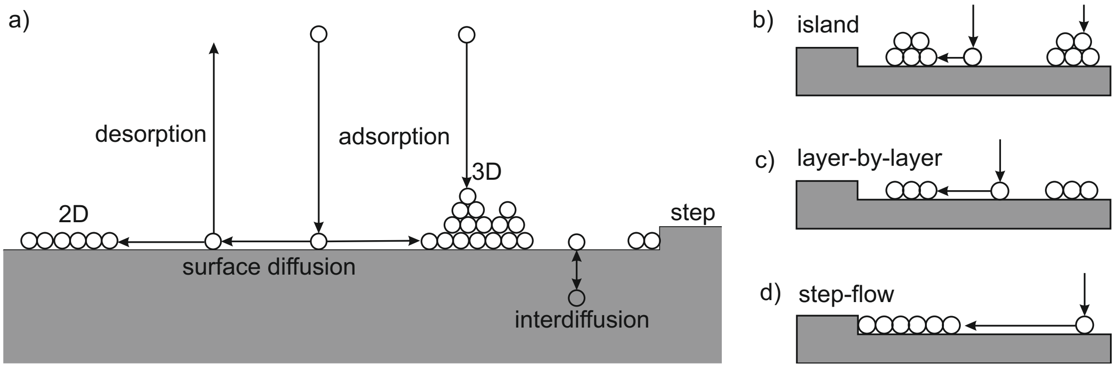

Figure 4.2: Schematic depiction of the fundamental processes involved in film growth by physical vapor phase deposition.

The ablated material then travels toward the substrate where it condenses. An interplay of succinct adsorption, desorption, surface-diffusion, and inter-diffusion fundamentally determines the particulars of film growth, as depicted in Fig. 4.2 a). The adsorption to desorption rate for example determines the net influx of ad-atoms, which may shift, based on factors like gas pressure and substrate temperature, and may vary based on ad-atom species. In the case of highly volatile materials such as Bi, non-stoichiometry in films can be compensated by overabundance in the target [90]. Likewise, the choice of O_2 as process gas, or post-annealing in higher O_2 pressure at high temperature can mitigate the effects of oxygen deficiency created during growth.

Depending on material-specific mobility, particle influx and temperature, four generally recognized growth modes can occur: (I) island-growth (known as *Volmer-Weber* growth), (II) mixed island and monolayer growth (*Stranski-Krastanov* growth), (III) layer-by-layer growth (*Frank-van der Merwe* growth) and (IV) step-flow growth [155, 160]. Surface diffusion allows an ad-atom to move about on the surface. This movement can be terminated when the atom arrives at a nucleation site, i.e. a substrate step, 2D or 3D island, as shown in Fig. 4.2 a). A particularly low surface mobility will lead to the formation of 3D islands, as the mean diffusion length is decreased. This case is depicted in Fig. 4.2 b). If the surface mobility is increased, e.g. by raising the growth temperature, the ad-atoms will tend to form 2D islands instead, resulting in layer-by-layer growth, see Fig. 4.2 c). A mixed 3D island and 2D layer growth occurs if the ad-atom-substrate interaction is far more favorable than the one between ad-atoms, leading to an initial 2D coverage and a succinct 3D growth. In the extreme case of very high ad-atom mobility, which is the case at elevated growth temperatures, surface diffusion is terminated only when a step on the growth surface is reached. As depicted in Fig. 4.2 d), the ad-atom attaches to the step edge, thereby forming the new step edge. The temperature required for step-flow growth can be reduced by increasing the substrate miscut angle and thereby reducing the lateral distance between steps.

Both the advantage and crux of the PLD technique is the multitude of parameters that can have an influence on the film growth. The laser repetition frequency, energy density determined by lens position and laser pulse energy, ablation spot size, target to substrate distance and lateral offset, as well as gas choice and pressure all influence the amount, energy and composition of ablated material that reaches the substrate surface. Typical growth rates range from 0.01 to 0.1 Å/pulse. To reach the desired film thickness, pulse numbers were determined by first calibrating the growth rate from single-layer films via X-ray reflectometry (XRR).

Two almost identical deposition chamber setups were used in the course of this thesis. The earlier samples, labeled with the naming scheme G$XXXX$ were grown in the so-called chamber G, which was operated together with a *Lambda Physik LPX 305 F* KrF excimer laser (first installed in 1991). In 2018, a new *Coherent LPX PRO 305 F* KrF excimer laser and a new chamber of identical build, named chamber F (sample names FYYY) were installed. Both chambers were designed and built in-house. Chamber F, pictured in Fig. 4.3, was built in 2017 within the framework of the collaborative research center *SFB 762: Functionality of Oxide Interfaces* and was exclusively used

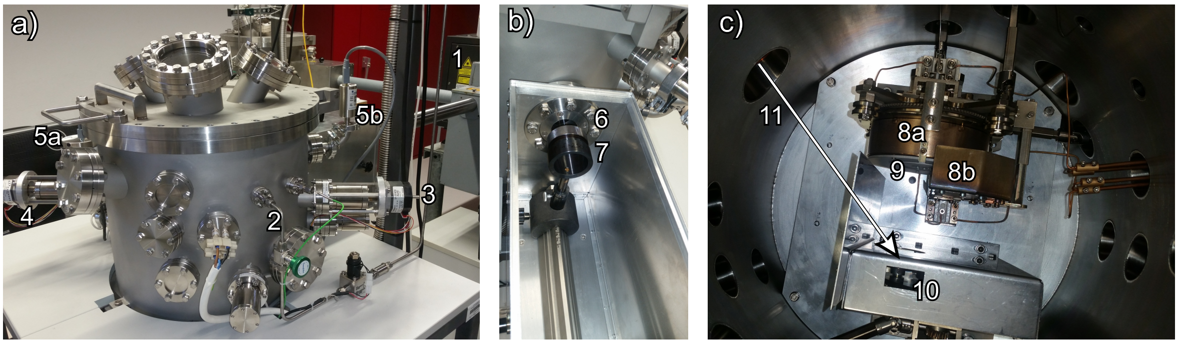

Figure 4.3: Photographic images of chamber *F*. **(a)** outside view, **(b)** focusing lens and **(c)** inside view. Main components as labeled in **(a)-(c)**: 1: laser (in the background), 2: gas inlet, 3: substrate rotation motor, 4: target rotation and (not visible) translation motor, 5: pressure sensors (two out of four in total), 6: laser window, 7: focusing lens, 8: substrate heater (front and back parts), 9: substrate holder, 10: target carousel, 11: laser beam path.

for the material systems discussed in this thesis to reduce cross-contamination. The lasers produce laser light at a wavelength of 248 nm with an energy set to 650 mJ per pulse and a repetition rate of 1 to 20 Hz. A plane-convex UV-fused silica lens, pictured in Fig. 4.3 b), focuses the laser light onto the target surface, leading to a laser energy density ρ_L at the target surface of approximately $2.0\,\mathrm{J\,cm^{-2}}$ at a lens-chamber distance *L* of 0 mm for chamber *G*. The explicit *L*-dependence of ρ_L for chamber *F* was determined experimentally and is presented in Fig. 4.4 (for details see the caption text).

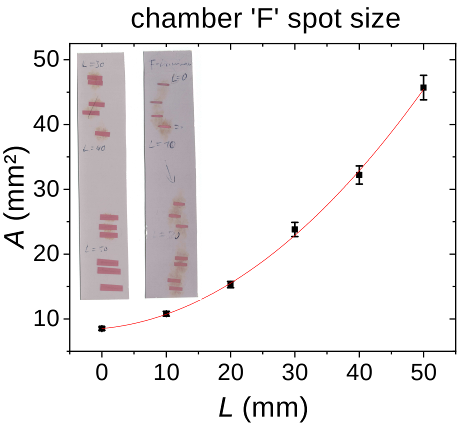

L (mm)	ρ (J/cm²)
0	3.8
5	3.3
10	2.9
15	2.4
20	2
25	1.8
30	1.5
40	1
50	0.7

Figure 4.4: Spot size and related approximate energy density in relation to parameter *L* for chamber *F*. The spot size was determined at the position of a fresh target using photosensitive paper (see inset). The energy density is based on the total energy of a nominal 650 mJ pulse as measured by energy monitor before passing through the lens and chamber window, after passing through a 24 mm × 10 mm rectangular aperture. The attenuation of the beam intensity by lens and chamber window is approximately 10 % each.

A combination of lateral and rotational movement of the target ensures an uniform ablation from the whole target surface area. A revolving target holder (10 in

Fig. 4.3 c)) with four slots for targets was used to switch the ablation target during the process without breaking the vacuum. The substrate holder (9 in Fig. 4.3 c)), at a distance of 10 cm from the target, is heated by a set of two resistive heaters (back and front, 8a and 8b in Fig. 4.3 c)), suitable to reach temperatures up to ca. 850 °C. The temperature is measured by thermocouple behind the resistive heating elements, the substrate temperature is estimated to be ∼50 to 80 °C lower than the process temperature T_p stated. Note that the process temperature quoted throughout this thesis always refers to the temperature measured by the thermocouple, not the estimated substrate temperature. A lateral offset QM relative to the ablation spot and rotation of the sample holder during ablation ensures an on average homogeneous spread of incoming particles across the substrate surface. A QM-value of 3, indicating three turns of the adjustment screw, equals a lateral offset value of $o_\mathrm{lat} = 10\,\mathrm{mm}$. At a QM-value of 0, the centers of target and substrate holder are positioned face to face. The 25 mm diameter substrate holder used throughout the framework of this thesis can hold up to four 5 mm × 5 mm substrates and is made from heat resistant 1.4828 stainless steel. All films were deposited using O_2 as background gas.

Standard Conditions

The great majority of samples produced in the framework of this thesis were deposited using the standard conditions listed in Table 4.1.

Table 4.1: Standard deposition conditions for BTO-BFO multilayers used in the framework of this thesis.

parameter	value
p_{O_2}	0.25 mbar
T_p	$700 \pm 5\,°\mathrm{C}$
f	15 Hz
ρ_L	$2.0\,\mathrm{J\,cm^{-2}}$
o_lat	9 mm

4.1.2 Eclipse–PLD

A special sub-form of PLD is the so-called eclipse-PLD, which is specifically designed to deal with the problem of droplets [161]. As depicted in Fig. 4.5, a shadow mask is introduced between target and substrate, blocking the direct path between the ablation area defined by the laser spot on the target. The mask size and position are adjusted in such a way that the substrates are fully shielded from the light emitted from the ablation area (i.e. eclipsed). Since the linear target-substrate path is blocked, heavy

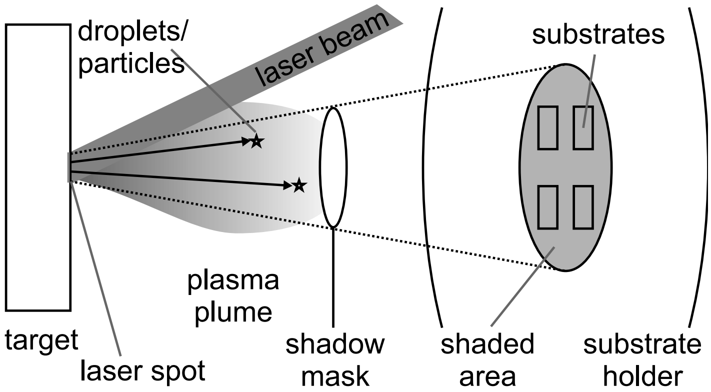

Figure 4.5: Schematic depiction of the eclipse PLD process. A shadow mask is set up in such a way between target and substrate holder that it projects a shadow from the bright ablation spot on the target onto the entire substrate area.

particles such as droplets and larger atomic clusters do not reach the substrate. Only lighter particles that have been redirected around the shadow mask by multiple scattering events will reach the substrate surface, which significantly reduces the deposition rate.

4.1.3 Target Preparation

The polycrystalline targets were prepared in-house by ball-milling, calcination, pressing, and sintering. Barium titanate was used as-received as 5N $BaTiO_3$ powder and sintered for 6 h at 1300 °C in air. Bismuth ferrite targets with 10 at% Bi excess were prepared by first milling 5N Bi_2O_3 and 5N Fe_2O_3 powders, calcinating for 4.5 h at 750 °C in air, milling again, and sintering for 10 h at 810 °C in air. An increase in relative density of the $Bi_{1.1}FeO_3$ targets from 0.75 to 0.85 was achieved by prolonging the calcination and sintering steps to 24 h. All samples in this thesis were grown using over-stoichiometric targets, the simplified designation BFO is used. The Gd-doped bismuth ferrite target was prepared from stoichiometric amounts of 5N Bi_2O_3, 3N Gd_2O_3, and 5N Fe_2O_3 powders to yield $Bi_{0.95}Gd_{0.05}FeO_3$, calcinating for 4.5 h at 750 °C in air, milling again, and sintering for 10 h at 810 °C in air. In reference to the 5 % Gd substitution films are referred to with the denomination BGFO.

4.1.4 Substrate Preparation

The initial growth process, beginning with nucleation at the substrate surface and continuing with diffusion across said surface, is highly dependent on the substrate morphology (roughness, kinks, steps) and surface chemistry (termination). Hence it is desirable to provide a well defined substrate surface. For the chosen substrate material

$SrTiO_3$, it is possible to generate a stepped, TiO_2-terminated surface by etching with a buffered HF solution and annealing for 2 h at 800 °C in 700 mbar O_2, for details see [50, 51]. The resulting surface exhibits unit-cell stepped terraces, the width of which is determined by the sample's miscut relative to the nominal crystallographic plane.

(100) oriented $SrTiO_3$ were purchased from *Crystal GmbH* (Berlin, Germany) and $SrTiO_3$:Nb with 0.05 wt %, 0.1 wt % and 0.5 wt % Nb content were purchased from *CrysTec GmbH* (Berlin, Germany).

4.1.5 Sputter Deposition

Metallic contacts for FE and ME measurements were deposited using shadow masks with DC magnetron sputtering. Sputtering uses the bombardment of a target with plasma ions to evaporate material. In DC magnetron sputtering, the plasma is generated by applying a high voltage to anode and target (cathode) in a low pressure gas atmosphere. Here, Ar was used as background gas for the deposition of Pt at a pressure of 0.025 mbar. Sputtering for 60 s at 30 W yielded ~100 nm Pt films. The substrate was not heated for this deposition.

4.2 X–Ray Diffraction

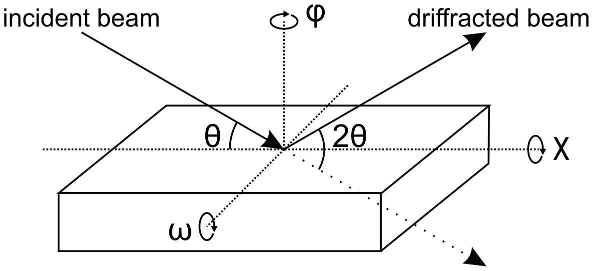

Figure 4.6: Schematic depiction of the angles involved in XRD measurements using a four-circle diffractometer.

The X-ray diffraction (XRD) measurements were performed with a *PANalytical X'pert MRD PRO* four-circle diffractometer with a X-ray tube, a parabolic mirror and *PIXcel*^{3D} detector, or a proportional detector in case of XRR scans. Since no monochromator was used, Cu $K_{\alpha 1}$ (wavelength λ =1.5406 Å) and $K_{\alpha 2}$ (λ =1.5444 Å, half intensity of $K_{\alpha 1}$) radiation components are both present. Fig. 4.6 schematically depicts the four angles involved in a four-circle diffractometer measurement: ω, θ, φ, and χ. Typically, the source of the X-ray beam is fixed, ω, φ and χ represent the possible movement angles of the sample stage and 2θ the movement angle of the detector arm relative to the incident beam.

4.2.1 $2\theta - \omega$ Scans

The diffraction of X-ray radiation results from the interaction of an electromagnetic wave with a structure of periodically modulated electron density, i.e. a crystal lattice. Constructive interference occurs when the *Bragg* condition is met:

$$2d \sin\theta_n = n\lambda \ . \tag{4.1}$$

Here, d can refer to the distance d_{hkl} between crystallographic planes with the *Miller* indices $h,\ k,\ l$. In a cubic lattice, the lattice parameter a can be derived from a *Bragg* peak position at the angle θ_n as $a = d_{hkl}/\sqrt{h^2+k^2+l^2}$ if the order n and wavelength λ are known. Likewise, the repetition of alternating layers in a multilayer stack also represents a periodic modulation of electron density in the growth direction. Accordingly, additional multilayer fringe peaks appear superimposed on the constituent layer peaks. The order n is not necessarily known for any given multilayer fringe peak, as only the ones close to the constituent material peaks possess significant intensities [162]. Hence, the multilayer periodicity, or double-layer thickness d_{dl} can be derived from the distance of two adjacent peaks as:

$$d_{\mathrm{dl}} = \frac{\lambda}{2} \frac{1}{\sin\theta_n - \sin\theta_{n-1}} \ . \tag{4.2}$$

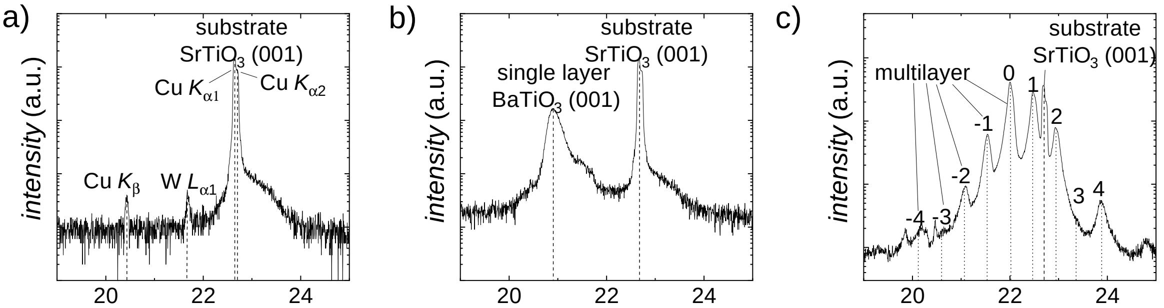

Figure 4.7: Exemplary 2θ-ω measurements near the SrTiO$_3$ (001) *Bragg* peak for **(a)** a bare SrTiO$_3$ substrate, clearly showing Cu $K_{\alpha1}$ and $K_{\alpha2}$ splitting as well as Cu K_{β} and W $L_{\alpha1}$ components, **(b)** a single-layer of BaTiO$_3$ on SrTiO$_3$ and **(c)** a BaTiO$_3$-BiFeO$_3$ multilayer SrTiO$_3$ with d_{dl} of 20 nm with clearly visible multilayer fringes, labeled by order. The 0th order peak corresponds to the (001) *Bragg* peak of the average out-of-plane (OOP) lattice parameter of the multilayer stack.

In a 2θ-ω scan, the $(00l)$ planes are probed by only scanning ω coupled with $2\theta = 2\omega$ and keeping χ at zero. The *PIXcel*$^{3\mathrm{D}}$ detector was used as a 1D line scanning detector with all 255 channels active to measure a 2.511° range per step. Three typical scans close to the (001) $SrTiO_3$ peak can be seen in Fig. 4.7. Cu $K_{\alpha1}$ and $K_{\alpha2}$ splitting is visible for sharp peaks such as the single crystal substrate peak in Fig. 4.7 a). Weaker Cu K_{β} (wavelength 1.3923 Å) and stray W $L_{\alpha1}$ (wavelength 1.4764 Å, from the X-ray tube's W filament) components are visible at lower angles due to the shorter wavelength. Fig. 4.7 b) shows a 2θ-ω scan of a single-layer. Note that the layer peak is much broader than the substrate peak due to finite size effects and local lattice parameter variation in imperfect crystals. The film's OOP lattice parameter can be extracted both from the total angle, as well as from the separation from the substrate peak, in which case the (known) substrate peak position functions as internal standard. A number of θ-angle dependent effects such as X-ray absorption and eccentricity of the beam relative to the center of the diffractometer cause shifts of the actual measured peak positions [163]. As these errors are minimized for $\theta \to 90°$, it is desirable to use high order peaks for lattice parameter determination, or better yet extrapolate from several peaks using e.g. the formalism proposed by *Nelson-Riley* [163]. This involves plotting the lattice parameters as measured from peaks at the angle θ versus the *Nelson-Riley* function $0.5\left(\frac{\cos\theta^2}{\sin\theta} + \frac{\cos\theta^2}{\theta}\right)$ and extrapolating a linear fit to $\theta \to 90°$.

In case of multilayers, the reflections stemming from the individual layers is superimposed with the multilayer fringe peaks and often obscured by them, as can be seen in Fig. 4.7 c). Typically more than 10 fringe peaks are used to determine d_{dl} from such measurements for greater accuracy. For further details on XRD of multilayers, the reader is referred to [162, 164].

4.2.2 Reciprocal Space Mapping

A measurement probing 2D reciprocal space, typically around a substrate peak, is called a reciprocal space map (RSM). This can be done by performing multiple ω-2θ scans at various ω offsets using a 0D receiving slit detector, which was the technique used at the start of this thesis. A newer, frame-based method reads out all 255 x 255 channels of the *PIXcel*$^{3\mathrm{D}}$ detector to measure local 2.511° 2θ scans by integration along γ (direction normal to the 2θ axis on the detector) at each step of scanning ω-2θ. Most importantly, RSMs around asymmetric reflexes with an in-plane (IP) and out-of-plane (OOP) component, such as the (103) $SrTiO_3$ peak were measured. These

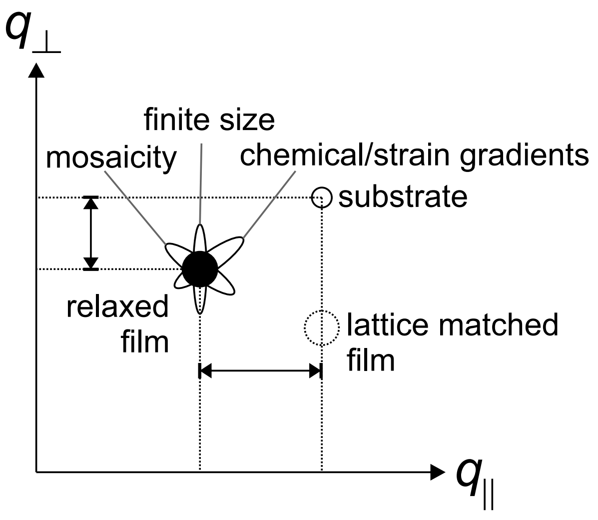

Figure 4.8: Schematic representation of the reciprocal space around an asymmetric substrate peak (empty circle) such as the STO (103) peak. A lattice matched film would appear as a horizontally matched peak (dashed circle), while a relaxed films are shifted (black circle). Possible origins of broadening are indicated after [165].

give an insight into the epitaxial relation between substrate and film, as Fig. 4.8 shows. The transformation from angular space to reciprocal space follows the relation:

$$q_{||} = \frac{1}{\lambda}\left(\cos\omega - \cos\left(2\theta - \omega\right)\right) \ , \quad q_\perp = \frac{1}{\lambda}\left(\sin\omega + \sin\left(2\theta - \omega\right)\right) \ . \tag{4.3}$$

Using the wavelength λ in units of nm gives the IP component $q_{||}$ and an OOP component $q_\perp$ in units of nm^{-1}.

In order to extract meaningful lattice parameters from a RSM, the position of a substrate peak is used as internal standard. This can be done by measuring the relative distances between film and substrate peak, as indicated in Fig. 4.8. Alternatively, the RSM can be put on an absolute scale by correcting any offset caused by misalignment of goniometer and sample, by aligning the measured substrate peak position with its nominal position [166, 167]. For a cubic system, the transformation from q to q_{corr} for a RSM around a substrate peak $(h0l)$ with an IP and OOP component is a simple rotation and expansion:

$$q_{||,\mathrm{corr}} = \frac{h}{s}\left(\cos\left(\alpha\right) \cdot q_{||} - \sin\left(\alpha\right) \cdot q_\perp\right) \ ; \quad q_{\perp,\mathrm{corr}} = \frac{l}{s}\left(\sin\left(\alpha\right) \cdot q_{||} + \cos\left(\alpha\right) \cdot q_\perp\right) \ ; \tag{4.4}$$

where α is the correction angle:

$$\alpha = \arccos\frac{q_{||,h} \cdot q_{||,H} + q_{\perp,l} \cdot q_{\perp,L}}{\sqrt{q_{||,H}^2 + q_{\perp,L}^2} \cdot \sqrt{q_{||,h}^2 + q_{\perp,l}^2}} \ ; \tag{4.5}$$

and s the expansion coefficient;

$$s = \frac{\sqrt{q_{\parallel,H}^2 + q_{\perp,L}^2}}{\sqrt{q_{\parallel,h}^2 + q_{\perp,l}^2}} \,. \tag{4.6}$$

Further, $q_{\parallel,h}$ and $q_{\perp,l}$ are the measured and $q_{\parallel,H} = h/a_{\text{sub}}$ and $q_{\perp,L} = l/a_{\text{sub}}$ the nominal substrate peak positions, as defined by the *Miller* indices h and l and the substrate lattice parameter a_{sub}. The reader is directed to [162,168] for further information about RSM measurements and to [166, 167] concerning correction of RSM data.

4.2.3 X–Ray Reflectivity

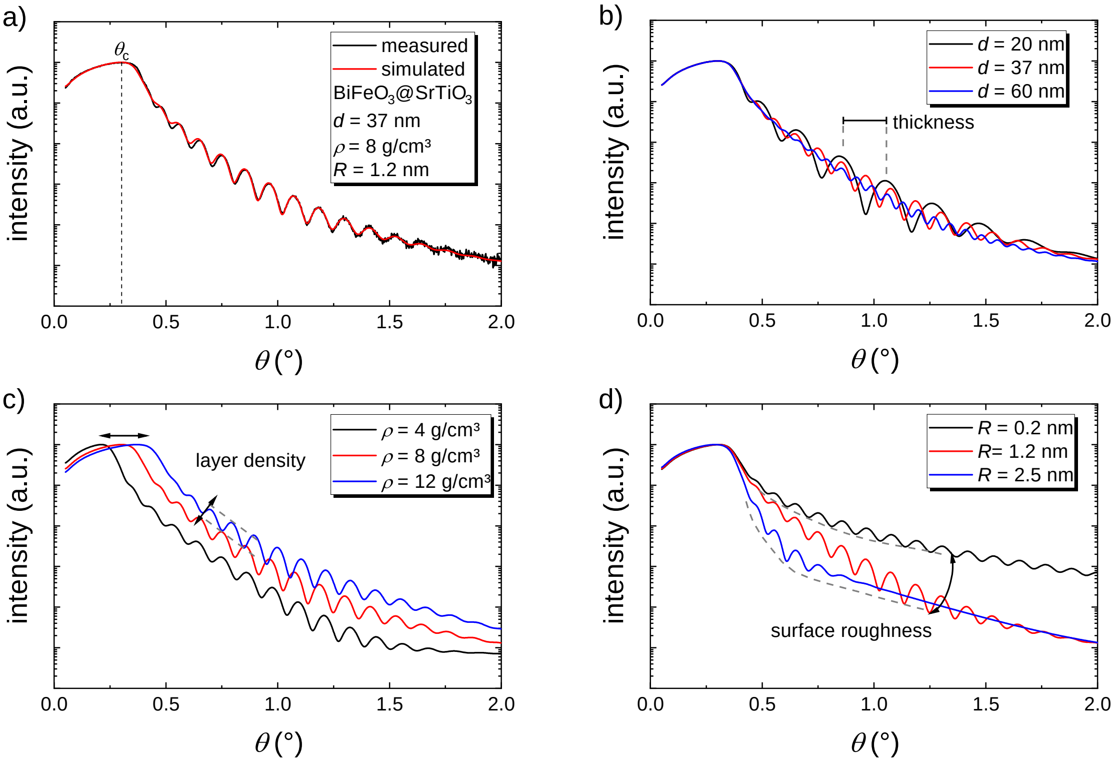

Figure 4.9: **(a)** Exemplary X-ray reflectometry scan (black) and simulated data (red) for a 37 nm BiFeO$_3$ film on SrTiO$_3$, **(b)-(d)** variation of the simulation parameters layer thickness (b), layer density (c) and surface roughness (d).

X-ray reflectometry (XRR) is a low-angle (0 to 5°) measurement used to determine layer thickness and roughness of thin films up to ~500 nm. As with 2θ-ω measurements, the detector and sample tilt are scanned in such a way that $\theta = \omega$. After the critical angle θ_C, at which total reflection occurs, reflected intensity decreases and intensity oscillations are observable, as shown in Fig. 4.9. The critical angle and spacing of the intensity oscillations depend on the thickness and refractive index of the substrate, layer(s) and surrounding medium (air). The amplitude of the oscillations and overall intensity decrease depends on the surface and interface roughness of the sample.

The software *X'Pert Reflectivity* was used to simulate XRR measurements. Fig. 4.9 shows a simulated scan fitted to the measured data. The refractive index of a layer is a function of the incident wavelength and the electron density within the sample. The local electron density is modeled as a combination of chemical composition and macroscopic density. Layer thickness, layer density and roughness are varied in the iterative fitting process to minimize the error between simulated and measured curve. For more details on XRR measurements on thin films and multilayers, the reader is referred to [169].

4.3 Microscopic Techniques

4.3.1 Scanning Probe Microscopy

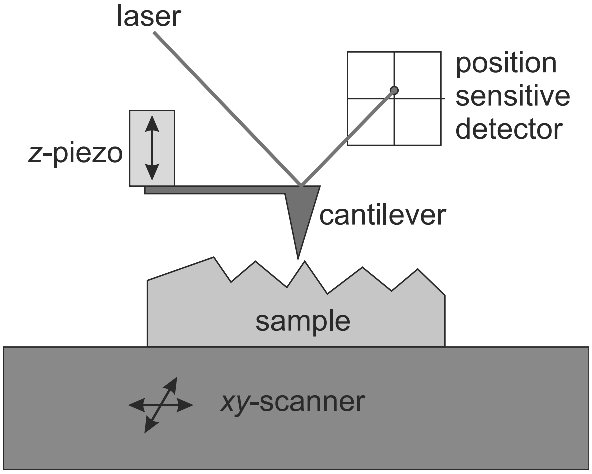

Figure 4.10: Schematic operational principle of atomic force microscopy.

A *Park Systems XE-150* atomic force microscope (AFM) operated in true non-contact mode was used to study the surface morphology of thin films and substrates. Atomic force microscopy is a type of scanning probe microscopy: a cantilever with a fine tip acts as probe that is scanned across a sample surface. The interaction of probe and sample is monitored with an infrared laser that is reflected off the cantilever backside onto a position sensitive detector, see the depiction in Fig. 4.10. The cantilever is excited to vibrate at its resonance frequency and is brought into close proximity with the surface (~1 to 10 nm), which causes a shift in resonance frequency and phase due to repulsive van-der-Waals interactions. The change is registered as a change in deflection amplitude. A feedback loop maintains a constant amplitude, i.e. a constant tip-sample distance, by modulating the height, called z-position, with a piezo-motor. The z-amplitude is used to generate a topographical image of the sample with sub-nm z-resolution.

The software *Gwyddion* [170] was used for data visualization and extraction of characteristic values. The root mean squared roughness parameter R_{rms} was used as a gauge for surface roughness:

$$R_{\mathrm{rms}} = \sqrt{\frac{1}{n}\sum_{i=1}^{n}\left(z_i - \bar{z}\right)^2}\ , \tag{4.7}$$

where $\bar{z}$ is the arithmetic mean value of all height values z_i.

4.3.2 Laser Scanning Microscopy

The film surface area for vibrating sample magnetometer (VSM) measurements, electrode areas for FE measurements and droplet densities were investigated with a *Keyence VK-X210* laser scanning microscope (LSM). The LSM generates two images: one regular optical microscopy image and a second one generated by scanning a 408 nm laser across the surface. In contrast to conventional microscopy techniques, LSM uses a so-called confocal optic, where a pinhole blocks out-of-focus information. The laser is scanned at multiple focal positions and the maximum intensity is recorded when the laser beam is focused on the sample surface. From this, a topological image can be constructed.

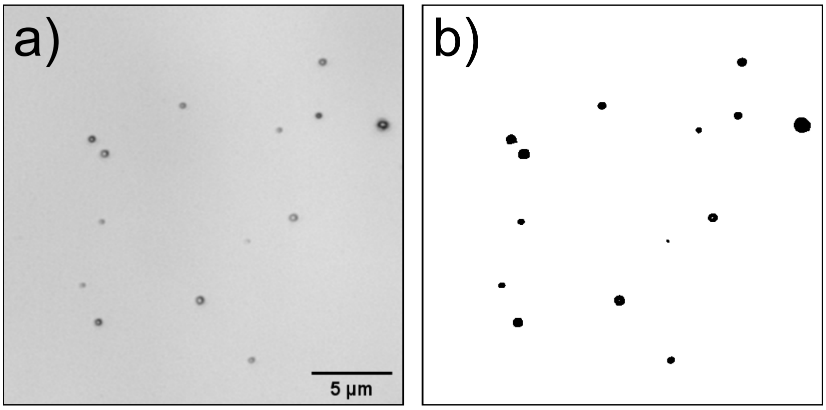

Figure 4.11: **(a)** Laser microscopy image at ×150 magnification and **(b)** mask generated with the analyze particles tool.

The high-contrast laser image was also used to identify droplets on the sample surface. The open source image analysis software *Fiji* [171] was used to mark irregularities (droplets) in LSM images, as shown in Fig. 4.11. After using the threshold tool, the analyze particle tool was used to mark particles with an area larger than 4 pixels, to reduce noise detection. The characteristic values determined were particles per area and particle size.

4.3.3 Transmission Electron Microscopy

Local structural analysis of thin film samples was performed with a transmission electron microscope (TEM). A *FEI TITAN*^{3} *G2 80-300* microscope operated at 300 keV and equipped with a *SuperX* energy-dispersive X-ray spectroscopy (EDX) analyzer was used to investigate thin film cross-sections with atomic resolution. Cross-sections along the (100) or (110) azimuth of the substrate were produced by wedge-polishing and subsequent ion milling. TEM cross-sections will accordingly be referred to as (100) or (110) oriented, with the implication, that the presented atomic structure is defined by the (100) or (110) and (001) directions of the substrate. Unlike XRD, which provides averaged information of a sample's structural properties, TEM can be used to image locally resolved geometrical features and defects in real space. Due to slight deviations from the ideal focus conditions, measured lattice constants are not calibrated exactly to an absolute scale. Where possible, the lattice parameters determined for the substrate was used as internal standard to correct these measurements.

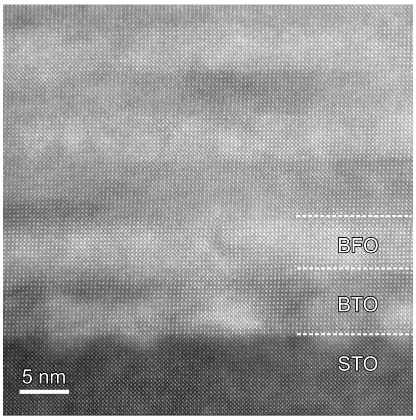

Figure 4.12: Exemplary high-resolution transmission electron microscopy (HR-TEM) image with atomic resolution. The image was created in scanning transmission electron microscopy (STEM) mode with a high-angle annular dark-field imaging (HAADF) detector. Depicted is a cross-section of a 15 × [$(BaTiO_3)_{5\ \mathrm{nm}}$ - $(BiFeO_3)_{5\ \mathrm{nm}}$] multilayer deposited using eclipse-PLD (sample F224).

High resolution TEM (HR-TEM) images with atomic number contrast (Z-contrast) were recorded with a high-angle annular dark-field imaging (HAADF) detector. As

Fig. 4.12 shows, this allows for atomic resolution imaging. Chemical distribution maps were recorded with the EDX analyzer in STEM mode.[1]

4.4 Chemical Analysis Techniques

4.4.1 Energy-Dispersive X–Ray Spectroscopy

Spatially resolved qualitative chemical analysis of films was carried out by STEM energy-dispersive X-ray spectroscopy (EDX). The technique relies upon the analysis of characteristic X-ray radiation, which results from the excitation of a sample with a high energy electron beam. The beam creates electron vacancies in the inner shells of atoms, which are then filled by higher-shell electrons under emission of an X-ray photon of characteristic wavelength. The emitted photons are detected by an energy dispersive detector. The spectrum is analyzed for the element- and transition-specific emission lines to create a laterally resolved elemental distribution map, as shown in Fig. 4.13..

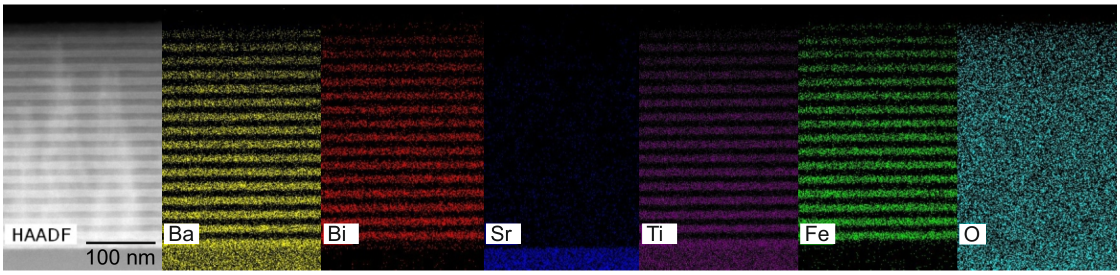

Figure 4.13: Exemplary HAADF TEM image and EDX elemental maps of the elements Ba, Bi, Sr, Ti, Fe, and O of a 15 × [$(\mathrm{BaTiO_3})_{10\ \mathrm{nm}}$ - $(\mathrm{BiFeO_3})_{10\ \mathrm{nm}}$] (sample F026). Note the overlap of the Ba and Sr signal due to similar characteristic wavelengths.

The *FEI TITAN*^{3} *G2 80-300* TEM was used in STEM mode to measure spacial distribution maps of elements in cross-sections using the *SuperX* EDX analyzer. The characteristic X-ray peaks used to map the various main elements in the samples presented in the framework of this thesis were: Ba L_α, Bi L_α, Fe K_α, O K_α, and Ti K_α. Due to the overlap of Ba L_α and Ti K_α, Ba appears to be present in the $SrTiO_3$ substrate as well, which is a common artifact, see Fig. 4.13.

---

[1] All TEM measurements in this thesis were carried out by *Christian Patzig* and *Susanne Selle* in the group of *Thomas Höche* at the *Fraunhofer-Institut für Mikrostruktur von Werkstoffen und Systemen* (*Center for Applied Microstructure Diagnostics*) in Halle, Germany.

4.4.2 Time-of-Flight Secondary Ion Mass Spectrometry

Qualitative chemical depth profiling was carried out by dynamic time-of-flight secondary ion mass spectrometry (ToF-SIMS). SIMS uses the positively and negatively charged secondary particles that are generated by bombarding a sample surface with an ion beam. The accelerated ions penetrate a few monolayers into the sample surface, displacing subsurface atoms in a so-called collision cascade, as described in further detail in Ref. 172. Sample atoms and clusters are ejected from the surface due to this collision cascade in a process generally termed sputtering. A portion of these ejected particles becomes ionized, which are the species used for analysis in SIMS. The time-of-flight mass spectrometer accelerates these ions with an electric field and measures the drift time through a field free region of space to distinguish the ionic species by mass and charge. In order to increase this technique's mass sensitivity, the analyzer ion beam is operated in a pulsed mode. Concentrations of any element are detectable down to the ppm level.

Depth profiling with ToF-SIMS was carried out using an *ION-TOF* (Münster, Germany) *TOF.SIMS 5* dual-beam instrument. In addition to the pulsed primary analyzer ion beam, this instrument uses a secondary ion beam to effectively ablate sample material. The primary Ga^+ ion gun was operated at 15 kV with a 2.47 pA beam current. The high current bunched mode was used for ToF analysis at 1.5 µA emission with a 3.9 ns bunch width. The analyzed area of 50 µm × 50 µm was set in the center of the sputtering area of 300 µm × 300 µm. When measuring negative ions, Cs^+ ions accelerated at 0.5 kV were used and O^+ ions accelerated at 1 kV when measuring positive ions, both sources were operated with 44.3 nA beam current and 0.24 µ A source current. The ToF analyzer was operated at a cycle time of 60 µ s, recording a mass range of 1 to 350 u with a mass resolution $m/\Delta m$ of approximately 5000 to 8500. Sputtering and ion spectra recording was carried out in alternating steps.

In static SIMS, about 95 % of measured ions stem from just the fist two monolayers at the sample surface [172]. Due to the finite ion penetration depth and the processes which are part of the collision cascade, ion displacement and intermixing from the top layers into underlying layers occurs. In dynamic SIMS with depth profiling the actual depth resolution is diminished further by the initial surface and interface roughness of a sample. Preferential sputtering can enrich lower yield material at the surface and also lead to roughening of the sputtered crater bottom. This effect is enhanced with progressive sputtering depth. On top of these complications, it is important to bear in mind that the generated measurement signals are detected over a large dynamic intensity range, which is why ToF-SIMS profiles are typically displayed in logarithmic scale. Furthermore, due to the variable ionization probabilities, which are additionally affected by matrix effects, quantitative analysis is only possible, if a suitable standard sample is available. For further details on the technique, the reader is directed to Refs. 172, 173 and H1.

The ToF-SIMS measurements presented in this thesis were carried out by *Jens Bauer* at the *Leibniz-Institut für Oberflächenmodifizierung* in Leipzig, who also analyzed the spectra using *Surface Lab 6* software (*ION-TOF* company).

4.5 Ferroelectric Characterization

Macroscopic ferroelectric (FE) measurements were carried out using a *TF 2000 HS* model thin film analyzer (*aixACCT Aachen*). In order to measure field dependent polarization $\boldsymbol{P}(\boldsymbol{E})$-loops, the current response I to an external voltage U is recorded across a sample capacitor structure with area A. $\boldsymbol{P}$ ($[\boldsymbol{P}] = \mu\mathrm{C\,cm^{-2}}$) is calculated from the generated charge Q using the relation:

$$\boldsymbol{P} = \frac{Q}{A} = \frac{\int I dt}{A} \, . \tag{4.8}$$

The field $\boldsymbol{E}$ ($[\boldsymbol{E}] = \mathrm{MV\,cm^{-1}}$) is calculated as $\boldsymbol{E} = U/d_{\mathrm{tot}}$, where d_{tot} is the thickness of the film sandwiched between the Pt top contact and the NSTO substrate, which functions as back contact. The setup uses the virtual ground method to record the current and is capable of dynamic leakage current compensation [174] and in-situ compensation of parasitic capacitance [175].

The most common measurement mode performed, was the dynamic hysteresis measurement (DHM), which is schematically depicted in Fig. 4.14. A series of four symmetric triangular voltage pulses with duration of $1/f$ is applied subsequently as shown in Fig. 4.14 a). The first and third pulses create a defined pre-polarized state (see Fig. 4.14 b)). After a delay time t_{delay} of typically 1 s the second and fourth pulse, respectively, is applied to measure the $I(\boldsymbol{E})$-loops (see Fig. 4.14 c)). The respective first halves of the measurements contain information pertaining to the loss of polarization that occurs during the delay between pulses. The respective second halves of the measurements are combined to yield the true $I(\boldsymbol{E})$- ($\boldsymbol{P}(\boldsymbol{E})$)-loops, which are used to extract the characteristic hysteresis parameters (see Fig. 2.3 b)). Note however, that the software shifts the measured data in such a way as to symmetrize the minimum and maximum polarization values.

To further illustrate the $\boldsymbol{P}(U)$ measurement procedure, a number of exemplary DHM measurements recorded on a resistor and capacitor at various frequencies f are depicted in Fig. 4.15. The individual components were chosen with a resistance R

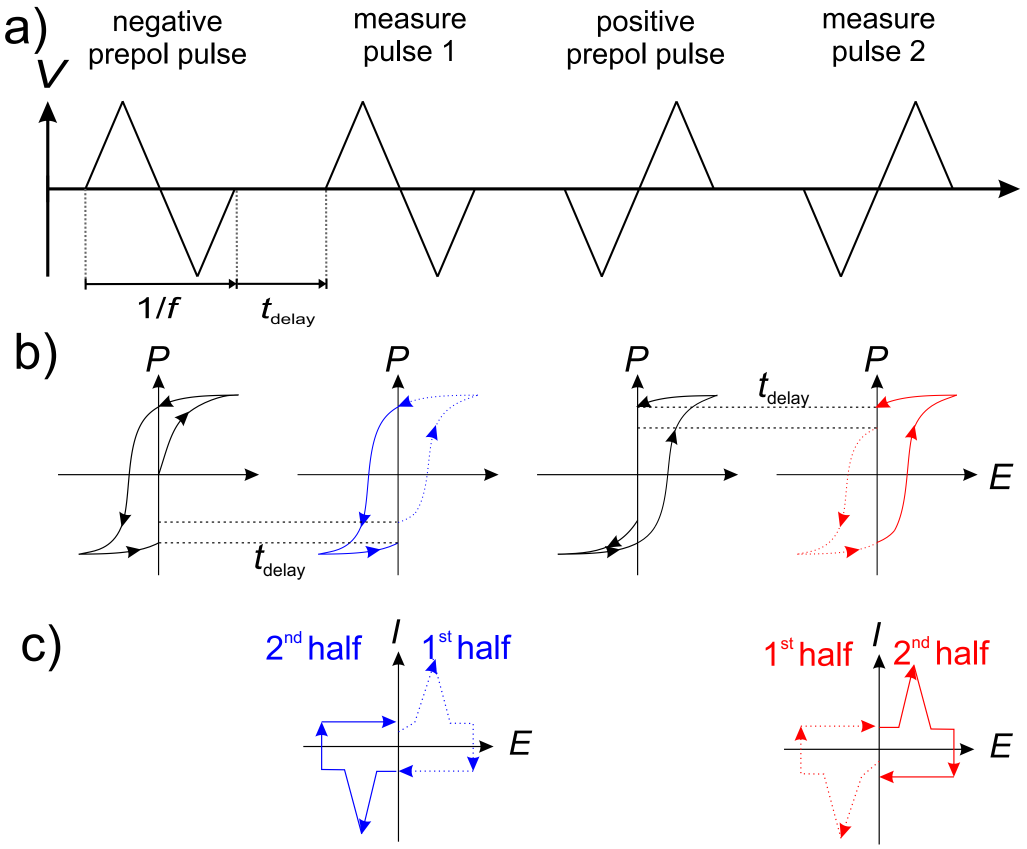

Figure 4.14: Schematic representation of the DHM measurement mode of the TF 2000 HS model: **(a)** sequence of triangular pulses consisting of pre-polarization pulses 1 and 3 and measurement pulses 2 and 4 (adapted from [176]), **(b)** corresponding $\boldsymbol{P}(\boldsymbol{E})$-loops and **(c)** according $I(\boldsymbol{E})$-loops for the two measurement pulses.

and capacitance C close to typical sample values to model a lossy dielectric without a ferroelectric component. As shown in Fig. 4.15 a), the ohmic resistor produces a linear $I(U)$-curve that is invariant under f-variation, according to the relation $I = U/R$. However, as $\boldsymbol{P}$ is calculated as $\boldsymbol{P} = \int I dt/A$, $\boldsymbol{P}(U)$ is a double parabola with dependence on f. For the capacitor, $I = C \cdot dU/dt$, and since triangular voltage pulses are used, this results in a constant charging current that scales with f as well as $U_{\max}$. The corresponding $\boldsymbol{P}(U)$-curve is a straight line, which is invariant under f. Figs. 4.15 c)-e) show the DHM measurements of resistor and capacitor in parallel at various frequencies. A combination of the former two, the opening of the $\boldsymbol{P}(U)$-loop created by the resistive component is diminished with increasing f. It is fairly common that curves such as in Fig. 4.15 c)-e) are mistaken for ferroelectric hysteresis loops [177]. While the general banana- or cigar-like shape of such a $\boldsymbol{P}(\boldsymbol{E})$-loop roughly approximates a ferroelectric hysteresis, no polarization switching occurs.

In fact, a ferroelectric sample, such as the BTO-BFO multilayers discussed in this thesis, behaves exactly like such a RC circuit if measured below its coercive voltage.

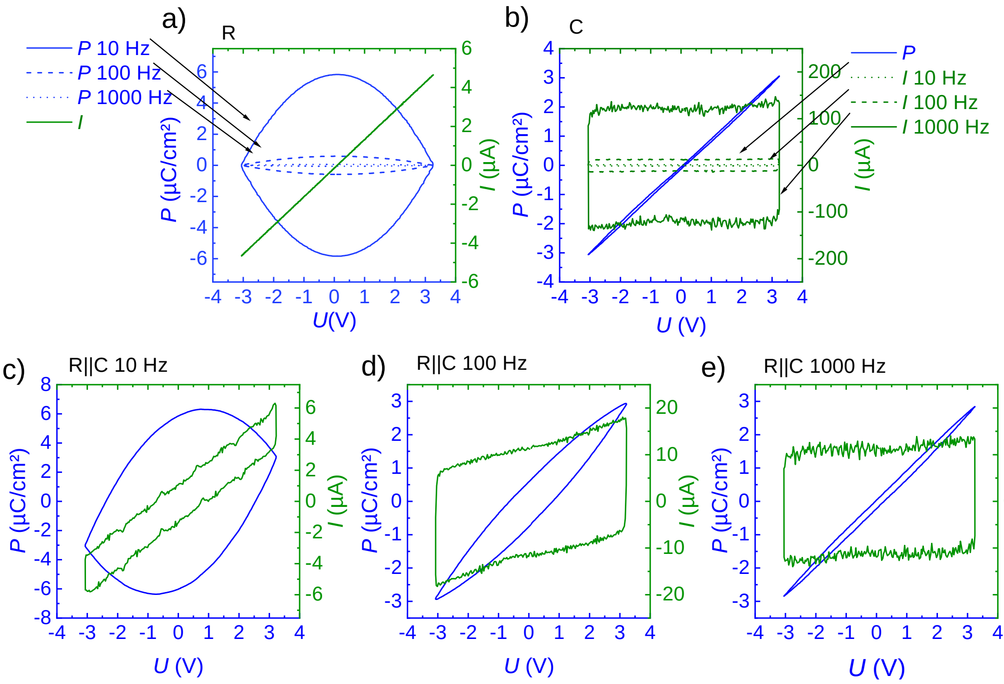

Figure 4.15: Exemplary $\boldsymbol{P}(U)$- and corresponding $I(U)$-loops recorded in the DHM mode at 10 to 1000 Hz for **(a)** a 0.7 MΩ resistor ($I(U)$ invariant under f-variation), **(b)** a 9.6 nF capacitor ($\boldsymbol{P}(U)$ invariant under f-variation) and both elements in parallel at **(c)** at 10 Hz, **(d)** at 100 Hz and **(e)** at 1000 Hz. An arbitrary area of 1 mm^2 was assigned to calculate $\boldsymbol{P}$.

This is exemplified by the measurement of a typical $15\times[(\mathrm{BaTiO_3})_{10\ \mathrm{nm}}$ - $(\mathrm{BiFeO_3})_{10\ \mathrm{nm}}]$ multilayer presented in Fig. 4.16 a). At intermediate maximum measurement voltages close to the coercive voltage, a curve such as depicted in Fig. 4.16 b) will be produced. And finally, if the applied maximum voltage exceeds the coercive voltage, a curve as shown in Fig. 4.16 c) is the result. In addition to the capacitive charging current and a leakage component, ferroelectric switching peaks can be observed. This current is the result of surface screening charges, compensating the sample polarization, flowing from one electrode to the other. Hence, the integrated current of the switching peaks is independent of f-variation, though the peak position can vary according to the material's specific switching dynamics. The resulting $\boldsymbol{P}(\boldsymbol{E})$-loop is that of a classic ferroelectric hysteresis loop overlaid with the $\boldsymbol{P}(\boldsymbol{E})$-loop generated by the RC circuit.

Due to the aforementioned frequency dependencies of the resistive and capacitive contributions, it is possible to identify them by changing the measurement frequency. Fig. 4.16 d) and e) show the corresponding measurements at 10 Hz and 100 Hz. It is clear from the $I(\boldsymbol{E})$-curves that there is a resistive, but non-linear contribution to the total current, adding a false opening of the $\boldsymbol{P}(\boldsymbol{E})$-loop. The *TF 2000*'s leakage compensation utilizes this frequency dependence to subtract the leakage current from the measurement by measuring at two adjacent frequencies, for further details see [174].

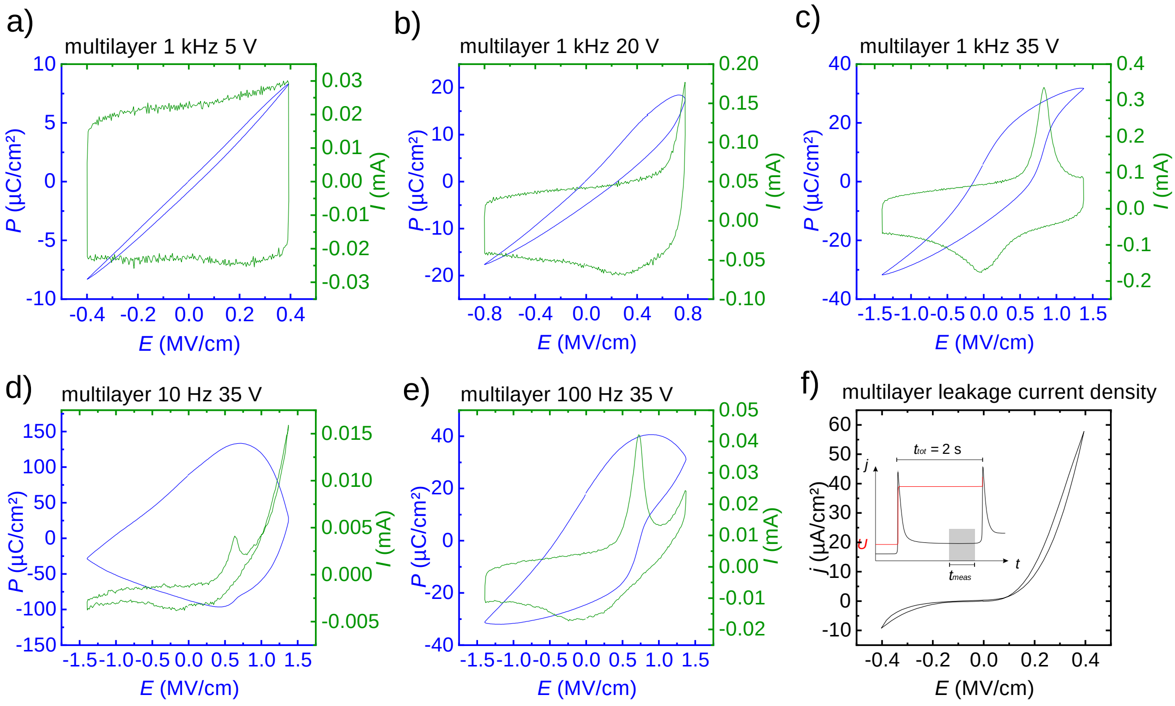

Figure 4.16: Exemplary $I(\boldsymbol{E})$- and $\boldsymbol{P}(\boldsymbol{E})$-loops recorded in the DHM mode at 1000 Hz for a $15 \times [(\mathrm{BaTiO_3})_{10\ \mathrm{nm}}\text{-}(\mathrm{BiFeO_3})_{10\ \mathrm{nm}}]$ multilayer on SrTiO$_3$:Nb at **(a)** 5 V, **(b)** 20 V and **(c)** 35 V, **(d)** at 10 Hz and 35 V and **(e)** 100 Hz and 35 V. **(f)** shows a leakage current density measurement on the same multilayer recorded at a maximum voltage of 10 V.

The explicit voltage dependence of the leakage current density j ($[j] = \mathrm{A/cm^2}$) can be measured by applying a stepped voltage, as depicted in the inset in Fig. 4.16 f). As the ferroelectric switching current and capacitive charging current flow only for a few ms after the near-rectangular voltage change [176], the leakage current is measured in the time frame of the last 70 to 90 % of the 2 s voltage step. The resulting leakage current depicted in Fig. 4.16 f) resembles that of an asymmetric back-to-back *Schottky*-diode. The reader is referred to section 5.1.4 for a more detailed discussion of the leakage current behavior. To briefly summarize:

- In order to identify a ferroelectric as such, it is imperative to not only consider the general shape of the $\boldsymbol{P}(\boldsymbol{E})$-loop, but also the corresponding $I(\boldsymbol{E})$-curve concerning switching peaks;
- If the measurement voltage is lower than the coercive voltage, partial switching peaks may falsely be identified as asymmetric leakage current;
- Leakage current and capacitive charging current contributions can be identified by variation of the measurement frequency.

Note also the asymmetry of the $I(\boldsymbol{E})$- and $\boldsymbol{P}(\boldsymbol{E})$-loops of the multilayer in Fig. 4.16. It is related to the phenomena of imprint and self-poling, which will be discussed in detail in Section 5.1.5.

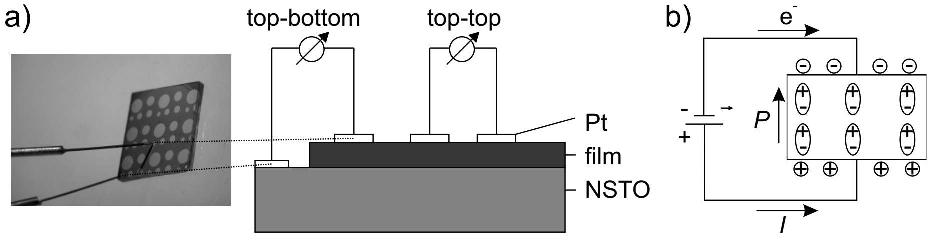

Figure 4.17: **(a)** Possible measurement geometries (top-bottom and top-top) for the FE measurement on a thin film sample with conductive substrate; **(b)** orientation of polarization, electron flow, technical (positive) current in a ferroelectric thin film capacitor.

The FE measurements were performed on thin film samples deposited onto conductive NSTO substrates. The corners of a substrate are not coated with a film, as they are shielded by the top plate of the PLD-substrate holder. Two possible measurement geometries arise, as depicted in Fig. 4.17: (I) top-to-bottom, where the top contact is a Pt-electrode on the film and the bottom contact is the NSTO substrate, which is contacted through a Pt-electrode on one of the corners of the substrate; (II) top-to-top, where both measurement contacts lie on the film surface, the substrate acting as conductive connection between the two capacitors. If not stated otherwise, the top-to-bottom geometry was used for the FE measurements. In all electric measurements performed throughout this thesis, the top contact is used as virtual ground. Hence, a positive switching current is observed for a positive bias voltage, when the polarization in the thin film capacitor is switched from a down (pointing to the substrate) to an up (pointing to the top contact) state, requiring the flow of screening charges into the top contact, see Fig. 4.17 (right).

4.6 Magnetic Property Measurements

Magnetic measurements were performed using a vibrating sample magnetometer (VSM). The working principle of this device makes use of *Faraday*'s law of induction: the changing magnetic flux caused by oscillating sample movement induces a voltage in a static first order gradiometer pickup coil pair. A lock-in amplifier is used to record the resulting induced voltage, which is used to calculate the sample's magnetic moment. The original setup designed by *Foner* in 1955 [178] used a simple loudspeaker to drive the sample. The setup used in this thesis is built into a *LOT Quantum Design Physical Property Measurement System* (PPMS). The sample is attached to a quartz paddle with varnish, which is connected to a linear motor outside the sample chamber by a long carbon fiber rod. The sample is driven at 40 Hz with a peak displacement amplitude of 2 mm. Due to the limited size of the pickup coils, centering the sample combined with repeated touchdown operations during measurement are necessary. The setup has a nominal noise level smaller than $0.6\,\mu$emu ($\hat{=}0.6 \times 10^{-9}\,\mathrm{A\,m^2}$) at 300 K [179], capable of operating in temperature ranges between 1.8 to 400 K and generating magnetic fields of up to 90 000 Oe ($\hat{=}$9 T). Both temperature dependent ($\boldsymbol{M}(T)$) and field dependent ($\boldsymbol{M}(\mu_0\boldsymbol{H})$) magnetization measurements were performed. Generally, $\boldsymbol{M}(\mu_0\boldsymbol{H})$-curves contain a linear paramagnetic contribution from the quartz sample holder and substrate, which needs to be subtracted from the $\boldsymbol{M}(\mu_0\boldsymbol{H})$-data by fitting the saturated high field portion of the curve. The magnetization $\boldsymbol{M} = \boldsymbol{m}/V = \boldsymbol{m}/(d_{\mathrm{tot}} \cdot A)$ is calculated from the measured magnetic moment $\boldsymbol{m}$ using the thickness d_{tot} derived from either multilayer fringes or XRR measurements and the film area A , as measured via LSM. $\boldsymbol{M}$ is expressed in units of $\mathrm{emu\,cm^{-3}}$ or μ_{B}/f.u.,[2] using the approximate unit cell volume $V_{\mathrm{f.u.}} = a_{\mathrm{ave}}^3$ calculated from the average lattice parameter of the film a_{ave}.

A brief discussion on the measurements concerning the non-linearity of the magnetic field generated by the superconducting magnet of the PPMS can be found in the Appendix B. Measurements of the magnetic background signal generated by the sample holder, substrates and artifacts created by contamination can also be found in Appendix B.

4.7 Measurement of the Magnetoelectric Coupling Coefficient

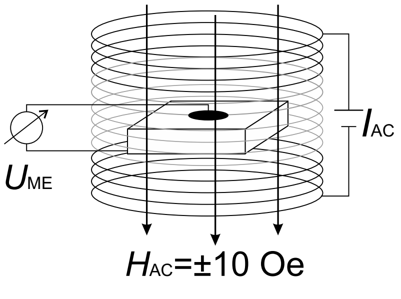

Figure 4.18: Measurement geometry for the linear longitudinal magnetoelectic voltage measurement.

The measurements of the ME coupling coefficient α_{ME} were carried out by *Vera Lazenka* and *Johanna K. Jochum* in the group of *Krisitaan Temst* and *André Vantomme* at

---

[2] $1\,\mathrm{emu} = 10^3\,\mathrm{A\,m^{-1}} = 1.0783 \times 10^{20}\,\mu_{\mathrm{B}}$, *Bohr* magneton $\mu_{\mathrm{B}} = 9.247 \times 10^{-24}\,\mathrm{J\,T^{-1}}$, f.u. is short for formula unit.

the *KU Leuven* in Belgium. In this thesis, α_{ME} is defined as the longitudinal first order electric field response U_{ME} to a changing magnetic field $\boldsymbol{H}$: $\alpha_{\mathrm{ME}} = d\boldsymbol{E}/d\boldsymbol{H} = \frac{1}{d_{\mathrm{tot}}} dU_{\mathrm{ME}}/d\boldsymbol{H}$, measured across a capacitor of thickness d_{tot}, see Sec. 2.2.1. In this work, the measurement units of α_{ME} are $\mathrm{Vcm^{-1}Oe^{-1}}$, for a detailed discussion of possible units of α_{ME}, see Refs. 180 and 181. The alternating magnetic field $\boldsymbol{H}_{\mathrm{AC}}$ is applied parallel to the substrate normal, i.e. parallel to the capacitor formed by the NSTO substrate, the film and the Pt top contact. The measurement geometry is depicted in Fig. 4.18. The resulting voltage was measured using a lock-in amplifier tuned to the excitation frequency. Both temperature dependent α_{ME} measurements in 0 Oe DC bias field and room temperature DC bias field dependent measurements in up to 6×10^4 Oe (6 T) were performed.

The setup in Leuven was built to work with a *LOT Quantum Design* PPMS system. A standard PPMS measurement puck was modified as sample holder with a small hand-wound coil with 1290 turns of AWG 36 phosphor brass wire. A *Keithley 6221* current source was used to drive the current through the solenoid. The current was set to generate a root mean square AC field strength of 10 Oe at 1 kHz. The root mean square of the voltage response was measured with a *Stanford Research SR830* lock-in amplifier. The internal magnet of the PPMS system was used to generate the DC magnetic bias field, also parallel to the substrate normal. The temperature was measured with the system's internal thermometer. For more details on the setup, see also Refs. 11, 121 and 182.

As the setup was first built, a great deal of effort went to excluding the influence of parasitic signals on the measurement. The functionality of the finished setup was tested by measuring samples with no ME coupling, such as glass substrates and bare BTO films, which returned negligibly small noise signals three orders of magnitude lower than that of a bare BFO film.

In the course of this thesis, a reproduction of the original setup was built in Leipzig. The details of the setup, including calibration of the solenoid, can be found in the Appendix A. However, due to the extreme sensibility of the measurement to the particular shielding and cable choices, the new setup has not produced any reliable, reproducible measurements, so far. Likewise, when the original setup was re-assembled in *Leuven* in 2019, only various parasitic signals were measured on all samples, including explicitly non-ME samples. The key expert with long-standing hands-on experience who mainly contributed to the operation of the measurement setup in the past was *Vera Lazenka.*

Chapter 5

$BaTiO_3$–$BiFeO_3$ Heterostructures

Before delving into novel insights gained over the course of this thesis, let us take a step back and re-examine the knowledge base that has been established in the forefront of this work. There are a number of key discoveries that will be the basis of further argumentation. Additionally, some directly prompt the fundamental questions which act as the underlying motivation behind the research conducted in the framework of this thesis. A more elaborate overview of these previous results has already been given in Sec. 3.5.4, the following is an abridged summary of the key findings:

- BTO-BFO multilayers show enhanced ME coupling relative to single-layers
- The α_{ME} -coefficient of multilayers saturates at 1 to 2 T bias magnetic field, while single-layers show a maximum at around 1 T
- Samples grown at lower p_{O_2} show lower α_{ME}-values than those grown at high p_{O_2}
- Reduced p_{O_2} during growth leads to higher degrees of OOT and microstrain
- High α_{ME} -coefficients occur in multilayers with a certain degree of intermixing at the interfaces
- Variable interface roughness and the presence of droplets complicate chemical depth profile measurements
- High leakage current in ferroelectric measurements hinders effective polarization measurements
- Decreasing BFO-thickness leads to stronger ME coupling and a shift in temperature dependence
- An increasing number of interfaces is correlated with increasing perpendicular magnetic anisotropy and higher α_{ME}-values

In particular the last two points shed a new light on some older discoveries. The investigation of the influence of the deposition pressure was carried out with samples generated with the same number of pulses, which led to profound changes in the thickness of individual layers and double-layers. This demands a second glance with more closely controlled multilayer design. In order to fill in the gaps of knowledge on the ME coupling in BTO-BFO multilayers and further improve the sample quality, this thesis will attempt to answer a number of fundamental questions:

- Which sample properties are inherently characteristic of BTO-BFO multilayers and single-layers?
- How can we positively affect the droplet-density, interface roughness and leakage current by means of:
    - Growth parameter optimization?
    - Multilayer design?
    - Advanced deposition techniques (eclipse-PLD)?
- How can we further enhance ME coupling in BTO-BFO multilayers and what can we learn about its origin?

The following chapter will be structured as follows: the first section will discuss the general properties commonly discovered in BTO-BFO multilayers particularly in comparison with single-layers. In the second section, changes in the morphologic, structural, magnetic and ferroelectric properties in response to variations of the process conditions in PLD thin film growth of BTO-BFO multilayers will be explored. The third section will cover the implications of multilayer design choices, divided into the simultaneous and isolated modification of double-layer thickness and constituent component ratio. With the background of the combined knowledge laid out in these sections, we will examine the magnetoelectric properties of BTO-BFO multilayers in relation to oxygen partial pressure during growth, BTO-BFO ratio and double-layer thickness.

5.1 General Properties of Single-Layers and Multilayers of $BaTiO_3$ and $BiFeO_3$

To begin with, we will examine the general properties of BTO-BFO multilayers. This will establish a baseline, which will be used to identify variations in the material properties, that are induced by changes in the growth conditions and multilayer design choices. In particular, the dominant differences between single and multilayers will be discussed. First, the structural aspects will be examined, followed by the electric, magnetic, and finally magnetoelectric properties of BTO and BFO single-layers and BTO-BFO multilayers.

5.1.1 Structural Properties

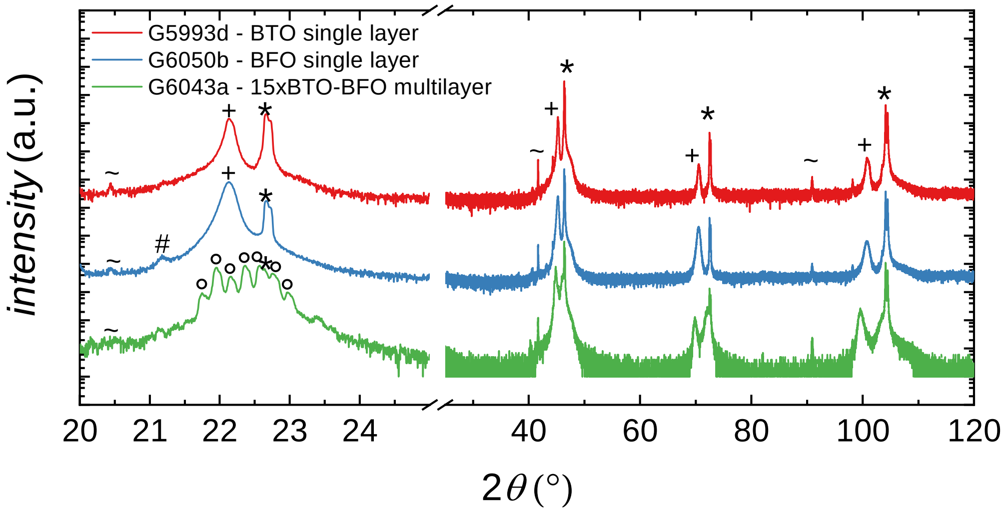

Figure 5.1: XRD 2θ-ω scans of a 240 nm BTO single-layer (G5993), a 363 nm BFO single-layer (G6050) and a 15 × $[(BaTiO_3)_{27\ nm}$ - $(BiFeO_3)_{16\ nm}]$ multilayer (G6043), deposited on STO under standard conditions. The 2θ range of 20 to 25° in vicinity of the STO (001) peak is presented in detail before the x-axis interruption. Various observable features are marked as follows: $\sim$: Cu K_β peak, #: W $L_{\alpha 1}$ peaks, $*$: STO $(00l)$ peaks, $+$: single-layer $(00l)$ peaks, $\circ$: multilayer fringe peaks.

The structural properties of any material have a profound influence on its physical properties. First, let us confirm that the single- and multilayers of BTO and BFO deposited at standard conditions form phase-pure and epitaxial, i.e. crystalline, well ordered and oriented layers on the STO substrate. Fig. 5.1 shows the XRD 2θ-ω scans of a typical BTO single-layer, a BFO single-layer and a BTO-BFO multilayer. Both single- and multilayers show only $(00l)$ film peaks close to the respective $(00l)$ substrate peaks, with no signs indicative of additional phases. This speaks of so-called *cube-on-*

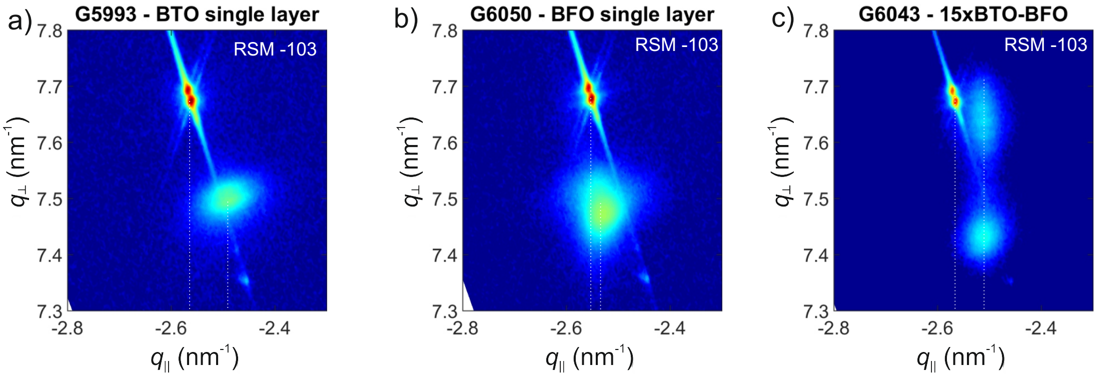

Figure 5.2: XRD RSMs around the ($\bar{1}03$) STO substrate peak of **(a)** a 240 nm BTO single-layer (G5993), **(b)** a 363 nm BFO single-layer (G6050) and **(c)** a $15 \times [(\mathrm{BaTiO_3})_{27\,\mathrm{nm}}\text{-}(\mathrm{BiFeO_3})_{16\,\mathrm{nm}}]$ multilayer (G6043), deposited on STO under standard conditions. The heat map colors represent measured intensities on a logarithmic scale, blue representing small values and red large values.

cube growth of the respective perovskite phases. The multilayer structure additionally produces multilayer fringe peaks, as marked in Fig. 5.1, which allow the determination of $d_{\mathrm{dl}} = 44 \pm 1\,\mathrm{nm}$. Fitting of a XRR measurement of this sample gives approximate BTO and BFO thicknesses of 27 nm and 16 nm, respectively.

Table 5.1: Lattice parameters of a 240 nm BTO single-layer (G5993), a 363 nm BFO single-layer (G6050) and a $15 \times [(\mathrm{BaTiO_3})_{27\,\mathrm{nm}}\text{-}(\mathrm{BiFeO_3})_{16\,\mathrm{nm}}]$ multilayer (G6043), deposited on STO under standard conditions. In-plane ($a_{||}$) and out-of-plane ($a_\perp$) lattice parameters are extracted from asymmetric ($\bar{1}03$) XRD RSM measurements using the STO peak as internal standard. Also listed: the full width at half maximum (FWHM) of the (002) peak in ω direction. The error of the lattice constants is estimated to be 0.015 Å and 0.005 Å for $a_{||}$- and $a_\perp$, respectively.

sample	$a_{\|\|\mathrm{BTO}}$ (Å)	$a_{\perp\mathrm{BTO}}$ (Å)	$a_{\|\|\mathrm{BFO}}$ (Å)	$a_{\perp\mathrm{BFO}}$ (Å)	FWHM_{002} (°)
G5993	4.021	3.997	–	–	0.267
G6050	–	–	3.943	4.012	0.305
G6043	3.986	4.033	3.986	3.922	0.209

As discussed in Sec. 4.2.2, a thin film can fully grow in-plane strained to the substrate, partially, or fully relaxed. Reciprocal space mapping around asymmetrical substrate peaks reveals these relations, as shown in Fig. 5.2 for the three exemplary samples. The lattice parameters extracted from these RSM measurements are tabulated in Table 5.1. It is clearly evident from the lack of horizontal alignment in Fig. 5.2 that neither single-layers nor multilayers grow fully strained to the substrate, but at least partially relaxed. The OOP lattice parameter $a_\perp$ of the single-layer BTO film is compressed relative to the IP parameter $a_{||}$, i.e. in the single-layer the tetragonal c-axis is oriented perpendicular to the OOP (001) substrate axis. However, no peak splitting is evident, which would be the case for a mixed a_1 and a_2 domain structure. In contrast, the multilayer presented in Fig. 5.2 c) and all other investigated BTO-BFO multilayers, show OOP c-axis orientation for BTO. Similarly, a small elongation (compression) of the BFO OOP lattice parameter $a_{\|}$ relative to the IP $a_{\perp}$-value can be found for the single (multi-) layer in XRD measurements, deviating slightly from the nominal pseudo-cubic symmetry.

A closer, more detailed examination of the lattice parameters is made possible by TEM measurements of high quality cross-sections, as depicted in Fig. 5.3. The first monolayer BTO is coherently strained to the substrate. As indicated in Fig. 5.3 a) and shown in greater detail by IP lattice parameter measurements in Fig. 5.3 b), relaxation of the films is confined to the first ~3 nm of BTO. After this critical thickness, no variation of the lattice parameters were found in any observed multilayer films across the entire film thickness. All subsequent BTO and BFO layers are coherently strained to one another, showing no explicit lattice parameter variation with distance from the interfaces. The lattice parameters as measured by TEM (using the STO lattice parameters for calibration) are: $a_{\|\mathrm{ave}} = 3.99 \pm 0.04\,\mathrm{Å}$, $a_{\perp\mathrm{BTO}} = 4.12 \pm 0.07\,\mathrm{Å}$, $a_{\perp\mathrm{BFO}} = 4.03 \pm 0.03\,\mathrm{Å}$. This confirms the c-axis orientation of BTO in the multilayer, the tetragonal distortion of the cubic BFO cell however is within the error margin of the lattice parameter determination. In Sec. 5.3, we will delve deeper into the matter of tuning the inter-layer strain via multilayer design choices.

Another feature common to most BTO-BFO multilayers is the reduced FWHM of the $(00l)$ peak relative to single-layer deposited under identical conditions and with similar total thicknesses. The FWHM of the (002) peak in ω-direction is listed in Table 5.1 for the above mentioned films. The extent to which a peak is broadened in ω-direction is a gauge for the mosaicity and micro-strain of a film. Since the ω-FWHM is lower in multilayers when compared to single-layers, this implies a mutually beneficial influence on the ordered growth of both materials when arranged in a multilayer structure. Strictly speaking, this is only true for intermediate BTO-BFO ratios, as discussed later in Sec. 5.3. For an overall comparison, the average FWHM of a nominally single-crystalline STO substrate is in the range of 0.03 to 0.06°.

Multilayer Stacking Effect

The evolution of strain states and the surface quality of multilayers was investigated on the basis of a series of samples with an increasing number of layers. The (multi-) layers of $n \times [(\mathrm{BaTiO_3})_{10\ \mathrm{nm}} \text{-} (\mathrm{BiFeO_3})_{10\ \mathrm{nm}}]$, where n is the number of double-layer repetitions, were deposited on annealed STO in chamber F using standard conditions. After growth rate calibration, 320 pulses were used for the BTO layers and 1200 pulses

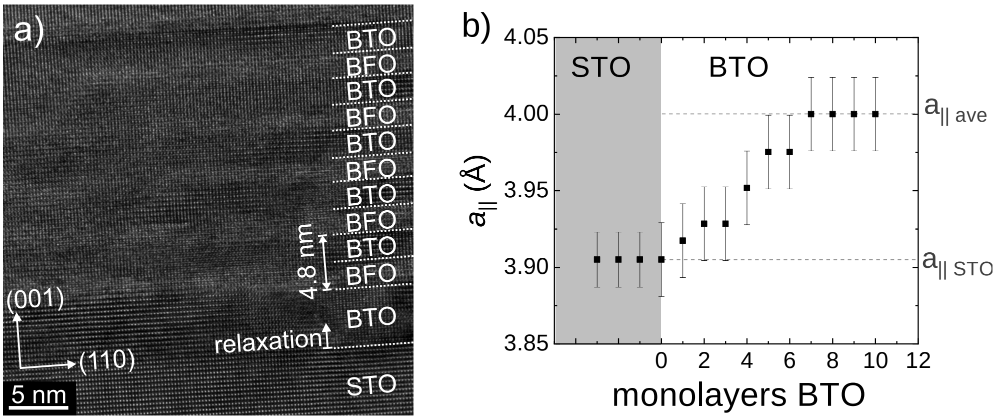

Figure 5.3: **(a)** (110)-oriented TEM cross-section of the first few layers of a 15 × [(BaTiO$_3$)$_{2.4\ \mathrm{nm}}$ - (BiFeO$_3$)$_{2.4\ \mathrm{nm}}$] multilayer (F032) at the interface to the STO substrate; **(b)** IP lattice parameters of the first ten monolayers of BTO averaged over 20 unit cells, showing gradual relaxation over the first seven monolayers (∼3 nm). Note that the first BTO layer is thicker than the rest of the BTO layers, as the film was grown with an additional buffer layer of BTO with 300 laser pulses at 1 Hz, which coincidentally results in a 3 nm layer. The lattice parameters presented in **(b)** are corrected using the nominal 3.905 Å lattice constant of STO [49] as reference. Graphs adapted from Ref. H5 (supplementary).

for the BFO layers. The values for n were selected as 0.5, 1, 1.5, 2, 4.5, 5, 14.5 and 15 double-layer repetitions. Half-integer values imply BTO-termination, integer values BFO-termination of the layer stack. Reciprocal space maps around the asymmetric (103) STO peak of these eight samples are presented in Fig. 5.4. Since the signal-to-noise ratio is relatively low for the first four samples, the peak-positions are marked by dashed lines. Note also that the RSM measurements are not corrected to match the observed STO peak position to the nominal bulk value. The relaxation of the first BTO layer is visible as an asymmetric smudging of the film peak in Fig. 5.4 a). All consecutive layers grow strained to the previous layer, as the horizontal alignment of film peaks in Fig. 5.4 b) through h) shows. After $n = 4.5$, superstructure fringe peaks emerge as a result of the repeated double-layer stacking.

The lattice parameters of the $n \times$ [(BaTiO$_3$)$_{10\ \mathrm{nm}}$ - (BiFeO$_3$)$_{10\ \mathrm{nm}}$] films are presented in Fig. 5.5 b). For $n = 0.5$ and 1, The films can be said to be nearly strained to the STO substrate. All following films are at least partially relaxed with respect to the substrate and show variations only in the range of the margin of error. All BTO films are c-oriented with a tetragonality of $a_\perp/a_\parallel =\sim 1.04$, all BFO layers show pseudo-cubic symmetry. As will be discussed in Sec. 5.3, the in-plane lattice parameter is not strictly determined by the first layer though, but a result of the relative BTO-to-BFO ratio.

The evolution of the surface roughness parameter R_{rms} with n is displayed in Fig. 5.5 a). The first 10 nm thick layer of BTO has a surface roughness comparable to that of a bare, annealed STO substrate. Subsequent layers show greater R_{rms}-values of up to

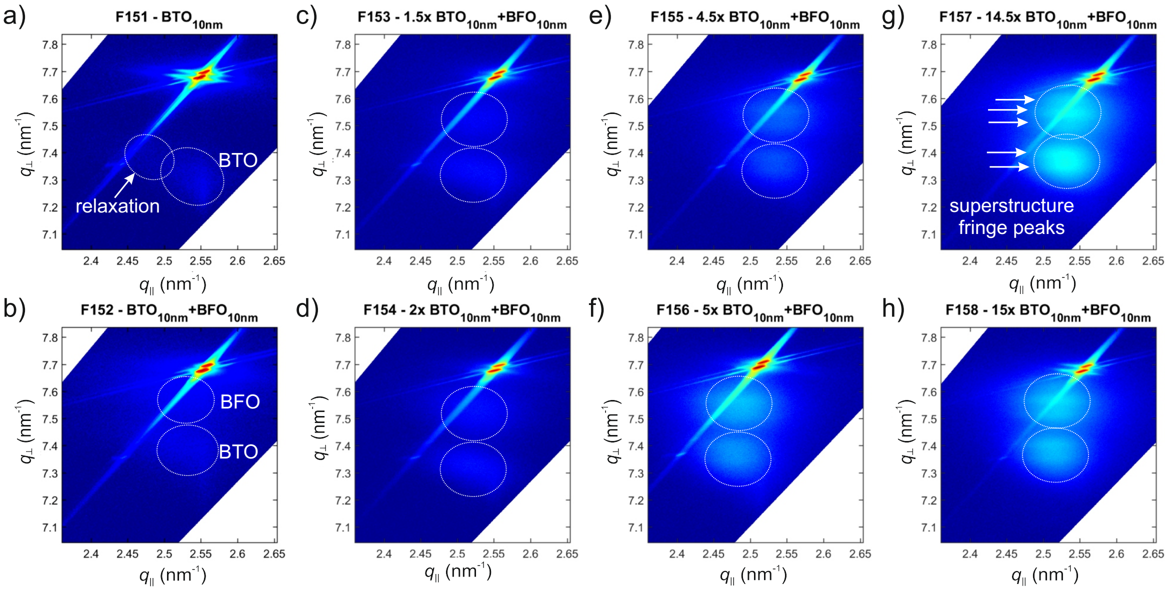

Figure 5.4: Reciprocal space maps around the (103) STO peak of $n \times [(\mathrm{BaTiO_3})_{10\ \mathrm{nm}}\text{-}(\mathrm{BiFeO_3})_{10\ \mathrm{nm}}]$ (multi-) layers with $n =$ **(a)** 0.5, **(b)** 1, **(c)** 1.5, **(d)** 2, **(e)** 4.5, **(f)** 5, **(g)** 14.5, and **(h)** 15, deposited under standard conditions on STO. The positions of peaks relating to BTO, BFO and superstructure fringes are marked, as well as the skewness of the first BTO peak indicating relaxation.

0.82 nm for $n = 14.5$ (BTO-terminated). The last, BFO-terminated sample again has a lowered R_{rms}-value of 0.46 nm. At this point it is worth pointing out that an ideal approach to investigating the layer stack effect would use only one sample that is examined at all stages of $0 \geq n \geq 15$ in-situ, without breaking the vacuum. Since this was not an option with our current setup, this series of samples was produced instead. This further compromised the integrity and significance of the surface-roughness measurements by AFM, which can be profoundly affected by the small sample area (typically 2.5 µm × 2.5 µm) and lateral position. However, in direct comparison with single-layer to multilayers with comparable thickness, the effect of layer stacking on the overall film roughness emerges very clearly. The R_{rms}-values of the three films discussed in the previous section (see Table 5.1) is: 1.07 nm for the 240 nm BTO single-layer (G5993), 2.24 nm for the 363 nm BFO single-layer (G6050) and 0.36 nm for the $15 \times [(\mathrm{BaTiO_3})_{27\ \mathrm{nm}}\text{-}(\mathrm{BiFeO_3})_{16\ \mathrm{nm}}]$ multilayer (G6043).

In other words, the growth of BTO and BFO as multilayer structure appears to result in a mutually beneficial growth mode, reducing the resulting surface roughness. A possible explanation for this phenomenon lies in the process sequencing. Every turnover between the two target types introduces an approximately 1 min gap in the ablation process, which could introduce a critical relaxation period of the only 10 nm individual layers. In analogy, the "imposed layer-by-layer growth", reported by *Koster et al.*, intersperses mono-layer pulse-bursts with relaxation periods [183]. However, depositing ∼300 nm BTO and BFO single-layer films with 1 min breaks in between 1000 pulse bundles had no similar effect.

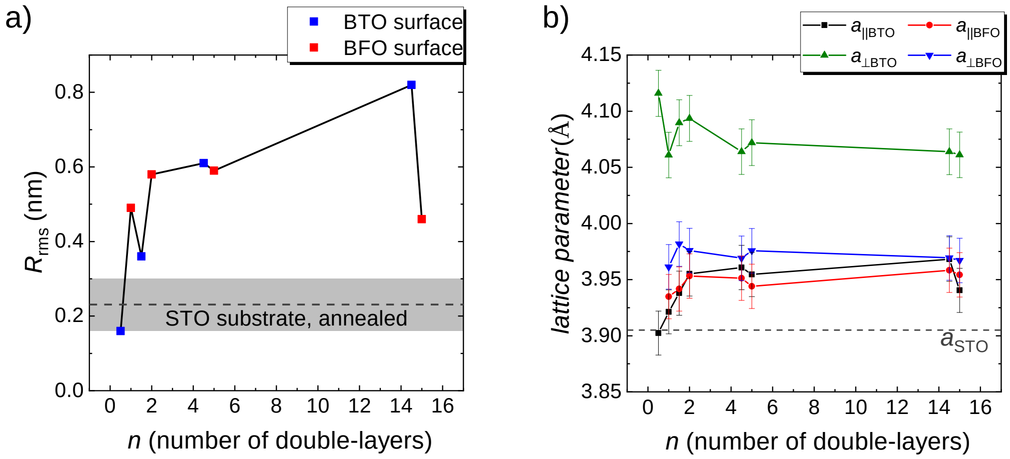

Figure 5.5: Evolution of the **(a)** surface roughness parameter R_{rms} , as measured by AFM, and **(b)** lattice parameters of BTO and BFO, as determined from RSMs, of $n \times [(\mathrm{BaTiO_3})_{10\ \mathrm{nm}}\text{-}(\mathrm{BiFeO_3})_{10\ \mathrm{nm}}]$ (multi-)layers with n (number of double-layers). The gray lines in a) and b) indicate surface roughness and the lattice parameter, respectively, of the STO substrate.

Oxygen Octahedral Tilt

As stated in Sec. 3.1, one of the most striking structural features of oxide perovskites is the tilt of oxygen octahedra, OOT. Due to its direct connection to bond angles and local geometry, OOT has profound influence on functionality [37]. In the particular case of BFO the tilt angle is linked to the materials' magnetism and magnetoelectric behavior via the Fe–O–Fe bond angle (see Sec. 3.4). Due to their cubic $Pm3m$ and tetragonal $P4mm$ symmetries, OOT is geometrically prohibited in both STO and BTO. In $R3c$ symmetric rhombohedral BFO, $a^-a^-a^-$ (*Glazer* notation [48]) OOT occurs, the oxygen octahedra tilted in all three spacial axes, with alternating signs of tilt angle. This ordered OOT sets up a new 2 × 2 × 2 unit cell. Accordingly, in fast-*Fourier*-transformation (FFT) images of (110)-oriented TEM cross-sections $a^-a^-a^-$ OOT leads to the appearance of half-order $(h+\frac{1}{2}, k+\frac{1}{2}, l+\frac{1}{2})$ peaks in addition to the main structure peaks. Accordingly, e.g. in (100)-oriented cross-sections, the alternation tilted O-atom columns would be imaged overlaid on one another and would not lead to the appearance of half-integer peaks in an FFT image.

Fig. 5.6 shows such an exemplary (110)-oriented TEM cross-section of a highly ordered $15 \times [(\mathrm{BaTiO_3})_{10\ \mathrm{nm}}\text{-}(\mathrm{BiFeO_3})_{10\ \mathrm{nm}}]$ multilayer grown by eclipse-PLD. In Fig. 5.6 b) and c), the selective area FFT images of the marked BTO and BFO areas

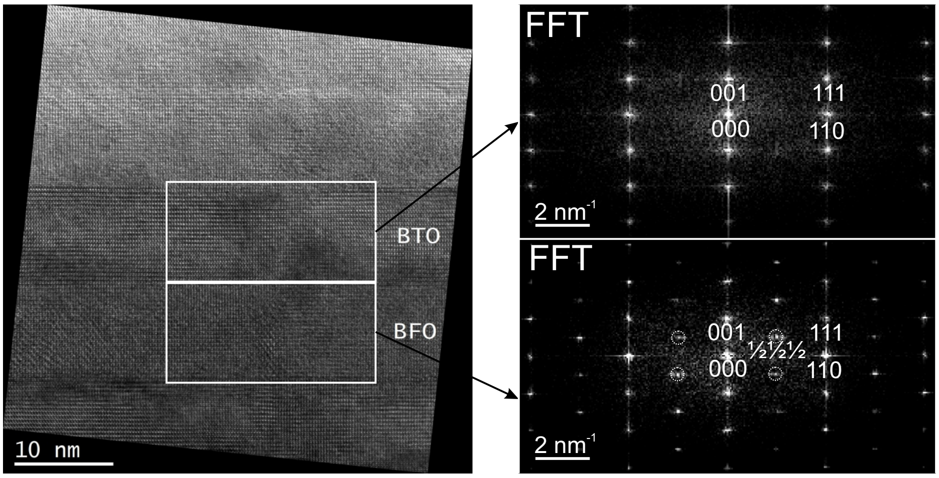

Figure 5.6: **(a)** (110)-oriented TEM cross-section and reduced FFT images of the indicated **(b)** BTO and **(c)** BFO areas of a $15\times[(\mathrm{BaTiO_3})_{10\ \mathrm{nm}}\text{-}(\mathrm{BiFeO_3})_{10\ \mathrm{nm}}]$ multilayer (F223). The reduced FFT image of the BFO layer clearly shows additional half-integer $(h+\frac{1}{2}, k+\frac{1}{2}, l+\frac{1}{2})$ peaks corresponding to the $a^-a^-a^-$ OOT system of BFO. These features are fully absent in the BTO layers.

marked in Fig. 5.6 a) are depicted. Both materials can be distinguished by their lattice parameters: $a_{\|} = 3.93 \pm 0.02\,\text{Å}$, $a_{\perp\mathrm{BTO}} = 4.07 \pm 0.02\,\text{Å}$, $a_{\perp\mathrm{BFO}} = 3.95 \pm 0.03\,\text{Å}$. The FFT image of the BTO region shows only the main structural peaks, while the FFT image of the BFO region clearly exhibits additional half-order peaks, indicative of $a^-a^-a^-$ OOT. This suggests that the OOT is firmly confined to the BFO phase and that both materials appear in their bulk symmetries.

However, this raises the question how this disparity between the two phases is reconciled at the interface. In principle, it is possible for OOT to propagate for a few unit cells into a material system, in which OOT is nominally forbidden, depending on the stiffness of the inter-atomic bonds [184]. However, it has also been found that just a single monolayer of BTO is capable of blocking the large angle OOT inherent to $\mathrm{GdScO_3}$ from propagating into a proximate $\mathrm{SrRuO_3}$ layer [38]. Conversely, *Borisevich et al.* found a total suppression of OOT in BFO at the hetero-interface to $\mathrm{La_{0.7}Sr_{0.3}MnO_3}$, which gradually relaxes over ~ 8 unit cells. Since OOT and the magnetic and magnetoelectric properties of BFO are deeply entwined, more detailed investigations of the actual interface structure of BTO-BFO multilayers may prove essential. Direct analysis of the tilt angles [185] or atomic column shape analysis [186] could give an unit cell resolved insight in the relaxation of the OOT at the interface. However, generating the very high-quality TEM images, such as used in [38, 184-187], as well as the necessary sub-pixel data analysis [188] go beyond the scope of this thesis.

5.1.2 Chemical Profile

We have recently published an in-depth study on the chemical depth profiles of two BTO-BFO multilayers in Ref. H1. In the study, we combined the techniques of ToF-SIMS, STEM-EDX and secondary neutral mass spectrometry for a better understanding of the chemical makeup of the multilayers. The measurements revealed a slight asymmetry of the Ba, Ti, Bi, and Fe distributions relative to the respective upper and lower interfaces. A number of trace elements such as Na, K, S, Si, P, and C were identified, with enhanced concentrations at the interfaces. There were also signs of chemical intermixing of $BaTiO_3$ into the $BiFeO_3$ layers. It has to be noted that the samples investigated in Ref. H1 suffered from large interface roughness in the nm-range, which likely lowered the actual depth resolution of the measurements at the interfaces. In particular, making statements about chemical intermixing were complicated due to this situation. Recently, a significant lowering of the interface roughness was achieved by eclipse-PLD. This enabled us to perform comparative chemical depth profile measurements with drastically reduced influence of the interface roughness, as will be discussed in detail in Sec. 5.4.

Lastly, we found a significant concentration of Bi in the first $BaTiO_3$ layer near the $SrTiO_3$ interface [H1]. The effect is detectable both in ToF-SIMS and in STEM-EDX measurements and exclusively occurs in the first BTO layer. We were able to reproduce this measurement for all samples that were investigated with STEM-EDX since, provided the quality of the cross-section allowed for high-resolution mappings. Fig. 5.7 b)-f) show the 2D elemental distribution of Ba, Bi, O, Ti, and Fe as measured by STEM-EDX near the interface of a recent $15 \times [(BaTiO_3)_{10\ \mathrm{nm}} - (BiFeO_3)_{10\ \mathrm{nm}}]$ multilayer deposited by eclipse-PLD (sample F223d). As can be seen by the Z-contrast in Fig. 5.7 a) (dark-field TEM image), the sample has sharp interface transitions with only ca. 1 unit cell interface roughness. Fig. 5.7 g) shows the normalized, horizontally averaged intensities of the elemental maps in OOP direction. The Bi enrichment at the STO interface stands out clearly. It is not accompanied by an enhanced Fe signal, but rather by a diminished Ba and Ti signal intensity. No other intermixing effects are apparent, apart from a 2 to 3 nm symmetric interface transition region, which can be ascribed to excitation in adjacent areas due to the non-negligible size of the electron beam interaction volume. Also in ToF-SIMS measurements, presented in Fig. 5.8, the Bi accretion at the bottom of the first BTO layer is detectable for this sample. Note that the data in Fig. 5.8 is presented logarithmically, whereas the scale in Fig. 5.7 g) is linear. An exact quantitative interpretation of either measurement is difficult due to matrix effects affecting the ionization probability in ToF-SIMS measurements and the high error level in EDX measurements. Nevertheless, it is evident that a significant

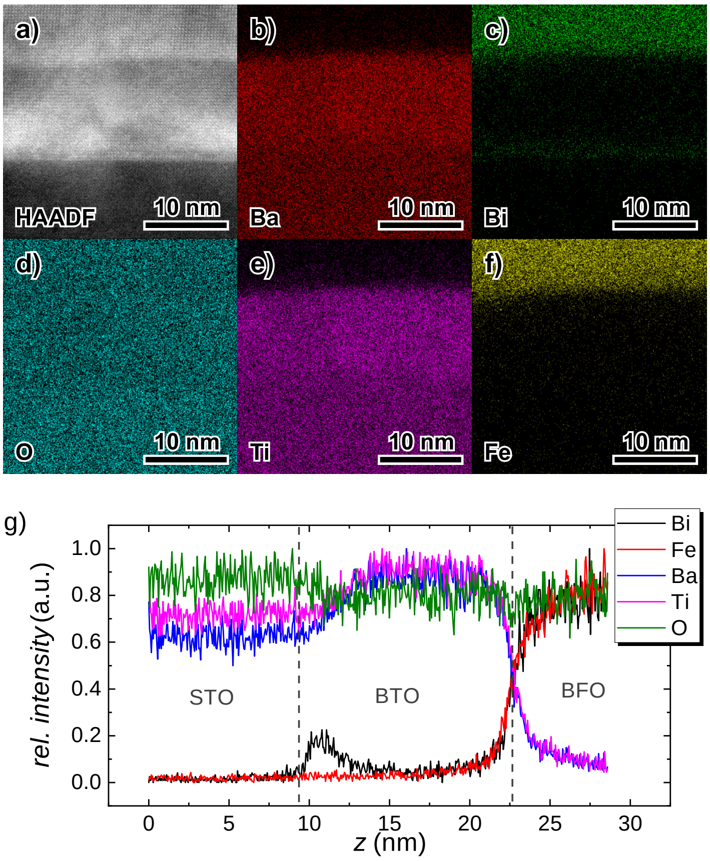

Figure 5.7: STEM(-EDX) images of sample F223d near the substrate: **(a)** HAADF image; **(b)-(f)** EDX distribution of Bi, Fe, O, Ba, and Ti, respectively; **(g)** vertical intensity profile of the EDX intensities shown in **(b)-(f)**. Note that the Ba intensity in the substrate region at the bottom of the image is due to an overlap of the Ba L_α and Ti K_α peaks, not due to the presence of Ba in the $SrTiO_3$ substrate.

amount of Bi in the order of magnitude of 10 at % relative to Ba and Ti is present near the substrate. The origin of this phenomenon is likely the re-evaporation of volatile Bi from the deposition chamber walls from previous deposition processes. Due to the large resistive heater used in our deposition chamber design, the entire chamber surrounding the heater and in particular the sample holder itself are heated. This leads to a surge in Bi desorption during the pre-heating process, a time period of up to 1 h during which the sample is brought up to process temperature.

5.1.3 Presence of Droplet Particles

Another ubiquitous feature common to all films is, as mentioned in Sec. 4.1.1, the presence of so-called droplets. Generated by non-equilibrium processes during pulsed laser ablation, these particles of up to several 100 nm do not necessarily share the same chemical makeup and phase of the surrounding thin film. Understanding the

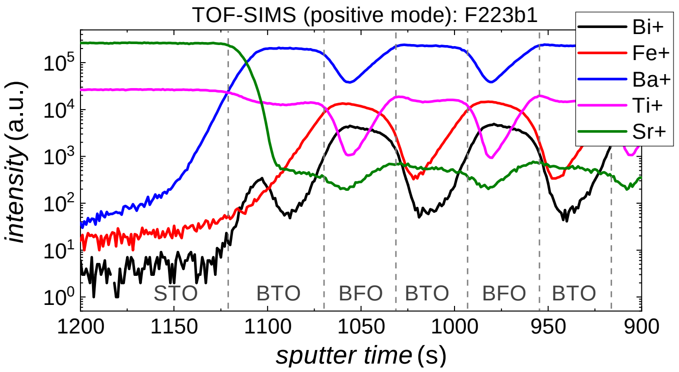

Figure 5.8: ToF-SIMS chemical depth profile of a typical BTO-BFO multilayer deposited by eclipse-PLD near the STO interface.

nature of these droplets is crucial to determining their impact on the overall sample properties. Fig. 5.9 shows the structure and elemental distribution of a cross-section of a typical BTO-BFO multilayer at a position containing droplets. As the STEM and STEM-EDX images show, the droplets reached the sample surface sometime during the deposition and were subsequently overgrown. All experimentally observed droplets contained mostly Fe and O. Rarely some amount of Bi is present in the droplets as well, as indicated in Fig. 5.9. In case of multilayers grown from 5 at % doped BGFO, the droplets were shown to be either Fe_xO_y, Gd_xO_y, or a mix of both, as presented in Fig. 5.10. No particles with Ba or Ti content were discovered. In short, droplets were only generated by ablation from the BFO targets. The most likely candidates for the precipitate phases are γ-Fe_2O_3, Fe_3O_4, Bi_2O_3, and Gd_2O_3. Both γ-Fe_2O_3 and Bi_2O_3 are commonly formed in thin film deposition of BFO with less-than-ideal process parameters [90,91] and possess significantly lower electrical resistivity. The presence of γ-Fe_2O_3 is often suggested to be the origin for high reported magnetization values in BFO thin films [90,91], due to its large magnetization of $1.25\,\mu_B/\mathrm{Fe}$. It has to be noted that no peaks indicative of any such phases have been detected in XRD measurements, which may be either due to a low overall percentage of the respective materials in the thin film matrix, or due to a lack of epitaxial alignment. The origin of iron oxide droplets generated by pulsed laser ablation of BFO was explained by *Ujimoto et al.* by the phase separation of $BiFeO_3$ into Fe_2O_3 and $Bi_2Fe_4O_9$ at the target surface due to the volatility of Bi [189].

Also visible in Figs. 5.9 and 5.10 are the different possible morphologies the droplets can exhibit. While in Fig. 5.9 the droplets appear to mold to the flat surface of the film, the droplet in Fig. 5.10 retained a spherical shape. Both types are common and lead to rough outgrowths on the sample surface. Large spherical particles such as the one shown in Fig. 5.10 can additionally disrupt the film growth by blocking incoming

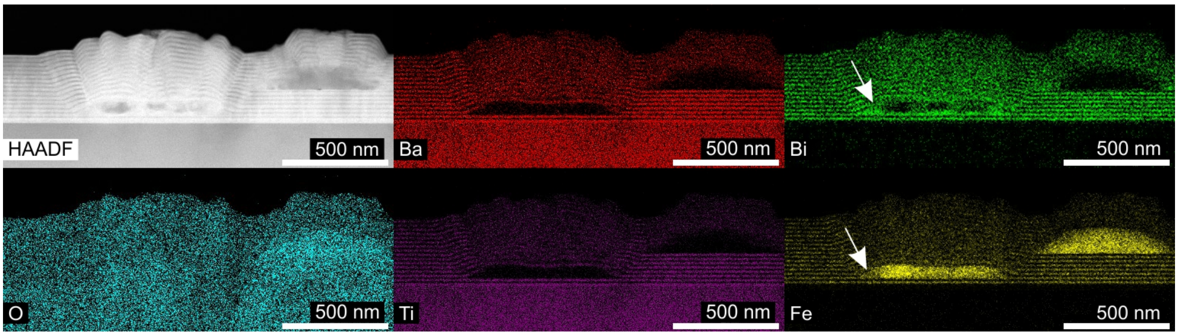

Figure 5.9: HAADF STEM image and STEM-EDX elemental distributions of Bi, Fe, O, Ba, and Ti, as indicated, of sample F026a showing two droplets. The arrows indicate an area of mixed Bi and Fe content in the droplet.

material. The result is a gap in the film that reaches as far down as the droplet. The deposition of the Pt top contacts for electric measurements by means of sputter deposition can fill these gaps, as shown in Fig. 5.10 (*middle, bottom row*). This is highly problematic for electronic measurements, as it can lead to premature electrode breakdown due to the locally increase of the electric field and cause short circuits.

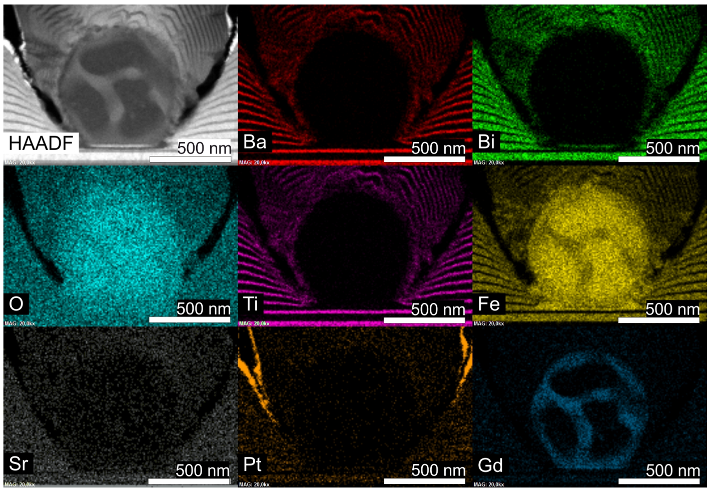

Figure 5.10: HAADF STEM image and STEM-EDX elemental distributions of Bi, Fe, O, Ba, Ti, Sr, Pt, and Gd, as indicated, of sample G5989c showing a droplet of mixed iron oxide and gadolinium oxide deposited after the second BTO layer.

In summary, droplets are generated only from the BFO target and are mostly iron oxide. They are likely candidates for premature electrode breakdown, which prevents fully saturated FE measurements, due to locally enhanced conductivity (cf. Ref. 90) and contacting of otherwise buried layers. LSM measurements show an average concentration of roughly 50 particles/100 μm^2 for samples deposited by conventional PLD. This leads to a staggering number of $2 \cdot 10^4$ particles in the 0.04 mm^2 area of the electrodes used for FE measurements. At a conservative estimate, assuming a 100 nm × 100 nm × 100 nm particle size, this is equal to 0.5 area%, or 0.17 vol% of a standard 300 nm film. This is the lower bound and LSM measurements suggest a median value closer to 1.5 area%. Considering the size of the droplets shown in Figs. 5.9 and 5.10, the droplet volume fraction in the film could be as large as 1 vol%. This has to be considered also when turning to magnetic measurements, as 1 vol% of γ-Fe_2O_3 ($2.5\,\mu_B$/f.u.) in a pure BFO film would falsely raise the measured saturation magnetization from $0.02\,\mu_B$/f.u. to $0.05\,\mu_B$/f.u. An exact determination of the phase and actual volume content was not possible so far and is complicated by the lack of according XRD peaks.

5.1.4 Leakage Current

As mentioned in Sec. 3.4, one of the greatest challenges when conducting experimental characterization of BFO thin films is a profound level of leakage current [97, 98]. In ferroelectric thin film capacitors, leakage current describes a flow of electrons between the electrodes of a ferroelectric capacitor structure that leads to a loss of polarization and obscures the ferroelectric switching peaks in dynamic $I(\boldsymbol{E})$-loop measurements, see Sec. 3.4. Due to the overlaid contributions of switching current, capacitive charging current and resistive (leakage) current in AC measurements, DC leakage current density measurements were performed. A further experimental issue is the destructive breakdown of BFO [98, 111]. The related breakdown field is dependent on the voltage dwell time, i.e. breakdown occurs at much lower voltages for DC compared to AC measurements [111]. As a result, DC leakage current measurements were limited to ±5 V. A significant improvement of the breakdown field was recently achieved for samples deposited with eclipse PLD, as will be discussed further in Sec. 5.4.

The incorporation of BTO into multilayer structures with BFO has a significant impact on the leakage current of NSTO-film-Pt capacitor structures. We performed $|j|\,(U)$ measurements on BFO and BTO single-layer and a selection of BTO-BFO multilayers, deposited under standard conditions. The maximum leakage current values at ±5 V are tabulated in Table 5.2.

Both the BTO single-layer and the BTO-BFO multilayer show significantly reduced leakage current densities compared to the BFO single-layer. Due to the asymmetric capacitor design of NSTO-film-Pt the values for positive and negative voltages diverge. In case of the multilayer, a further asymmetry is introduced to the capacitor design, as the first layer at the NSTO interface is BTO and the last layer at the Pt interface is BFO. Changing from a stoichiometric to an over-stoichiometric target has reduced the leakage current by an order of magnitude. The application of eclipse-PLD produced a further reduction of the leakage current, for details on samples produced by this technique, see Sec. 5.4. The improvements introduced by the multilayer design relative to the single-layer, as well as the improvements introduced by using an over-

Table 5.2: Leakage current density $|j|$ of various samples at ±5 V. Samples G6050, G5991 and F246 were grown using BFO targets with 10 % excess Bi, G5400 stems from the work of *Peter Schwinkendorf* and was grown using a stoichiometric BFO target. Sample F246 was deposited using eclipse PLD, the others using conventional PLD, all other growth parameters were nominally identical.

sample	description	d_{tot} (nm)	$\lvert j\rvert_{\mathrm{neg}}$ ($\mu\mathrm{A\,cm^{-2}}$)	$\lvert j\rvert_{\mathrm{pos}}$ ($\mu\mathrm{A\,cm^{-2}}$)
G6050	BFO single-layer	389	9.7×10^{1}	5.5×10^{4}
G5993	BTO single-layer	240	3.2×10^{2}	1.6×10^{-1}
G6044	overstoiciometric multilayer	536	1.2×10^{1}	6.9×10^{1}
G5400	stoichiometric multilayer	300	4.8	5.0×10^{2}
F246	eclipse multilayer	245	1.2	9.5

stoichiometric target and eclipse-PLD likely have one common source. All beneficial changes are connected to improved growth conditions, which is reflected in reduced mosaicity and roughness. Lowering of oxygen-deficiency through stoichiometric adjustment and reduction of ion bombardment damage lead to a reduction of defects. Similar results, utilizing growth-optimization of BFO-films, are commonly reported in literature [190, 191].

5.1.5 Imprint and Self-Poling

Concerning the ferroelectric properties of BTO-BFO multilayers, there is one key feature present in all samples produced in the framework of this thesis, which is called imprint. The term imprint or imprint field is used in reference to ferroelectric materials to denote a shift of the center of the ferroelectric hysteresis curve along the electric field axis [192-194]. This imprint signifies break of the degeneracy of the up and down polarization states. We have previously reported on this feature in Refs. H4, H5 and H3 for BTO-BFO multilayers. Notably, no sizable imprint is measurable for BTO-BFO composite thin films [11]. Due to substantial leakage current contributions and destructive breakdown, ferroelectric measurements of our BTO and BFO single-layer films are most often obscured by artifacts. However, we were able to demonstrate a horizontal shift of the ferroelectric hysteresis curve measured on BTO single-layer films in Refs. 11 and H3. Likewise, piezoresponse force microscopy measurements published in Ref. 87 suggest a preferential poling of single-layer BFO and rare-earth substituted BFO films. *Preferential poling* or *self-poling* is the term applied to formation of a predominant polarization direction without the presence of an applied electric field.

Both the horizontal shift due to imprint, as well as the effect of self-poling can be observed using the DHM ferroelectric hysteresis measurement, as discussed in Sec. 4.5. The hysteresis curves produced with DHM are recorded by measuring the current response to two bipolar, triangular voltage pulses. Each voltage pulse follows an identical pre-polarization pulse that leads to a positive (up) or negative (down) polarization state, given that the sample's coercive field is exceeded. After a waiting time of 1 s, the measurement pulse is applied, followed by the second pre-polarization and measurement pulses. If the first half of any of the two measurement curves does not match the second half of the corresponding other measurement curve, it must be due to processes taking place during the waiting period. To illustrate this notion, the $\boldsymbol{P}(\boldsymbol{E})$- and $I(\boldsymbol{E})$-curves measured on F198b, a generic $10 \times [(BaTiO_3)_{10\ \mathrm{nm}}\text{-}(BiFeO_3)_{10\ \mathrm{nm}}]$ multilayer produced by eclipse PLD, are presented in Fig. 5.11.

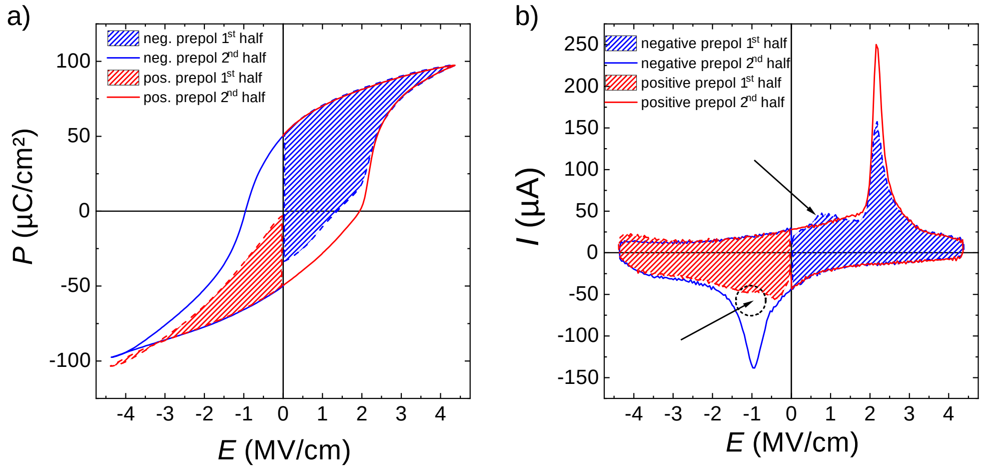

Figure 5.11: Details of the ferroelectric hysteresis measurement **(a)** $\boldsymbol{P}(\boldsymbol{E})$ and **(b)** $I(\boldsymbol{E})$-curves of sample F198b ($10 \times [(BaTiO_3)_{10\ \mathrm{nm}}\text{-}(BiFeO_3)_{10\ \mathrm{nm}}]$, eclipse PLD). The shaded areas represent the respective first halves of the measurement as measured by a bipolar, triangular voltage pulse following a respective pre-polarization pulse of the same form, as outlined in Sec. 4.5. The arrows in b) mark the presence of the extra positive switching peak and the lack of the negative switching peak. Both occur after the waiting period of 1 s following negative and positive pre-polarization pulses, respectively. The *TF 2000 HS*'s internal leakage compensation was employed for this measurement.

The horizontal shift of both curves is clearly visible. With an average coercive field of ~1.5 MV cm^{-1}, the imprint field of 0.5 MV cm^{-1} significantly shifts the equilibrium towards positive voltages (applied to the top electrode). The shaded areas denote the respective first halves of the two measurement segments (*red*: following positive (up) pre-polarization; *blue*: following negative (down) pre-polarization) which follow the 1 s waiting period after pre-polarization. As the $I(\boldsymbol{E})$-curves in Fig. 5.11 b) show, the negative (down) pre-polarization leads to the appearance of a secondary, smaller positive switching peak and a slight decrease of the primary positive switching peak in the blue shaded curve. The additional peak could point to a change in the switching dynamics based on the previous sample treatment. As BFO in $[001]_{\mathrm{p.c.}}$ orientation has four diagonal polarization directions corresponding to each up and down polarization direction of BTO, polarization switching in BFO is not limited to linear processes, but can be the product e.g. of lower energetic threshold limited 71° switching followed by ferroelastic relaxation [195]. More prominently, after the positive (up) pre-polarization pulse, the negative switching peak is absent in the red shaded curve. This is a clear indicator that the ferroelectric film reverts from an up to a down polarized state in the 1 s waiting period. This self-poling is a direct result of the loss of degeneracy as imposed by the significant built-in imprint field.

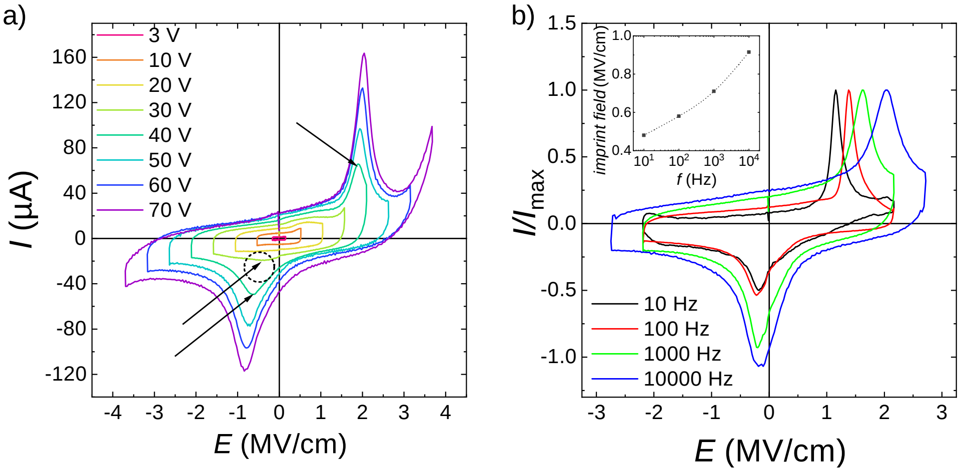

Figure 5.12: $I(\boldsymbol{E})$-curves recorded at **(a)** increasing maximum fields and **(b)** various frequencies of sample F198b ($10 \times [(\mathrm{BaTiO_3})_{10\ \mathrm{nm}}$ - $(\mathrm{BiFeO_3})_{10\ \mathrm{nm}}]$, eclipse PLD). The *TF 2000 HS*'s internal leakage compensation was employed for the measurement presented in **(b)**.

Independent of the previous treatment of the sample with different pre-polarizing voltage pulses, the negative switching peak appears in $I(\boldsymbol{E})$ measurements with successively increasing maximum voltages only after the positive coercive field is reached, as shown in Fig. 5.12 a). Note that the internal leakage compensation was not used for the measurements in Fig. 5.12 a). Variation of the measurement frequency, defined as the inverse of the bipolar pulse length, interestingly leads to a shift of the positive switching peak, but not of the negative switching peak. Fig. 5.12 b) shows the $I(\boldsymbol{E})$-curves measured on sample F198b at frequencies from 10 to 10 000 Hz. As shown in the inset in Fig. 5.12 b), the resulting imprint field shifts roughly with the logarithm of f from 0.5 MV cm^{-1} at 10 Hz to 0.9 MV cm^{-1} at 10 000 Hz. Notably, the peak positions vary between Fig. 5.11 b) and Fig. 5.12 a), and Fig. 5.12 b), despite the fact that two adjacent contact pads were used for the measurements. Such a discrepancy is quite common for all samples investigated in the framework of this thesis. This applies to all quantitative measurement values related to ferroelectricity, i.e. saturation and remanent polarization, as well as coercive field strength. Likely, this is a sign of local inhomogeneities and may be connected with the occurrence of droplets in the thin films, as no direct relation to other factors such as the size of the electrode pad or its position on the sample surface could be identified.

The phenomenon of imprint or self-poling of epitaxial ferroelectric films has long been explored by the scientific community. And though many theories pertaining to its origin have been produced, consensus about it is still lacking. One of the most common hypotheses is the involvement of so-called defect dipoles [196]. These are supposedly formed "when two or more oppositely charged point defects in a lattice couple or interact in such a manner to produce a negative energy of association" [197], e.g. by introduction of negatively charged acceptor ions and correlating positively charged oxygen vacancies [196]. These defect dipoles possess large coercive fields and switching processes are limited by "thermally activated diffusive jumping of the oxygen vacancies" [196]. If the defect dipoles are aligned with respect to the crystal lattice, this results in a shift of the ferroelectric hysteresis along the voltage axis. Such an alignment has even been demonstrated for bulk ceramic samples of BFO by introduction of a temperature gradient during cool-down [113]. Without such a constraint, polycrystalline ferroelectric materials, unlike epitaxial films, do not show imprint. *Damodaran et al.* showed that the bombardment damage as incurred during PLD deposition of BTO films at increasing laser fluence has a direct impact on the imprint field strength, which they linked to an increased number of defect dipoles [197]. They found that only BTO films deposited on substrates that impose compressive strain, like $DyScO_3$ or GdScO, produce an imprinted FE hysteresis loops. They attributed this to downward alignment of defect dipoles via the compressive strain gradient between substrate and film surface. Furthermore, they found a clear correlation of the positive coercive field with the measurement frequency, much as described above and in agreement with the idea of thermally activated oxygen vacancy jumping related switching [196, 197].

Similarly, the existence of a non-switching layer, or simply a layer with very high coercive field strength, at the interface to the bottom electrode, i.e. the substrate has been theorized [194, 198, 199]. *Abe et al.* found an asymmetric hysteresis and leakage current in BTO thin films deposited on $SrRuO_3$/STO, Pt/MgO and NSTO [194]. They correlated this phenomenon with thickness dependent film relaxation and concluded an "asymmetric crystal structure caused by misfit dislocations" close to the substrate interface as the cause. Similar to the alignment of defect dipoles, compressive strain of the substrate should lead to a downward polarization in this layer. In a later publication, based on a phenomenological free energy model function, they suggest that the presence of free charges, which compensate the innate polarization discontinuity introduced by a non-switching layer, may be responsible for the observed voltage shift [198]. As we have found both a 3 nm transient relaxation layer at the interface to STO (see Sec. 5.1.1) and a concentration gradient of Bi in the first BTO layer (see Sec. 5.1.2), the existence of such a non-switching layer is fairly plausible for our samples.

Strain gradients inducing self-poling via the flexoelectric effect have also been suggested for epitaxial films of $PbZr_{0.2}Ti_{0.8}O_3$ [200], BFO [114] and BTO [201]. By variation of the deposition temperature and film thickness, this leads to either upward or else downward self-poling for BFO thin films on $SrRuO_3$/STO [114]. Similarly, *Beekman et al.* showed that BFO layers on $LaAlO_3$ can be grown as either rhombohedral or monoclinic variant using slightly different $La_{0.3}Sr_{0.7}MnO_3$ buffer layers [202]. The rhombohedral variant showed upward self-poling and the monoclinic variant showed downward poling, which was attributed to differences in their strain states. *Chen et al.* note on the nature of self-poling in BTO thin films: “The upward self-polarization exists in the thin $BaTiO_3$ films with strong inhomogeneous compressive strain, while it disappears in thick $BaTiO_3$ films due to strain relaxation. Since the upward self-polarization is unchangeable when the p-type $La_{0.3}Sr_{0.7}MnO_3$ was replaced by the n-type SrRuO3 and Nb-SrTiO3, the depletion region and the polar discontinuity at interface are excluded to be their origins. Similarly, the density gradient of negative charged cation vacancies is not the main origin because it would introduce downward self-polarization” [201]. This non-dependence of the strain-induced upward self-poling effect was also observed in the case of $PbZr_{0.2}Ti_{0.8}O_3$ deposited on either $La_{0.3}Sr_{0.7}MnO_3$/STO, $SrRuO_3$/STO or NSTO [200].

Whatever the actual source of the self-poling effect observed in BTO-BFO multilayers may be, its existence is certain. A direct implication of a preferred polarization direction without the need for a previous poling action relates to the magnetoelectric measurements performed on such samples. Generally, a magnetoelectric multiferroic sample with randomly oriented FE domains averaging out to zero net polarization cannot produce a magnetically induced ME voltage [203-205]. However, our measurement procedure for the thin film ME effect does not include a FE poling procedure. Due to the self-poling nature of our samples however, we are able to measure α_{ME} nonetheless.

Effect Substrate Annealing on Ferroelectric Properties

It is a fairly common to pre-treat (100)-oriented $SrTiO_3$ substrates for thin film deposition by etching with diluted hydroflouric acid and annealing in oxygen rich atmosphere. The substrates are produced by cleaving larger crystals along the required lattice plane and polishing the surface upon which the film is to be deposited. The pre-treatment creates well-defined, unit cell stepped, TiO_2-terminated surfaces [50, 51]. As a substrate, STO is mostly used for the growth of perovskite materials such as oxide electrodes like $SrRuO_3$, ferroelectrics like $BaTiO_3$ and superconductors like $YBa_2Cu_3O_{7-x}$ [50,51,206].

The pre-treatment has been found to enable the growth of highly ordered, singly terminated thin film structures [206] and to promote true layer-by-layer and step-flow growth [50, 51]. The technique was also adapted in the framework of this thesis and all previous efforts to grow high-quality BTO-BFO heterostructures undertaken by our group. The effect, however, that the pre-treatment has on the properties of BTO-BFO multilayers has not been reported so far.

To this end, a series of $15 \times [(BaTiO_3)_{10\ \mathrm{nm}} \text{ - } (BiFeO_3)_{10\ \mathrm{nm}}]$ was deposited on NSTO substrates under standard conditions. Three deposition processes, each with one pristine (as received) and one annealed NSTO substrates, were carried out, the details of which can be found in Table 5.3. Eclipse-PLD was employed, as films generated with this technique tend to withstand the large fields required for ferroelectric testing, which increases the accessibility of the ferroelectric properties. A higher pulse count per layer was used to generate the samples labeled F220a and F220a, but yielded very similar thicknesses. The reason is the dependency of the deposition rate in eclipse-PLD films on the operating voltage of the excimer laser, more on this topic can be found in Sec. 5.4. In process F222, the first 300 pulses BTO used a repetition frequency of 1 Hz, all consecutive pulses and all pulses in process F220 and F221 used a repetition rate of 20 Hz. The reduced growth rate at the beginning of the deposition process is another technique used by *Lorenz et al.*, which is supposed to promote relaxation in the early growth process and has been adapted for most samples throughout this work.

Table 5.3: List of samples used for the study of the effect of substrate annealing. The identifiers a and b refer to one sample deposited on pristine NSTO (a) and another on annealed NSTO (b), respectively. F222a, b: first 300 pulses BTO were deposited at 1 Hz.

sample	U_{laser} (kV)	pulses per layer		d_{dl} (nm)	$\boldsymbol{P}_{\mathbf{max}}$ $\mu\mathrm{C\,cm^{-2}}$		$\boldsymbol{E}_{\mathbf{coer}}$ $\mathrm{MV\,cm^{-1}}$		E_{imprint} $\mathrm{MV\,cm^{-1}}$	
		BTO	BFO		prist.	ann.	prist.	ann.	prist.	ann.
F220a, b	18.1	1250	4500	18.5 ± 0.4	50.6	57.5	1.20	1.10	1.37	0.97
F221a, b	17.4	1200	2750	19.1 ± 0.3	56.8	59.8	1.01	0.81	1.43	1.16
F222a, b	17.6	1200	2750	18.5 ± 0.5	53.6	58.4	0.92	0.85	1.45	1.19

2θ-ω scans of the samples show no appreciable differences between the samples of each process deposited on either pristine or annealed NSTO. The regions around the fist and fourth substrate peak are depicted in Fig. 5.13. In both the high and low angular regions, the respective 2θ-ω scan pairs match to a high degree. The similarity is replicated in RSM measurements (not shown here), with identical symmetric and asymmetric peak-widths in ω -direction measured for F220a and F220b. The consecutively deposited samples F221a, b and F222a, b have extremely similar peak structures with respect to one another. Samples F220a, b exhibit slightly higher superstructure peaks. This attests to a slightly higher crystalline quality of the sample, possibly due to the slower growth rate at the elevated laser operating voltage. XRR measurements of sample F220a suggest an approximate individual layer thickness of 9.5 nm for BTO and 8.8 nm for BFO, fairly close to the supposed standard sample values of 10 nm each.

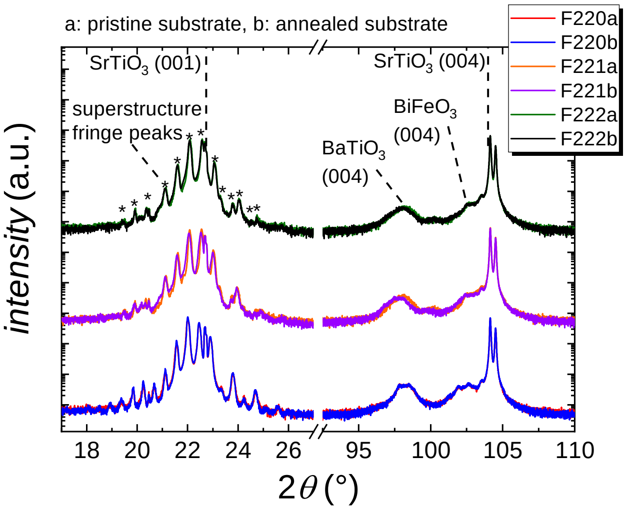

Figure 5.13: XRD 2θ-ω scans of samples F220, F221 and F222 a and b used for the study of the effect of substrate annealing. The identifiers a and b refer to one sample deposited on pristine NSTO (a) and another on annealed NSTO (b), respectively.

The surface morphologies of all six samples was probed by AFM. Topographical AFM images of all six samples are depicted in Fig. 5.14. All samples show almost identical morphologies, as both on pristine and annealed substrates unit cell stepped irregular terraces are present. The surface roughness R_{rms} is 0.20 ± 0.03 nm for all samples. This highlights the excellent sample quality produced by eclipse-PLD, see Sec. 5.4.

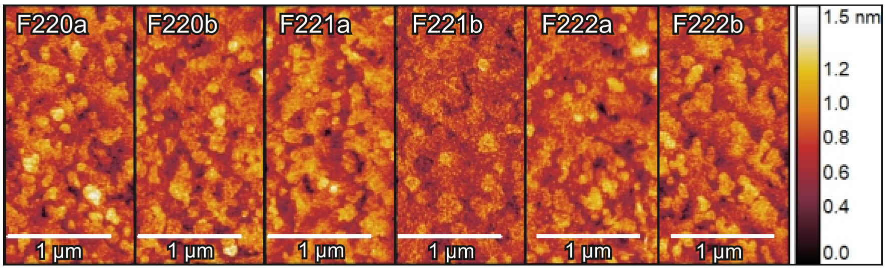

Figure 5.14: Topographic AFM images taken on samples F220, F221 and F222 a and b. The identifiers a and b refer to one sample deposited on pristine NSTO (a) and another on annealed NSTO (b), respectively.

In addition to the samples structural and morphological homogeneity, all samples showed a small and noisy ferromagnetic hysteresis loop in $\boldsymbol{M}(\mu_0\boldsymbol{H})$ VSM measurements at 300 K (not shown). All samples showed a saturation magnetization of

$2.0 \pm 0.2\,\mathrm{emu\,cm^{-3}}$, ca. $0.015\,\mu_\mathrm{B}$/f.u. and a coercive field of $40 \pm 5\,\mathrm{mT}$. The one distinct difference between samples deposited on pristine or annealed NSTO substrates was found in ferroelectric measurements. The key ferroelectric measurement parameters of all six samples are presented in Table 5.3. On each sample, three top-electrodes were selected for measurements, with different distancing from a single bottom-contact, i.e. with distances of ca. 1 mm, 3 mm and 6 mm to one substrate corner. This creates a higher statistical significance to the measurements. In addition, it allows the simultaneous investigation of a possible influence of the substrate through the electrode-to-electrode distance. All three sample pairs showed similar trends between pristine and annealed substrate samples, hence only the $\boldsymbol{P}(\boldsymbol{E})$ and $j(\boldsymbol{E})$ measurements of samples F220a and F220b are presented exemplary in Fig. 5.15. Note that, to maximize comparability, the electrode areas were determined individually via LSM and in Fig. 5.15 a), the current density j is plotted instead of I. Between the three measurement points labeled close, center and far, no systematic changes with the electrode-electrode distancing were found, only small randomized deviations due to minor local inhomogeneities in the sample. In all three sample pairs, the respective negative and positive switching peaks occur at larger fields in $j(\boldsymbol{E})$ measurements. In the corresponding $\boldsymbol{P}(\boldsymbol{E})$ measurements, the change is mirrored only in the positive coercive field, the negative coercive field is largely unaffected. Most notably, the imprint fields of samples deposited on annealed substrates is 18 to 29 % smaller than for samples deposited on pristine substrates. At the same time, the maximum polarization is increased buy up to 14 % for samples on annealed substrates. The increased polarization is, however, likely linked to a marginally larger leakage current at large positive fields, as indicated by the upwards bend in the blue, purple and violet $j(\boldsymbol{E})$-curves shown in Fig. 5.15 a). Furthermore, there is no visible difference between the samples deposited with and without an initially slower laser repetition rate for the first BTO layer (F221 and F222).

In summary, the effect of NSTO substrate annealing on the general material properties of BTO-BFO multilayers is only minute. No significant changes in structure, morphology and magnetic properties were found. A reduction in coercive and imprint fields in ferroelectric measurements however suggest that a certain influence on the polarization state is manifested during growth. As discussed in the previous section, initial layer growth and interface-bound defects are thought to play an elementary role in the formation of ferroelectric imprint and large coercive fields [194,198,199]. In the presented case, it seems that the substrate annealing reduces such effects. At the same time, a reduction of the laser repetition rate from 20 to 1 Hz for the first 300 pulses has no effect to that end. At the very least, not in the case of eclipse-PLD, which may be due to the already low deposition rate of only $\sim 1\,\mathrm{\AA\,s^{-1}}$ at 20 Hz.

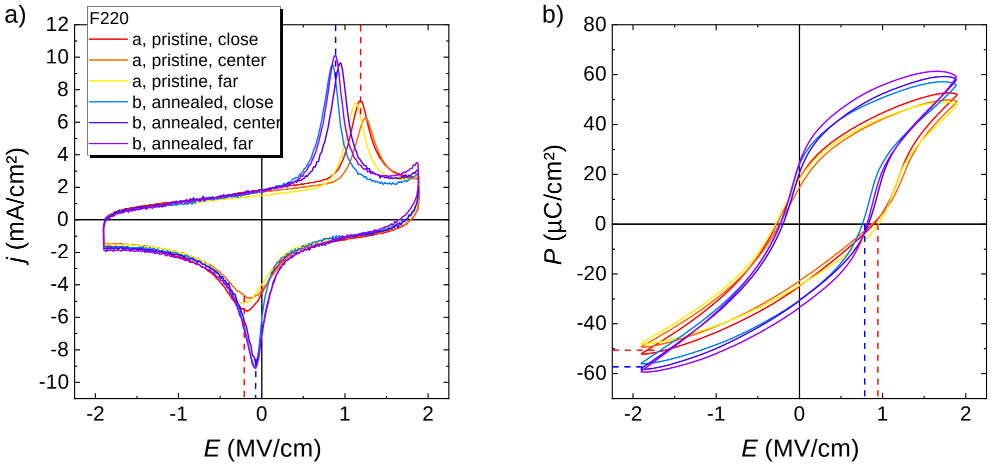

Figure 5.15: (a) $\boldsymbol{P}(\boldsymbol{E})$ and **(b)** $j(\boldsymbol{E})$-loops measured on Pt-NSTO-multilayer-Pt capacitor structures on samples F220a (pristine NSTO) and F220b (annealed NSTO). The nominal Pt electrode areas were 8500 µm^2, the actual area sizes diverged slightly and were explicitly measured by LSM to conserve comparability. The distance from the *bottom* electrode on one corner of the sample to the *top* contacts labeled *close*, *center* and *far* were 1 mm, 3 mm and 6 mm, respectively. The *red* and *blue* dashed lines indicate the average switching peak positions in a) and the maximum (negative) polarization and the positive coercive field in b).

5.1.6 Magnetoelectric Properties

The base value of the ME coupling coefficient α_{ME}, measured at 300 K in 0 T, is, generally speaking, larger in multilayers and solid solution films of BTO-BFO than insingle-layer of BFO [11]. By measuring the bias magnetic field and temperature dependence of the α_{ME}-coefficient, certain characteristic traits unique to the film types become evident. This suggests an underlying difference of the origin of the ME effect inherent to the sample architecture. In Fig. 5.16, exemplary $\alpha_{\mathrm{ME}}(\mu_0\boldsymbol{H}_{\mathrm{DC}})$ and $\alpha_{\mathrm{ME}}(T)$ measurements of a 363 nm BGFO single-layer (G6051) and a 15×23 nm BTO-BGFO multilayer (G5992) are depicted. The inclusion of 5 % Gd in the BFO layers does not change the characteristics of the α_{ME}-curves, for comparison see Fig. 12 in Ref. H5 .

The α_{ME} DC bias field dependency of single-layer of BFO, as shown in Fig. 5.16 a), typically shows a maximum around 1 T, after which α_{ME} decreases monotonously. This behavior is persistent across all of our sample series up to date and also holds for the solid solution films [11, 147, H3]. A similar behavior was found in the original report on ME coupling on BFO thin films by *Wang et al.* [9], albeit with a maximum at much lower fields. In stark contrast, all BTO-BFO multilayers investigated so far show an increase in α_{ME} with $\mu_0\boldsymbol{H}_{\mathrm{DC}}$ which saturates at 2 to 3 T [11, 148, 152, H3]. So far, we have only found one exception to this rule - measured for a multilayer with particularly large BGFO thickness - which will be discussed in Sec. 5.5.

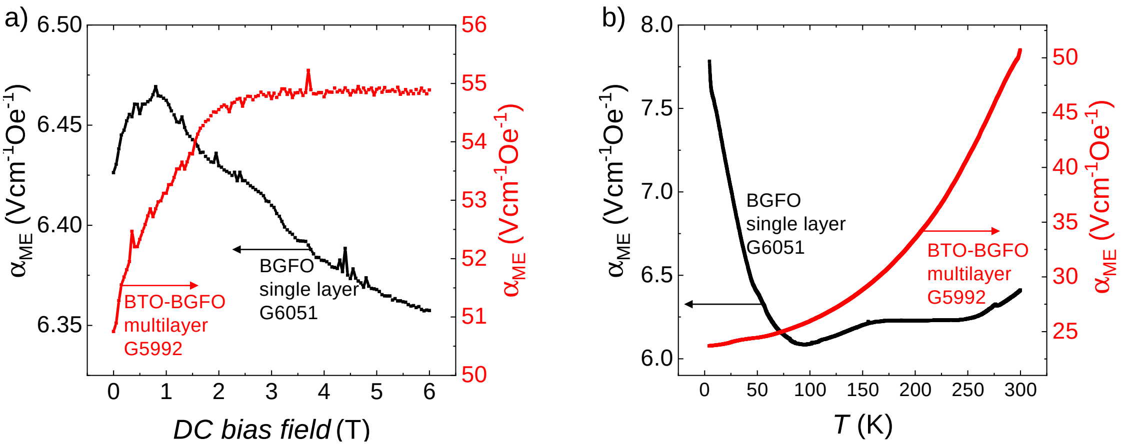

Figure 5.16: **(a)** DC bias magnetic field dependent and **(b)** temperature dependent α_{ME} -coefficient measurements of an exemplary 363 nm BGFO single-layer (G6051) and a 15×23 nm BTO-BGFO multilayer (G5992). The $\alpha_{\mathrm{ME}}(\mu_0\boldsymbol{H}_{\mathrm{DC}})$-curves in a) were recorded at 300 K and the $\alpha_{\mathrm{ME}}(T)$ in b) were recorded in 0 T $\mu_0\boldsymbol{H}_{\mathrm{DC}}$. Data was originally published in Ref. H3.

With decreasing temperature, the α_{ME}-coefficient of BFO single-layer decreases from 300 to ~100 K and subsequently increases below 100 K, see Fig. 5.16 b). The $\alpha_{\mathrm{ME}}(T)$-curve of the multilayer depicted in Fig. 5.16 b) is monotonously falling with decreasing temperature. Unlike with the bias field dependency, the curve shown for the multilayer is not universal to all BTO-BFO multilayer samples. *Jochum et al.* showed that the temperature dependency of a series of multilayers with constant BTO thickness and varying BFO thickness resembles the curves shown for single-layer and multilayers in Fig. 5.16 b) overlaid with one another [152]. As d_{BFO}, and hence d_{dl}, decreases, $\alpha_{\mathrm{ME}}(T)$ continuously changes from the single-layer behavior to the multilayer behavior [152]. As we will see in Sec. 5.5, this change in temperature dependency with varying d_{BFO} is not always as straightforward. Nevertheless, we have confirmed a monotonously falling α_{ME} behavior with decreasing temperature in all samples grown in chamber F with d_{dl} below 20 nm [H4] (see also Sec. 5.2.2 and Sec. 5.3).

5.1.7 Summary

To briefly summarize the general properties that distinguish multilayers of BTO and BFO from the respective single-layers:

- BTO grows in *c*-domains in multilayers, but in *a*-domains in single-layers
- The first few nm of BTO show signs of relaxation and Bi-contamination
- BTO-BFO multilayers show lower mosaicity and interface roughness than the respective single-layers
- OOT is confined to the BFO layers
- Droplets are generated during the ablation of BFO
- Multilayers show decreased leakage current density relative to single-layers and ferroelectric self-poling
- BTO-BFO multilayers and BFO single-layers have distinct dependencies on the applied magnetic field and the measurement temperature

Overall, the growth of BTO and BFO combined in multilayer structures has several advantages for the structural, morphological and electrical qualities of the samples. A particularly interesting distinction is the change in α_{ME}-behavior. Where BFO single-layers experience a minor surge and subsequent decrease of α_{ME} in a growing magnetic bias field, all multilayers show saturating behavior. The dependence of α_{ME} on the measurement temperature will be the subject of further scrutiny in Sec. 5.5. The presence of droplets is disruptive for both ferrelectric and magnetic measurements, as they can cause short-contacts and falsely enhance the measured magnetization of the multilayer samples. Hence, the efforts of sample-optimization by parametric variation, presented in Sec. 5.2, and by eclipse-PLD, presented in Sec. 5.4, revolve to a large extent around the elimination of droplet particles.

5.2 PLD–Growth of $BaTiO_3$–$BiFeO_3$ Multilayers

Exploring the results of systematic variation of the deposition parameters serves two primary functions. On one hand, it is a necessary step to optimize the deposited layers for specific purposes. In practice, this commonly concerns e.g. improving resistivity of the ferroelectric layer, reducing the amount of droplets for the sake of homogeneity and increased electric breakdown field, or the reduction of surface or interface roughness. In particular a high interface roughness of multilayers is disadvantageous for the informative value of chemical depth profiling and increases the interface area between the constituent materials. On the other hand, changes of a measurement parameter based on the variations of single deposition parameters can be used to infer explanations on the origin of a given phenomenon. One such example is the perceived dependence of α_{ME} on the deposition pressure reported in Refs. 148 and 147, which was the prompt to investigate the importance of oxygen vacancies introduced by lowering the oxygen supply during growth. In the following section we will explore the influence of the growth temperature, pressure, laser fluence and lateral offset on the structural and morphological properties of BTO-BFO-multilayers. Furthermore a quick insight in the influence of substrate annealing and the evolution of stacking of alternating BTO and BFO layers will be given. Lastly, the effects of introducing a shadow mask (eclipse PLD) will be discussed. The influence of multilayer design choices will be the topic of the subsequent section.

5.2.1 Effect of Substrate Temperature

As *Bea et al.* point out, phase pure growth of BFO is confined to a narrow parametric window of process temperature T and oxygen pressure p_{O_2} [90]. Deviations from the ideal parameter range lead to the formation of secondary phase precipitates, as oxygen concentration and relative re-desorption rates of different elements, in particular that of volatile Bi, shift [89, 92]. Even low concentrations of precipitates that go undetected in regular XRD measurements can have a profound influence on the overall layer properties. For example, Bi_2O_3 has been found to form low resistance channels in BFO host material [90] and the Fe_2O_3 has often been stated as the source of the anomalously large magnetism reported in some BFO films, as its saturation magnetization lies two orders of magnitude above that of BFO [91, 207]. Apart from these concerns, the growth temperature also takes part in determining the growth mode of any given material. As mentioned before, it is desirable to generate particularly flat interfaces and surfaces for multilayer growth.

To re-evaluate the process temperature of 680 to 700 °C used by *Lorenz et al.* in Refs. 11, 121, 148, 149, a series of $15 \times [(BaTiO_3)_{8\ \mathrm{nm}} - (BiFeO_3)_{8\ \mathrm{nm}}]$ multilayers was deposited in 0.25 mbar at temperatures between 570 to 725 °C. Note that, while in the mentioned publications the temperature given is the estimated substrate temperature, ca. 50 °C lower than the measured process temperature, in the framework of this thesis the process temperature is reported instead.

Morphology

The surface morphologies of BTO-BFO multilayers grown at different temperatures, as measured by AFM, are presented in Fig. 5.17, the R_{rms} roughness and grain sizes are plotted in Fig. 5.18. With increasing temperature, the grain size continuously increases, while the surface roughness is minimal for 670 °C. Beginning at a growth temperature of 700 °C a certain amount of pitting occurs. For the 725 °C sample pits in the nanometer range are clearly visible. It appears that at the lowest and highest process temperatures, 3D growth is favored, while at intermediate temperatures of 670 to 700 °C, a more two-dimensional growth occurs, as the dip in the R_{rms}-curve in Fig. 5.18 suggests. A fairly similar temperature dependency was reported by *Jiang et al.* for the PLD-growth of BFO [89]. So while high temperatures are certainly advantageous for highly ordered growth of BTO-BFO multilayers, excessive heat appears to disrupt layer-by-layer growth. The volatility of Bi is likely to play an integral role in this process [89].

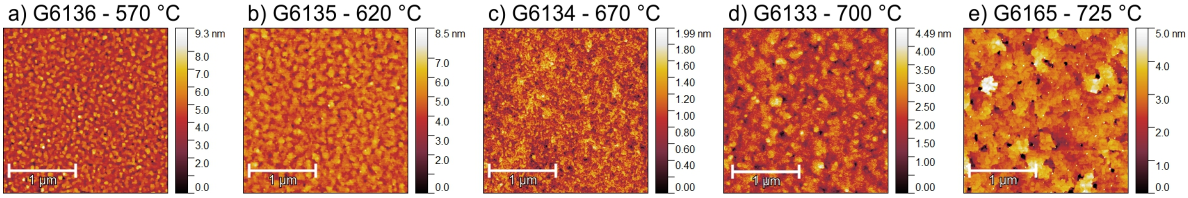

Figure 5.17: Topographic AFM images for multilayers of $15 \times [(BaTiO_3)_{8\ \mathrm{nm}} - (BiFeO_3)_{8\ \mathrm{nm}}]$ multilayers deposited at varying temperatures in deposition chamber *G*.

Structural Properties

XRD 2θ-ω scans, shown in Fig. 5.19, variate only ever so slightly with the process temperature. All films show superstructure fringe peaks up to the fourth order close to the (001) and (002) substrate peaks with similar peak-to-valley ratios, indicating a comparable interface roughness, despite the variable surface roughness, for all temperatures. The film deposited at 725 °C is the only exception with only up to second order fringe peaks visible. None of the films deposited in the entire 570 to 725 °C range display any signs of secondary phases, in line with the findings of both *Bea et al.* [90] and *Jiang et al.* [89].

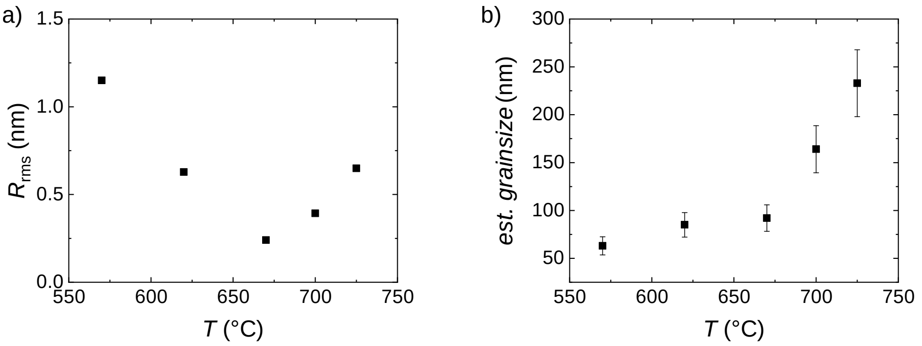

Figure 5.18: Evolution of **(a)** the roughness parameter R_{rms} and **(b)** evolution of the estimated grain size with the deposition temperature T for multilayers of $15 \times [(\mathrm{BaTiO_3})_{8\ \mathrm{nm}}\text{-}(\mathrm{BiFeO_3})_{8\ \mathrm{nm}}]$ deposited in deposition chamber G.

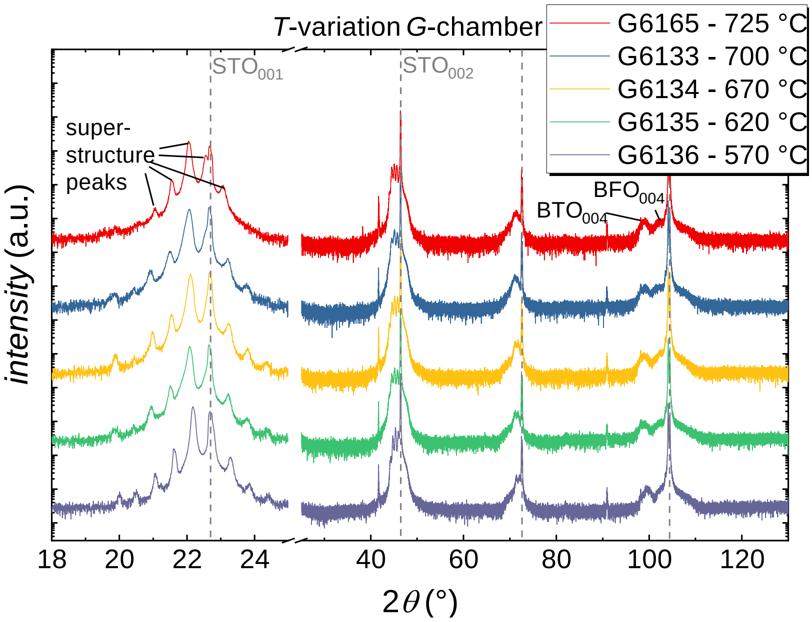

Figure 5.19: XRD 2θ-ω scans for $15 \times [(\mathrm{BaTiO_3})_{8\ \mathrm{nm}}\text{-}(\mathrm{BiFeO_3})_{8\ \mathrm{nm}}]$ multilayers deposited at varying temperatures in deposition chamber G.

Magnetic Properties

The magnetic properties of the multilayers deposited at various temperatures were probed by VSM measurements. $\boldsymbol{M}(\mu_0\boldsymbol{H})$-curves recorded at 300 K are presented in Fig. 5.20 a), the determined values of $\boldsymbol{M}_{\mathbf{sat}}$ measured at 1 T and $\boldsymbol{M}_{\mathbf{rem}}$ are depicted in Fig. 5.20 b). The ratio of remanent to saturation magnetization is stable within the margin of error throughout the series. All films show a magnetic hysteresis that saturates at ~ 0.4 T, with a small coercive field of 13 ± 5 mT. The saturation magnetization values vary from 1.7 to 3.9 emu cm^{-3}, equal to ~ 0.01 to 0.03 μ_{B}/f.u. Though half of the layer is composed of non-magnetic BTO, these values genuinely conform with the commonly stated 0.02 μ_{B}/f.u. of pure BFO films [69].

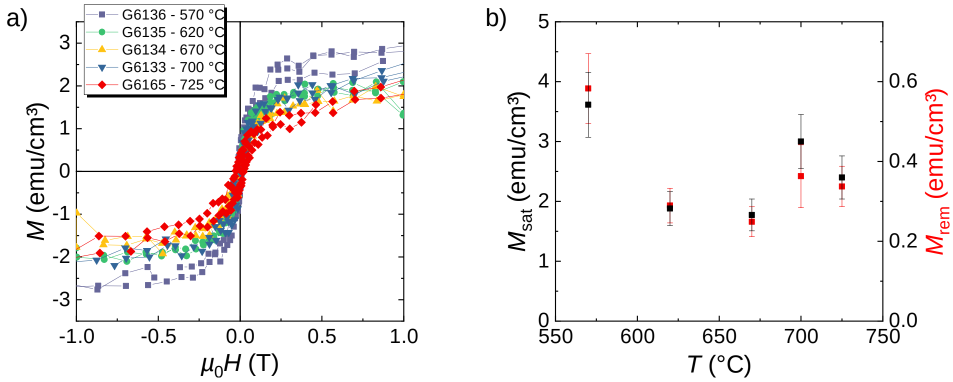

Figure 5.20: **(a)** $\boldsymbol{M}(\mu_0 \boldsymbol{H})$-curves recorded at 300 K, **(b)** values of $\boldsymbol{M}_{\mathbf{sat}}$ measured at 1 T and $\boldsymbol{M}_{\mathbf{rem}}$ for multilayers of 15 × $[(BaTiO_3)_{8\ \mathrm{nm}}$ - $(BiFeO_3)_{8\ \mathrm{nm}}]$ deposited at varying temperatures.

Let it be noted that the presented series was deposited in chamber *G*. For the sake of reproducibility and comparability, another temperature series was grown when transitioning to deposition chamber *F*. The results (not shown here) lead to analogous conclusions, confirming that both deposition chambers provide sufficiently similar temperature conditions based on the process temperature measurement. Overall, a deposition temperature of around 700 ± 30 °C appears sensible and was adopted as standard set value.

5.2.2 Influence of Oxygen Pressure During Deposition

When working with metal oxide materials, the partial oxygen pressure p_{O_2} may play a crucial role in affecting film properties. The stoichiometric transfer from target to substrate is dependent on the scattering probabilities of the involved ablation species and desorption rate from the surface. At a less than adequate oxygen pressure, oxygen vacancies can form, which typically results in an increased mosaic spread and increase in the unit cell volume [89, 147-149, 208]. Under certain circumstances, ordered defect superstructures can form, as observed in BTO-BFO multilayers [147]. In the case of BFO, the film stoichiometry is profoundly affected by the oxygen pressure during growth, leading to the formation of iron oxide below 10^{-2} mbar [207]. Oxygen pressure can also determine the morphology of a film. *Jiang et al.* found a narrow temperature and pressure window for the step-flow growth of BFO between ca. 650 to 700 °C and 0.10 to 0.15 mbar p_{O_2} [89]. Outside of this range they observed an increasingly three dimensional growth mode. In the case of BTO, *Chen et al.* report high roughness nanocolumnar growth at ~0.27 mbar (200 mtorr) [208]. At a reduced p_{O_2} of 0.007 mbar (5 mtorr), the BTO roughness is greatly decreased, but TEM images reveal strong bombardment damage, due to the increased mean free path of high energetic particles at lower pressure [208].

The oxygen pressure dependence of BTO-BFO multilayers was previously investigated by *Lorenz et al.* in Refs. 11, 148 and 149. They compared multilayers of 15× BTO-BFO deposited at 0.01 to 0.25 mbar with an identical number of pulses for all layers. A strong correlation between α_{ME} and p_{O_2} was found, which will be discussed in depth in Sec. 5.5. At a structural level, lower oxygen pressure introduced increased micro-strain, visible in TEM cross-sections as strain contrast [149] and an increase of mosaicity [148]. More pronounced half-order peaks indicative of increased OOT in low-p_{O_2} films were connected with increased oxygen vacancies [148]. Surprisingly, when comparing two films grown at 0.01 mbar and 0.25 mbar, a larger OOP lattice parameter was found for the high-p_{O_2} sample [149], contrary to generally reported trends [89, 208]. In terms of morphology, two observations were made: the surface roughness of 0.01 mbar samples was lower than that of 0.25 mbar samples [11,148], but displayed an amorphous interface layer of 2 nm thickness [149].

As will be discussed later in this thesis, the double-layer thickness d_{dl} of a BTO-BFO multilayer plays an intricate role in determining the film properties. As a result of the unchanging number of pulses used to generate the samples discussed in Refs. 148 and 149, the thicknesses of the films examined were of strongly varying nature. It is therefore important to re-evaluate the above-mentioned findings under a more strict adherence to a steady film thickness. For this purpose, p_{O_2}-dependent single-layer thicknesses determined by XRR (not shown here) were cross-referenced against the film thicknesses from Ref. 148. The resulting growth rates were used to determine the appropriate number of pulses per layer to create a series of $16 \times [(\mathrm{BaTiO_3})_{10\ \mathrm{nm}}\text{-}(\mathrm{BiFeO_3})_{10\ \mathrm{nm}}]$ multilayers for p_{O_2} ranging from 0.01 to 0.25 mbar. The films were deposited in chamber *F* at 700 °C. The lens position was set to $L = 0\,\mathrm{mm}$, leading to an energy density of $\rho_{\mathrm{L}} = 3.8\,\mathrm{J\,cm^{-2}}$. The results obtained for this series have been partially published in Ref. H4 .

Growth Rate, Structure and Morphology

Table 5.4 lists the growth conditions and main structural parameters of the static thickness p_{O_2} series. With the minor exception of the 0.05 mbar sample F030, all samples possess a d_{dl} of 20 nm within the margin of error. The average combined growth rate of BTO and BFO decreases roughly with the logarithm of the process pressure in the range of 0.01 to 0.25 mbar, as indicated by the straight lines in the logarithmic plot in Fig. 5.21 a). This confirms the trend observed in Ref. 148, albeit as Fig. 5.21 a) further shows, at approximately half the previous growth rate. A change

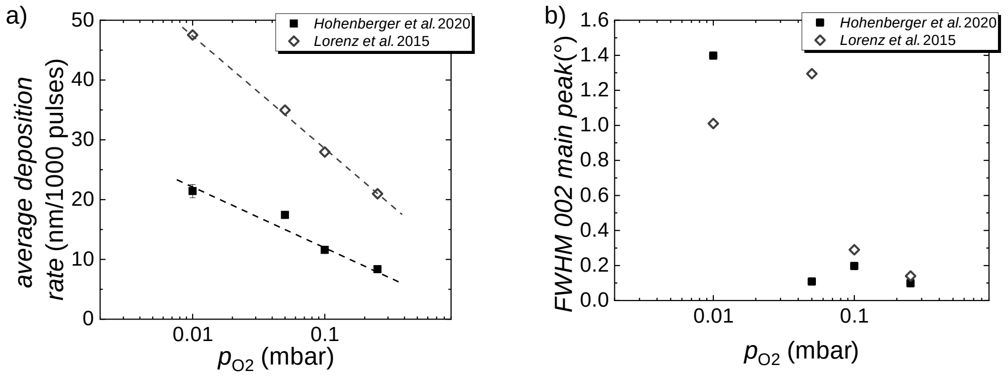

Figure 5.21: **(a)** Average combined growth rate of BTO and BFO and **(b)** FWHM of the main (002) superstructure peak for multilayers of 16 × [$BaTiO_3$-$BiFeO_3$] with d_{dl} of 20.0 ± 0.2 nm deposited at pressures of 0.01 to 0.25 mbar compared to the values published in Ref. 148.

in the deposition rate between the two series is hardly surprising, as they were grown in two nominally similar, but slightly different deposition chambers, years apart, with different targets. As discussed in Sec. 5.2.3 however, non-ideal reproduction of the laser fluence ρ_{L} used to ablate the target material for these films may be the cause. Due to a conversion error, the early films grown in chamber *F*, up to sample no. F113, were grown using $\rho_{\mathrm{L}} = 3.8\,\mathrm{J\,cm^{-2}}$, instead of the $2.0\,\mathrm{J\,cm^{-2}}$ used in chamber *G*. The change resulted in a reduction of the ablation spot area from 15.3 to $8.5\,\mathrm{mm}^2$, reducing the total ablation rate.

Table 5.4: Deposition parameters and structural characteristics of the samples of the p_{O_2} -variation series. Double-layer thicknesses are calculated from superstructure fringe peaks in XRD 2θ-ω scans. In-plane ($a_{\|}$) and out-of-plane ($a_{\perp}$) lattice parameters are extracted from asymmetric (103) XRD RSMs using the STO (103) peak as internal standard. The error margin for lattice parameters due to goniometer error and peak position accuracy is estimated to be 0.015 Å and 0.005 Å for $a_{\|}$- and $a_{\perp}$, respectively. FWHM_{002} is the full width at half maximum of the main superstructure peak near the STO (002) peak in ω-direction.

sample	p_{O_2}	pulses per layer		d_{dl}	$a_{\|\mathrm{ave}}$	$a_{\perp\mathrm{BTO}}$	$a_{\perp\mathrm{BFO}}$	FWHM_{002}
ID	(mbar)	BTO	BFO	(nm)		(Å)		(°)
F029	0.01	400	515	19.6 ± 0.3	3.970	–	3.938	1.398
F030	0.05	565	725	22.5 ± 1.0	3.998	4.180	3.936	0.109
F036	0.10	755	970	20.0 ± 0.7	4.008	4.101	–	0.197
F026	0.25	1066	1337	20.1 ± 0.2	3.978	4.065	3.958	0.098

In order to explore the crystalline properties, reciprocal space maps around the (001), (002) and (103) STO peak were recorded. The (001) and (103) RSM measurements are presented in Fig. 5.22. In Fig. 5.21 b), the FWHM in ω-direction of the main (002) superstructure peak is plotted, which acts as an indicator for the sample mosaicity. The FWHM values are listed along with the lattice parameters extracted from (103) RSM measurements in Table 5.4. Superstructure fringe peaks are visible in all symmetric (001) RSM measurements, see Fig. 5.22 a)-d), although very faint and smeared out for the 0.01 mbar sample, indicating a high degree of disorder within the film. The asymmetric (103) RSM measurements generally display a bimodal film peak structure, indicative of the constituent phase components of BTO and BFO, with underlying superstructure peaks. The only exception is again the sample grown at 0.01 mbar, for which only a faint BFO peak, but no BTO or superstructure peak is visible. The same is true for the high and low pressure samples examined in Ref. 149. The FWHM of the (002) peak is drastically increased for the lowest pressure sample relative to the highest pressure sample by more than one order of magnitude. This largely conforms with the findings in Ref. 148, as a comparison of the obtained values in Fig. 5.21 b) shows. The astonishing exception is made by the 0.05 mbar sample, which has a similarly low tilt mosaicity as the 0.25 mbar sample. In contrast, this deposition pressure produced the sample with the largest tilt mosaicity in Ref. 148.

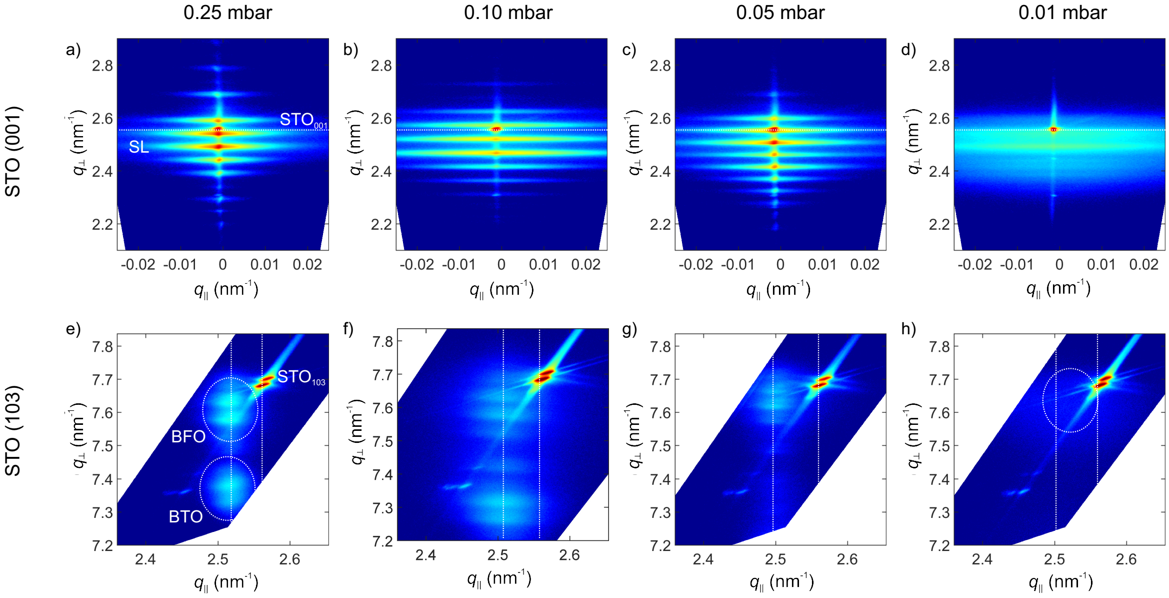

Figure 5.22: RSMs around the STO (001) ((**a**)-(**d**)) and (103) ((**e**)-(**h**)) peaks for multilayers of 16 × [BaTiO$_3$-BiFeO$_3$] with d_{dl} of 20.0 ± 0.2 nm deposited at pressures of 0.01 to 0.25 mbar, as indicated. The vertical lines in (**e**)-(**h**) mark the in-plane position of the superstructure and STO (103) peaks, respectively, as labeled in (**e**). The heat map colors represent measured intensities on a logarithmic scale, blue representing small values and red large values. Graph adapted from Ref. H5 (supplementary).

TEM cross-sections were prepared for the samples deposited at 0.25 mbar, 0.10 mbar and 0.01 mbar. A selection of HAADF TEM images of these cross-sections is presented in Fig. 5.23. As shown in Fig. 5.23 a) and d), the film deposited at 0.25 mbar has a very low interface roughness in the order of a few unit cells, indicating a coherent, fully relaxed growth in line with the low tilt mosaicity indicated by the low FWHM of 0.098°. The growth of the 0.10 mbar film is disturbed by a number of outgrowths, depicted in detail in Fig. 5.23 b). Fig. 5.23 e) shows a larger section of the same sample, highlighting the large number of said outgrowths. In between and on top of the outgrowths however, multilayer growth is still fairly smooth. This changes considerably for the 0.01 mbar sample. As Fig. 5.23 c) shows, the dark BTO layers have a consistent thickness, but are disturbed by highly irregular light BFO layers. Overall, the low-p_{O_2} sample TEM images were thoroughly obstructed by strain contrast and lattice parameter and layer thickness determination was solely possible for the 0.25 mbar sample. XRR measurements confirmed the same ratio for the 0.05 mbar sample, the model function converging at $d_{\text{BTO}} = 11.4 \pm 0.4$ nm and $d_{\text{BFO}} = 11.3 \pm 0.6$ nm. The poor layer homogeneity observed for the low-p_{O_2} samples was not previously observed in Ref. 149 and is most likely linked to bombardment damage caused by the aforementioned high laser fluence used during deposition.

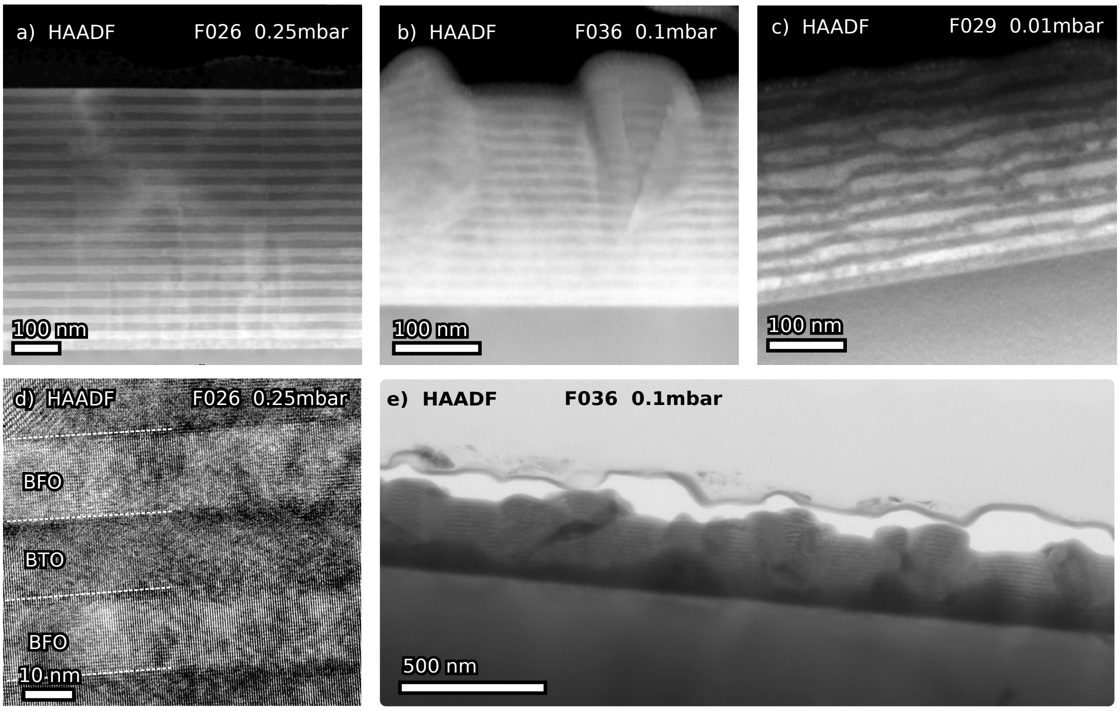

Figure 5.23: HAADF TEM cross-section images of multilayers of 16 × [$BaTiO_3$-$BiFeO_3$] with d_{dl} of 20.0 ± 0.2 nm deposited at pressures of 0.01 to 0.25 mbar. **(a)** overview 0.25 mbar sample, **(b)** overview 0.10 mbar sample, **(c)** overview 0.01 mbar sample, **(d)** detail 0.25 mbar sample, **(e)** larger overview 0.10 mbar sample.

The double-layer thickness of the 0.25 mbar sample as measured by TEM is 19.6 nm ±0.2 nm, a precise match with the value obtained from superstructure fringe peaks. The BTO and BFO thicknesses were measured to be 9.5 ± 0.5 nm and 10.3 ± 0.5 nm, respectively, close to the expected 1:1 ratio. The lattice parameters determined for the 0.25 mbar sample are as follows: IP $a_{\|\mathrm{ave}} = 3.98 \pm 0.02$ Å for both materials, OOP $a_{\perp\mathrm{BTO}} = 4.11 \pm 0.04$ Å and $a_{\perp\mathrm{BFO}} = 3.94 \pm 0.03$ Å for BTO and BFO, respectively. No change in the lattice parameters with distance from the substrate was found except for the thin relaxation layer discussed in Sec. 5.1.1. These values are, within the margin of error, in agreement with the values obtained from RSM measurements, as tabulated in Table 5.4. Over the range of deposition pressures, the IP lattice parameter $a_{\|\mathrm{ave}}$ decreases slightly for intermediate pressures, but changes very little overall, considering the measurement uncertainty. The BFO OOP lattice parameter $a_{\perp\mathrm{BFO}}$ is consistent with a cubic unit cell for all samples. In contrast, the BTO OOP lattice parameter $a_{\perp\mathrm{BTO}}$ increases with decreasing deposition pressure, though for the 0.01 mbar sample, no BTO peak was observed, leading to a gap in the data. In Ref. 149 an opposite trend was found via TEM measurements comparing a 0.01 mbar and 0.25 mbar sample. However, the increase in $a_{\perp\mathrm{BTO}}$ with decreasing pressure is in line with both the findings of *Lorenz et al.* on BTO-BFO solid solutions [147] and general expectations [89, 208].

Magnetic Properties

Magnetic hysteresis measurements on the films of the p_{O_2}-series were carried out at 300 K. The resulting $\boldsymbol{M}(\mu_0\boldsymbol{H})$-curves and key measurement parameters are presented in Fig. 5.24 a) and b), respectively. All sample show well defined magnetic hysteresis curves with small coercive fields $\mu_0\boldsymbol{H}_{\mathrm{coer}}$ of only 7 to 15 mT. The saturation magnetization $\boldsymbol{M}_{\mathbf{sat}}$ ranges from 0.9 to 5.8 emu cm^{-3}, equal to 0.006 to 0.04 μ_{B}/f.u., with remanent magnetization $\boldsymbol{M}_{\mathbf{rem}}$-values of on average 12 % of $\boldsymbol{M}_{\mathbf{sat}}$. Overall, the $\boldsymbol{M}_{\mathbf{sat}}$ -values are lower for intermediate growth pressures, while the $\mu_0\boldsymbol{H}_{\mathrm{coer}}$-values exhibit the opposite trend. The sharp rise of $\boldsymbol{M}_{\mathbf{sat}}$ displayed in Fig. 5.24 b) for the 0.01 mbar sample may be a sign of initial formation of a small amount of iron oxide due to oxygen deficient growth conditions, or a sign of defect magnetization.

Ferroelectric Properties

Observing ferroelectricity in samples with high leakage current or breakdown fields lower than the coercive fields poses one of the profound challenges in working with materials such as BFO [98]. The destructive breakdown of NSTO-multilayer-Pt capacitor structures occurred at 1.0 MV cm^{-1}, 0.6 MV cm^{-1}, 0.8 MV cm^{-1} and 0.9 MV cm^{-1} for the 0.01 mbar, 0.05 mbar, 0.10 mbar and 0.25 mbar samples, respectively. Fig. 5.25 shows the unsaturated $\boldsymbol{P}(\boldsymbol{E})$- and $I(\boldsymbol{E})$-loops measured on the samples deposited at the highest and lowest p_{O_2}-values.

Both $I(\boldsymbol{E})$-loops exhibit small negative switching peaks at positive fields, indicating an imprint field larger than the coercive field, leading to self-polarization. A similarly

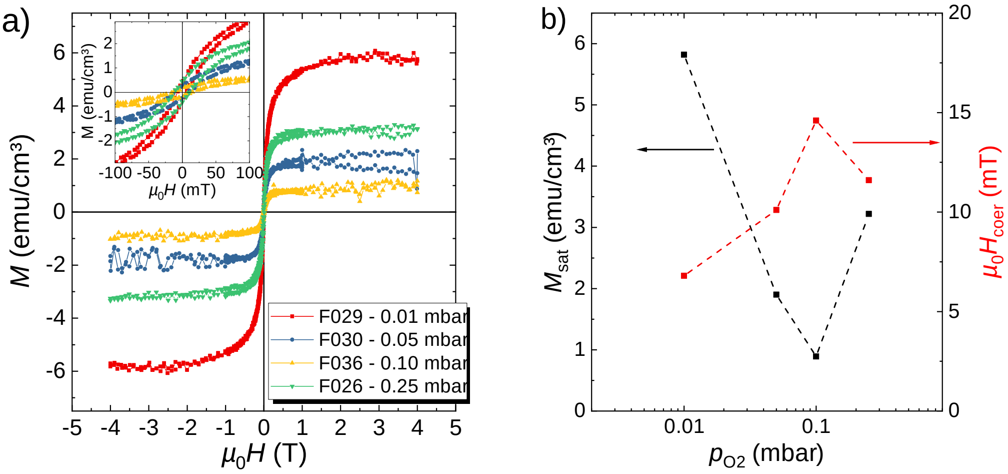

Figure 5.24: **(a)** $\boldsymbol{M}(\mu_0\boldsymbol{H})$-curves measured at 300 K and **(b)** values of saturation magnetization $\boldsymbol{M}_{\mathbf{sat}}$ and coercive field $\mu_0\boldsymbol{H}_{\mathrm{coer}}$ for multilayers of 16 × [BaTiO$_3$-BiFeO$_3$] with d_{dl} of 20.0 ± 0.2 nm deposited at pressures of 0.01 to 0.25 mbar.

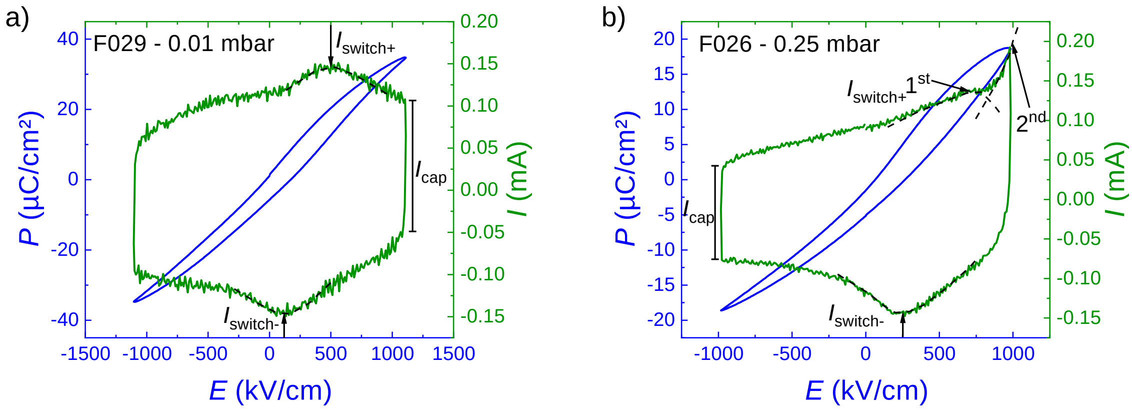

Figure 5.25: $\boldsymbol{P}(\boldsymbol{E})$- (blue) and $I(\boldsymbol{E})$- (green) loops measured at 1 kHz on NSTO-multilayer-Pt capacitors of a BTO-BFO multilayer deposited at **(a)** 0.01 mbar and **(b)** 0.25 mbar. The contributions of capacitive charging current and polarization switching induced screening current peaks are indicated.

small and spread out positive switching peak at around 0.5 MV cm^{-1} can also be seen in both curves. In Fig. 5.25 b), the initial rise of a second, larger positive switching peak is discernible. As discussed in Sec. 5.1.5 and shown in Fig. 5.12 a), the two small, spread out switching peaks observed in Fig. 5.25 are likely signs of only partially switched polarization due to insufficient applied electric field. Generally speaking, the ratio $I_{\mathrm{switch}}/I_{\mathrm{cap}}$ of switching peak current to capacitive charging current is larger than 1 for all saturated hysteresis loops recorded for similar multilayer samples in this work. Values of $I_{\mathrm{switch}}/I_{\mathrm{cap}} \approx 3$ are not uncommon. Both the 0.01 mbar and 0.25 mbar sample show similar capacitive charging and switching currents of ca. 0.15 mA and 0.05 mA, with an $I_{\mathrm{switch}}/I_{\mathrm{cap}}$-ratio of only ~0.3, underlining the assessment as unsaturated hysteresis loops. Hence the majority of measured polarization is due to the leakage current component, which is visible as the ~0.05 mA cm MV^{-1} slant in the $I(\boldsymbol{E})$-curves.

In summary, most film properties do not change significantly and in any clear relationship with the deposition pressure. The exceptions are the film morphology and mosaicity, which are negatively affected by the oxygen deficiency during growth, as well as the drastically increased growth rate. In contrast, the films compared in Refs. 148 and 149 did not show a similar increase of interface roughness with decreasing p_{O_2}. In Sec. 5.5, we will return to the topic of the influence of p_{O_2} on BTO-BFO multilayers when discussing magnetoelectric properties.

5.2.3 Variation of Lens Position and Lateral Offset

Both the energy density ρ_L of the incident laser beam at the target surface and geometric constraints, such as target-substrate distance and lateral offset o_{lat} between the two, can profoundly alter the properties of PLD derived thin films. For example, deviations from ideal stoichiometric transfer between target and film depend both on incongruous ablation and varying scattering rates of ablated species in the background gas. *Wicklein et al.* found that the ideal fluence ρ_L for stoichiometric growth of STO shifts from 1 to 2 J cm^{-2} as the target-to-substrate distance was increased from 40 to 48 mm [158]. The increased distance results in a larger amount of scattering events, enhancing the inhomogeneous angular distribution of ablated species, as lighter particles have a larger scattering probability. Likewise, a change in lateral offset o_{lat} will likely affect both growth rate and stoichiometry of a film, which will result in changes to the surface morphology. *Kan et al.* reported that BTO grows Ti-deficient at fluences smaller than 1.3 J cm^{-2}, which leads to the loss of ferroelectricity for ρ_L smaller than 0.9 J cm^{-2} [209]. *Jaber et al.* investigated the growth of BFO from a 10 % Bi over-stoichiometric target at 700 °C and 0.2 mbar - close to the standard values used in the framework of this thesis - in a ρ_L range of 1 to 1.72 J cm^{-2} [210]. They found an increase of both the OOP lattice parameter and the growth rate with increased laser fluence. The Bi-Fe ratio was close to unity for films deposited at ρ larger than 1.62 J cm^{-2} [210].

Here, we will primarily focus on the effect that the fluence ρ_L and lateral offset o_{lat} have on the morphology, droplet density and deposition rate of BTO and BFO films. Droplets, large particles ejected from the target surface, are not affected by background gas scattering. The processes leading to droplet generation usually result in preferential trajectory normal to the target surface, or in the direction of the incident laser beam [211]. As *Cultrera et al.* report, one can take advantage of the angular inhomogeneous spread of droplets to reduce the droplet density [211]. Likewise, it has been found that an increased laser fluence resulted in the decrease of the amount of droplets generated during the pulsed laser ablation of $YBa_2Cu_3O_{7-x}$ films [212]. The investigation of the influence of the lens position was carried out in chamber F in part to recreate the conditions used in chamber G more accurately for the sake of comparability.

Laser Fluence Variation via Lens Position

The energy density of laser light at the target surface, called fluence ρ_L, can be altered in the PLD process either by changing the total output energy E_out or the distance $x_\mathrm{t-l}$ between target and lens. By changing E_out, the ablation area is kept constant, whereas changing $x_\mathrm{t-l}$ of the single-lens focusing setup changes the ablation area with the square of the distance. See Sec. 4.1.1 and in particular Fig. 4.4 for details on the spot size and fluence calculation for PLD chamber F. Variation of ρ_L via E_out has the disadvantage that the excimer laser devices have a limited range of energies for stable operation with optimized resource consumption. The variation of $x_\mathrm{t-l}$ is limited by the confines of the chamber setup used, i.e. by the chamber-lens distance L. At $L = 0\,\mathrm{mm}$, the upper limit of ρ_L at $E_\mathrm{out} = 650\,\mathrm{mJ}$ is $3.8\,\mathrm{J\,cm^{-2}}$. Larger energy densities are rarely used in PLD of oxide materials [154, 157, 213].

A number of single-layer films of BTO, as well as BFO was deposited on STO in the range of $\rho_\mathrm{L} = 3.8\,\mathrm{J\,cm^{-2}}$ to $1.5\,\mathrm{J\,cm^{-2}}$, using standard conditions otherwise. A list of these samples along with the pulse numbers, process temperatures and measured thicknesses is presented in Table 5.5. The individual and averaged deposition rates of BTO and BFO are depicted in Fig. 5.26 a). The rate of BTO deposition changes roughly with the area of the laser spot on the target surface, which is plotted as the dotted line associated with the right ordinate in Fig. 5.26 a). The deposition rate of BFO does not follow this trend, but has the lowest deposition rate at $1.5\,\mathrm{J\,cm^{-2}}$ with $4.4\,\mathrm{nm}$ per 1000 pulses and the maximal deposition rate of $9.8\,\mathrm{nm}$ per 1000 pulses at $2.0\,\mathrm{J\,cm^{-2}}$. If the deposition rates are normalized to the ablation area, the BTO rate exhibits a maximum at $2.0\,\mathrm{J\,cm^{-2}}$ and the BFO rate is stable from 2.0 to $3.8\,\mathrm{J\,cm^{-2}}$, with a sharp reduction of the BFO rate at $1.5\,\mathrm{J\,cm^{-2}}$. In chamber G, the ratio of the BTO rate to the BFO rate was ~ 2.4. This is most accurately reproduced at $2.0\,\mathrm{J\,cm^{-2}}$ with a value of 2.5.

Fig. 5.26 b) additionally shows the dependence of the droplet density on the fluence ρ_L, as determined by optical microscopy (see Sec. 4.3.2). The droplet densities are normalized to a layer thickness of $100\,\mathrm{nm}$ for comparability. For all BTO films, negligible amounts of particles were detected on the sample surface. All BFO films showed significant amounts of surface particles, the density of which clearly correlates strongly

Table 5.5: List of samples used for the study of the effect of laser fluence ρ_L variation through change of the lens position L. All samples were grown in 0.25 mbar O_2 with a lateral offset o_{lat} of 10 mm ($QM = 3$). The layer thicknesses were measured by X-ray reflectometry (XRR). †: thickness measured with a profilometer.

sample	material	n_{pulses}	T (°C)	L (mm)	ρ_L ($J\,cm^{-2}$)	d^{XRR} (nm)
F110	BTO	10000	661	0	3.8	67
F109	BFO	10000	676	0	3.8	77
F111	BFO	10000	664	0	3.8	80
F116	BTO	1000	674	10	2.9	12.5
F118	BFO	10000	668	10	2.9	65
F117	BTO	1000	664	20	2	24
F122	BFO	10000	664	20	2	97
F126	BFO	10000	697	20	2	92
F130	BTO	10000	701	30	1.5	$315^{\dagger}$
F128	BFO	10000	698	30	1.5	44
F129	BFO	22700	691	30	1.5	90

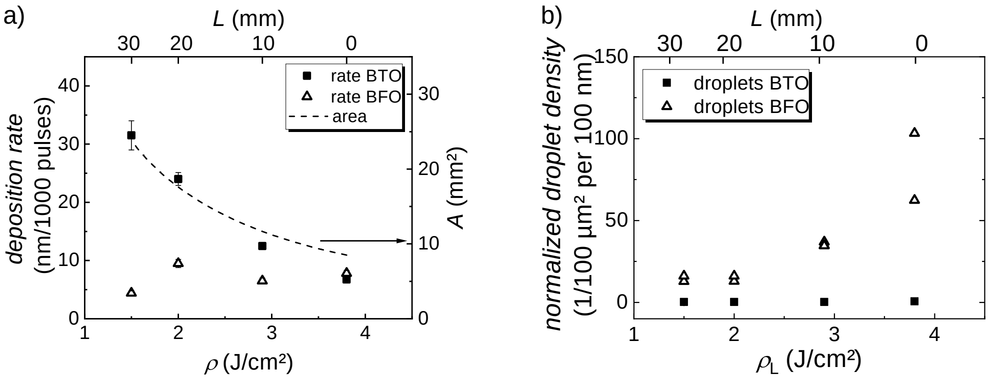

Figure 5.26: **(a)** Deposition rates and **(b)** normalized droplet densities of BTO (blue) and BFO (red) single-layer films deposited at laser fluences ρ_L of 1.5 to 3.8 $J\,cm^{-2}$.

with ρ_L. The smallest droplet densities are measured for the smallest ρ_L-values. Subsurface heating of the target material is generally assumed to be one of the leading causes of droplet generation [159]. With increasing ρ_L, this phenomenon is enhanced, additionally so if inhomogeneities in the beam profile exist.

Combining the requirements of minimal droplet density and maximized deposition rate for both BTO and BFO, the optimal laser fluence in chamber F was determined to be 2.0 J cm^{-2}. The same value was nominally used in chamber G. The comparability is backed by the analogous ratio of the respective deposition rates of BTO and BFO.

Lateral Offset of the Substrate Relative to the Ablation Target

As mentioned above, the lateral offset o_{lat} between target and substrate holder, or more accurately between their respective rotation axes, is likely to have a substantial influence over the particle density and morphology of a PLD film. Four 5× BTO-BFO multilayers were deposited on STO using standard conditions and lateral offsets in the range from 0 to 23.3 mm. The sample details and key measurement results are summarized in Table 5.6.

The deposition rate drops as expected with increasing o_{lat}, as shown in Fig. 5.28 a) (see also values in Table 5.6). As a first measure of the multilayer quality, XRD 2θ-ω scans (depicted in Fig. 5.27) were recorded for all four samples. The sharpest peak structures are observed for $o_{\mathrm{lat}} = 0$ mm. With increasing o_{lat}, the XRD peaks become gradually smudged out until, at $o_{\mathrm{lat}} = 23.3$ mm, no superstructure peaks beyond the first order are visible. This trend is mirrored by the surface-roughness parameter R_{rms}, depicted in Fig. 5.28 b) and tabulated in Table 5.6. The corresponding topographical AFM images are presented in Fig. 5.29. With increasing o_{lat}, the surface BFO layer transitions from an irregularly stepped appearance to a 3D insular appearance. It is reasonable to assume that, as the influx of ablated particles is reduced, the growth rate drops below

Table 5.6: List of samples used for the study of the effect of lateral offset o_{lat} variation through change of the offset setting QM. All samples were grown in 0.25 mbar O_2 with a laser fluence ρ_L of 2 J cm^{-2} ($L = 20$ mm) and at 700 °C process temperature. For each film, 5 double-layers were deposited with 320 pulses BTO and 1200 pulses BFO. The layer thicknesses were estimated from superstructure fringe peaks observed in 2θ-ω scans.

sample	QM	o_{lat} (mm)	d_{dl} (nm)	R_{rms} (nm)	droplet density per 100 nm (1/100 μm^2)	deposition rate (nm/1000 pulses)
F165	0	0.0	25.0	0.26	12.4	16.4
F164	3	10.0	18.6	0.35	10.7	12.2
F166	5	16.7	19.2	0.47	3.2	12.6
F174	7	23.3	10.6	1.13	1.6	7.0

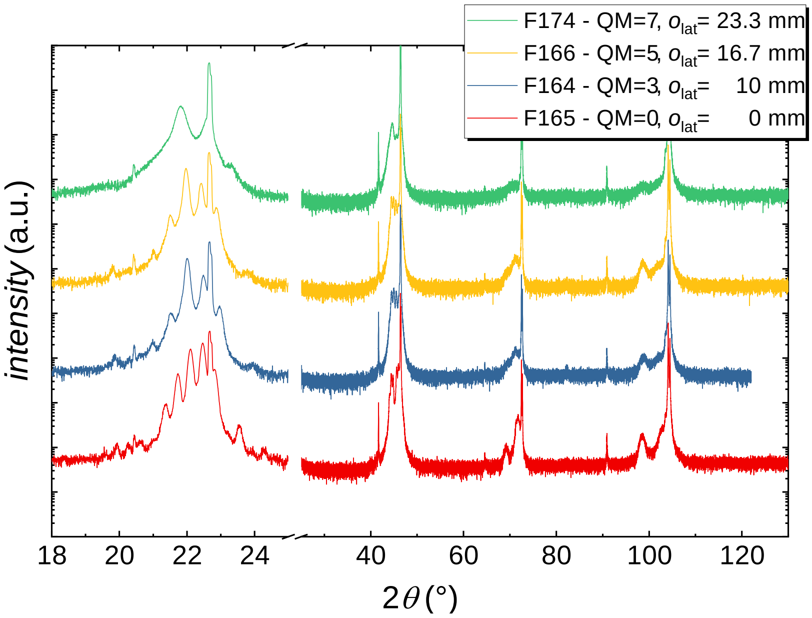

Figure 5.27: XRD 2θ-ω scans of 5× BTO-BFO multilayers deposited with varying lateral offset o_{lat}.

the deposition rate needed for step-flow growth [160]. The normalized droplet density is depicted in Fig. 5.28 c). As o_{lat} is increased beyond the radius of the substrate holder (12.5 mm) the droplet density drastically decreases. As discussed earlier, this is likely due to a preferential directionality of the droplets owing to the droplet generation process. In summary, adjusting the lateral offset o_{lat} between target and substrate can

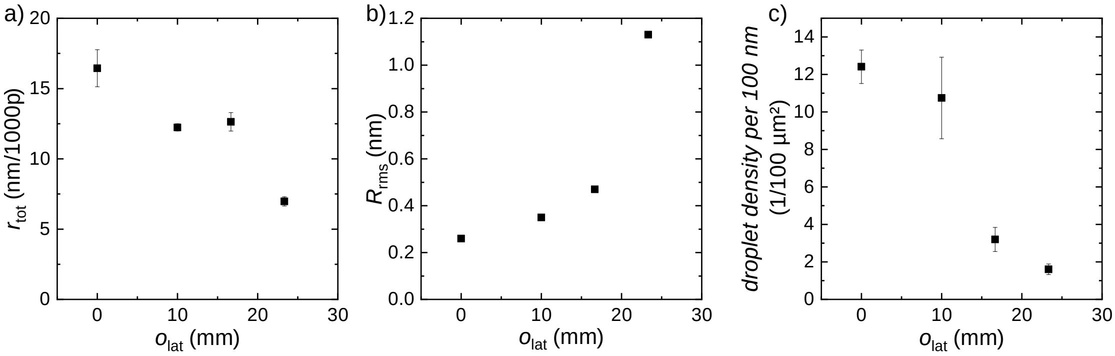

Figure 5.28: **(a)** Average deposition rate, **(b)** surface-roughness parameter R_{rms} and **(c)** normalized droplet density of 5× BTO-BFO multilayers deposited with varying lateral offset o_{lat}.

in principle be used to reduce the droplet rate on the surface of BTO-BFO multilayers. However, this comes at the cost of drastically increased surface-roughness and is hence ill-advised. Likewise, a reduction of ρ_{L} led to a reduction in droplet density, but the deposition rate of BFO dropped below practical values for $\rho_{\mathrm{L}} \leq 2\,\mathrm{J\,cm^{-2}}$.

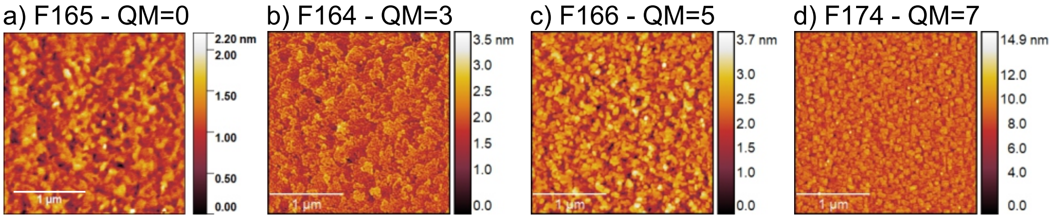

Figure 5.29: Topographical AFM images of 5×BTO-BFO multilayers deposited with lateral offset o_{lat} of **(a)** 0 mm ($QM = 0$), **(b)** 10 mm ($QM = 3$), **(c)** 16.7 mm ($QM = 5$), and **(d)** 23.3 mm ($QM = 7$).

5.2.4 Summary

The overall most beneficial growth conditions for high-quality BTO-BFO multilayers were found to be 670 to 700 °C in 0.25 mbar p_{O_2} using a laser fluence of 2.0 J cm^{-2} at a lateral offset of 10 mm between substrate and target. The resulting film samples are phase-pure, with minimized roughness and mosaicity. Temperatures below 600 °C lead to the formation of parasitic phases and above 700 K, pitting occurs. In the range of 0.01 to 0.25 mbar, the deposition rate changes approximately inverse to p_{O_2}. At low oxygen pressures, rough interfaces and increased micro-strain are formed in the multilayers. At elevated laser fluences, the droplet rate increases. Increased lateral offset reduces the droplet rate, but at the cost of increased surface roughness. Despite the demonstrated control that can be exerted over the sample properties by means of parametric optimization, not all desired improvements of the sample quality could be attained. For example, continuing presence of droplet particles and related electric breakdown still impedes quantitative FE measurements. Consequently, we adapted our strategy by modifying the deposition setup with the introduction of a shadow mask, as detailed in Sec. 5.4.

5.3 Manipulation of Multilayer Properties through Design

Having contemplated the generalized properties of BTO-BFO multilayers, explored the influence of various growth parameters and the implementation of eclipse-PLD, we will now turn to the topic of multilayer design choices. Using standard conditions in chambers *G* and *F*, three multilayer layout changes were implemented. The first alteration retained a constant BTO-thickness, while varying the nominal BFO-thickness from 5 to 50 nm. The resulting shift in BTO-BFO ratio was replicated in a second series under the constraint of retaining a constant double-layer thickness. The third and final series was constructed with a constant 1 : 1 BTO-BFO ratio with varying double-layer thicknesses from 4.6 to 20 nm.In the following section, we will explore the influence of these design choices on the structural and ferroic properties of BTO-BFO multilayers. The subsequent section will ultimately treat the magnetoelectric properties of BTO-BFO multilayers with respect to variations of oxygen pressure during growth and the aforementioned design choices.

5.3.1 Samples

In case of the d_{BFO}-variation, two 15×BTO-BFO multilayer series were deposited using a 5 at% Gd-doped BGFO target and another using a regular 10 % Bi-over-stoichiometric BFO target. The results of the d_{BGFO} sample series were previously published in Ref. H3 . Table 5.7 lists samples of both series, along with the key structural values. The data on the samples of the ratio-series and the d_{dl}-series were published in Ref. H4. The sample names and key structural data can be found in Tables 5.8 and 5.9 for the ratio- and d_{dl}-series, respectively.

Table 5.7: Structural characteristics of the BTO-BGFO d_{BGFO}-variation and BTO-BFO d_{BFO}-variation series. Double-layer thicknesses are calculated from superstructure fringe peaks in XRD 2θ-ω scans. In-plane ($a_{\|}$) and out-of-plane ($a_{\perp}$) lattice parameters are extracted from asymmetric ($\bar{1}03$) XRD RSMs using the STO peak as internal standard. Similarly, the STO lattice parameters were also used as internal standard for TEM lattice parameter measurements. The error for of all layer thicknesses is estimated around ~5 %, to 0.015 Å and 0.005 Å for $a_{\|}$- and $a_{\perp}$-parameters derived by XRD, and to 0.015 Å and 0.05 Å for $a_{\|}$- and $a_{\perp}$-parameters derived by TEM.
†: single-layer thickness estimated from XRR measurements of thinner single-layer films; ‡: measured by TEM; *: estimated by interpolation; *: estimated by XRR fit;

					RSM			TEM	
sample	$d_{\mathrm{dl}}^{2\theta-\omega}$	d_{BTO} (nm)	d_{BFO}	$a_{\|\mathrm{ave}}$	$a_{\perp\mathrm{BTO}}$ (Å)	$a_{\perp\mathrm{BFO}}$	$a_{\|\mathrm{ave}}$	$a_{\perp\mathrm{BTO}}$ (Å)	$a_{\perp\mathrm{BFO}}$
G5989	63.0	$19^{\ddagger}$	$44^{\ddagger}$	3.958	4.059	3.928	3.94	4.03	3.91
G5990	35	17^{*}	19^{*}	3.974	4.046	3.915	–	–	–
G5991	26	17^{*}	9^{*}	3.987	4.037	3.913	–	–	–
G5992	23	$16.5^{\ddagger}$	$6.3^{\ddagger}$	3.989	4.029	–	3.98	4.07	3.98
G5993	–	$240^{\dagger}$		4.021	3.997	–	–	–	–
G6051	–	–	$363^{\dagger}$	3.943	–	4.012	–	–	–
G6041	69	$25.6^{\ddagger}$	$43.6^{\ddagger}$	3.976	4.046	3.936	3.98	4.05	3.95
G6043	44	$27^{\star}$	$16^{\star}$	3.986	4.033	3.922	–	–	–
G6044	36	$28^{\star}$	$8^{\star}$	3.991	4.019	3.921	–	–	–
G6045	30	$26^{\ddagger}$	$4.4^{\ddagger}$	4.004	4.012	–	3.98	4.00	3.96
G6049	–	$320^{\dagger}$	–	4.013	3.996	–	–	–	–
G6050	–	–	$389^{\dagger}$	3.942	–	4.012	–	–	–

Table 5.8: Structural characteristics of the samples of the BTO-BFO ratio-variation series. The sample nomenclature used in Ref. H4 is also used here to denote the nominal BTO-content: R0X - nominal thickness ratio $0.X = d_{\mathrm{BTO}}/d_{\mathrm{dl}}$. Double-layer thicknesses are calculated from superstructure fringe peaks in XRD 2θ-ω scans. In-plane (a) and out-of-plane (c) lattice parameters are extracted from asymmetric ($\bar{1}03$) XRD RSMs using the STO peak as internal standard. Similarly, the STO lattice parameters were also used as internal standard for TEM lattice parameter measurements. The error for of all layer thicknesses is estimated around ~5 %, to 0.015 Å and 0.005 Å for a- and c-parameters derived by XRD, and to 0.015 Å and 0.05 Å for a- and c-parameters derived by TEM.
‡: measured by TEM; *: estimated by XRR fit.

sample	$d_{\mathrm{dl}}^{2\theta-\omega}$	d_{BTO}	d_{BFO}	$a_{\mathrm{ave}}^{\mathrm{RSM}}$	$c_{\mathrm{BTO}}^{\mathrm{RSM}}$	$c_{\mathrm{BFO}}^{\mathrm{RSM}}$	$a_{\mathrm{ave}}^{\mathrm{TEM}}$	$c_{\mathrm{BTO}}^{\mathrm{TEM}}$	$c_{\mathrm{BFO}}^{\mathrm{TEM}}$
F022 (R09)	19.4	$15.7^{\star}$	$3.8^{\star}$	4.004	4.009	–	4.03	4.00	4.05
F023 (R01)	20.0	$2.1^{\star}$	$17.5^{\star}$	3.962	–	3.962	3.94	4.09	3.94
F024 (R07)	19.6	$13.4^{\star}$	$6.0^{\star}$	3.981	4.051	–	–	–	–
F025 (R03)	19.4	$6.0^{\star}$	$13.3^{\star}$	3.971	4.063	3.967	–	–	–
F026 (R05)	20.1	$8.5^{\dagger}$	$11.0^{\dagger}$	3.978	4.065	3.958	3.98	4.11	3.94

Table 5.9: Structural characteristics of the samples of the d_{dl}-variation series. The sample nomenclature used in Ref. H4 is also used here to denote the nominal double-layer thickness: DZZZ - $d_{\mathrm{dl}}^{\mathrm{nom}} = ZZZ$ Å. Double-layer thicknesses are calculated from superstructure fringe peaks in XRD 2θ-ω scans. In-plane ($a_{\|}$) and out-of-plane ($a_{\perp}$) lattice parameters are extracted from asymmetric ($\bar{1}03$) XRD RSMs using the STO peak as internal standard. Similarly, the STO lattice parameters were also used as internal standard for TEM lattice parameter measurements. The error for of all layer thicknesses is estimated around ~5 %, to 0.015 Å and 0.005 Å for $a_{\|}$- and $a_{\perp}$-parameters derived by XRD, and to 0.015 Å and 0.05 Å for $a_{\|}$- and $a_{\perp}$-parameters derived by TEM.
‡: measured by TEM *: estimated by XRR fit

sample	$d_{\mathrm{dl}}^{2\theta-\omega}$	d_{BTO} (nm)	d_{BFO}	RSM $a_{\|\mathrm{ave}}$	RSM $a_{\perp\mathrm{BTO}}$ (Å)	RSM $a_{\perp\mathrm{BFO}}$	TEM $a_{\|\mathrm{ave}}$	TEM $a_{\perp\mathrm{BTO}}$ (Å)	TEM $a_{\perp\mathrm{BFO}}$
F032 (D48)	4.6	2.5	2.1	3.971	–	–	3.99	4.12	4.03
F033 (D96)	9.6	4.7	4.6	3.979	–	–	–	–	–
F034 (D144)	14.3	7.2	7.1	3.971	–	–	–	–	–
F035 (D192)	17.7	9.2	9.2	3.973	–	–	–	–	–
F026 (D200)	20.1	8.5†	11.0†	3.978	4.065	3.958	3.98	4.11	3.94

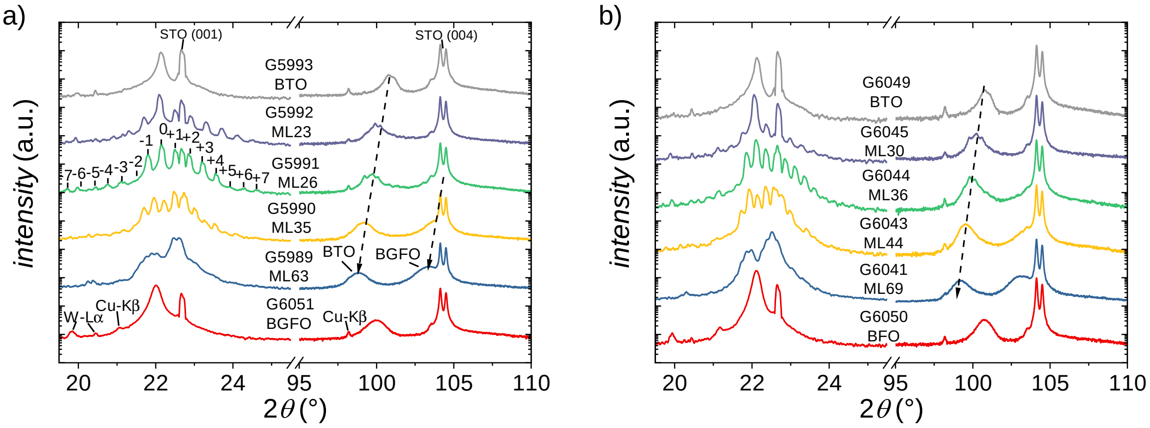

Figure 5.30: XRD 2θ-ω scans for multilayers of $15 \times [BaTiO_3\text{-}BiFeO_3]$ on STO with varying d_{BFO} and constant d_{BTO} denoted by their respective d_{dl} in nm as MLXX and reference BTO and BFOsingle-layer. Samples in **(a)** are grown using a stoichiometric BFO target with nominally 5 at% Bi substituted by Gd, whereas samples in **(b)** were grown from an over-stoichiometric target with 10 at% excess Bi relative to the Fe content. Graph **(a)** adapted from Ref. H3.

5.3.2 Effect of Multilayer Design on Structure and Morphology

The influence of design choices on the structural properties on $15\times$BTO-BGFO and $15\times$BTO-BFO multilayers was probed by performing a combination of XRD 2θ-ω scans, reciprocal space mapping, XRR measurements and TEM imaging. The numerical values obtained from these measurements for the parameters d_{dl}, d_{BTO}, d_{BFO}, and the lattice parameters are listed in Tables 5.7, 5.8 and 5.9. To begin with, let us examine the samples of the two sample series of d_{BGFO}- and d_{BFO}-variation with constant d_{BTO}-thickness. The d_{BGFO}-series has a BTO-thickness of 17.1 ± 1.0 nm and BGFO-thicknesses varying from 6.3 to 44 nm, the d_{BFO}-series has an average BTO-thickness of 26.5 ± 1.1 nm and BFO-thicknesses varying from 3.5 to 44 nm, as estimated from XRR and TEM measurements. Fig. 5.30 shows the 2θ-ω scans of the two sets of four multilayer samples along with two respective single-layer of the constituent materials BGFO, BFO and BTO. clearly visible at low angles are the superstructure fringe peaks due to multilayer stacking. As the BGFO- and BFO-thicknesses progressively increase, these fringe peaks are being masked by the broader constituent material peaks. At high angles, around the (004) STO substrate peaks, the BTO peak and, for the two thickest samples of both series, the BGFO or BFO peak are distinguishable.

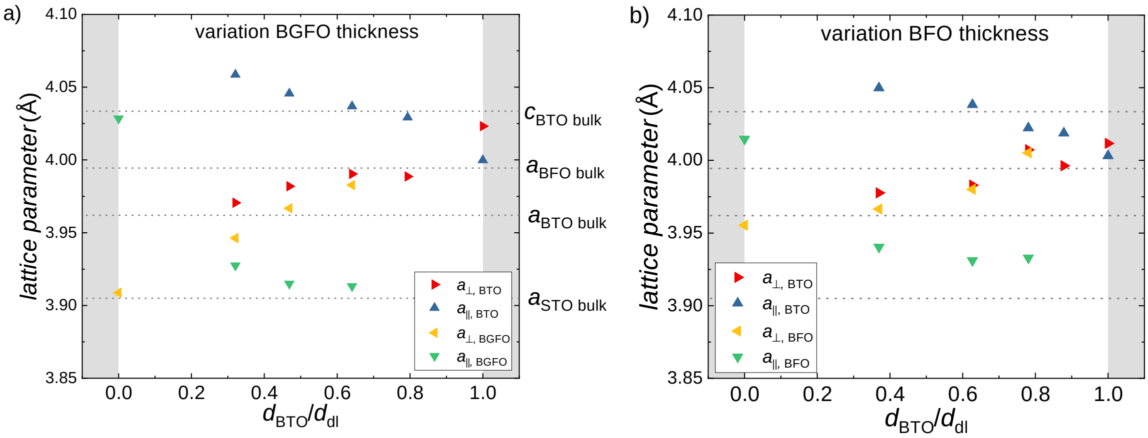

Figure 5.31: Evolution of the lattice parameters of **(a)** BTO-BGFO and **(b)** BTO-BFO multilayers in relation to the relative BTO thickness fraction, as determined from asymmetric (103) RSMs. Graph **(a)** adapted from Ref. H3.

As the BGFO and BFO layer thicknesses, respectively, increase, the BTO peak is shifted from the position of the relaxed BTO single-layer toward lower angles, indicating an elongation of the OOP lattice constant. In RSM measurements (see Ref. H3), this shift is accompanied by a change of the common IP lattice parameter, as the representation of the lattice parameters with respect to the relative BTO-content in Fig. 5.31 shows. Within both thickness series, the OOP and IP lattice parameters a being continuously strain tuned with an approximately linear dependency on the relative BTO-content. The BGFO single-layer grows strained to the substrate, while the BFO single-layer appears to be partially relaxed. In all cases except for the multilayers with the highest BGFO and BFO contents, the unit cell of BGFO and BFO appear tetragonally distorted from their cubic bulk form. A closer look using HR-TEM reveals that this is not necessarily the case, the values noted in Table 5.7, suggest cubic symmetry for both high and low BFO-thicknesses.

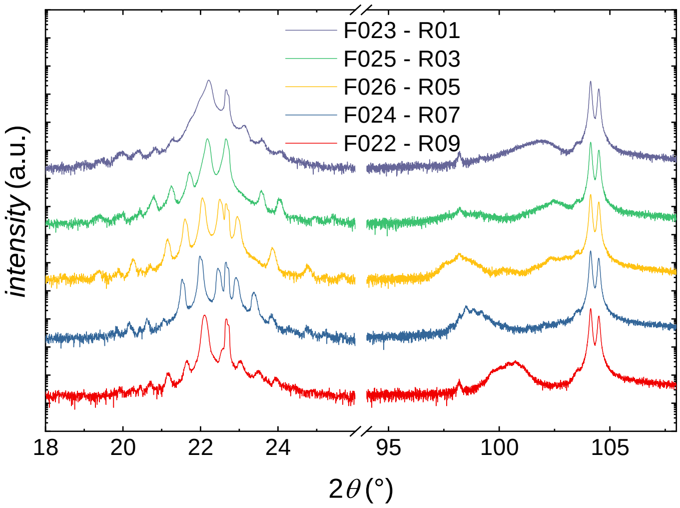

Figure 5.32: XRD 2θ-ω scans for multilayers of $15 \times \left[(\mathrm{BaTiO_3})_x\text{-}(\mathrm{BiFeO_3})_{x-1}\right]$ with varying nominal $d_{\mathrm{BTO}}/d_{\mathrm{dl}}$ ratios of 0.1 to 0.9 and constant d_{dl} of 19.7 ± 0.3 nm. Graph adapted from Ref. H4 (supplementary).

Fig. 5.32 shows the 2θ-ω scans of the samples of the BTO-BFO ratio series grown with nearly constant d_{dl} (19.7 ± 0.3 nm). Unlike the d_{BGFO}- and d_{BFO}-series, all multilayers from this series show a large number of fringe peaks, albeit slightly dampened for the two samples with the highest and lowest $d_{\mathrm{BTO}}/d_{\mathrm{dl}}$-ratio. The same trend of dependency of the common IP lattice-parameter $a_{\|\mathrm{ave}}$ as observed for the d_{BGFO}- and d_{BFO}-series also persists for the constant d_{dl}-ratio series, see Table 5.8. As a matter of fact, said trend can be extended to the entirety of BTO-BFO multilayer samples created at standard conditions throughout the framework of this thesis, as Fig. 5.33 a) shows. This strict adherence to the strain tuning through relative constituent layer thicknesses is made possible by the high temperature epitaxy performed to create the multilayer samples. However, in order to accommodate this wide range of lattice parameter tuning, growth defects such as mosaic tilt and dislocations are induced in the multilayers. Fig. 5.33 b) shows the FWHM in ω-direction of the main (002)-peak of the multilayer samples of the three BTO-BFO ratio series. With a minimum around 0.6 to 0.8 $d_{\mathrm{BTO}}/d_{\mathrm{dl}}$-ratio, the multilayers show an increase of the FWHM value, indicative of larger mosaic tilt, towards higher and lower $d_{\mathrm{BTO}}/d_{\mathrm{dl}}$-ratios.

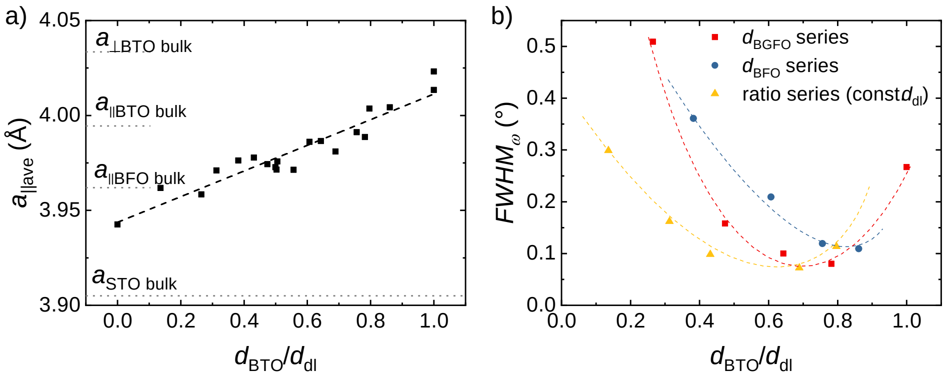

Figure 5.33: **(a)** Average IP lattice parameter of allsingle-layer and multilayers deposited at standard conditions within the framework of this thesis; **(b)** FWHM of the main (002)-peak in ω-direction for BTO-BFO multilayer samples of varying $d_{\mathrm{BTO}}/d_{\mathrm{dl}}$ ratios.

Evidence of the growth defects associated with the increased FWHM were also identified in TEM measurements. Fig. 5.34 shows exemplary TEM cross-sectional images of three samples of the constant d_{dl} ratio series with high, low and intermediate $d_{\mathrm{BTO}}/d_{\mathrm{dl}}$-ratios. In case of the high $d_{\mathrm{BTO}}/d_{\mathrm{dl}}$-ratio sample (Fig. 5.34 a)), intense strain-contrast is present, indicative of a high number of dislocations, as well as a significant interface roughness originating in the BTO layer. A similar trend has been shown in TEM imagery for the d_{BGFO}-series in Ref. H3 and the d_{BFO}-series (not shown here) for low-d_{BFO} samples. It appears that BFO, given a sufficient individual layer thickness, is capable of acting as a buffer to the rough surface structure of the BTO-sublayers, as the medium- and high-$d_{\mathrm{BTO}}/d_{\mathrm{dl}}$-ratio samples do not show a similar interface roughness. However, the low-$d_{\mathrm{BTO}}/d_{\mathrm{dl}}$-ratio sample (Fig. 5.34 b)) also shows intense strain-contrast and several areas with *Moiré* patterns caused by low-angle misaligned grains. The sample with the lowest strain contrast and overall highest degree of order is the medium-$d_{\mathrm{BTO}}/d_{\mathrm{dl}}$-ratio sample (Fig. 5.34 c)). For this reason, the $1:1$ BTO-BFO ratio was subsequently set as the ideal reference design.

Confirmation that the $d_{\mathrm{BTO}}/d_{\mathrm{dl}}$-ratio and not the individual layer thickness is responsible for the structural property changes of BTO-BFO multilayers can be found in the d_{dl}-variation series with constant $d_{\mathrm{BTO}}/d_{\mathrm{dl}}$-ratio. Fig. 5.35 shows the 2θ-ω scans for four BTO-BFO multilayers with $d_{\mathrm{BTO}}/d_{\mathrm{dl}}$ ratio of 0.52 ± 0.03 and varying d_{dl} of 4.6 to 17.7 nm. All samples show superstructure fringe peaks at low angles with a very stable central peak position, which indicates the very stable $d_{\mathrm{BTO}}/d_{\mathrm{dl}}$-ratio. For the thinnest sample F032, only the superstructure film peak can be observed at high angles. All other samples show the BTO (004) peak at an unchanging position.

Furthermore, the excellent multilayer quality is evidenced by the high number of fringe peaks visible in RSM scans in Fig. 5.36. The asymmetric RSM measurements in

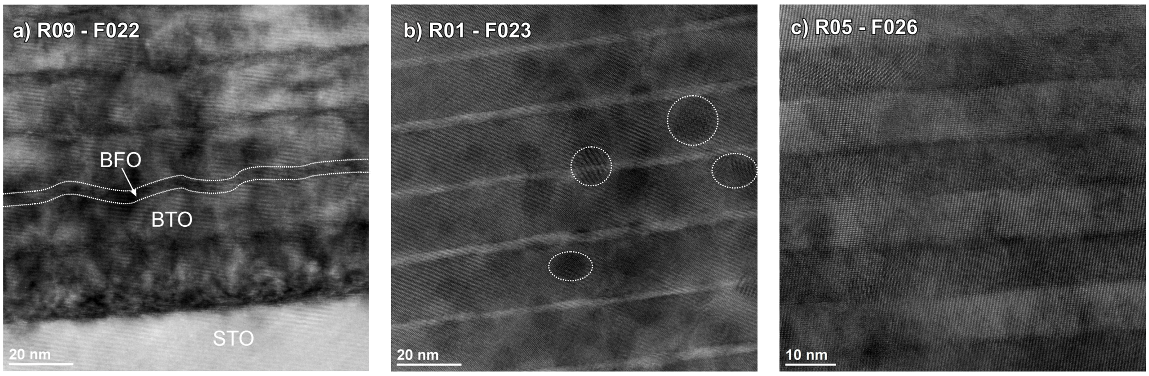

Figure 5.34: TEM cross-sectional images of **(a)** sample F022 with a nominal $d_{\mathrm{BTO}}/d_{\mathrm{dl}}$ ratio of 0.9, **(b)** sample F023 with a nominal $d_{\mathrm{BTO}}/d_{\mathrm{dl}}$ ratio of 0.1, and **(c)** sample F026 with a nominal $d_{\mathrm{BTO}}/d_{\mathrm{dl}}$ ratio of 0.5. Note the high strain contrast and interface roughness in a), as well as the *Moiré* patterns in b), some of which are marked by dashed circles. Graph a) adapted from Ref. H4.

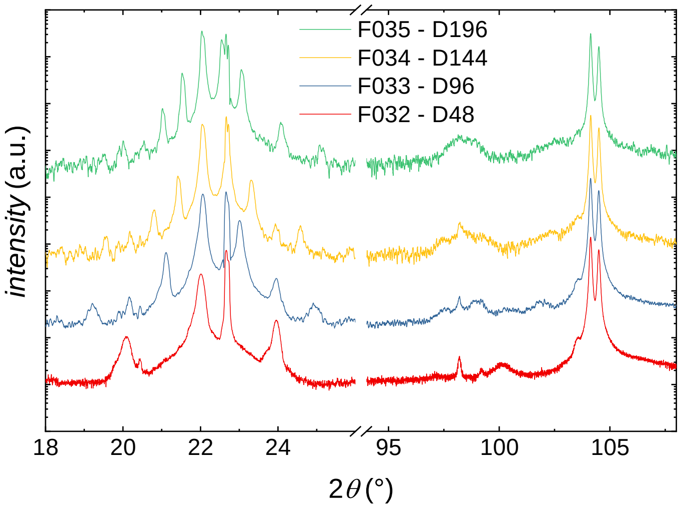

Figure 5.35: XRD 2θ-ω scans for multilayers of $15 \times$ [BaTiO$_3$-BiFeO$_3$] with constant $d_{\mathrm{BTO}}/d_{\mathrm{dl}}$ ratio of 0.52 ± 0.03 and varying d_{dl} of 4.6 to 17.7 nm. Graph adapted from Ref. H4.

Fig. 5.36 e)-h) also show the conservation of the same IP lattice constant throughout this sample series, as the horizontal position of the multilayer peaks is unchanged. Furthermore, TEM measurements (see Ref. H4) confirm that, for the thickest and thinnest multilayers of the d_{dl}-series, the OOP and IP lattice parameters are identical within the margin of error (see also Table 5.9). Thus it is advantageous for the exploration of the impact of strain-tuned lattice parameters or the double-layer thickness to explicitly separate the variation of individual and overall layer thickness, with the condition that the respective second parameter is kept constant.

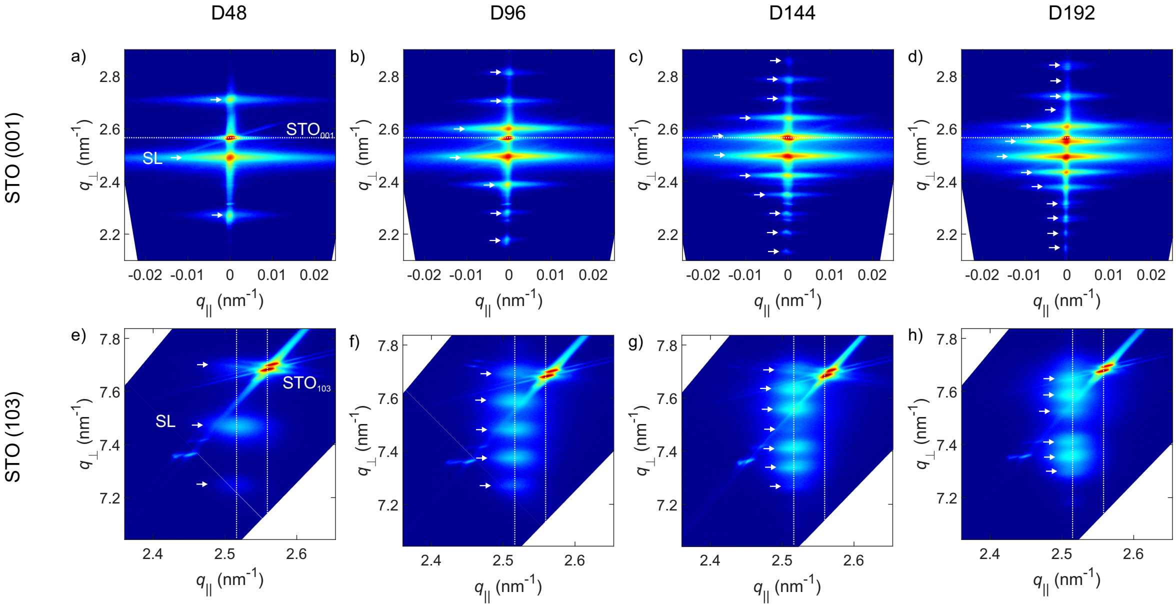

Figure 5.36: RSMs around the STO (001) ((**a**)-(**d**)) and (103) ((**e**)-(**h**)) peaks for multilayers of 16 × [BaTiO$_3$-BiFeO$_3$] with constant $d_{\mathrm{BTO}}/d_{\mathrm{dl}}$ ratio of 0.52 ± 0.03 and varying d_{dl} of 4.6 to 17.7 nm. The vertical lines in (**e**)-(**h**) mark the in-plane position of the superstructure and STO (103) peaks, respectively, as labeled in (**e**). The heat map colors represent measured intensities on a logarithmic scale, blue representing small values and red large values. Graph adapted from of Ref. H5.

5.3.3 Manipulation of Ferroic Properties Through Design

Both ferroelectric and magnetic properties were probed with respect to the multilayer design parameters of relative and absolute layer thickness. All samples proved to be ferroelectric, showing at the least partial switching peaks in ferroelectric hysteresis measurements. Exemplary $\boldsymbol{P}(\boldsymbol{E})$- and $I(\boldsymbol{E})$-curves of the d_{BFO}-series are presented in Fig. 5.37 along with measurements performed on both BTO and BFO single-layer samples. Additionally, corresponding representative measurements were published for the d_{BGFO}-series in Ref. H3 and for the d_{dl}- and BTO-BFO ratio series in Ref. H4 . As Figs. 5.37 e) and f) show, the BTO single-layer sample suffered from electric field induced breakdown before the initial switching peak was completed leading to an unsaturated polarization loop. The BFO single-layer experienced severe leakage current in positive fields, thus obscuring any ferroelectric properties in the measurement. As shown in Figs. 5.37 a) through d), the BTO-BFO multilayer samples typically showed double switching peaks, but also suffered from premature breakdown before fully saturated hysteresis loops could be recorded. The same misgivings are shared by the samples of the d_{BGFO}-, the d_{dl}- and BTO-BFO ratio series. So while ferroelectricity persists irrespective of BTO-BFO ratio or double-layer thickness, systematic observation of the influence of these design parameters on the saturation polarization and coercive fields was not possible.

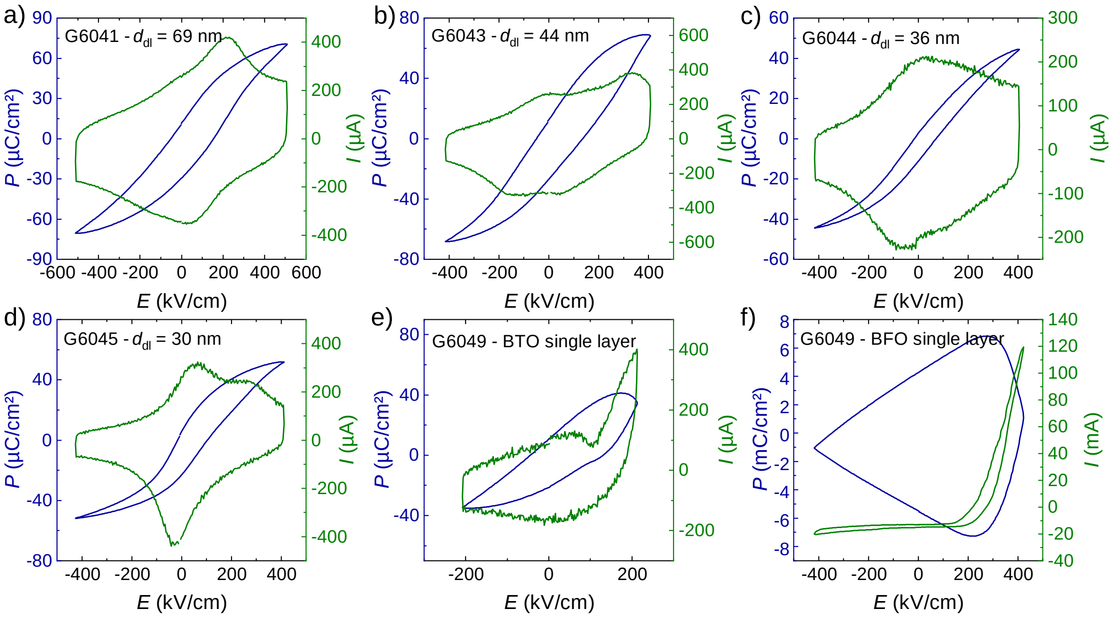

Figure 5.37: *Blue*: $\boldsymbol{P}(\boldsymbol{E})$- and *green*: $I(\boldsymbol{E})$-loops measured at 1 kHz on NSTO-film-Pt capacitors of **(a)-(d)** BTO-BFO multilayers with constant BTO and varying BFO thickness, as well as **(e)** a BTO and **(f)** a BFO single-layer.

Contrary, the magnetic property measurement by VSM does not suffer the same disadvantages. For the BTO-BFO ratio series, $\boldsymbol{M}(\mu_0\boldsymbol{H})$-curves measured at 300 K are presented in Fig. 5.38 a) along with depictions of the characteristic magnetic hysteresis parameters of $\boldsymbol{M}_{\mathbf{sat}}$ and $\boldsymbol{M}_{\mathbf{rem}}$ with respect to the BTO-BFO ratio in Figs. 5.38 b) and c). Like the samples of the d_{BGFO}- and d_{BFO}-series (cf. magnetic measurements of the d_{BGFO}-series published in Ref. H3), all BTO-BFO multilayer samples discussed in this section were found to possess a ferromagnetic-like magnetic hysteresis. As the slim opening of the $\boldsymbol{M}(\mu_0\boldsymbol{H})$-curves in Fig. 5.38 a) show, the coercive fields are fairly minute, in the range of 18 ± 5 mT for the samples of the BTO-BFO ratio series, with no explicit verifiable dependence on the BTO-content. Likewise, the saturation field strength of ~250 mT appears unaffected by the BTO-BFO ratio. However, the saturation and remanent magnetization values indicate a show a clear dependence on the BTO-content in the multilayer structures. The range of the saturation magnetization from 1.0 to 3.2 emu cm^{-3} equates to 0.007 to 0.022 μ_{B}/f.u., or 0.01 to 0.08 μ_{B}/Fe (normalized to the BFO-content). For comparison, the 360 nm BFO single-layer sample G6050 has a saturation magnetization equal to 0.02 μ_{B}/f.u., in line with the majority of publications on stoichiometric BFO thin films films grown by PLD from over-stoichiometric targets [69, 90, 91]. As the red data points in Fig. 5.38 b) show, the

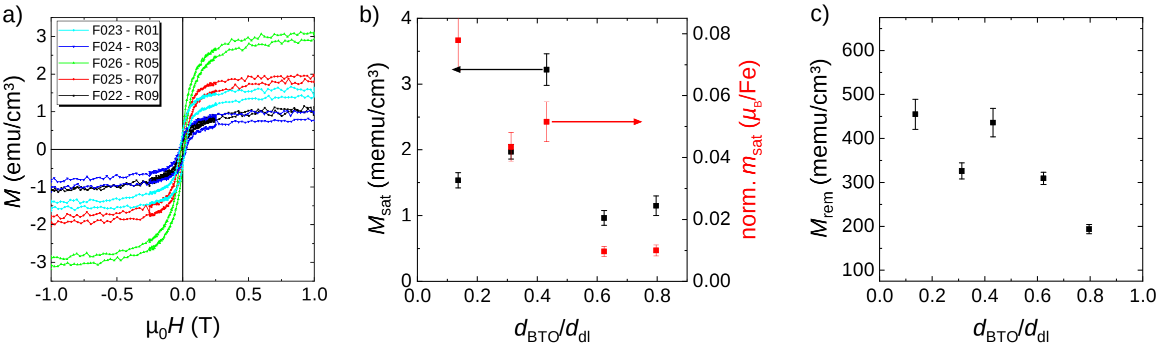

Figure 5.38: **(a)** $\boldsymbol{M}(\mu_0\boldsymbol{H})$-curves measured at 300 K, **(b)** values of saturation magnetization $\boldsymbol{M}_{\mathbf{sat}}$ and saturation magnetic moment in μ_B per Fe atom and **(c)** $\boldsymbol{M}_{\mathbf{rem}}$ for multilayers of $16 \times$ [BaTiO$_3$-BiFeO$_3$] with varying nominal $d_\mathrm{BTO}/d_\mathrm{dl}$ ratios of 0.1 to 0.9 and constant d_dl of 19.7 ± 0.3 nm.

saturation magnetization in BTO-BFO multilayers, when normalized to the magnetic Fe atoms, is enhanced by a factor of 2 to 3 relative to BFOsingle-layer, but suppressed to $\sim$0.01 μ_B/Fe when the relative BTO-content surpasses 60 % at a double-layer thickness of 19.7 ± 0.3 nm. Unlike the sharp drop in $\boldsymbol{M}_{\mathbf{sat}}$, the remanent magnetization decreases approximately linearly with the BTO-BFO ratio from 450 to 180 memu cm^{-3}.

Depicted in Fig. 5.39 are the corresponding $\boldsymbol{M}(\mu_0\boldsymbol{H})$ measurements and values for $\boldsymbol{M}_{\mathbf{sat}}$ and $\boldsymbol{M}_{\mathbf{rem}}$ for the samples of the d_dl -series. The relative BTO-content for these samples is 0.51 ± 0.02. As Figs. 5.39 a) and b) show, the saturation magnetization is approximately constant across the d_dl-range of 4.6 to 17.7 nm. The average value of $\boldsymbol{M}_{\mathbf{sat}}$ is $0.016 \pm 0.002\,\mu_\mathrm{B}$/f.u. for the multilayer structures, or $0.032 \pm 0.005\,\mu_\mathrm{B}$/Fe. The value of $\boldsymbol{M}_{\mathbf{rem}}$ increases from 310 to 610 memu cm^{-3} as d_dl is lowered from 17.7 to 4.6 nm. For the d_BFO- and d_BGFO-series with constant BTO-thicknesses of 27 nm and 17 nm, respectively, the trend for $\boldsymbol{M}_{\mathbf{rem}}$ with overall d_dl is reversed, decreasing from 300 to 120 memu cm^{-3} and 380 to 80 memu cm^{-3}, respectively, in line with the trend observed for the ratio-series. The saturation magnetization at 300 K is constant at $0.020 \pm 0.004\,\mu_\mathrm{B}$/Fe for the d_BFO-series, but varying significantly, but non-systematically around $0.023 \pm 0.013\,\mu_\mathrm{B}$/Fe for the d_BGFO-series. At 10 K, the noise level in the $\boldsymbol{M}(\mu_0\boldsymbol{H})$-curves is greatly reduced, returning constant Fe-normalized values of $0.020 \pm 0.020\,\mu_\mathrm{B}$/Fe and $0.060 \pm 0.010\,\mu_\mathrm{B}$/Fe for the d_BFO- and d_BGFO-series, respectively. The enhanced saturation magnetization was also previously observed by *Lazenka et al.* [87] for rare-earth-doped BFO single-layer films. In Ref. 87, the $\boldsymbol{M}_{\mathbf{sat}}$-values for 110 nm and 170 nm, respectively, thick single-layer films of BiFeO$_3$ and Bi$_{0.95}$Gd$_{0.05}$FeO$_3$, each grown from a stoichiometric target, were reported as 0.073 μ_B/Fe and 0.119 μ_B/Fe, respectively. Both values are larger than the $\boldsymbol{M}_{\mathbf{sat}}$-values of 0.02 μ_B/f.u. 0.09 μ_B/f.u. obtained for the corresponding BFO and BGFO films G6050 and G6051, re-

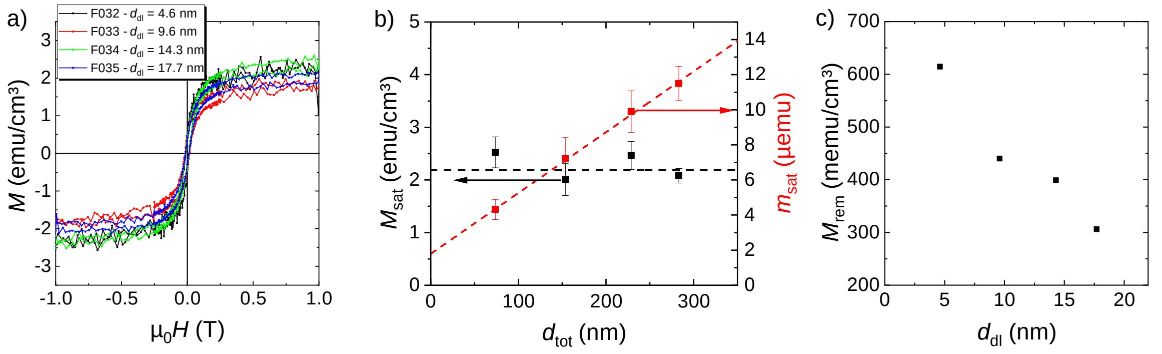

Figure 5.39: **(a)** $\boldsymbol{M}(\mu_0\boldsymbol{H})$-curves measured at 300 K, **(b)** values of saturation magnetization $\boldsymbol{M_{\mathrm{sat}}}$ and **(c)** $\boldsymbol{M_{\mathrm{rem}}}$ for multilayers of 16 × [BaTiO$_3$-BiFeO$_3$] with constant $d_{\mathrm{BTO}}/d_{\mathrm{dl}}$ ratio of 0.51 ± 0.02 and varying d_{dl} of 4.6 to 17.7 nm.

spectively. This could be due the samples' to increased layer thicknesses (about 360 nm) compared to the films in Ref. 87, a commonly reported effect for BFO-films [9, 207].

In-depth analysis of the magnetic configuration of BTO-BFO multilayers was carried out by *Lazenka et al.*, and continued by *Jochum et al.*, using conversion electron *Mössbauer* spectroscopy (CEMS). Using BFO targets enriched with *Mössbauer*-sensitive ^{57}Fe, they investigated the hyperfine field distribution of $n\times[(\mathrm{BaTiO_3})\text{ - }(\mathrm{BiFeO_3})]$ ($n =$ 2 to 20, fixed d_{dl}) [151] and $15\times[(\mathrm{BaTiO_3})_{10\ \mathrm{nm}}\text{ - }(\mathrm{BiFeO_3})_{x\ \mathrm{nm}}]$ ($x = 5$ to 50) [152]. Asymmetric peaks observed in the CEMS hyperfine field distribution of these BTO-BFO multilayers are indicative of the disruption of the spin cycloid present in the G-type anti-ferromagnetic BFO [151]. From the peak intensity ratio, it can be inferred that the angle between magnetic moments to the cycloid plane (defined by the cycloid direction $[1\bar{1}0]$ and polarization direction [111]) increases with the double-layer repetition n [151]. Plainly speaking, this causes a progressive tilt the average magnetic spin orientation towards an out-of-plane direction with n. When reducing the BFO layer thickness, an increasing hyperfine field peak skewness served as an indicator that the relative amount of ferromagnetically coupled Fe is enhanced [152]. It was argued that this is due to the increased relative amount of uncompensated spin at the interface between BTO and BFO.

Reliable measurement of such a perpendicular magnetic anisotropy with direct macroscopic magnetic measurement techniques such as SQUID (Superconducting QUantum Interference Device) magnetometry or VSM is far from an easy task. For one, the measurement of the particularly low magnetization of the canted anti-ferromagnet BFO, in particular when considering the minute quantity of sample material present in thin film samples, is highly susceptible to sources of stray magnetization, such as contamination from laboratory environment [56]. On top of that, contributions of surface magnetism of STO substrates may play a problematic role [53]. For a discussion of

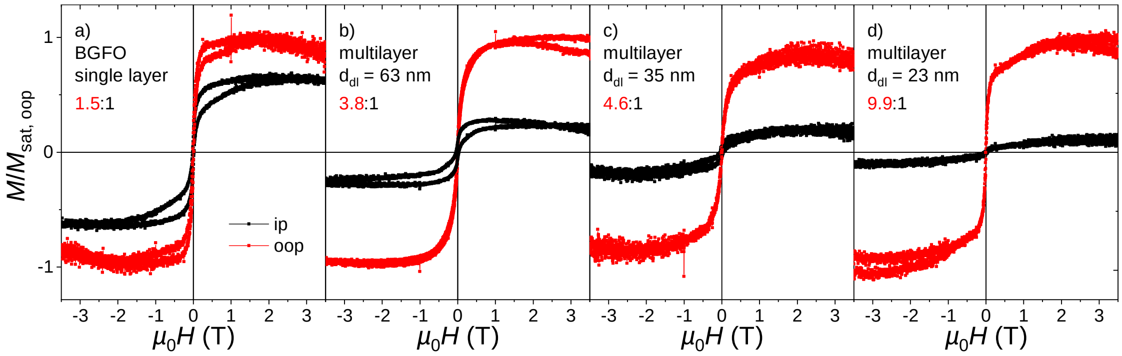

Figure 5.40: In-plane (black) and out-of-plane (red) $\boldsymbol{M}(\mu_0\boldsymbol{H})$-curves measured at 300 K for **(a)** a BGFO single-layer and **(b)** a 63 nm, **(c)** a 35 nm and **(d)** a 23 nm thick 15×BTO-BGFO multilayer with constant BTO-layer thickness.

the inherent measurement artifacts encountered in the PPMS VSM module used in the framework of this thesis, see Appendix B. The limited radial space available inside the gradiometer pickup-coils further complicates the measurement procedure. In the in-plane configuration, entire 5 mm × 5 mm samples can be glued to the substrate holder. In the out-of-plane configuration, samples need to be sawed in half, the edges trimmed (saw-blades are a source of contamination, requiring a stringent cleaning procedure), and glued onto the semicircular quartz-rods using further glass brackets for support. Additionally, form-factor dependent erroneous signal contributions are enhanced for thin film samples mounted perpendicular to the pickup-coil axis, and likewise the relative contribution of possible magnetic contaminant particles to the overall signal is greatly increased at larger radial positions [214].

Nevertheless, we have been able to measure the relative IP and OOP magnetization of the samples of the d_{BGFO}-series. Due to the above-mentioned reasons, however, these measurements should be taken with a grain of salt, and have not been repeated for other sample series. Presented in Fig. 5.40 are comparisons of the respective IP and OOP $\boldsymbol{M}(\mu_0\boldsymbol{H})$ measurements of a BGFO single-layer and samples of the d_{BGFO} multilayer series. As can be clearly observed, the relation of OOP to IP saturation magnetization of the thickest multilayer (Fig. 5.40 b)) is more than doubled relative to the BGFO single-layer (Fig. 5.40 a)) and increases with decreasing BGFO layer thickness. This result, published in [H3], confirms the trends observed by CEMS by *Jochum et al.* in [152]. Additional SQUID magnetometry measurements in Ref. 152 likewise show an increase of the OOP saturation magnetization with decreasing BFO layer thickness. As we will discuss in the next chapter, the increased OOP orientation of magnetic moments were correlated with an increase in α_{ME}, in the case of the variation of n [151], as well as the variation of d_{BFO} [152] and d_{BGFO} [H3].

5.3.4 Summary

In conclusion, the primary tuning parameter concerning the design of BTO-BFO multilayers was shown to be the relative individual layer thickness ratio of the constituent materials. The overall double-layer thickness only plays a subordinate role, as the total multilayer mosaicity and lattice parameters of both BTO and BFO change only in response to variation of d_{BFO} with constant d_{BTO}, as well as to variation of the relative ratio with constant d_{dl}, but are invariant for samples with constant ratio but changing d_{dl}. The minimum strain and likewise mosaicity are maintained for values of $d_{\mathrm{BTO}}/d_{\mathrm{dl}}$ between approximately 0.4 and 0.8. Samples with a $1:1$ BTO-BFO ratio also show the lowest strain contrast and interface roughness in TEM-measurements.

All multilayer samples irrespective of individual or double-layer thickness were found to be both ferroelectric and possess a ferromagnetic-like hysteresis. The leakage current present in FE hysteresis measurements is drastically decreased in multilayer samples relative to single-layer samples. However, quantitative analysis of the ferroelectric properties were hindered by low breakdown field strengths. As will be made evident in the next section, a repetition of these design variation experiments using eclipse-PLD, which produces BTO-BFO multilayers with drastically enhanced breakdown fields, would be an interesting avenue for future investigations. Existence of perpendicular magnetic anisotropy previously demonstrated by *Mössbauer* spectroscopy [151, 152] could be confirmed by VSM measurements conducted on a sample series with varying BGFO-thickness and was found to increase with decreasing d_{BGFO}. While the general relationship between design and magnetic properties do not paint a straightforward picture, it seems that the remanent magnetization is enhanced with decreasing double-layer thickness. In order to deepen the insight in the connection of the coupled ferroic properties with design choices and local strain states, it is advisable to combine structural measurements, such as HR-TEM, with both depth resolved magnetic and polarization measurements, such as PNR and *Lorentz*-TEM, and first-principles calculations.

5.4 Effectiveness of Eclipse–PLD

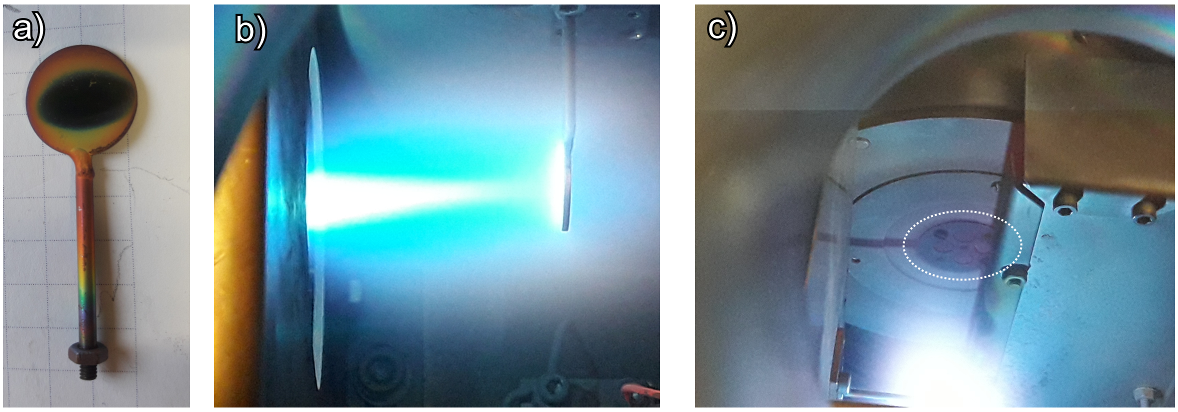

Figure 5.41: Photographic images of **(a)** the eclipse mask used in the eclipse-PLD setup, **(b)** side-view of the plasma plume being blocked by the eclipse mask and **(c)** frontal view of the sample holder being shaded from the bright light emitted from the ablation spot by the eclipse mask.

A number of common approaches for the parametric optimization of oxide multilayers grown by PLD were presented in the previous sections, including growth parameter optimization and the avenue of multilayer design choices. The general focus was set primarily on a reduction of the droplet density and interface roughness in the multilayer samples. While the variation of deposition parameters, such as o_{lat} and ρ_{L} show a limited, but insufficient efficiency in reducing the number of droplet particles in BTO-BFO thin films, the technique known as eclipse-PLD offers a more direct approach. A shadow mask, also called eclipse mask or blind, is placed in the direct path between the ablation spot on the target and the substrate. Heavy particles such as droplets travel in a linear path and are blocked, while gaseous ablation species can be redirected around the mask by multiple scattering events.

Fig. 5.41 shows the setup installed in chamber *F*. A number of circular masks with diameters from 10 to 15 mm were fabricated, depicted in Fig. 5.41 a) is the mask with a diameter of 13 mm. The dark spot visible in the center of the mask shows the position of the highest particle flux in the center of the plasma plume. Fig. 5.41 b) illustrates the persistence of a plasma plume behind the mask due to multiple scattering. In Fig. 5.41 c), the eclipsing of the 2×2 substrate holder by the mask relative to the bright ablation spot on the target is visible as a shadow. The shadow image was used to align the mask and as a basis to choose the 13 mm mask over the smaller 10 mm mask. The lateral offset was maintained at $o_{\mathrm{lat}} = 0\,\mathrm{mm}$ and the blind position was varied using spacers. The fluence was set to $\rho_{\mathrm{L}} = 2\,\mathrm{J\,cm^{-2}}$, $p_{\mathrm{O_2}}$ to 0.25 mbar and T_{p} to $700 \pm 10\,°\mathrm{C}$. The introduction of the eclipse-mask reduced the average deposition rate by a factor between 3 and 4.

5.4.1 Influence of Excimer Laser Voltage on the Deposition Rate

During the initial experimental stage of implementing eclipse-PLD for the growth of BTO-BFO multilayers, severe variations in the deposition rates were observed. Predictability of a process outcome is a key factor for the conservation of comparability and a necessity for the precise implementation of target sample designs. The variation in deposition rates, up to 50 % relative to the maximum rate, was soon linked to the operation voltage of the excimer laser U_{laser}. Excimer lasers generate laser emission by stimulation of a gas mixture by high voltage. Over time, the gas mixture - in the case of our system Kr and F - degrades due to surface reactions with the container [215]. In order to maintain the same 650 mJ per pulse output, the excimer laser controller applies increasingly large high voltage fields to compensate the gas mixture degradation. Depending on the laser system's range of stable operation parameters, the gas mixture hence needs to be replenished after a certain time-frame, re-starting the U_{laser} adjustment-loop.

A side effect of an aging gas mixture can be that the overall beam profile, i.e. the lateral distribution of emitted intensity, changes. This can change both the local fluence across the ablation spot and the total energy on the ablation site. A rectangular beam aperture is typically used to only admit the central area of the gaussian shaped beam profile. While the total energy before the aperture may be kept constant by adjusting U_{laser}, changes in the beam profile can lead to a changed actual fluence ρ_{L} at the ablation site after the beam passes the aperture. As discussed in Sec. 5.2.3, the deposition rate of BFO is highly sensitive to changes in ρ_{L}, while the deposition rate of BTO only depended on the actual ablation area.

Fig. 5.42 depicts the deposition rates, as determined from superstructure fringe peaks in XRD 2θ-ω scans and XRR measurements for a) eclipse-PLD films and b) a sample series deposited using conventional PLD (see the figure caption for details). The green and black points in Fig. 5.42 a) represent the average total deposition rate of the multilayers. The initial samples, assuming a static deposition rate are represented by the green dots. The later introduced adaptive selection of pulse numbers, aiming at a constant 1:1 BTO-BFO ratio, produced the samples represented by the black dots. Over the short U_{laser} range of 17.5 to 18.0 kV, the overall deposition rate dropped from 0.05 to 0.03 Å per pulse. XRR measurements allowed the determination of individual deposition rates. Across all excimer laser voltages, the BTO deposition rate scattered around 0.083 ± 0.010 Å per pulse, but with no clear dependence on U_{laser}. The BFO deposition rate, however, followed the same trend as the overall deposition rate, dropping from 0.04 to 0.02 Å per pulse. In comparison, all three deposition rates changed

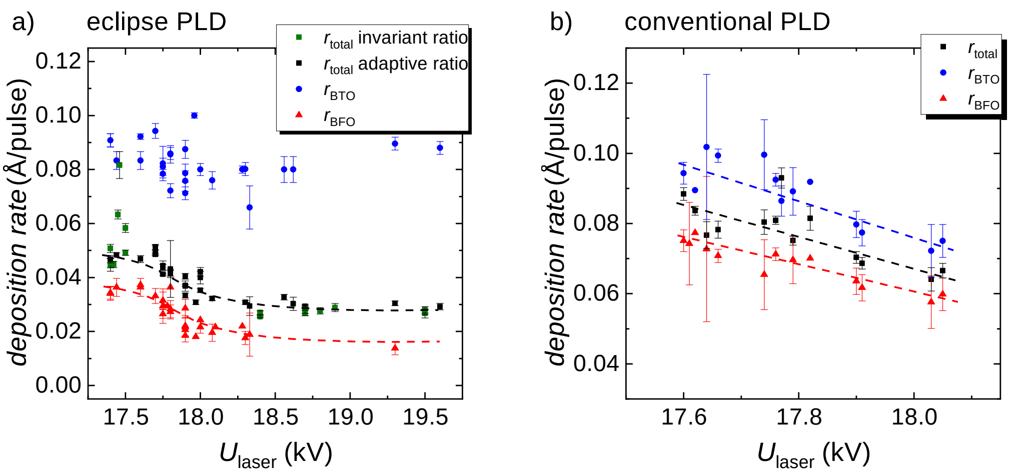

Figure 5.42: Deposition rates of BTO and BFO and the average multilayer deposition rate in dependence of the excimer laser voltage U_{laser}, required for an output of 650 mJ per pulse. **(a)** sample range F178-F247, deposited using eclipse-PLD $\rho_{\text{L}} = 2.0\,\text{J}\,\text{cm}^{-2}$ $(L = 20)$ and a 14 mm diameter blind; **(b)** sample range F020-F040, reported in Ref. H4 d_{dl}, deposited using conventional PLD with $\rho_{\text{L}} = 3.8\,\text{J}\,\text{cm}^{-2}$ $(L = 0)$.

Table 5.10: Sample parameters of three 15×BTO-BFO multilayers deposited on NSTO by eclipse-PLD using standard conditions at various excimer laser operation voltages U_{laser}. Double-layer thicknesses d_{dl} were determined from superstructure fringe peaks in XRD 2θ-ω scans, individual BTO and BFO thicknesses were determined by fitting XRR curves.

sample	n(BTO)	n(BFO)	U_{laser} (kV)	d_{dl} (nm)	d_{BTO} (nm)	d_{BTO} (nm)
F220	1250	4500	18.1	18.5 ± 0.5	9.5	8.8
F221	1250	2750	17.4	19.1 ± 0.3	–	–
F223	1250	3250	17.8	19.7 ± 0.5	10.1	10.2

linearly with U_{laser} in the conventional PLD process, as depicted for the samples published in Ref. H4 in Fig. 5.42 b). The total change in the deposition rate over the range of 17.6 to 18.1 kV was only about 5 % for these samples.

A qualitative fit of the BFO deposition rates, arbitrarily using the sigmoidal *Boltzmann* function, was used to predict appropriate pulse numbers based on U_{laser}. The predictive practicability of this naive fit is illustrated in a series of three samples deposited at U_{laser}-values from 17.4 to 18.1 kV, the details of which are given in Table 5.10. While the number of BTO pulses remained constant, the number of BFO pulses was changed from 2750 to 4500 according to the current U_{laser}-value determined just before the process. The resulting double-layer and individual thicknesses vary only by less than 10 %, though the BFO deposition rate varied from 0.020 to 0.036 Å per pulse.

In summary, the deposition rate of BFO in the eclipse-PLD process was found to change drastically in response to minor changes in the excimer laser's operation voltage U_{laser}. The variation is predictable, but nevertheless unfavorable. A possible solution eliminating this problem would be a more advanced projection setup, as described by

Opel et al. in Ref. 216. They used a fully motorized set of five lenses in a telescopic arrangement to homogenize the beam profile and create a sharp image of the laser aperture on the sample surface. An in-situ measurement of the pulse energy inside the deposition chamber with a pyroelectric detector facilitates an accurate adjustment of the laser fluence.

5.4.2 Reduction of Droplet Particle Density

Initially, a number of films was deposited using the 10 mm mask with imperfect eclipse-alignment. Using the shadow area for alignment, the remaining films were deposited with the 13 mm mask. The resulting droplet particle densities of these films, normalized to represent a 100 nm BFO film thickness, are presented in Fig. 5.43 a), in comparison to films produced by conventional PLD in chambers G and F. The normalization to the BFO thickness is introduced for comparability, as overall thicknesses varied and BTO does not contribute to the droplet count (compare Fig. 5.26 b)). The films deposited in chamber G under standard conditions have comparable droplet densities as the films deposited with $L = 10\,\mathrm{mm}$ and $L = 20\,\mathrm{mm}$ in chamber F, around 10 to 40 particles per 100 nm BFO and $100\,\mu\mathrm{m}^2$ area. At $L = 0\,\mathrm{mm}$, the droplet density is the largest, two to three times higher than for the other films. Using the partially aligned 10 mm mask, the density is reduced to under 20 particles per 100 nm BFO and $100\,\mu\mathrm{m}^2$ area. When aligned, the slightly larger 13 mm mask fully eclipses the 2×2 substrate holder, as a result the droplet density is drastically and permanently reduced to less than 1 particle per $100\,\mu\mathrm{m}^2$, on par with light contamination with dust particles due to storage in regular lab environment, which can be shown for annealed and ultrasonically cleaned substrates.

5.4.3 Improved Breakdown Field

The use of an eclipse blind and the associated reduction of particles embedded in the multiferroic BTO-BFO multilayer films has a clear impact on the films' ferroelectric performance. Fig. 5.43 b) shows the ferroelectric key parameters imprint field, positive (in the direction of imprint) coercive field and, most notably, electric breakdown field for BTO-BFO multilayers deposited via conventional PLD and eclipse-PLD. The breakdown field indicates the applied electric field under which the film and top-electrode undergo a destructive transformation. This can lead to undesirable premature breakdown, i.e. destruction of the electrode at a voltage that is too low to record a fully saturated ferroelectric hysteresis at the selected frequency (1 kHz). Generally, the width of ferroelectric switching peaks in this work ranges from 1 to $2\,\mathrm{MV\,cm^{-1}}$.

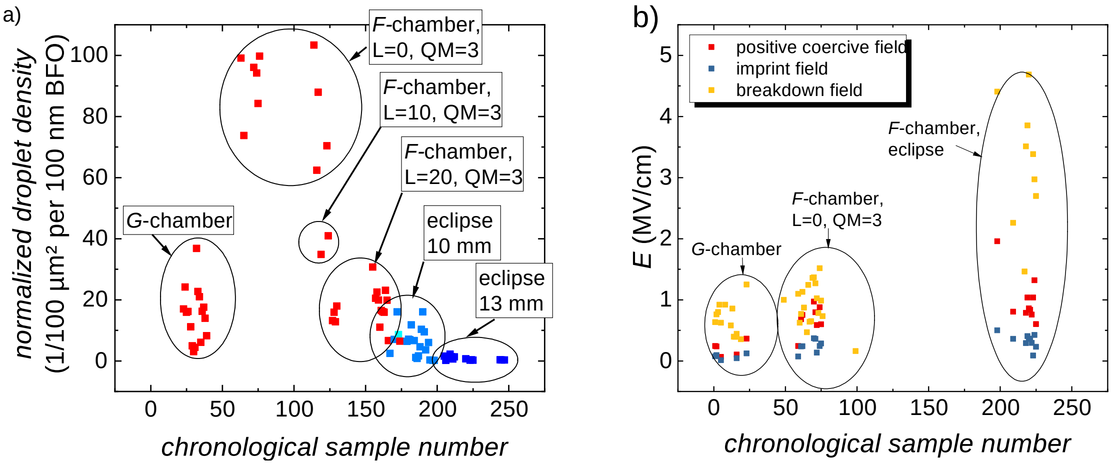

Figure 5.43: **(a)** Droplet particle density measured by LSM normalized to a virtual 100 nm BFO thickness based on XRR measurements; **(b)** electric breakdown fields, ferroelectric coercive and imprint fields measured at 1 kHz for samples deposited in chambers G and F using conventional PLD and eclipse-PLD.

Hence, in order to measure a fully saturated ferroelectric hysteresis, the sample needs to withstand electric fields at least 0.5 to 1 $\mathrm{MV\,cm^{-1}}$ larger than the positive coercive fields (typically 0.5 to 1 $\mathrm{MV\,cm^{-1}}$). As Fig. 5.43 b) illustrates, the films deposited using conventional PLD showed breakdown fields of only $0.8 \pm 0.3\,\mathrm{MV\,cm^{-1}}$. In contrast, the films deposited using eclipse-PLD showed breakdown fields of $3.2 \pm 1.0\,\mathrm{MV\,cm^{-1}}$, the highest values ranging close to 5 $\mathrm{MV\,cm^{-1}}$. This drastic improvement is indicative for not just of the absence of droplet particles, but also for a highly ordered, defect-poor growth mode, as electrode breakdown typically originates at highly conductive defect sites. Measurements taking advantage of the improved breakdown field of eclipse-PLD multilayers have been used to demonstrate a number of ferroelectric features within the framework of this thesis, such as the nature of imprint and the influence of substrate annealing (see Sec. 5.1.5).

5.4.4 Effect of Eclipse-PLD on Morphology

One of the central aims of the optimization process of system parameters and the application of the eclipse-PLD technique was to reduce the number of droplets, but also in particular to decrease the interface and surface roughness. While the influence of interface roughness on the multiferroic and magnetoelectric properties of BTO-BFO multilayers is currently unclear, a reduced interface roughness improves the informative value of certain depth-resolved measurement techniques. In particular chemical depth profiling techniques are highly affected by interface roughness. In both cross-sectional TEM-EDX mapping and ablative ToF-SIMS depth profiling, lateral irregularities due to interface roughness are indistinguishable in the measurements from intermixing effects. Another depth-resolved technique that stands to benefit from reproducible, uniformly smooth interfaces is polarized neutron reflectometry (PNR). In an analogy to XRR, PNR curves can be fitted with layer-based model functions and through the use of up- and down-polarized neutron channels, an additional magnetic moment depth profile can be constructed. The more uniform the sample is constructed, the higher the magnetic contrast will be, and thus a greater precision in the magnetic depth-profile information is obtained.

Fig. 5.44 shows exemplary topographical AFM scans for 5×BTO-BFO multilayers deposited using conventional PLD and eclipse-PLD with 10 mm and 13 mm masks. The sample depicted in Figure 5.44 a) was deposited with $\rho_L = 2.0\,\mathrm{J\,cm^{-2}}$ at 0 mm lateral offset. As mentioned in Sec. 5.2.3, multilayers deposited using these parameters already show improved surface roughness of 0.26 nm, compared to 0.65 ± 0.27 nm for samples grown under similar conditions in chamber G (cf. Ref. H3) and 3.9 ± 1.8 nm for samples deposited in chamber F with $\rho_L = 3.8\,\mathrm{J\,cm^{-2}}$ at 10 mm lateral offset. As the AFM image shows, the surface is smooth but irregular, possibly due to ion bombardment damage. The samples deposited using eclipse-PLD with a 10 mm and 13 mm mask have similar R_{rms}-values of 0.23 nm and 0.19 nm, respectively. As Fig. 5.44 b) and c) show, the surface structure is more regular with articulated overlapping plateaus. In particular in case of the 13 mm mask, a washed-out terrace structure akin to that of the underlying STO substrate is formed, as the tilted AFM scan in Fig. 5.44 d) reveals. The low surface roughness is highly reproducible and was determined to vary around 0.23 ± 0.07 nm for over 50 multilayer samples deposited using eclipse-PLD, including samples of 15×BTO-BFO with total thicknesses of up to 550 nm.

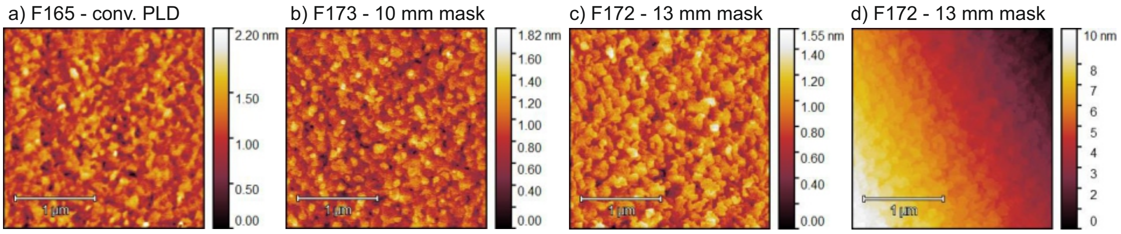

Figure 5.44: AFM topography scans of 5×BTO-BFO multilayers deposited on STO using **(a)** conventional PLD (sample F165), **(b)** eclipse-PLD with a 10 mm mask and a **(c)** 13 mm mask. Subfigure **(d)** is the same image as **(c)**, but tilted to reveal the stepped nature of the surface structure. All samples were deposited at 700 °C with $\rho_L = 2.0\,\mathrm{J\,cm^{-2}}$ at 0 mm lateral offset.

The low interface and surface roughness is also evident in TEM cross-section images, presented in Fig. 5.45. The homogeneity of layer thicknesses and interface roughness across the entirety of the $15 \times [(BaTiO_3)_{10\ \mathrm{nm}}\text{-}(BiFeO_3)_{10\ \mathrm{nm}}]$ eclipse-PLD multilayer

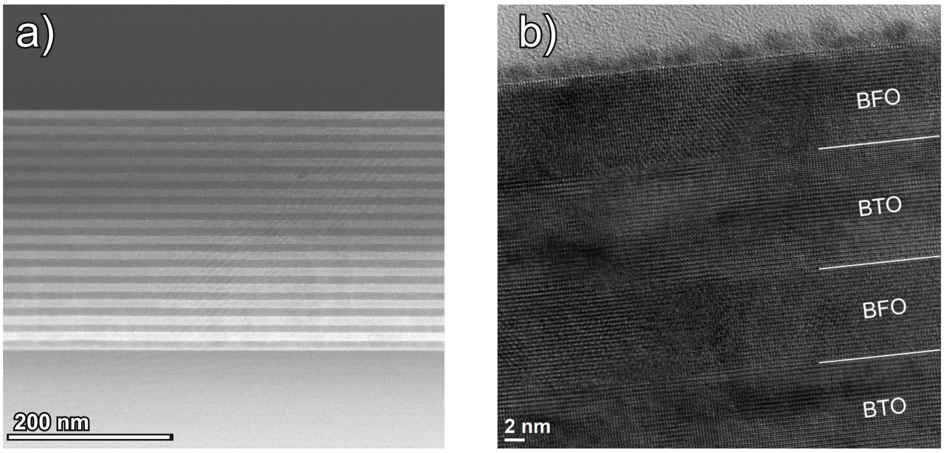

Figure 5.45: TEM cross-sections of a 15 × [$(\mathrm{BaTiO_3})_{10\ \mathrm{nm}}$ - $(\mathrm{BiFeO_3})_{10\ \mathrm{nm}}$] multilayer deposited by eclipse-PLD (sample F223) recorded in HAADF mode. **(a)** Overview of the entire film thickness, **(b)** HR-TEM image of the last four layers.

F223 can be seen in Fig. 5.45 a). The sample was deposited using the aligned 14 mm mask and 1250 and 3250 pulses for BTO and BFO layers, respectively. The double-layer thickness as inferred by multilayer fringe peaks of 19.7 ± 0.5 nm fits well with the value measured by TEM, 20.1 ± 0.3 nm. In the first BTO layer (appearing dark in Fig. 5.45 a)), evidence of Bi-enrichment near the substrate is visible as a bright contrast, as discussed in Sec. 5.1.2. HR-TEM imaging, as presented in Fig. 5.45 b), reveals an interface roughness in the order of one to three unit cells. The image in Fig. 5.45 b) was taken near the surface of the ~300 nm thick multilayer and shows the atomically flat topology of the terminating BFO layer. This confirms the atomically stepped nature of the ~200 nm wide terrace structures observed in AFM measurements, cf. Fig.5.44 c). The high degree of uniformity of the deposited layers directly

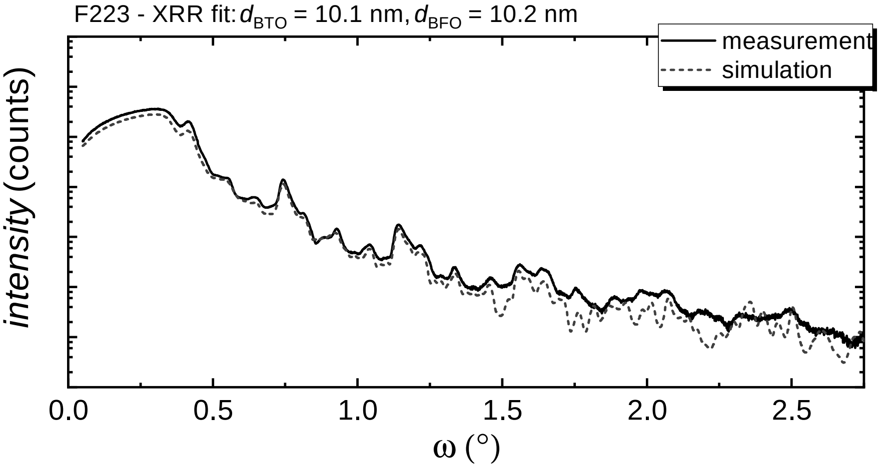

Figure 5.46: XRR measurement and simulated curve of BTO-BTO multilayer F223, deposited by eclipse-PLD.

affects the applicability of certain experimental techniques that require simulation of the film structure. This is exemplified by the accuracy of simulated XRR curves, as Fig. 5.46 shows. The layer-thicknesses of the fit-model for BTO and BFO layers are $10.1 \pm 0.4\,\mathrm{nm}$ and $10.2 \pm 0.4\,\mathrm{nm}$, respectively. For comparison, the values determined by TEM-measurements are $10.2 \pm 0.4\,\mathrm{nm}$ and $9.9 \pm 0.3\,\mathrm{nm}$, respectively, which validates the accuracy of the XRR fit. This demonstrates the unprecedented control over interface roughness and layer thickness facilitated by the implementation of eclipse-PLD.

5.4.5 Structural Properties of Eclipse-PLD Multilayers

One major concern connected to the use of a mask intercepting the direct path of ablated material in PLD is the possibility of drastic changes to the sample chemistry. As only particles that have been subjected to multiple scattering events can circumnavigate this obstacle, differences in scattering probabilities could be enhanced and hypothetically alter the composition of particles that reach the substrate. Fig. 5.47 shows the XRD 2θ-ω scans of a thin film deposited by conventional PLD in comparison with samples deposited by eclipse-PLD using a 10 mm and 13 mm mask. All samples show similarly well defined superstructure fringe peaks. Note that the respective double-layer thicknesses and hence the periodicity and intensity of the fringe peaks varies from sample to sample (see caption). The only systemic difference between the conventional PLD and eclipse-PLD samples is a minor increase of the BTO OOP lattice constant from 4.07 to 4.10 Å, whereas the BFO lattice constant remains virtually unchanged at about 3.95 Å, as determined from the layer peaks near the STO (004) peak. While these changes may point to a shift in stoichiometry, they are certainly within the range of typical parameter variations, which can occur due to any number of minor process parameter instabilities. It can be said that the eclipse-PLD BTO-BFO multilayers appear, in structural XRD measurements, to be indistinguishable from their counterparts grown by conventional PLD, albeit with slightly more pronounced superstructure peaks.

5.4.6 Chemical Depth Profile Measurements

Previous attempts at unraveling the chemical depth profiles of BTO-BFO multilayers were made difficult by the large interface roughness that occurs in samples deposited with conventional PLD. In Ref. H1 we used a combination of STEM-EDX, ToF-SIMS and Secondary Neutral Mass Spectrometry (SNMS) to investigate the differences be-

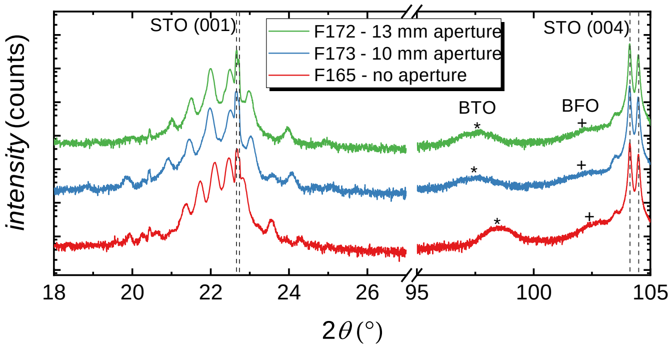

Figure 5.47: XRD 2θ-ω scans of 5×BTO-BFO multilayers on STO deposited using conventional PLD (F165) and eclipse-PLD with 10 mm (F173) and 13 mm (F172) masks. The double-layer thicknesses are 25.0 nm, 17.0 nm and 18.5 nm for samples F165, F173 and F172, respectively. Depicted are the angular ranges around the first and fourth STO (00l) *Bragg* peak.

tween several high- and low-α_{ME} multilayers deposited by conventional PLD technique. The focus lay on two samples of $15 \times [(\mathrm{BaTiO_3})_{10\ \mathrm{nm}}$ - $(\mathrm{BiFeO_3})_{20\ \mathrm{nm}}]$ (high α_{ME}-value) and $15 \times [(\mathrm{BaTiO_3})_{10\ \mathrm{nm}}$ - $(\mathrm{BiFeO_3})_{5\ \mathrm{nm}}]$ (low α_{ME}-value) multilayers deposited on STO. One key feature that persists throughout all BTO-BFO multilayers was, as discussed previously in Sec. 5.1.2, an accumulation of Bi near the STO-interface. We also found an asymmetry in the intensity distribution of the Bi, Ba and Ti signal, as well as an apparent inter-diffusion of ca. 2 at% of Ba and Ti into the BFO layers. Both effects are enhanced in the sample with the higher α_{ME}-value and a nominal 5 nm BFO layer thickness. However, TEM measurements revealed an asymmetric interface roughness of ∼4 nm for the BTO-BFO interfaces caused by the BTO layer roughness. The BFO layers remained smooth with roughness smaller than 1 nm, leading to thickness modulations of the BFO layers in the order of magnitude of the 5 nm thickness. In STEM-EDX, such lateral irregularities may lead to false measured intermixing effects due to trans-illumination, compounding with effects of the electron beam interaction radius, scattering of emitted X-rays and the detection limit of 0.1 to 1 at%. ToF-SIMS depth profiling uses sequential sputtering and is hence susceptible to preferential sputtering and averaging over lateral inhomogeneities. As in ToF-SIMS, the local relative ion yield rates are highly dependent on the electric configuration of the surrounding atoms, this further complicates evaluation of depth-profiles.

Taking advantage of the drastically reduced interface roughness achieved via eclipse-PLD, here we re-evaluate the chemical depth profiles of BTO-BFO multilayers with three different individual layer thicknesses. The details of these three samples are listed in Table 5.11. All samples have nominally identical BTO and BFO thicknesses

Table 5.11: Sample parameters of three 15×BTO-BFO multilayers used for chemical depth profiling, deposited on NSTO using eclipse-PLD under standard conditions. Double-layer thicknesses d_{dl} were determined from superstructure fringe peaks in XRD 2θ-ω scans, individual BTO and BFO thicknesses were determined by fitting XRR curves.

sample	n(BTO)	n(BFO)	d_{dl} (nm)	d_{BTO} (nm)	d_{BTO} (nm)
F224	625	1650	10.1 ± 0.4	5.1	4.9
F223	1250	3250	19.7 ± 0.5	10.1	10.2
F225	2500	6500	37.1 ± 0.4	19.6	17.2

with double-layer thicknesses of 15×10 nm, 20 nm and 37 nm. Exemplary for all three samples, Fig. 5.48 a) shows cross-sectional elemental maps recorded by STEM-EDX around the seventh double-layer pair of the 15×20 nm sample (F223). The horizontally averaged intensities of the main constituent elements are depicted in Fig. 5.48 b). An elemental map from near the STO-interface of this sample was discussed in Sec. 5.1.2 (Fig. 5.7). Near the interface, the Bi accumulation can be confirmed, as is the case for all other investigated samples. In Fig. 5.48 a), atomically smooth interfaces are visible both in the HAADF signal, as well as the EDX signal. Crossover between regions of BTO and BFO is limited to a 0.3 nm (less than one unit cell) region of symmetrical decrease and increase of the respective elemental signal intensities. The signal intensity of Ba and Ti in the BFO layers, as well as Bi and Fe in the BTO layers, is limited to a homogeneous signal intensity in the order of the background noise level. The same trends are also observable for the 15×10 nm and 15×37 nm samples (not shown here).

An advanced ToF-SIMS technique was used to analyze the three samples, which allows a three-dimensional visualization of the elemental distribution in the samples. In 3D-ToF-SIMS, the ion beam used for analysis is scanned across the sample surface to include lateral information. Depth information is gained by alternating periods of analysis with periods of sputtering, using a more intense ion beam for the latter than the first. The ablation area is kept significantly larger (300 µm × 300 µm) than the analysis area (50 µm × 50 µm) to exclude the formed pit edges from the measurement. One such 3D-ToF-SIMS visualization is presented in Fig. 5.49 for the 15×20 nm sample (F223). Depicted are the intensities measured for the main constituent binary oxides TiO^-, BaO^-, SrO^-, FeO^-, and BiO^-, as well as ions of selected trace elements MgO^-, S^-, C^-, Mg^+, Ca^+, Na^+, and K^+. Additionally, the averaged intensity depth profiles of the main constituent ions of all three samples are presented in Fig. 5.50. The trace ion intensity profiles of sample F223 are depicted in Fig. 5.51, representative for all three samples. In Fig. 5.49, the multilayer structure is clearly visible in the alternating, laterally homogeneous 3D-profiles of TiO^-, BaO^-, FeO^-, and BiO^-. Even though the layers are overall very smooth, a small structural irregularity can be seen near the

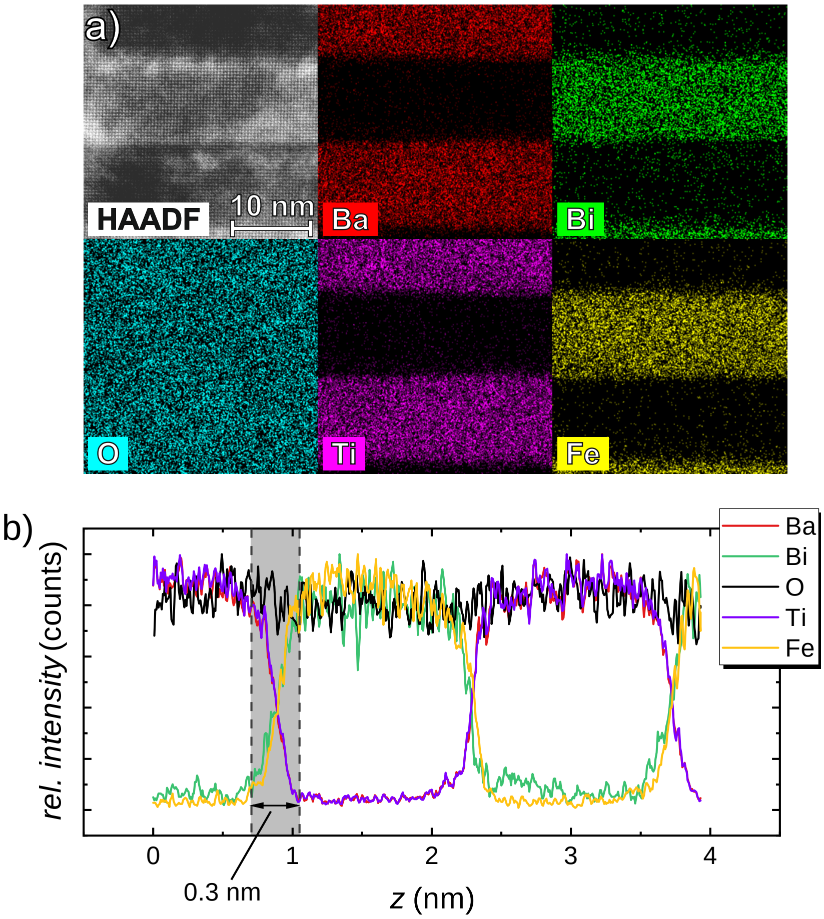

Figure 5.48: **(a)** STEM-EDX elemental mapping of a cross-section of a 15 × $[(\mathrm{BaTiO_3})_{10\ \mathrm{nm}}\text{-}(\mathrm{BiFeO_3})_{10\ \mathrm{nm}}]$ multilayer deposited by eclipse-PLD (sample F223). Presented for reference is a HR-TEM image recorded in HAADF mode, as well as the laterally resolved gray value intensities of EDX signals associated with the elements Ba, Bi, O, Ti, and Fe. **(b)** Horizontally averaged vertical profiles of relative intensities of all five elements. The indicated gray area is a narrow 0.3 nm transition range between the two phases.

surface, which is gradually smoothed out by the successive layers. In this case, the irregularity appears to be a titanium oxide particle. As droplets appear to exclusively originate from the BFO target (cf. Sec. 5.1.3) and are being blocked by the eclipse mask (cf. Sec. 5.4.2), the source is likely a contamination from the lab environment or the pre-treatment of the STO substrate.

Contamination of the multilayer with a number of trace elements is also clearly visible in Fig. 5.49. Most impurities are distributed throughout the film and do not penetrate into the STO substrate, apart from a small amount of C. Additionally, increased concentrations of S, C, Mg, Ca, Na, and K can be found on the sample surface. This indicates a contamination from storage in regular lab environment post-growth. similarly, contamination of the targets during storage or fabrication may be responsible for the presence of said elements in the multilayer structure. The presence of Sr in the

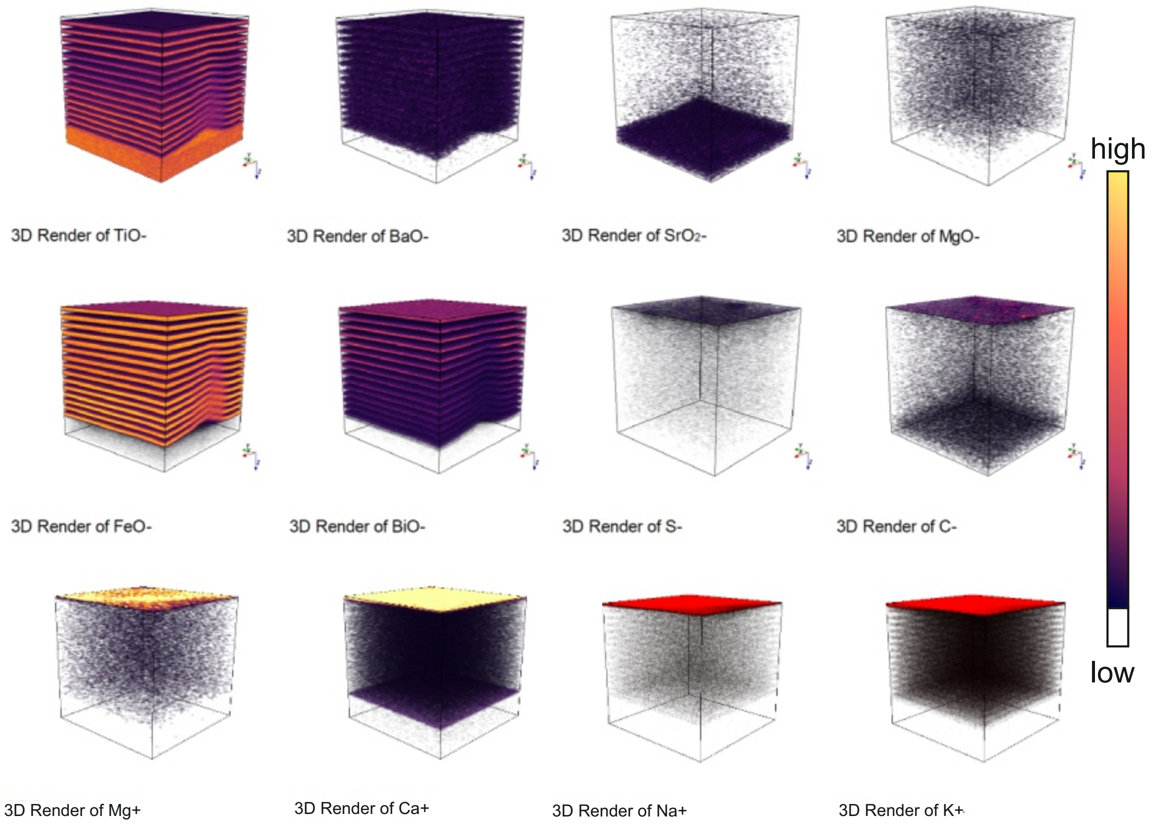

Figure 5.49: 3D ToF-SIMS chemical depth-profiles of a 50 µm × 50 µm area of a 15 × $[(BaTiO_3)_{10\ nm}$ - $(BiFeO_3)_{10\ nm}]$ multilayer deposited by eclipse-PLD (sample F223). Depicted are the intensities detected for the bi-atomic negative ions TiO^-, BaO^-, SrO^-, MgO^-, FeO^-, and BiO^-, as well as the single negative and positive trace ions S^-, C^-, Mg^+, Ca^+, Na^+, and K^+. The color gradient is set to a logarithmic intensity scale.

multilayers may be due to diffusion at the elevated growth temperatures, or otherwise sputtering of the substrate material due to particle bombardment.

The modulation of elemental depth profiles in Fig. 5.50 is extremely homogeneous across the layer thickness. The absence of dependency of the profile shape from the distance to the substrate can be attributed to the low interface roughness and homogeneous growth conditions throughout the deposition process. Note that the intensities of the ${O_2}^-$ are also periodically modulated by a factor of ~ 2, even though the stoichiometry of all layers is nominally ABO_3. While for the thinnest sample the effect is not as pronounced, the two thicker samples show two maxima in the ${O_2}^-$ signal, one at the upper interfaces and a larger one in the center of the BFO layers, but none at the lower interfaces. This is the first sign that the local ion yields are strongly affected by the electronic configuration of the surrounding material (cf. Ref. H1). BTO and BFO possess inherent spontaneous polarization with different polarization vectors (along $\langle 001 \rangle_t$ and $\langle 111 \rangle_{p.c.}$), which might contribute to other matrix effects. Other

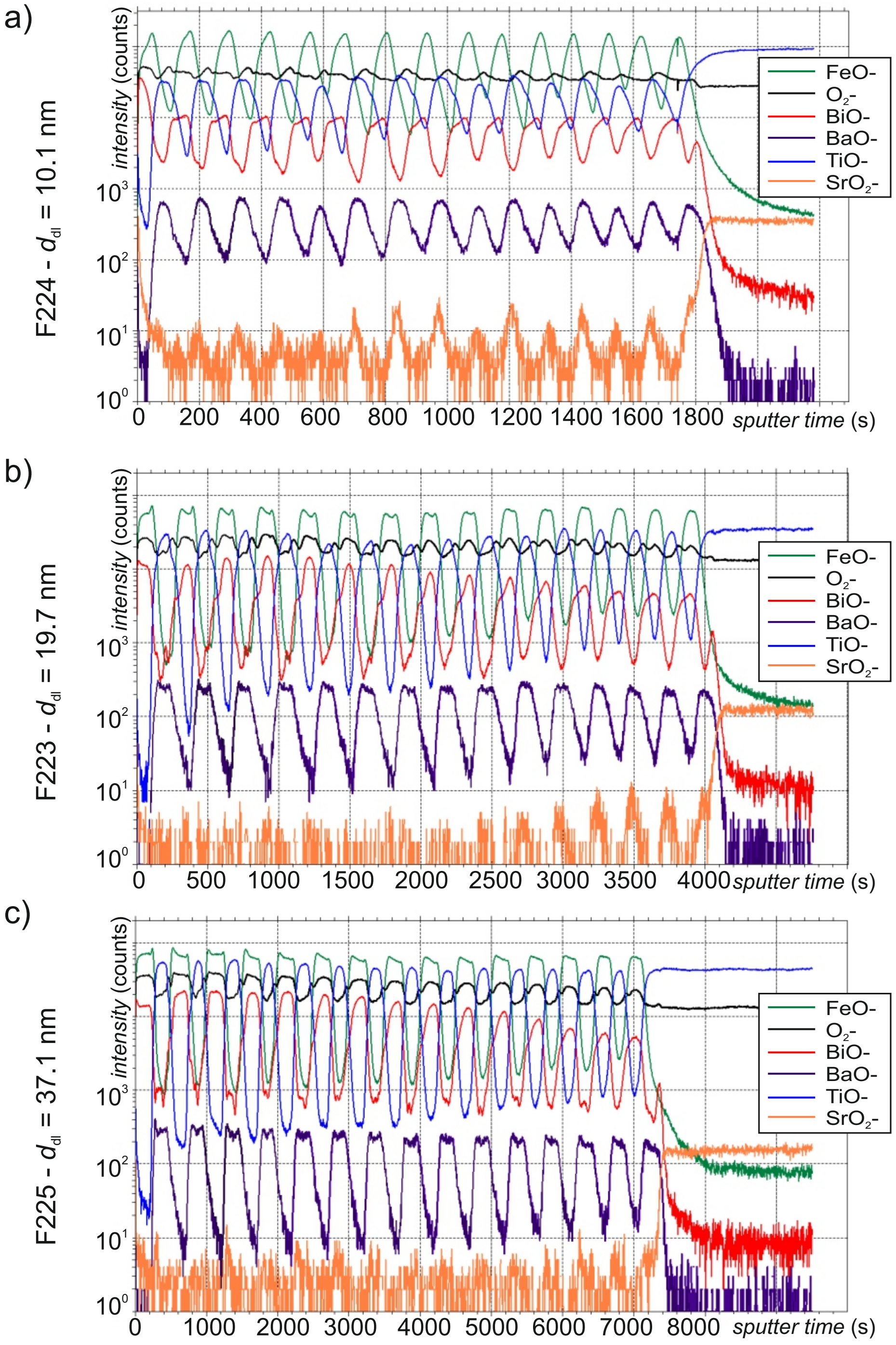

Figure 5.50: ToF-SIMS chemical depth-profiles of 50 µm × 50 µm areas of 15 × [$BaTiO_3$-$BiFeO_3$] multilayers of three different thicknesses as indicated, deposited by eclipse-PLD (samples F224, F223 and F225). Presented are the intensities of the main constituent bi-atomic oxide ion signals of TiO^-, BaO^-, SrO^-, FeO^-, and BiO^-. The profiles use a region of interest masking of the surface area, excluding large structural irregularities, like the one visible in Fig. 5.49.

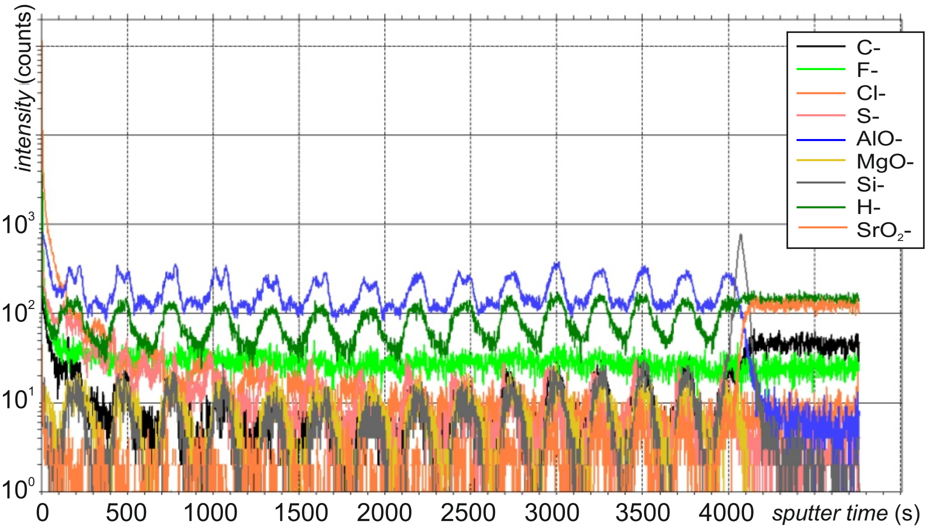

Figure 5.51: ToF-SIMS depth-profile of trace elements for a 15 × $[(BaTiO_3)_{10\ \mathrm{nm}}\text{-}(BiFeO_3)_{10\ \mathrm{nm}}]$ multilayer deposited by eclipse-PLD (sample F223). Presented are the intensities measured for the trace ions C^-, F^-, Cl^-, S^-, AlO^-, MgO^-, Si^-, H^-, and $SrO_2{}^-$.

than that, all profiles are fairly symmetrical and approach a top-hat shape with growing double-layer thickness. A minor asymmetry can be seen in the BiO^- profiles, much as was discussed in Ref. H1, as well as the previously discussed accumulation of Bi near the STO surface. All profile modulations amplitudes progressively increase with the double-layer thickness, indicating that the low squareness of the profiles recorded for sample F224 in Fig. 5.50 b) may be due to either a limited diffusion length in the order of a few nm, or else due to carryover from the previous layers.

In terms of impurities, the highest concentration of C, F, Cl, S, Al, Mg, and H can be found on the sample surface (see Fig. 5.51). Apart from F, all elements are modulated with peak intensities coinciding with the BTO layers. In Ref. H1, we found an enhancement of trace element concentrations near the interfaces, which seems to be absent in this case. Due to the matrix effect in ToF-SIMS, it is not given that these intensity modulations are strictly to be attributed to a higher chemical concentration of impurities in the BTO layers, but might rather be down to the local ionic yields. Interestingly, a sharp spike of Si contamination appears near the STO surface, in the same area as the Bi accumulation.

Overall, the presented depth-profiles reinforce the findings we published in Ref. H1, with one exception. We reported a small amount of inter-diffusion of Ba and Ti into the BFO layers for the sample with only 5 nm thick BFO layers, which had an interface roughness of a few nm. By comparing the measurements from Ref. H1 with the ToF-SIMS depth-profiles of the three eclipse-PLD derived multilayers within the double-layer thickness range from 10 to 37 nm and high quality HR-TEM and STEM-EDX imaging, the BTO inter-diffusion appears to be related to either an interface-roughness related measurement artifact, or higher diffusion rates during conventional PLD, e.g. due to a higher amount of high energetic ion bombardment.

5.4.7 Preliminary Polarized Neutron Reflectometry (PNR) Measurements

Despite the concentrated efforts of the last two decades of the research of magneto-electric multiferroics, thorough in-depth theories of the coupling mechanisms of electric polarization and magnetization are still lacking. This is in part due to the inaccessibility of detailed local states of strain, electronic configuration and magnetic order. In recent years, this gap is being slowly filled through the use of advanced sample characterization techniques such as atomically resolved HR-TEM [30, 125, 217], X-ray magnetic circular dichroism [217] and polarized neutron reflectometry (PNR) [30, 125, 217-219], complemented by density functional theory calculations. In particular PNR has gained much interest in the research of BFO based heterostructures, as this measurement technique allows the formulation of depth-resolved magnetic profiles, even for small magnetic moments such as the small ferromagnetic moment induced *Dzyaloshinski-Moriya*-interaction in canted anti-ferromagnets such as BFO. This requires the measurement of the neutron reflectivity of high quality samples in a magnetic and/or electric field with the distinction of an up or down polarized beam. Using PNR, e.g. *Singh et al.* were able to determine the presence of ferromagnetic order in the BFO sub-layers of ultra-short period BFO-LSMO superlattices [219, 220]. In similar BFO-LSMO heterostructures with a higher BFO thickness, parallel magnetic coupling was found to be limited to a few unit cells near the interface [125]. *Guo et al.* have suggested that this is due to interfacial atomic reconstruction forced by the interaction of the different OOT systems of both materials [125]. *Spurgeon et al.* found a graded magnetic depth profile for LSMO-PZT heterostructures, which they attributed to local strain states and electric screening near the ferromagnetic-ferroelectric interface [30].

In continuation of the fruitful collaboration with *Johanna K. Jochum*, formerly at *KU Leuven*, Belgium, we were recently able to conduct first PNR experiments on BTO-BFO multilayers. The experiments in the framework of proposal no. 15287, initiated by *J. K. Jochum*, were carried out under the highly appreciated technical guidance of *Yury Khaydukov* at *NREX+* [221] at the neutron source facility *FRM-II* in Garching, Germany. One of the challenges when transferring the application of this measurement type to a material system in which any robust ferromagnetic order is absent lies primarily within the sample quality. The overall neutron reflectivity is determined by the nuclear scattering length density, differences in up- and down polarized neutron reflectivity appear as modulations based on the magnetic scattering length density. If the absolute variation of the magnetic moment in a multilayer is very small, as is the case with the canted anti-ferromagnet BFO sandwiched between layers of non-magnetic BTO, observation of deviations between the up- and down-polarized channels is advantaged by the existence of sharp, intense superstructure-*Bragg* peaks [169]. This condition is met for multilayers with extremely homogeneous periodicity and atomically smooth interfaces, which was one of the motivations to optimize the multilayer growth by exploiting the advantages of eclipse-PLD.

Table 5.12: Sample parameters of three 15×BTO-BFO multilayers used for PNR experiments, deposited on NSTO by eclipse-PLD using standard conditions. Double-layer thicknesses d_{dl} were determined from superstructure fringe peaks in XRD 2θ-ω scans, individual BTO and BFO thicknesses were determined by fitting XRR curves.

Sample	U_{laser} (kV)	n_{BTO}	n_{BFO}	d_{dl} (nm)	d_{BTO} (nm)	d_{BFO} (nm)
F244	18.3	625	2300	8.6 ± 1	4.1 ± 0.5	4.3 ± 0.4
F245	18.3	1250	4600	16.3 ± 0.7	9.7 ± 0.5	7.6 ± 0.5
F247	17.9	2500	8000	35.0 ± 0.9	17.8 ± 0.6	14.8 ± 0.7

A series of three 15×BTO-BFO samples was deposited by eclipse-PLD for the use in PNR experiments. Using optimized growth conditions and pulse numbers adapted to the laser operation voltage U_{laser} (kV), the ratio of BTO to BFO was kept at ca. $1:1$, while varying the double-layer thickness d_{dl}. The deposition parameters and resulting double-layer and individual layer thicknesses are tabulated in Table 5.12. By design, these samples were generated in analogy to the sample series used for chemical depth profiling by ToF-SIMS and HR-TEM, discussed in the previous subsection. In order to increase the signal-to-noise intensity, $10\,\mathrm{mm} \times 10\,\mathrm{mm}$ NSTO substrates were used, which coincides with the length scale of sample illumination by the neutron beam at low angles $\leq 1°$. The double-layer thicknesses were chosen, as will be discussed in the following chapter, to encompass multilayers well below, at and above the transition thickness, at which bulk- and interface-driven coupling dominates the magnetoelectric coupling. The assumption is that, in analogy to BFO-LSMO heterostructures [125], the supposed interface-driven magnetoelectric coupling mechanism is expressed by magnetic order restructuring at the interface. In this case, a magnetic scattering length function, used to fit hypothetical differences between spin up and down channels, should show clearly distinguishable features for all three samples. In particular in the case of multilayers with a 1:1 thickness ratio of the individual layers, the strongest variance between the up- and down-polarized signal is expected around the second superstructure *Bragg* peak. In such perfectly symmetrical multilayers, the even numbered *Bragg* peaks are forbidden due to a phase shift by π, and the re-emerging of those peaks hints at an interfacial magnetic order reconstruction [222].

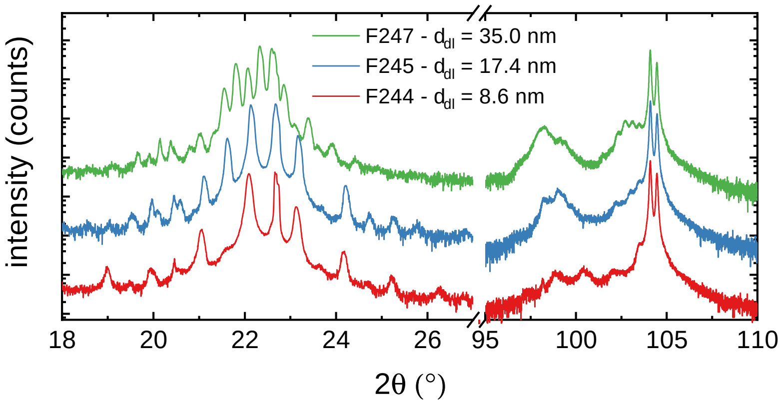

Figure 5.52: XRD 2θ-ω scans measured on three BTO-BFO multilayer samples used for PNR measurements.

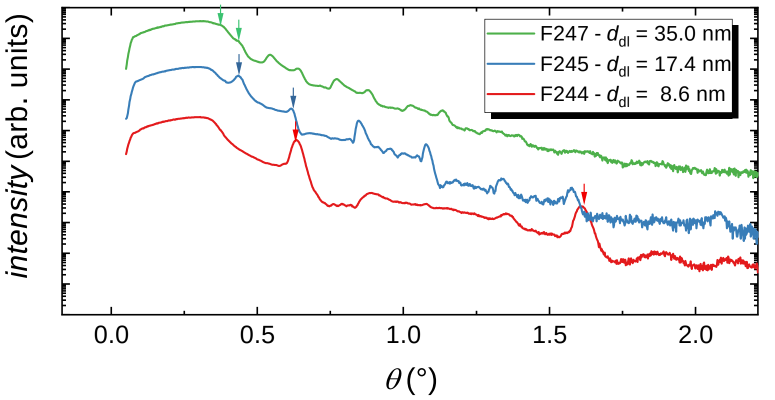

Figure 5.53: XRR curves measured on three BTO-BFO multilayer samples used for PNR measurements. The first two visible superstructure *Bragg* peaks of each measurement curve are indivated by arrows.

In Figures 5.52 and 5.53, 2θ-ω scans and XRR curves of the three samples are displayed. The high epitaxial quality and low interface roughness is indicated by the presence of a number of sharp, distinguished superstructure peaks visible in Fig. 5.52, both at low and high diffraction angles (shown are the areas around the (001) and (004) NSTO peak). The double-layer thicknesses determined from superstructure fringe peaks are 8.6 nm, 17.4 nm and 35.0 nm. In Fig. 5.53, superstructure *Bragg* peaks are clearly visible along with underlying shorter period oscillations indicative of the total film thickness. The individual layer thicknesses resulting from fits of these XRR measurements are listed in Table 5.12.

Two exemplary PNR measurement of the thinnest (F244) and thickest (F247) multilayer sample are presented in Figs. 5.54 and 5.55. The measurements were carried out

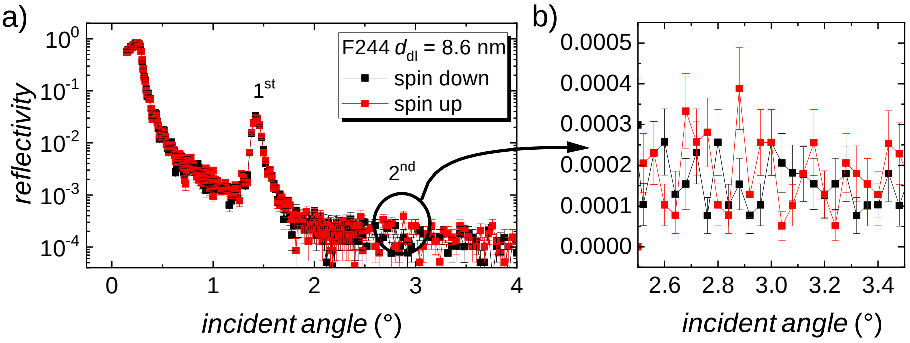

Figure 5.54: Preliminary PNR scan of a 15 × [$(BaTiO_3)_{4.1\ nm}$ - $(BiFeO_3)_{4.3\ nm}$] multilayer deposited by eclipse-PLD (sample F244). A OOP magnetic field of 4.5 kOe and an electric field of 60 kV cm^{-1} (9 kV applied to a capacitive sample holder with a 1.5 mm gap) were applied during the measurement. **(a)** Full scan, **(b)** detail around the second *Bragg* peak. The *black* data points were recorded using the spin down, the *red* using the spin up channel.

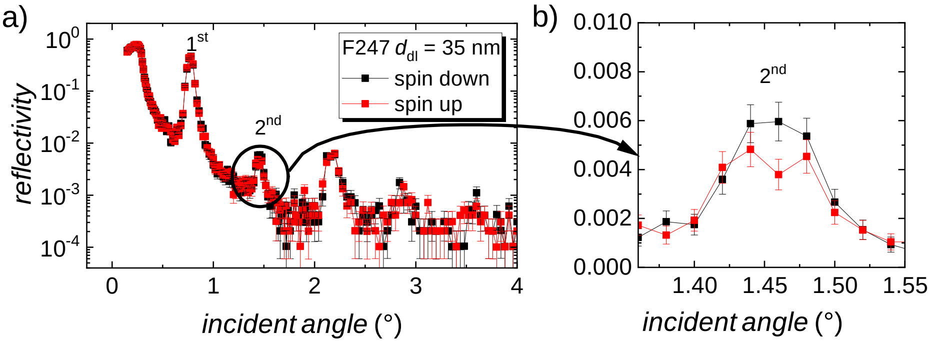

Figure 5.55: Preliminary PNR scan of a 15 × [$(BaTiO_3)_{18\ nm}$ - $(BiFeO_3)_{15\ nm}$] multilayer deposited by eclipse-PLD (sample F247). A OOP magnetic field of 4.5 kOe and an electric field of 60 kV cm^{-1} (9 kV applied to a capacitive sample holder with a 1.5 mm gap) were applied during the measurement. **(a)** Full scan, **(b)** detail around the second *Bragg* peak. The *black* data points were recorded using the spin down, the *red* using the spin up channel.

in a magnetic field of magnetic field of 4.5 kOe, oriented parallel to the sample surface and the neutron beam polarization direction. A capacitive voltage of 9 kV was applied normal to the sample surface, generating an electric field of 60 kV cm^{-1}. During the measurements, the sample chamber was kept at 300 K pumped to below 10^{-2} mbar after flooding with He gas. Note the absence of the second *Bragg* peak in Fig. 5.54. This confirms the highly symmetrical nature of the multilayer structure of sample F244 (cf. Table 5.12). However, the noise level above 2° was in the same order of magnitude as the signal and the signal-to-noise ratio could not be improved significantly by increasing the measurement integration time within reasonable temporal limits. Overall, no difference between the spin up and down channels was observed for this sample. In contrast, for the thickest sample (F247), a non-zero intensity was measured also for even numbered *Bragg* peaks (see Fig. 5.55). This is due to the difference in BTO and BFO thickness for this sample (17.8 nm and 14.8 nm, respectively). A detailed view of the second *Bragg* peak is shown in Fig. 5.55 b). While the second order peak in the spin down channel is symmetrical, in the spin up channel the peak is split into two sub-peaks and slightly lower in total intensity. The intensity difference lies just outside the standard error margin, the absolute peak height ratio is 2 : 3.

These preliminary results are certainly interesting and call for further experiments. In case of the multilayers with the thinnest double-layer thickness, the overall sample thickness should be improved by increasing the number of double-layer repetitions, in order to improve signal-to-noise ratio. In case of the thicker multilayers, it might be desirable to adjust the BTO-BFO ratio in such a manner that the second *Bragg* peak either disappears or is enhanced. One factor that might require an additional workaround is that, given the sample holder geometry, magnetic and electric fields are applied perpendicularly to one another. All of our measurements of the magnetoelectric coupling in BTO-BFO multilayers generally apply a longitudinal, out-of-plane geometry. Contrary to that, the geometry applied here would probe the transverse coupling of magnetic and electric order. Additionally, we know from *Mössbauer* experiments that the preferential magnetic orientation of BTO-BFO multilayers is out-of-plane, while the applied field and spin polarization directionality is in-plane with respect to the sample. Further in-depth analysis of these preliminary PNR measurements and modeling of the layer structure are still in progress at the time of writing this thesis.

5.4.8 Summary

The application of eclipse-PLD to the deposition of BTO-BFO multilayers drastically improved the overall sample quality. A greatly reduced droplet density was achieved, which results in increased breakdown field strengths of up to $5\,\mathrm{MV\,cm^{-1}}$. Consequently, this enabled more thorough insights into the ferroelectric properties of BTO-BFO multilayers. A reduction of interface and surface roughness to within one unit cell persists also for thick (550 nm) multilayers. In the absence of a significant interface roughness, ToF-SIMS and TEM-EDX measurements did not show any intermixing of the sub-layers, in contrast to previous studies [H1]. In the presented preliminary PNR measurements, we showed minor differences in the spin-up and spin-down channel signals under application of an electric field. Further PNR measurements on such high-quality samples are expected the detailed magnetic depth-profile present in BTO-BFO multilayers. The only disadvantage of eclipse-PLD is the strong dependence of the deposition rate of BFO on U_{laser}, i.e the age of the excimer gas mixture. However, after depositing an appropriate number of samples, we are now able to predict the deposition rate based on U_{laser}, which grants an unprecedented level of control over the sub-layer thicknesses in multilayers.

5.5 Enhanced ME Effect in $BaTiO_3$–$BiFeO_3$ Multilayers

In the previous sections, the general properties of epitaxial BTO-BFO multilayers grown on STO substrates were laid clear and contrasted with the properties of individual single-layer. The implications of growth conditions and design choices on the structural and ferroic properties were discussed, highlighting the efficient control of mosaicity, morphology and strain. In pursuit of further mitigation of impeding factors such as high interface roughness, inadvertent presence of droplet particles and low electric breakdown field strength, the advanced PLD-technique of eclipse-PLD was presented as a promising avenue for future investigations. In particular the examination of structural, chemical and magnetic depth-profiles, as well as the systematic evaluation of ferroelectric properties was shown to greatly benefit from this deposition technique. Now, we will ultimately turn to the key property that warrants the intense scrutiny given to the detailed investigation of all aspects of these BTO-BFO multilayers: magnetoelectric coupling. A brief glimpse into this subject was already given in Sec. 5.1.6, in which the key differences between the ME coupling measured on BFO single-layer and BTO-BFO multilayer samples were introduced.

5.5.1 Review of Previous Investigations

Before approaching the topic of ME coupling measured for samples created in the framework of this thesis, let us revisit the results of the previous studies pertaining to the ME coupling in BTO-BFO multilayers conducted by our group and our collaborators at the *KU Leuven*, prior to the framework of this thesis. A brief overview over this collaborative work was already given in Sec. 3.5.4. In this following section, we will discuss the phenomenological side of these past investigations. Key factors that were used to characterize the ME coupling in these films were the dependence on the DC magnetic bias field and measurement temperature T, as well as the room temperature α_{ME} base value measured in $0\,\mathrm{T}$, as determined through AC longitudinal voltage measurements, as described in Sec. 4.7. All measurements used a $10\,\mathrm{Oe}$ AC magnetic field.

The first experiments into BTO-BFO heterostructures compared the ME coupling in BTO and BFO single-layer films with that in variable ratio composite films and multilayers deposited at $0.01\,\mathrm{mbar}$ and $0.25\,\mathrm{mbar}$ [11]. In both composite and multilayer films, the magnetization was enhanced with respect to BFO single-layer reference films. The α_{ME} base value was found to be enhanced relative to the $3\,\mathrm{V\,cm^{-1}\,Oe^{-1}}$ published for BFO single-layer films [9], reaching $20.7\,\mathrm{V\,cm^{-1}\,Oe^{-1}}$ for the $67\,\%$ BTO-content composite film grown at 0.25 mbar and $8.8\,\mathrm{V\,cm^{-1}\,Oe^{-1}}$ for the 15×BTO-BFO multilayer sample grown at 0.01 mbar with a d_{dl}-value of 29.3 nm [11]. In this study, the characteristic magnetic field dependencies of single- and multilayer films was first reported. The single-layer samples, and in this case the composite films, show a slight increase up to a maximum around 0.5 to 2 T, with a subsequent decrease below the base value, similar to the behavior observed in bulk BFO-samples [121]. Contrary to this, the multilayer films show a slight increase from the base value and a saturation above 3 T, within the measurement range of 0 to 6 T. These trends were confirmed for all single-layer BFO, composite and multilayer samples investigated since [147,148,150-152, H1, H3-H5], as mentioned previously in Sec. 5.1.6.

Further investigations into the correlation of oxygen pressure $p_{\mathrm{O_2}}$ during deposition and α_{ME} produced an enhanced α_{ME}-value of $49.7\,\mathrm{V\,cm^{-1}\,Oe^{-1}}$ for a 0.25 mbar multilayer sample with $d_{\mathrm{dl}} = 14\,\mathrm{nm}$. This is contrasted by the $13.4\,\mathrm{V\,cm^{-1}\,Oe^{-1}}$ measured for a 0.01 mbar multilayer sample with $d_{\mathrm{dl}} = 38\,\mathrm{nm}$ [147]. Opposing trends of T-dependency, falling and rising with increasing temperature for the low- and high-$p_{\mathrm{O_2}}$ samples, respectively, led to the conclusion of varying dominance of competing coupling mechanisms. Increased oxygen octahedral tilt (OOT) [148], micro-srtain and oxygen deficiency [147] were found in the low-$p_{\mathrm{O_2}}$ sample and were correlated with the difference in T-dependency and overall α_{ME}-value. The α_{ME} base values published in Ref. 148 for a sample-series of BTO-BFO multilayers deposited in a range of 0.01 to 0.25 mbar are depicted in Fig. 5.57 a). These samples were deposited using identical pulse numbers for all pressures, leading to vastly different d_{dl}-values, as the lower x-axis in Fig. 5.57 a) shows. Due to overlap of the α_{ME} data points displayed versus the $p_{\mathrm{O_2}}$- and d_{dl}-values, it is difficult to separate any correlation of α_{ME} with either individual parameter.

An analysis of the ME coupling of multilayers with constant BTO thickness and varying BFO thickness was conducted by *Jochum et al.* [152]. The α_{ME} base value increased from 11 to $56\,\mathrm{V\,cm^{-1}\,Oe^{-1}}$ as the BFO thickness was decreased from nominally 50 to 5 nm. The magnetic bias field dependence remained unchanged, whereas the T-dependency changed from a single-layer-like monotonically decreasing with rising temperature for the highest BFO-thickness, via curves with a minimum for intermediate thicknesses, to a monotonically increasing behavior for the lowest BFO-thickness. This indicates a change in the dominant ME coupling mechanism from the mechanism intrinsic to BFO thin films to an interface-driven or strain-mediated effect. As mentioned in Sec. 5.3, the lowering of the BFO-thickness was accompanied by an increase in the skewness of the *Mössbauer* spectroscopy hyperfine field distribution, indicative of increasing perpendicular magnetic anisotropy. Likewise, *Lazenka et al.* found that

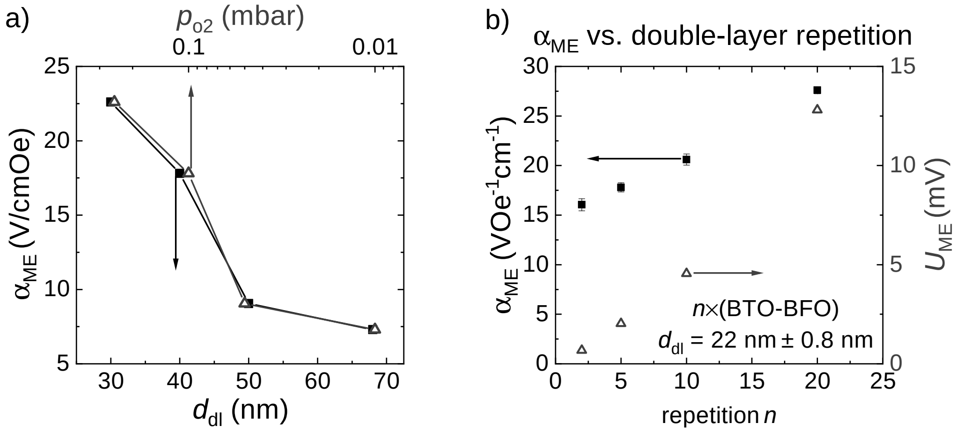

Figure 5.56: ME coupling coefficient α_{ME} measured at 300 K in 0 T for BTO-BFO multilayers **(a)** deposited in the p_{O_2}-range of 0.01 to 0.25 mbar (data adapted from Ref. 148 and **(b)** with double-layer repetition n in the range of 2 to 20 (data adapted from Ref. 151). Note the doubled x-axis and associated color-coded data points in a), the lower axis (black) denoting the d_{dl}-value, the upper axis (red) denoting the p_{O_2}-value during deposition. Likewise, in b), the left (black) y-axis refers to the normalized α_{ME}-value, while the right y-axis (red) gives the absolute, raw U_{ME} voltage values.

the α_{ME} base value for BTO-BFO multilayers with a d_{dl} of 22.0 ± 0.8 nm increases from 16 to 28 V cm^{-1} Oe^{-1}, as the number of double-layers increases from n =2 to 20 [151]. The α_{ME} data points from this study are presented in Fig. 5.56 b), along with the unadjusted U_{ME} ME voltage values. As the graph shows, the α_{ME}-values do not approach 0 V cm^{-1} Oe^{-1} for small n, but a value more than twice as large as the value of 3 V cm^{-1} Oe^{-1} reported for BFO single-layers [9]. This serves as another indicator of an interface effect at the origin of the enhanced ME coupling in BTO-BFO multilayers. They also showed that the magnetic anisotropy, which is characteristic of BTO-BFO multilayers, but not of BFO single-layers [150], also increases with n. This dependency of α_{ME} on the BFO layer thickness and the amount of double-layers in a multilayer stack raised the question, whether the trend observed for the samples grown at various oxygen pressures might instead be connected to the changing double-layer thickness. This knowledge-base served as the starting point for the experiments conducted throughout the framework of this thesis. The design of the samples presented in the following was constructed to separate the influence of oxygen pressure, individual and double-layer thickness on the magnitude of the ME coupling coefficient α_{ME}.

5.5.2 Samples

Over the course of this thesis, we were able to measure the ME coupling coefficients of five multilayer sample series, along with respective single-layer reference samples. Table 5.13 gives an overview of these samples, listing the oxygen pressure during growth, double-layer thicknesses, BTO-BFO thickness ratio and α_{ME} base value at 300 K and 0 T. All samples were previously presented in Sec. 5.2 and Sec. 5.3, where we focused on the structural and ferroic properties of these samples in relation to the respective altered parameters.

The purpose of the single-layer samples was to establish a baseline of the inherit ME coupling strength, as well as magnetic field and temperature dependence, in BTO-, BFO- and BGFO-films with comparable thicknesses to the average multilayer investigated in this thesis. The p_{O_2}-series was kept at a relatively constant double-layer thickness, in contrast to the films investigated in Refs. 11 and 148, to reduce any possible influence of the double-layer thickness on the α_{ME}-coefficient. The two d_{BFO}- and d_{BGFO}-thickness series were constructed in analogy to the study conducted by *Jochum et al.* [152], which explicitly varied the magnetic phase in order to explore to investigate correlated magnetic and magnetoelectric changes in the multilayer structures. As these sample series combined a simultaneous alteration of both BTO-BFO ratio and d_{dl}, the two final sample series vary these two parameters individually, while keeping the other constant.

At this point, let us briefly revisit the core changes introduced in the multilayer properties by the various parameter changes. With decreasing p_{O_2}, the interface quality and mosaicity of the deposited multilayers drastically decreases in the pressure range from 0.25 mbar down to 0.01 mbar. The sample deposited at 0.10 mbar showed the largest IP lattice parameter and the lowest saturation magnetization. The variation of the BTO-BFO ratio causes a systematic IP and OOP lattice parameter tuning, irrespective of the overall d_{dl}, which does not affect the lattice parameters. The BTO-BFO ratio also affects the multilayers' mosaicity, with the lowest FWHM values measured around $d_{\mathrm{BTO}}/d_{\mathrm{dl}} = 0.6$ to 0.8, depending on the sample series. Both the reduction of the $d_{\mathrm{BTO}}/d_{\mathrm{dl}}$ quotient and the overall d_{dl} were found to increase the remanent magnetization in BTO-BFO multilayer samples. Additionally, we could show an increased OOP tilt of the magnetization axis with reduction of the BGFO thickness.
The results obtained for the d_{BGFO}-series have been published in Ref. H3 and the results obtained for the p_{O_2}-, ratio- and d_{dl}-series have been published in Ref. H4 .

Table 5.13: Deposition parameters, layer thicknesses and ME coefficients of the samples of the reference single-layers, the p_{O_2}-, d_{BGFO}-, d_{BFO}-, ratio, andd_{dl}-series. The multilayer samples with sample IDs beginning with G consist of 15 double-layers deposited on STO, those with sample IDs beginning with F consist of 16 double-layers. $*$: BGFO; †: single-layer thickness.

sample ID	p_{O_2} (mbar)	d_{dl} (nm)	$d_{\mathrm{BTO}}/d_{\mathrm{dl}}$	$\alpha_{\mathrm{ME\ (300K,\ 0T)}}$ $\mathrm{V\,cm^{-1}\,Oe^{-1}}$
single-layer reference samples				
G5993	0.25	$240 \pm 8^{\dagger}$	1	0.01
G6050	0.25	$360 \pm 15^{\dagger}$	0	4.2
G6051*	0.25	$360 \pm 15^{\dagger}$	0	6.4
p_{O_2}-series				
F029	0.01	19.6 ± 0.3	n.a.	110.1
F030	0.05	22.5 ± 1.0	0.50	88.9
F036	0.10	20.0 ± 0.7	n.a.	71.9
F026	0.25	20.1 ± 0.2	0.48	106.4
d_{BFO}-series				
G6041	0.25	69.0 ± 4.0	0.37	6.8
G6043	0.25	44.0 ± 3.0	0.63	13.2
G6044	0.25	35.7 ± 0.8	0.78	21.3
G6045	0.25	30.0 ± 2.0	0.88	34.2
d_{BGFO}-series				
G5989	0.25	63.0 ± 3.0	0.30	6.1
G5990	0.25	35 ± 1.0	0.49	25.5
G5991	0.25	26 ± 0.4	0.67	19.2
G5992	0.25	23 ± 0.3	0.72	50.8
ratio-series				
F022	0.25	19.4 ± 0.6	0.81	114.5
F024	0.25	19.6 ± 0.4	0.69	111.7
F026	0.25	20.1 ± 0.1	0.48	106.4
F025	0.25	19.4 ± 0.6	0.31	113.3
F023	0.25	20.0 ± 1.0	0.11	111.4
d_{dl}-series				
F032	0.25	4.6 ± 0.2	0.54	480.4
F033	0.25	9.6 ± 0.2	0.51	241.1
F034	0.25	14.3 ± 0.2	0.50	143.1
F035	0.25	17.7 ± 0.3	0.50	132.0

5.5.3 Measurements of the ME Coupling Effect

The most pressing question was certainly that of the precise influence of the oxygen pressure on the ME coupling in BTO-BFO multilayers. The samples discussed in Refs. 11 and 148, as presented in Fig. 5.56 a), showed a monotonous increase of α_{ME} with the correlated increase of p_{O_2} and decrease of d_{dl}. The α_{ME}-coefficients measured for the new sample series of relatively constant $20.6 \pm 1.1\,\mathrm{nm}$ d_{dl} are presented in Fig. 5.57. The previously reported trend is not repeated here, after a dip from 106 to $72\,\mathrm{V\,cm^{-1}\,Oe^{-1}}$ is measured going from 0.25 to 0.10 mbar, increasing again from 89 to $110\,\mathrm{V\,cm^{-1}\,Oe^{-1}}$ as the deposition pressure is further decreased from 0.05 to 0.01 mbar, as Fig. 5.57 a) shows. This represents no correlation with the steady increase in mosaicity and interface roughness with decreasing p_{O_2}, in contrast to the conclusions of Refs. 11 and 148, which pointed out the correlation of the decrease of α_{ME} with an increase of micro-strain and oxygen vacancies for samples deposited at lower oxygen pressures. The overall strain state of the multilayer structure might nevertheless play a role in determining strength of ME coupling interaction, as the negative correlation of the average IP lattice parameter in Fig. 5.57 b) suggests. There also exists a positive correlation between the remanent magnetization and the α_{ME} base value, also depicted in Fig. 5.57 b). Neither parameter has a linear relationship with the oxygen pressure during the deposition for this sample series, which makes this existing correlation all the more striking.

There are no differences among the four p_{O_2}-samples in terms of temperature dependence, as all of them show a monotonous incline with rising T, as Fig. 5.57 c) shows. This suggests that the same inherent coupling mechanism is at work in all four samples, irrespective of the deposition pressure. Overall, the previously reported dependency of α_{ME} on p_{O_2} could not be reproduced, if d_{dl} is kept relatively constant. In fact, the α_{ME} base values for the 0.01 mbar and 0.25 mbar samples are almost identical, despite vast structural and morphological differences between the two samples. To re-iterate: the FWHM of the main superstructure peak, indicative of the in-plane mosaicity, of the 0.01 mbar is more than one order larger than that of the 0.25 mbar sample and while the high-p_{O_2} sample has an interface roughness in the unit cell scale, the low-p_{O_2} sample shows variations in the scale of the individual layer thickness.

In Figs. 5.58 and 5.59, the dependence of α_{ME} on the magnetic bias field, in the range of 0 to 6 T at 300 K, as well as the dependence on the measurement temperature, in the range from 10 to 300 K in 0 T bias field, are presented for the d_{BFO}- and d_{BGFO}-series, respectively. Included in these graphs are the α_{ME}-curves for the BFO and BGFO single-layers. Not shown are the measurement results for the BTO single-layer film, which shows a static signal equal to $0.01\,\mathrm{V\,cm^{-1}\,Oe^{-1}}$ across all fields and

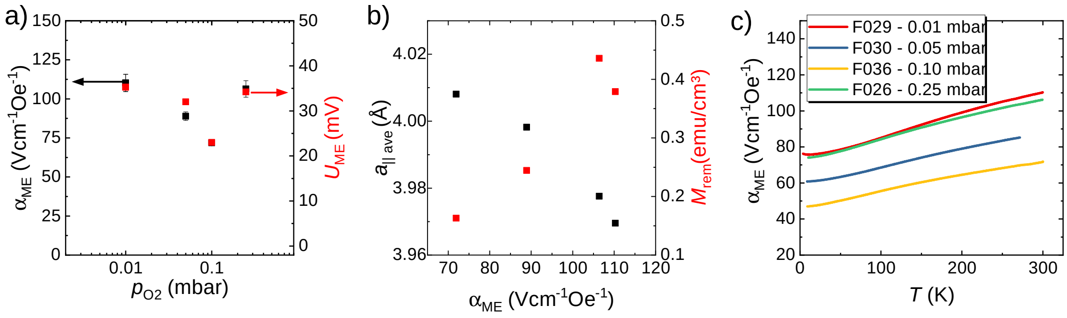

Figure 5.57: (a) α_{ME} and U_{ME} at measured 300 K in 0 T bias field and **(b)** $a_{\|\mathrm{ave}}$ and M_{rem} compared to the respective α_{ME}-values and **(c)** T-dependent α_{ME} for the samples of the p_{O_2} -series. Graphs a) and c) adapted from Ref. H4.

temperatures. This is the noise floor if the same measurement settings (sensitivity, gain, etc.) as for the multilayer samples are used. Both the BFO and BGFO single-layer film show a small peak around 0.5 to 1.0 T with a subsequent decline of α_{ME}, mimicking the behavior of both bulk BFO [81, 121] and BFO thin films [9, 150]. Both α_{ME}-values are increased by three orders of magnitude relative to values reported for bulk BFO [11, 81, 121]. With α_{ME} base values of 4.2 and 6.4 V cm^{-1} Oe^{-1} for the BFO and BGFO single-layers, respectively, these samples outperform other BFO thin films investigated prior to this thesis. To cite just two, the original publication by *Wang et al.* quotes a maximum value of 3 V cm^{-1} Oe^{-1} for a 70 nm BFO thin film on STO [9] and the first BFO single-layer α_{ME}-coefficient reported by *Lazenka et al.* was measured to be 1.8 V cm^{-1} Oe^{-1} for a 500 nm BFO film on STO [150]. The T-dependence for both films is monotonously falling as T is increased from 10 to 300 K.

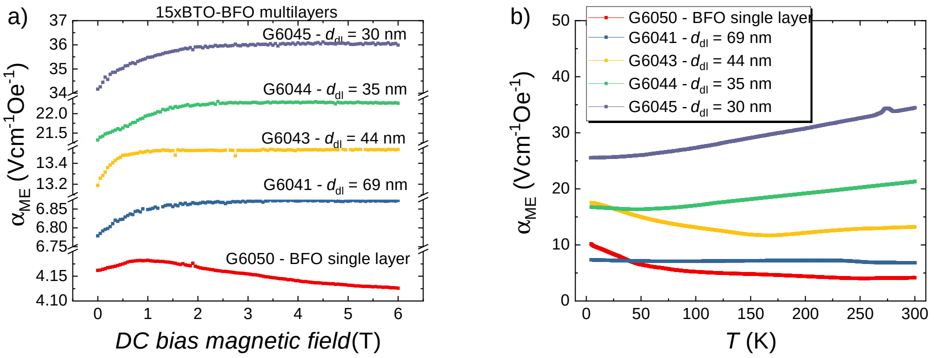

Figure 5.58: (a) DC bias magnetic field dependent and **(b)** temperature dependent α_{ME}-coefficient measurements for the samples of the d_{BFO}-thickness series.

The samples of the d_{BFO}-series genuinely reproduce the results for α_{ME} obtained by *Jochum et al.* for a similar sample series [152]. I.e. all multilayer samples show a saturating behavior with respect to the bias magnetic field and a transition from the single-layer-like decrease of α_{ME} with T to a monotonous increasing behavior as

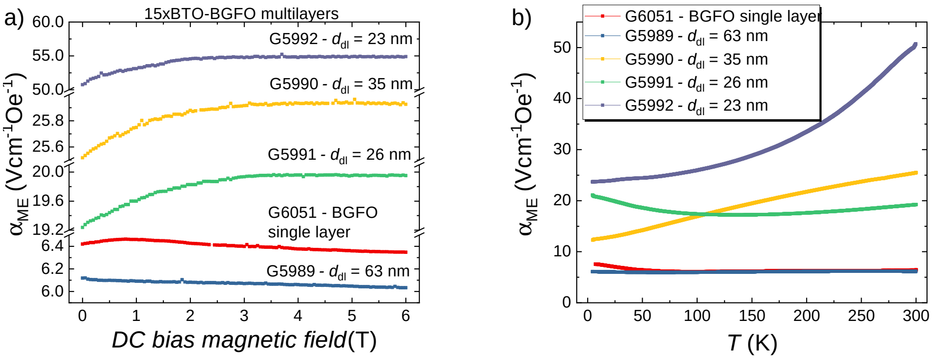

Figure 5.59: **(a)** DC bias magnetic field dependent and **(b)** temperature dependent α_{ME}-coefficient measurements for the samples of the d_{BGFO}-thickness series. Graphs adapted from Ref. H3.

the BFO thickness is decreased, as Figs. 5.58 a) and b), respectively, show. The α_{ME} base value increases from 6.8 to 34.2 V cm^{-1} Oe^{-1} as the BFO thickness decreases from approximately 44 6nm. For the d_{BGFO}-series, this clear trend is not present as clearly. While most multilayers show the same saturating behavior with respect to the bias magnetic field, the thickest multilayer with $d_{\mathrm{dl}} = 63$ nm closely mimics the behavior of the single-layer BGFO sample with a slightly lowered α_{ME} base value of 6.1 V cm^{-1} Oe^{-1}. The changes in T-dependency and α_{ME} base value generally adhere to the same trend as for the d_{BFO}-series, as can be observed in Figs. 5.59 a) and b). The exception here is the $d_{\mathrm{dl}} = 26$ nm sample, which at 10 K shows a α_{ME} -value between that of the 35 nm and 23 nm sample, but drops below the value obtained for the 35 nm sample, as T is increased to 300 K.This oddity also persisted with multiple measurement repetitions and remains inexplicable, as it contradicts the trends observed for the remaining sample series. More consistently, for both the d_{BFO}- and d_{BGFO}-series, the difference between the 0 T and 6 T α_{ME}-value increases monotonically with decreasing BFO (BGFO) thickness, from 1.3 to 5.5 V cm^{-1} Oe^{-1} for the d_{BFO}-series and from -1.3 to 8.2 V cm^{-1} Oe^{-1} for the d_{BGFO}-series. Additionally, among both sample series, the highest α_{ME}-values of 34.2 V cm^{-1} Oe^{-1} and 50.8 V cm^{-1} Oe^{-1} were measured for the samples with the lowest BFO and BGFO thicknesses, respectively.

What remains ambiguous up to this point is whether the increase in the α_{ME} base value and associated changes in the T-dependency are due to the decrease of the BFO thickness, the double-layer thickness, or simply the thickness ratio between BTO and BFO. With the ratio- and d_{dl} -series, the $d_{\mathrm{BTO}}/d_{\mathrm{dl}}$-ratio range from 0.11 to 0.81 is covered, as well as the associated thickness ranges of BTO from 2.1 to 15.7 nm and BFO from 2.6 to 17.5 nm and the d_{dl}-range from 4.6 to 20.0 nm. The α_{ME} base values, along with the absolute as-measured ME voltage values, and temperature dependent α_{ME}-curves are presented in Fig. 5.60. For reference, the α_{ME}-values for the $d_{\mathrm{BTO}}/d_{\mathrm{dl}}$

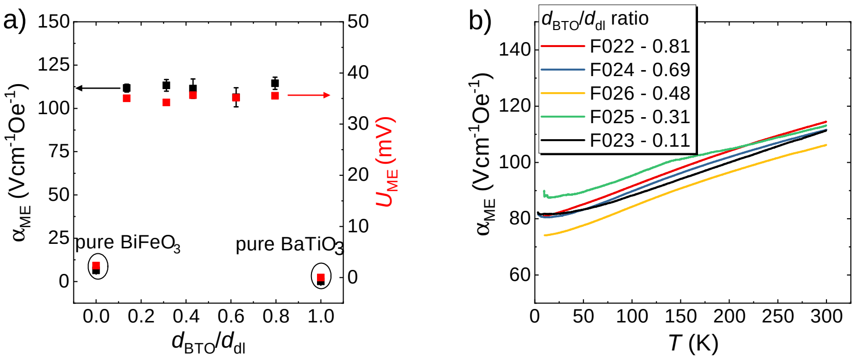

Figure 5.60: **(a)** α_{ME} and U_{ME} measured at 300 K in 0 T bias field and **(b)** $\alpha_{\mathrm{ME}}(T)$ for the samples of the ratio series. Graphs adapted from Ref. H4.

extremes 0 and 1, i.e. single-layers of BFO and BTO, are depicted in Fig. 5.60 a), as well. Over the entire composition range, the α_{ME}-value remains fairly stable at $111 \pm 3\,\mathrm{V\,cm^{-1}\,Oe^{-1}}$. The variation is in the same order of magnitude as the standard deviation of the double-layer thickness of 19.7 ± 0.3 nm used to normalize the U_{ME}-values. Likewise, the T-dependency of all layers shows the same quasi-linear increase from around 80 to $110\,\mathrm{V\,cm^{-1}\,Oe^{-1}}$ in the range from 10 to 300 K, as depicted in Fig. 5.60 b). This invariability with respect to the BTO-BFO thickness ratio is a profound contrast to the non-linear variation of the multilayers' $\boldsymbol{M}_{\mathbf{sat}}$-values and the linear decrease of $\boldsymbol{M}_{\mathbf{rem}}$ with increasing BFO content (cf. Fig. 5.38). It also suggests that the changes in α_{ME} observed for the d_{BFO}- and d_{BGFO}-series, which also cover the composition-range from 0.3 to 0.88, are in response to one of the other parameter-changes introduced with the BFO and BGFO thickness variation. That is, either the overall double-layer thickness, the BFO and BGFO layer thickness itself, or the lattice-parameter tuning associated with the ratio-variation are the source of the enhanced ME coupling. The latter can almost certainly be excluded, as the same lattice parameter tuning also occurs for the constant-d_{dl} ratio series presented in Fig. 5.60. Likewise, the individual layer thicknesses of BTO and BFO seem to have no significant impact. And just as was observed for the p_{O_2}-series, there is no correlation between the elevated FWHM of the multilayer peak at the extremes of the $d_{\mathrm{BTO}}/d_{\mathrm{dl}}$-range with the strength of ME coupling.

This leaves only the overall double-layer thickness as the potential fundamental determining factor for the enhancement of α_{ME} in BTO-BFO multilayers. The multilayer samples of the d_{dl}-series presented here possess the lowest double-layer thicknesses of all the BTO-BFO multilayers investigated by our group, so far. The samples range in d_{dl} from 4.6 nm - only 5 to 6 monolayers per individual layer - to 20.1 nm, while maintaining a constant $d_{\mathrm{BTO}}/d_{\mathrm{dl}}$-value of 0.51 ± 0.02. The α_{ME}- and U_{ME}-values measured at 300 K in 0 T magnetic bias field are presented in Fig. 5.61 a), the $\alpha_{\mathrm{ME}}(T)$-curves

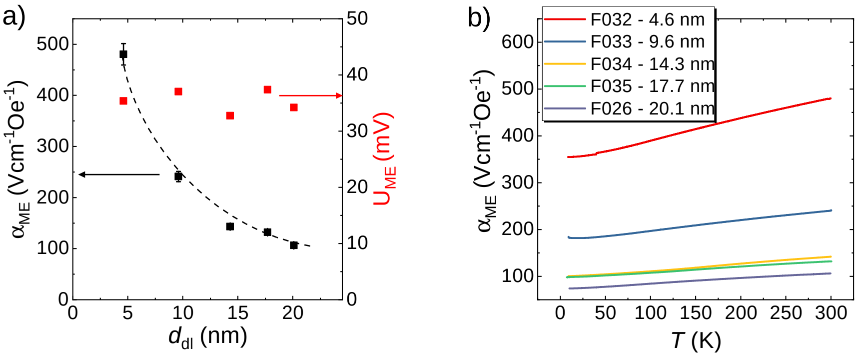

Figure 5.61: **(a)** α_{ME} and U_{ME} at measured 300 K in 0 T bias field and **(b)** $\alpha_{ME}(T)$ for the samples of the d_{dl}-series. Graphs adapted from Ref. H4.

are shown in Fig. 5.61 b). All α_{ME}-values increase quasi-linearly by $26 \pm 3\,\%$ as the temperature is increased from 10 to 300 K, indicating no change in the inherent coupling mechanism. In contrast, for the d_{BGFO}- and d_{BFO}-series discussed above and in Ref. 152, profound changes in the temperature dependence were found. However, these sample series included only multilayers with double-layer thicknesses down to 30 nm, 15 nm and 23 nm for the d_{BFO}-series from this work, from Ref. 152 and the d_{BGFO}-series, respectively. The maximum α_{ME} base values measured for these three thinnest multilayers were, in the same order, 34.2 V cm^{-1} Oe^{-1}, 55.5 V cm^{-1} Oe^{-1} and 50.8 V cm^{-1} Oe^{-1}.

As shown in Fig. 5.61 a), all samples of the d_{dl}-series showed roughly the same U_{ME}-values, with the result of an increase of α_{ME} scaling approximately with $1/d_{dl}$. Consequently, a new record value of 480.4 V cm^{-1} Oe^{-1} was measured for the thinnest ($d_{dl} = 4.6$ nm) multilayer, two orders of magnitude larger than the values reported for BFO-multilayers [9,11,150]. Even the thickest 20.1 nm d_{dl} sample reaches a α_{ME}-value of 106.2 V cm^{-1} Oe^{-1}, roughly twice the value previously reported for the thinnest samples of the d_{BFO}- and d_{BGFO}-series. It has to be noted at this point that the d_{BFO}- and d_{BGFO}-series were deposited in the older PLD-chamber G, while the samples of the d_{dl}-series were deposited in the newer chamber F. And while the deposition conditions were re-created closely, due to the transition from one laser-system, lens and chamber to another, minor changes were inevitably introduced. E.g. the actual extension of the plasma plume was slightly reduced in chamber F, leading to a reduction in bombardment damage. Furthermore, the use of a newer, slightly more dense, over-stoichiometric BFO target could also have contributed to the further enhancement of the α_{ME}-value.

5.5.4 Summary and Discussion

With a maximum of 480.4 V cm^{-1} Oe^{-1} measured for the thinnest sample with a d_{dl} of 4.6 nm, we have realized the highest α_{ME}-value for BTO-BFO multilayers to date. This off-resonance value ranges in the same order of magnitude as the largest values at-resonance reported for laminated composites like langanate-Metglas [223] or AlN-(Fe$_{90}$Co$_{10}$)$_{78}$Si$_{12}$B$_{10}$ [224]. The presented ME coupling measurements demonstrate conflicting correlations between the α_{ME}-coefficient and a number of sample parameters. The previously reported dependence of α_{ME} on p_{O_2} during deposition disappeared, when the double-layer thickness was kept constant. The minor variations of α_{ME} with p_{O_2} can be correlated with the average in-plane lattice parameter of the multilayer structure and the remanent magnetization at 300 K. However, neither of these correlations persists for the explicit variation of the BTO-BFO ratio under conservation of d_{dl}, which affects both parameters, but not the α_{ME}-value. Lowering the BFO-thickness from around 50 to 5 nm while maintaining a constant BTO-thickness leads to a coupled increase of the α_{ME} base value and transformation of the temperature dependence from decreasing to increasing with rising temperature. For a large BFO thickness, the temperature and - in case of the thickest sample of the d_{BGFO}-series - the bias magnetic field dependence resemble the behavior and strength of the ME coupling measured for BFO single-layer films. All multilayer samples deposited in chamber *F*, which had a maximum d_{dl} of 22.5 nm, showed the same monotonically increasing temperature dependence and higher α_{ME} base values than all previously investigated films.

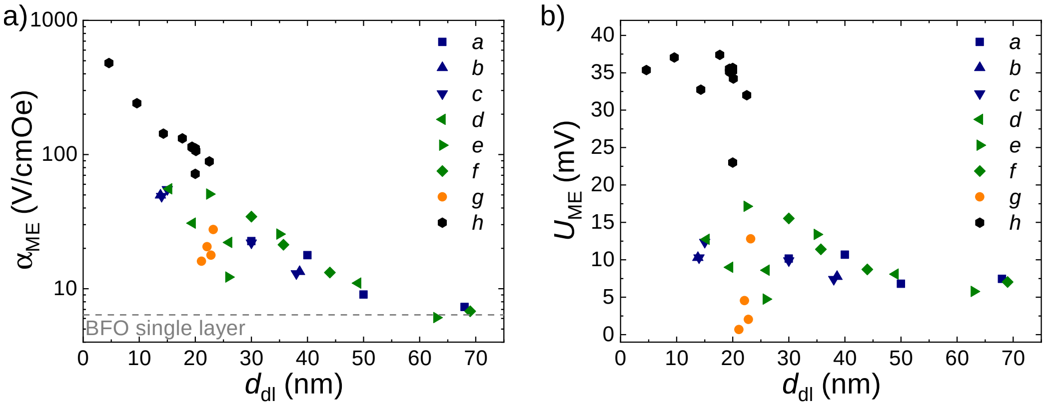

Figure 5.62: Overview of the **(a)** α_{ME}-coefficients and **(b)** U_{ME}-values of BTO-BFO multilayers measured at 300 K in 0 T as reported in Refs. *a*) 148, *b*) 149, *c*) H1, *d*) 152 , *e*) H3, *f*) this work, *g*) 151, and *h*) H4. *Blue* data points: samples deposited at various oxygen pressures with invariant pulse counts; *green* data points: samples deposited with variable BFO- and fixed BTO-thickness; *orange* data points: samples deposited with fixed double-layer thickness repeated 2-20 times; *black* data points: samples discussed in Sec. 5.5. Graph adapted from Ref. H4.

The most profound impact on the extent of α_{ME} at 300 K in 0 T was shown to be the double-layer thickness. Fig. 5.62 re-contextualizes the α_{ME}-coefficients with respect to d_{dl} for the entirety of BTO-BFO multilayer samples investigated by this group up until the publication of this thesis [147-149, 151, 182, H1, H3, H4]. Note the logarithmic scaling of the α_{ME} y-axis in Fig. 5.62 a). As the double-layer thickness decreases, α_{ME} increases for all sample series. Some individual samples fall behind, but the graph suggests a maximum coupling coefficient in dependence of d_{dl}, given an optimized sample quality. As the overlap of *blue* and *green* data points ($p_{\mathrm{O_2}}$-series and d_{BFO}-series, respectively) shows, the variation of α_{ME} with $p_{\mathrm{O_2}}$, previously reported in Refs. 11 and 147, can readily explained by the differences in d_{dl}. The most recent samples, represented by *black* data points, reach the largest α_{ME}-values measured for BTO-BFO multilayers so far. As the U_{ME}-values in Fig. 5.62 b) show, the increase of α_{ME} with d_{dl} has two general regions: above ~20 nm, U_{ME} increases, but saturates below this d_{dl}-value. These two regions are also characterized by the slow alteration of the temperature dependency with d_{dl} above ~20 nm, followed by uniformly monotonically rising temperature dependency for films below 20 nm d_{dl}.

These overall trends related to the double-layer thickness d_{dl} , in combination with with the dependence on the double-layer repetition n [151] (see *orange* data points in Fig. 5.62), highly suggest an interface-driven origin of the enhanced ME coupling in BTO-BFO multilayers. A coexistence with the conventional ME coupling inherit to BFO single-layer films is likely, with a changing dominant contribution depending on the d_{dl}-value. This is supported by the shift in T-dependence [152].

Pinpointing the exact underlying physical phenomenon that mediates this enhanced, likely interface-driven ME coupling is, however, far from trivial. The coexistence of multiple ferroelecric, magnetic and other ferroic order parameters within multiferroic thin films alone is the topic of wide ranging discussions. In laminated or epitaxial thin film heterostructures, discontinuity-related phenomena arise at the interfaces, additionally. The most commonly cited coupling mechanism in artificial multiferroic heterostructures is generally the, more or less macroscopic, strain-coupling of a piezoelectric and a magnetostrictive phase [5, 10, 27, 225, 226]. When considering lower-scale epitaxial heterostructures, several additional interface-driven phenomena need to be considered. In particular in the case of perovskite oxide heterostructures, various oxygen octahedral tilt (OOT) systems, which are deeply entwined with the nano-scale ferroic order in these materials, have to be consolidated with one another the interfaces [187, 227]. In connection with the discontinuities arising in the electronic configurations at the interfaces, novel ME-coupling mechanisms driven by charge-ordering [34] and orbital-reconstruction [33, 34] were recently discovered.

In previous publications, we have hypothesized that strain-coupling plays a central role in the enhanced ME coupling measured in BTO-BFO multilayers [149, 152]. The strongest argument for strain-mediation lies within the rising α_{ME}-value with rising temperature for low-d_{dl} multilayer samples. The temperature dependence of both the magnetostrictive and piezoelectric coefficients, which influence the strain-mediated ME coupling as a product property, for perovskite ferroics increases with rising temperature, as literature confirms for materials like PZT [228] and bulk BTO-BFO composites [229]. However, theoretical calculations [26, 27] predict a strong dependence of the strength of ME coupling on the composition of strain-mediated heterostructures, which has also been confirmed experimentally [5, 10, 225]. Such an effect is clearly absent in BTO-BFO multilayers, as both our experiments on BFO-thickness variation [152, H3] and constant-d_{dl} ratio-variation [H4] show. Furthermore, most strain-mediated heterostructures reported in literature rather show a decline of α_{ME} with rising temperature [29, 230], though various other temperature dependencies have also been published [223]. Furthermore, the saturating behavior found for BTO-BFO multilayers in increasing magnetic bias fields also does not match experimental observations on strain-mediated heterostructures [226, 231].

It is possible that strain-mediated ME coupling coexists with another coupling mechanism in BTO-BFO multilayers, leading to a thickness dependent competition of the dominant effect. A number of heterostructure material systems, for which such a cross-over of the dominant ME coupling mechanism occurs in response to thickness-variations, have been identified in recent years. For example, a change from strain- to charge-mediated ME coupling was found to exist in $La_{0.7}Sr_{0.3}MnO_3/PbZr_{0.2}Ti_{0.8}O_3$ [30] and Permalloy/PMN-PT [31] heterostructures. Likewise, *Hu et al.* point out a transition thickness in $Fe/BaTiO_3$ and $(La,Sr)MnO_3/BaTiO_3$ heterostructures, below which charge, not strain, becomes the dominant factor. However, such interface driven phenomena as charge-ordering and interfacial orbital reconstruction commonly produce much smaller effects (in the range of a few $10^{-3}\,\mathrm{V\,cm^{-1}\,Oe^{-1}}$, rather than $\mathrm{V\,cm^{-1}\,Oe^{-1}}$) than we have measured for BTO-BFO multilayers [33, 34].

As we have hinted at before, another phenomenon inherent to perovskite oxides, namely oxygen octahedral tilt (OOT), has recently risen to the attention of the scientific community as a potential source of interface functionalisation [37]. At the interfaces of tetragonal BTO and rhombohedral BFO, not only two different systems of ferroelectric polarization directions coincide (along the [001]-direction for BTO, along the $\langle 111 \rangle_{\mathrm{p.c.}}$-directions for BFO), but also $a^0a^0a^0$ and $a^-a^-a^-$ OOT systems (in Glazer notation [48]). OOT, which directly affects bond angles, plays a crucial role determining many key properties of oxide materials, in particular ferroelectric and magnetic order [37]. In the particular case of BFO, the high angle of OOT of up to 14° is linked to both the canted anti-ferromagnetism and magnetoelectric effect via the *Dzyaloshinsky-Moriya* vector [69]. The influence of a disruption of a OOT-system via geometric constraints can penetrate up to a few nm into an adjacent layer [35,37,187]. In fact, our own investigations using HR-TEM imaging have unearthed a correlation of antiphase octahedral rotations with an enhanced α_{ME}-coefficient [148].

A final contributing factor that may help explain the drastically enhanced ME-coupling measured in BTO-BFO multilayers is the effect of imprint discussed in Sec. 5.1.5. This self-poling effect is likely the reason why we are able to measure a ME coupling effect without a prior ferroelectric poling procedure. A possible interplay with the electrical discontinuity introduced by the confrontation of the [001]- and $\langle 111 \rangle_{\mathrm{p.c.}}$ polarization directions at the BTO-BFO interfaces should also be considered. As a closing remark, eliminating the influence of stray electrical signals in the newly built ME measurement setup in Leipzig, described in Appendix. A, is till an ongoing effort. If successful, it would be of immense interest to perform additional α_{ME} -measurements on the BTO-BFO multilayers deposited by eclipse-PLD.

Chapter 6

Summary and Outlook

The field of multiferroic magnetoelectrics has seen a lot of attention from the scientific community in the past two decades. This has led to a number of advancements in this field of study towards the enhancement and applicability of the ME effect. The most promising route was determined to be the implementation of heterostructure architectures, which has led to the discovery of a number of novel effects. However, a deeper understanding of the origin and mechanism of ME coupling in heterostructures is still lacking. In this thesis, we have explored the enhanced ME coupling in multilayers of $BaTiO_3$ and $BiFeO_3$ deposited on $SrTiO_3$ single crystals by PLD. We used a phenomenological approach, exploring the ME effect in BTO-BFO multilayers, centered around the growth and design of these multilayers.

In Chapter 1, the topic was introduced and motivated. Chapter 2 gave an overview of the underlying theory of intrinsic and extrinsic multiferroics and magnetoelectric coupling therein. The key properties of the constituent materials BTO and BFO were summarized in Chapter 3. BFO, as one of the few intrinsic room temperature multiferroics, has been the issue of vast amounts of research, since the discovery of a significant ME coupling effect in thin film form [9]. A great deal of studies consequently exists on BFO-based heterostructures, as portrayed in Section 3.5. The previous efforts undertaken towards the exploration of BTO-BFO heterostructures by the Semiconductor Physics group at the *University of Leipzig* in cooperation with our colleagues from the *KU Leuven*, Belgium, within the framework of the collaborative research center *SFB 762: Functionality of Oxide Interfaces* were described in Section 3.5.4. The experimental techniques employed in the course of this thesis were presented in Chapter 4.

Results

In chapter Chapter 5, we discussed the experimental results gained within the framework of this thesis. By combination of a variation of deposition parameters and design choices with structural (XRD, TEM), morphological (LSM, AFM, TEM), chemical (TEM-EDX, ToF-SIMS) and ferroic (DHM, VSM, α_{ME}) measurements, we explored the growth and characteristics of BTO-BFO multilayers. We first presented the general properties of BTO-BFO multilayers in comparison to single-layers of the constituent materials in Sec. 5.1. We proceeded to explore the implications of various growth conditions (Sec. 5.2) and multilayer design choices (Sec. 5.3). The usefulness of eclipse-PLD was discussed in Sec. 5.4. We concluded the chapter on the experimental results with measurements of the ME coupling BTO-BFO multilayers in Sec. 5.5. In the following, we give will a brief summary of the respective sections.

General Properties of Single-layers and multilayers of BTO and BFO

The single-layer samples of BTO and BFO deposited on STO substrates throughout the framework of this thesis grow relaxed, i.e. free from IP strain with respect to the substrate. Both materials occur in their respective bulk symmetries. In HR-TEM investigations we were able to show that the epitaxial strain caused by the lattice parameter mismatch between sample and film is relaxed within the first 3 nm of BTO layer. Multilayers of BTO-BFO showed a lower mosaicity and surface roughness than respective single-layers of similar thickness.

In TEM measurements of high quality multilayer samples, evidence for the BFO-inherent $a^-a^-a^-$ OOT was shown to be confined to the BFO sub-layers. For all multilayer samples, the BTO sub-layers show *c*-domains aligned with the OOP axis of the substrate. Ferroelectric switching peaks and slim ferromagnet-like magnetic hystereses were measured for all multilayer films. The leakage current in ferroelectric hysteresis measurements was drastically lower in BTO-BFO multilayers compared to BTO and BFO single-layers. However, electric breakdown fields were often barely larger than the coercive fields and saturation magnetization values did not always conform to simple trends. Both these detrimental phenomena were found to be connected to the presence of droplets. These large particles, consisting primarily of iron oxide, are generated during the laser ablation of BFO during deposition.

Overall, the arrangement of BTO and BFO into multilayers is advantageous for the structural, morphological, electric and magnetoelectric properties, when compared to the respective single-layers.

Deposition Conditions

We re-evaluated the deposition conditions used in our group's former publications to deepen our knowledge of the growth process, optimize sample quality and facilitate the re-production of previous results in a newly built deposition chamber. The deposition temperature range of 670 to 700 °C produces the multilayer samples with the lowest surface roughness, while temperatures below 600 °C leads to the formation of parasitic phases and temperatures above 700 °C cause pitting. Lowering the deposition pressure from 0.25 to 0.01 mbar significantly increases interface roughness and mosaic tilt, which re-affirmed $p_{\mathrm{O}_2} = 0.25\,\mathrm{mbar}$ as the ideal pressure for high quality BTO-BFO multilayer growth. At a laser fluence of $\rho_{\mathrm{L}} = 2\,\mathrm{J\,cm^{-2}}$, the highest combined growth rate was achieved. Increasing ρ_{L} beyond this value leads to a drastic increase of the droplet particle density and should hence be avoided. A promising route to mitigate the number of droplets on the sample surface is the increase of lateral offset between the substrate and ablation target rotation axes, however this also causes an inadvertent surge of surface roughness.

Multilayer Design

We explored three adjustments to the multilayer design: first, we varied the sub-layer thickness of the BFO layers from nominally 5 to 50 nm, while maintaining a constant BTO thickness; second, we adjusted the BTO-BFO thickness ratio in the range of 0.1 to 0.8 while maintaining a double-layer thickness of 20 nm; third, we changed the double-layer thickness from 20 nm down to 4.6 nm while adhering to a BTO-BFO thickness ratio of 1 : 1. Changes to the BTO-BFO thickness ratio tune the average IP lattice parameter linearly from the value of a relaxed single-layer of BFO to that of a relaxed single-layer pf BTO. The overall double-layer thickness has no effect on the lattice parameters throughout the thickness range explored. These results were confirmed both by XRD RSM measurements and HR-TEM imaging. The ideal thickness ratio range was found to be in the range from 0.6 to 0.8 $d_{\mathrm{BTO}}/d_{\mathrm{dl}}$. Higher BTO content leads to heightened interface roughness and very low BTO content leads to a large number of misaligned grains. Furthermore, the remanent magnetization increases with decreasing BFO thickness. Tentative OOP VSM measurements support findings by *Lazenka et al.* [151], who found an increasing perpendicular magnetic anisotropy with decreasing BFO thickness. Due to the low saturation magnetization of the multilayers ($\sim 0.02\,\mu_{\mathrm{B}}/\mathrm{f.u.}$) and the premature electric breakdown during ferroelectric measurements, a thorough systematic analysis of the ferromagnetic and ferroelectric properties with respect to deposition parameters and design were not possible.

Eclipse-PLD

The introduction of a shadow mask between ablation target and substrate was shown to be an efficient strategy to eradicate the presence of droplet particles. The multilayer samples produced by this so-called eclipse-PLD showed particularly low interface and surface roughness, even at a total thickness of up to 0.5 µm. TEM measurements revealed particularly low defect densities in multilayers grown by this technique. Most importantly, the electric breakdown field was improved from $0.8\,\mathrm{MV\,cm^{-1}}$, for multilayers deposited by conventional PLD, to on average $3.2\,\mathrm{MV\,cm^{-1}}$. Consequently, fully saturated ferroelectric hysteresis loops could reliably be recorded for BTO-BFO multilayers deposited by eclipse-PLD. The reduced interface roughness is advantageous for advanced depth-profiling techniques. Accordingly, we were able to show the absence of inter-diffusion between the sub-layers in 3D ToF-SIMS measurements and have conducted preliminary PNR measurements, aimed at generating electric field dependent magnetic depth profiles.

Enhanced ME coupling in BTO-BFO multilayers

We have measured the magnetoelectric coupling coefficients of a number of sample series deliberately designed to distinguish the influence of oxygen pressure during growth, BTO-BFO thickness ratio and double-layer thickness. The multilayer samples showed characteristic saturating bias field dependence across all series, distinct from the behavior of single-layers. The temperature dependence changes from falling to rising with the measurement temperature, as the double-layer thickness is lowered. The BTO-BFO thickness ratio appears to have little to no influence over the value of α_{ME} at 300 K and 0 T. The reduction of the double-layer thickness, however, enhances the α_{ME}-value significantly and leads to a $1/d_{\mathrm{dl}}$-dependency below a double-layer thickness of approximately 20 nm. A previously reported reduction of α_{ME} with decreasing oxygen pressure during deposition could not be re-produced, the former results are likely also due to changing double-layer thicknesses of the samples. All multilayers except the samples with $d_{\mathrm{dl}} > 50\,\mathrm{nm}$ showed significantly higher ME-coefficients then the $4\,\mathrm{V\,cm^{-1}\,Oe^{-1}}$ measured for BFO single-layers. The record value of $480\,\mathrm{V\,cm^{-1}\,Oe^{-1}}$ was measured for a sample with only 4.6 nm d_{dl} , equivalent of ~ 6 unit cells of BTO and BFO per double-layer. From the characteristic dependencies on the magnetic bias field and temperature, as well as the double-layer thickness, we concluded an interface-dependent coupling mechanism at the core of the enhanced ME effect in BTO-BFO multilayers.

Outlook

We were able to significantly increase our sample quality through the application of eclipse-PLD. More importantly, we were able to increase the off-resonance room temperature magnetoelectric coupling in BTO-BFO multilayers to rival the magnitude of α_{ME} measured at resonance for the strongest magnetoelectric materials currently known [2]. The gathered experimental evidence points to an interface-driven ME effect that enhances, or rather transforms the magnetoelectric coupling in BTO-BFO multilayers relative to BFO single-layers. Conventional strain-coupling is not supported by the independence on the constituent material ratio, nor are effects like charge transfer or orbital reconstruction likely candidates, as they generally do not produce ME effects in the presented order of magnitude. We have suggested the conflict of differing ferroelectric polarization directions and incompatibility of OOT systems at the interfaces as possible fields of inquiry for future work, as both are directly linked to both the magnetic and ferroelectric order in the multilayers. A crucial next step in the investigation of the interface geometry could be the use of advanced TEM techniques. With high quality samples, such as the samples obtained by eclipse-PLD recently, unit-cell resolved mapping of the oxygen octahedra [185] and nano-scale ferroelectriciy [232] is possible, which could be supplemented by magnetic domain sensitive techniques like *Lorentz*-TEM. As we have shown in our preliminary measurements, PNR is another promising technique, which could reveal the magnetic depth profile in BTO-BFO multilayer samples. Additional steps should be taken to maximize the observable signal, e.g. increasing the number of double-layers and adjusting the measurement layout to a longitudinal geometry.

Ultimately, comprehension of the ME coupling mechanism in BTO-BFO multilayers will require a consolidation of detailed structural and ferroic measurements with simulation. Recently, *Wang et al.* have published a study on BTO-BFO multilayers employing density functional theory [233]. They used a simplified model, assuming tetragonal symmetry for both BTO and BFO with both ferroelectric polarization axes parallel to the OOP direction. They point out the central role of the *Dzyaloshinsky-Moriya* interaction vector, which mediates the ME-coupling in BFO, as well as the discontinuity of the electronic configuration and polarization of the sub-layers.

In conclusion, the study of BTO-BFO multilayers revealed an effective tool to enhance the ME effect in multiferroic heterostructures by means of design. With this, one further step towards the applicability of magnetoelectrics in practical applications was made.

Appendix A

Magnetoelectric Measurement Setup

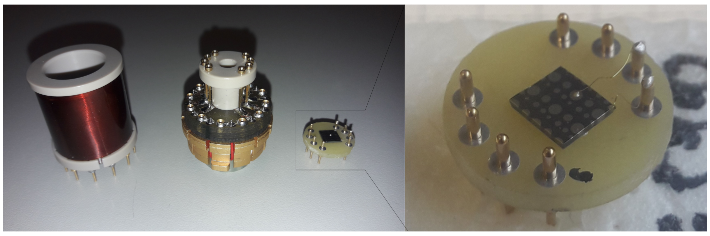

Figure A.1: Photographic image of the ME measurement setup

Within the course of this thesis, a reproduction of the magnetoelectric voltage measurement setup that was used at the *KU Leuven* in Belgium was built. The setup is built to operate in a *LOT Quantum Design* PPMS, the sample holder, depicted in Fig. A.1 is a based on a standard PPMS sample puck. The other main components, as discussed in Sec. 4.7, are a solenoid, a *Keithley 6221* AC current source and a *Stanford Research SR830* lock-in amplifier. The sample holder and solenoid were built in cooperation within the project *SFB762* at the *University of Halle* with the kind help of *Prof. Ebbinghaus.* The following specifications apply to the solenoid-sample holder combination:

- $N = 1174$ windings of 0.14 mm enameled copper wire
- Solenoid height l 20 mm, diameter d 18 mm
- Sample holder height places the film surface of a 0.5 mm thick sample exactly in the center
- DC resistance 80.7 Ω
- Up to 8 sample contacts

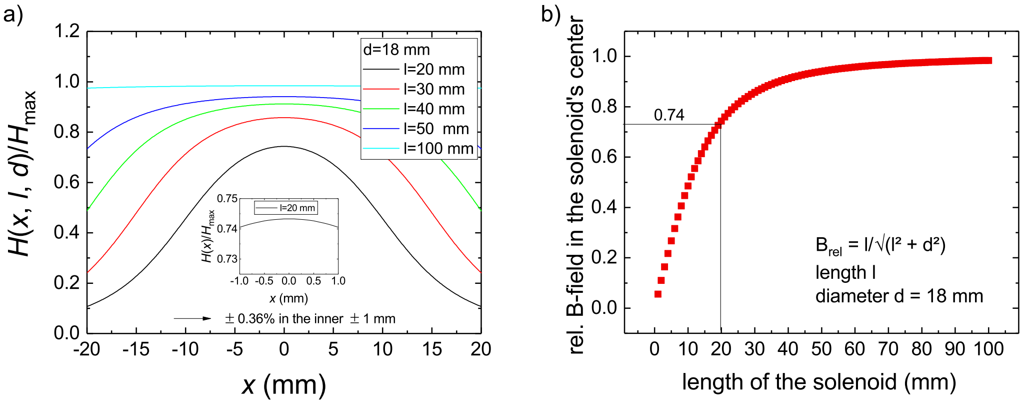

Figure A.2: Field calculations inside a solenoid.

The magnetic induction $\boldsymbol{B}$ of an ideal solenoid of length l with with N windings and a current I running through it is calculated as

$$\boldsymbol{B} = \mu_0 \frac{IN}{l} . \tag{A.1}$$

For the given solenoid, a 10 mA current would result in an induction of 7.38 Gauss or a $\boldsymbol{H}$-field in air of 7.38 Oe. The field $\boldsymbol{H}(x, l, d)$ in a finite solenoid with diameter d at an axial position x relative to the center of the solenoid can be expressed as:

$$\boldsymbol{H}(x)/\boldsymbol{H}_{\text{infinite}} = \frac{l + 2x}{2\sqrt{d^2 + (l + 2x)^2}} + \frac{l - 2x}{2\sqrt{d^2 + (l - 2x)^2}} , \tag{A.2}$$

as depicted for a fixed diameter of 18 mm and various lengths in Fig. A.2 a). For a solenoid with $l = 20$ mm, the variation of $\boldsymbol{H}(x)$ within ±1 mm of the center position is only ±0.36 %. The relative field in the center of an arbitrarily long and thick solenoid simplifies to:

$$\boldsymbol{H}(x = 0, l, d)/\boldsymbol{H}_{\text{infinite}} = \frac{l}{\sqrt{d^2 + l^2}} , \tag{A.3}$$

which results in an approximate field of 0.743×7.38 Oe $= 5.48$ Oe for our solenoid. The DC magnetic field generated in the center of the solenoid was measured in the range of 5 to 100 mA with a commercial DC teslameter inside the sample wiring test station (see Fig. A.3 a)). For AC field measurements, a *Honeywell* SS495A1 integrated circuit linear *Hall*-sensor operated at 5 V DC with an output of 3.125 ± 0.094 mV/Gauss and a null-voltage of 2.500 ± 0.075 V was used. The frequency dependent output was measured with a lock-in amplifier in the sample wiring test station and inside the PPMS with a peak current of 10 mA at frequencies from 10 to 10 000 Hz (see Fig. A.3 b)). With 5.3 Oe DC and 5.37 Oe at 10 Hz AC, the measured values fall only slightly short of the above approximation. The DC current dependence is perfectly linear as to be expected,

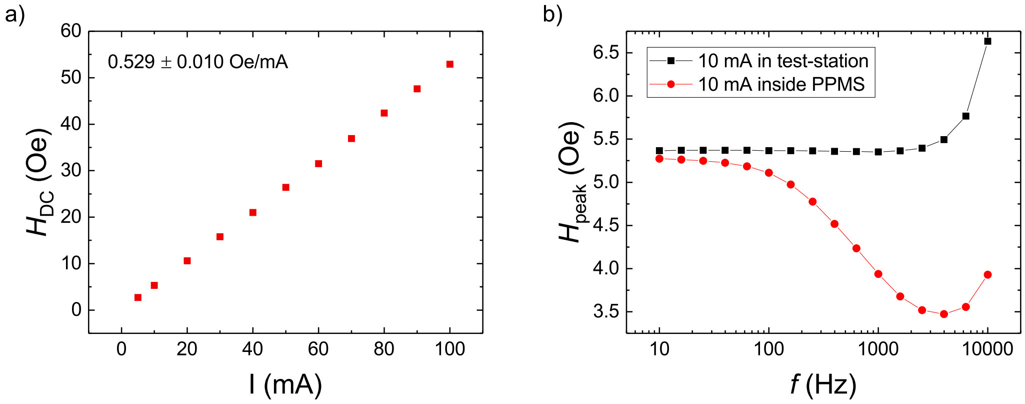

Figure A.3: Measured $\boldsymbol{H}$-field in the center of the solenoid **(a)** measured with a DC teslameter at different current settings, **(b)** measured with a *Hall*-sensor at different frequencies both in the sample wiring test station and inside the PPMS.

with a slope of 5.29 ± 0.01 Oe/mA. The frequency dependence in the test fixture and inside the PPMS differ significantly. In the test-fixture, $\boldsymbol{H}$ is largely independent of f up to ca. 2 kHz. However, the field generated by the solenoid inside the PPMS varies strongly with f.

To test the measurement setup, we measured a number of test samples which show no ME-coupling, such as glass-substrates, a BTO-single-layer and a parallel connected pair capacitor and resistor. Additionally, we checked a BFO single-layer and some BTO-BFO multilayers, which were previously measured at the *KU Leuven*. A number of different cables, connection schemes, shielding setups, and Lock-In settings, both inside the PPMS and in the test fixture, using an AC magnetic field of 10 Oe. The overall functionality of the measurement setup has been confirmed in principle by the *Hall*-sensor measurements, which appeared to be free of significant noise levels. The voltage recorded for the *Hall*-sensor also lies in the same mV-range as the signal expected for our multilayer samples. However, all test samples showed signals in the 10 to 50 µV-range. For comparison, the inductive voltage of a conductive loop with an area of 10 mm^2 showed an inductive voltage of 25 µV. Unlike the inductive voltage of the loop, or the signal of the *Hall*-sensor, however, the voltage measured for the test samples varied widely with any changes to the setup settings, which could not be explained or alleviated. As a last resort, we added a high-impedance pre-amplifier to the system, which is generally used to reduce the noise level in voltage measurements performed on high-impedance samples, but to no avail.

Likewise, the original setup in *Leuven* is currently not operational. Finding the actual source of error is likely to require the concentrated efforts of a few dedicated scientists versed in the field of electronics.

Appendix B

Magnetic Background Measurements

We checked the magnetic field hysteresis of the superconducting magnet using the paramagnetic palladium sample provided by *Quantum Design*. Presented in Fig. B.1 are $m(\mu_0 H)$-curves measured on the Pd sample at 10 K, 150 K and 300 K. In the -4 to 4 T range presented, the magnetization is linear with the applied field, as expected. As the insert shows, a small hysteresis of <2 mT exists. This minor offset is an artifact caused by processes like flux trapping in the superconducting magnet. Typical magnetic coercive fields measured for the multilayer samples in this thesis are just one order of magnitude larger, which is nor cause to assume the films' hysteresis is an artifact, but serves as a caveat for the evaluation of absolute coercive field values.

Magnetization measurements were also performed on bare substrate holders. Presented in Fig. B.2 a) are magnetization measurements of a quartz sample holder used for in-plane magnetization measurements. Surprisingly, the sample holder shows a non-linearity at around 5 T, which disappears at 10 K. A similar non-linearity was also measured for the brass sample holder with quartz brackets used for out-of-plane measurements, as shown in Fig. B.2 b). Such non-linearity can originate from impurities

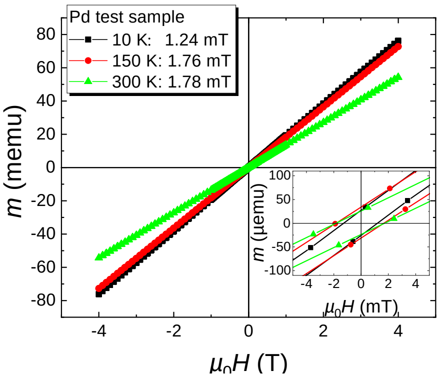

Figure B.1: Magnetization loops measured for the palladium test sample at 10 K, 150 K and 300 K in the field range of -4 to 4 T.

in the quartz component, but is poorly understood. A typical multilayer of BTO-BFO shows a saturation magnetization of only ∼15 µemu, in the same order of magnitude as the non-linearstray magnetic signal from the sample holders. Consequently, we have limited our magnetic hysteresis measurements to the range of −4 to 4 T.

Fig. B.3 shows a comparison of magnetic hysteresis measurements of a quartz sample holder, an annealed STO substrate and a typical BTO-BFO multilayer. In the range of −4 to 4 T, the magnetic background signal from the sample holder is insignificant, when compared to the signal obtained for the multilayer. As the red curve shows, we have measured a minor ferromagnet-like signal for the STO substrate, which, however, does not saturate and shows only a hysteresis in the order of magnitude found also for the Pd reference sample. Hence, these stray signals are noteworthy when compared to the weak magnetic signal of the multilayers, but can be easily distinguished.

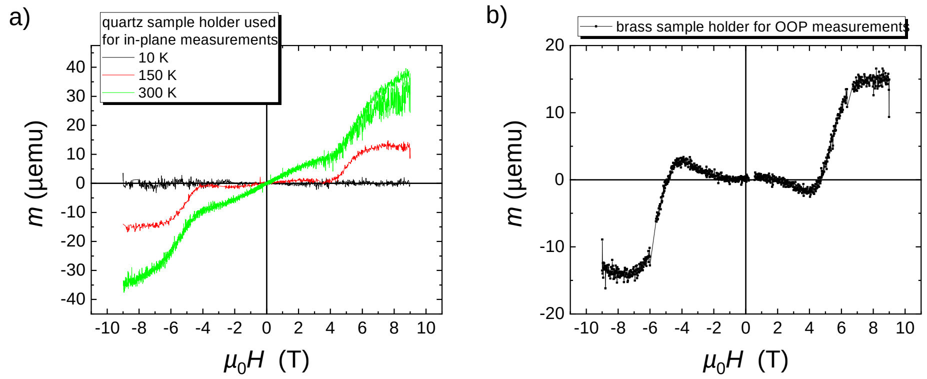

Figure B.2: Magnetization loops measured for **(a)** the quartz sample holder used for in-plane measurements at 10 K, 150 K and 300 K in the field range of −9 to 9 T and **(b)** The brass sample holder and quartz brackets used for out-of-plane measurements at 300 K in the field range of −9 to 9 T.

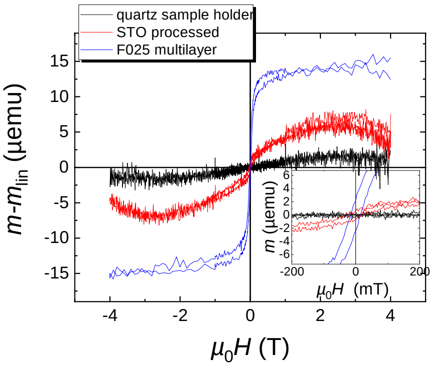

Figure B.3: Magnetization loops measured for a quartz sample holder, an annealed STO substrate and a BTO-BFO multilayer at 300 K in the field range of −4 to 4 T.

Appendix C

Polarized Neutron Reflectometry

The polarized neutron reflectometry (PNR) experiments percormed in the framework of this thesis were conducted at the *NREX* reflectometer, at the *Research Neutron Source Heinz Maier-Leibnitz (MLZ, FRM II)*, operated by the *Max Planck Institute for Solid State Research*. The experiments were made possible thanks to the research grant by the *MLZ* organization. *Johanna K. Jochum* acted as the instigator main proposer for the grant proposal no 15287: “To unravel the mechanism of the ME coupling in BTO-BFO superlattices and the effect of epitaxial strain in BFO layers on magnetoelectricity, we have to study their magnetic behavior while applying an electric field. We therefore propose to determine the magnetization depth profile of the BTO-BFO superlattices with different BFO layer thicknesses using polarized neutron reflectivity (PNR) during the application of an electric field. PNR with neutron spin analysis is the ideal method to study such superlattice structures, since it allows the resolution of the magnetization direction and amplitude along the depth of the film as well as within the individual layers.” (excerpt fro the proposal). The experiments were performed primarily by the beamline scientist *Yury Khaydukov*. The reflectometer *NREX*, depicted in Fig. C.1, operates at a wavelength of 4.28 Å and can apply in-plane magnetic fields of up to 7.5 T [221].

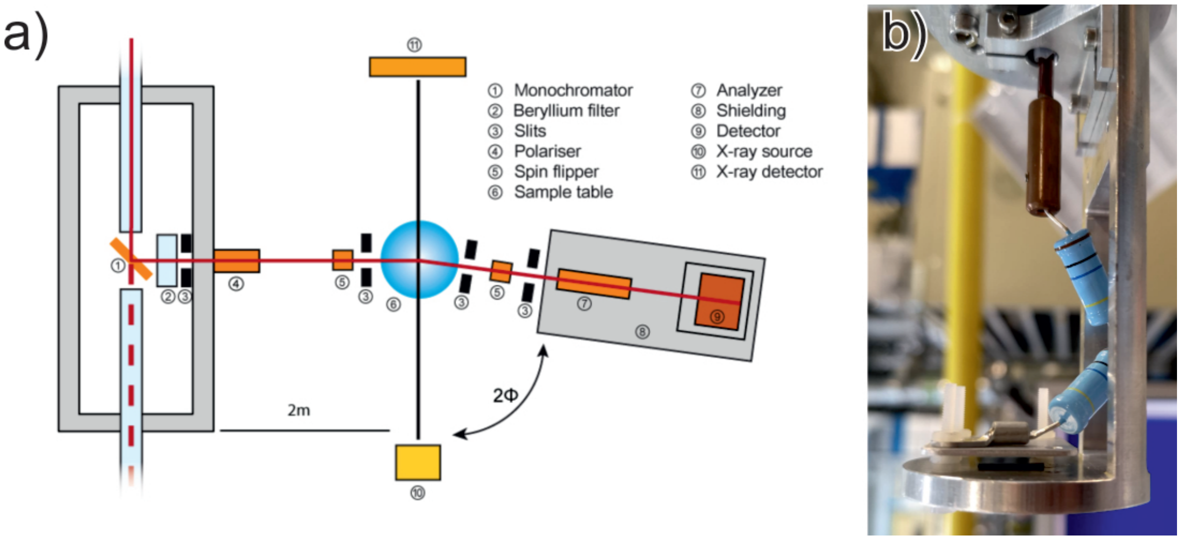

Figure C.1: **(a)** Schematic setup of the polarized neutron reflectometer *NREX*, adapted from Ref. 221, **(b)** photo of the capacitive high-voltage sample holder.

Literature

[1] Eerenstein W., Mathur N.D., and Scott J.F.; 2006 *Nature* **442** 759; doi:`10.1038/nature05023`.

[2] Srinivasan G., Priya S., and Sun N.; 2015 *Composite Magnetoelectrics*; Woodhead Publishing, Amsterdam; 1 edition.

[3] Fusil S., Garcia V., Barthélémy A., and Bibes M.; 2014 *Annu. Rev. Mater. Res.* **44** 91; doi:`10.1146/annurev-matsci-070813-113315`.

[4] Wang Y., Li J., and Viehland D.; 2014 *Mater. Today* **17** 269; doi:`10.1016/j.mattod.2014.05.004`.

[5] Srinivasan G.; 2010 *Annu. Rev. Mater. Res.* **40** 153; doi:`10.1146/annurev-matsci-070909-104459`.

[6] Tu C., Chu Z.q., Spetzler B., Hayes P., Dong C.z., Liang X.f., Chen H.h., He Y.f., Wei Y.y., Lisenkov I., *et al.*; 2019 *Materials (Basel).* **12** 2259; doi:`10.3390/ma12142259`.

[7] Singer A., Dutta S., Lewis E., Chen Z., Chen J.C., Verma N., Avants B., Feldman A.K., O'Malley J., Beierlein M., *et al.*; 2020 *Neuron* doi:`10.1016/j.neuron.2020.05.019`.

[8] Hill N.A.; 2000 *J. Phys. Chem. B* **104** 6694; doi:`10.1021/jp000114x`.

[9] Wang J., Neaton J.B., Zheng H., Nagarajan V., Ogale S.B., Liu B., Viehland D., Vaithyanathan V., Schlom D.G., Waghmare U.V., *et al.*; 2003 *Science (80-.).* **299** 1719; doi:`10.1126/science.1080615`.

[10] Vaz C.a.F., Hoffman J., Ahn C.H., and Ramesh R.; 2010 *Adv. Mater.* **22** 2900; doi:`10.1002/adma.200904326`.

[11] Lorenz M., Lazenka V., Schwinkendorf P., Bern F., Ziese M., Modarresi H., Volodin A., Van Bael M.J., Temst K., Vantomme A., *et al.*; 2014 *J. Phys. D. Appl. Phys.* **47** 135303; doi:`10.1088/0022-3727/47/13/135303`.

[12] Schmid H.; 2008 *J. Phys. Condens. Matter* **20** 434201; doi:`10.1088/0953-8984/20/43/434201`.

[13] Scott J.F.; 2013 *NPG Asia Mater.* **5** e72; doi:`10.1038/am.2013.58`.

[14] Spaldin N.a., Cheong S.w., and Ramesh R.; 2010 *Phys. Today* **63** 38; doi:`10.1063/1.3502547`.

[15] Fiebig M., Lottermoser T., Meier D., and Trassin M.; 2016 *Nat. Rev. Mater.* **1** 16046; doi:`10.1038/natrevmats.2016.46`.

[16] Barone P. and Picozzi S.; 2015 *Comptes Rendus Phys.* **16** 143; doi:`10.1016/j.crhy.2015.01.009`.

[17] Choi E.m.M., Kleibeuker J.E., Fix T., Xiong J., Kinane C.J., Arena D., Langridge S., Chen A., Bi Z., Lee J.H., *et al.*; 2016 *Adv. Mater. Interfaces* **3** 1500597; doi:`10.1002/admi.201500597`.

[18] Fiebig M.; 2005 *J. Phys. D. Appl. Phys.* **38** R123; doi:`10.1088/0022-3727/38/8/R01`.

[19] Vidal J.V., Timopheev A.A., Kholkin A.L., and Sobolev N.A.; 2016 in I. Tiginyanu, P. Topala, and V. Ursaki, editors, *Nanostructures Thin Film. Multifunct. Appl.*; chapter 6, pages 189–226; Springer International Publishing; 1st edition; ISBN 978-3-319-30197-6; doi:`10.1007/978-3-319-30198-3_6`.

[20] Brown W.F., Hornreich R.M., and Shtrikman S.; 1968 *Phys. Rev.* **168** 574; doi:`10.1103/PhysRev.168.574`.

[21] Newnham R., Skinner D., and Cross L.; 1978 *Mater. Res. Bull.* **13** 525; doi:`10.1016/0025-5408(78)90161-7`.

[22] van Suchtelen J.; 1972 *Philips Res. Rep.* **27** 28.

[23] Palneedi H., Annapureddy V., Priya S., and Ryu J.; 2016 *Actuators* **5** 9; doi:`10.3390/act5010009`.

[24] Ortega N., Kumar A., Scott J.F., and Katiyar R.S.; 2015 *J. Phys. Condens. Matter* **27** 504002; doi:`10.1088/0953-8984/27/50/504002`.

[25] Hu J.M., Duan C.G., Nan C.W., and Chen L.Q.; 2017 *npj Comput. Mater.* **3** 1; doi:`10.1038/s41524-017-0020-4`.

[26] Avellaneda M. and Harshé G.; 1994 *J. Intell. Mater. Syst. Struct.* **5** 501; doi:`10.1177/1045389X9400500406`.

[27] Bichurin M.I., Petrov V.M., and Srinivasan G.; 2003 *Phys. Rev. B* **68** 054402; doi:`10.1103/PhysRevB.68.054402`.

[28] Israel C., Mathur N.D., and Scott J.F.; 2008 *Nat. Mater.* **7** 93; doi:`10.1038/nmat2106`.

[29] Israel C., Kar-Narayan S., and Mathur N.D.; 2010 *IEEE Sens. J.* **10** 914; doi:`10.1109/JSEN.2009.2037728`.

[30] Spurgeon S.R., Sloppy J.D., Kepaptsoglou D.M.D., Balachandran P.V., Nejati S., Karthik J., Damodaran A.R., Johnson C.L., Ambaye H., Goyette R., *et al.*; 2014 *ACS Nano* **8** 894; doi:`10.1021/nn405636c`.

[31] Nan T., Zhou Z., Liu M., Yang X., Gao Y., Assaf B.A., Lin H., Velu S., Wang X., Luo H., *et al.*; 2015 *Sci. Rep.* **4** 3688; doi:`10.1038/srep03688`.

[32] Hu J.M., Nan C.W., and Chen L.Q.; 2011 *Phys. Rev. B - Condens. Matter Mater. Phys.* **83** 1; doi:`10.1103/PhysRevB.83.134408`.

[33] Cui B., Song C., Mao H., Wu H., Li F., Peng J., Wang G., Zeng F., and Pan F.; 2015 *Adv. Mater.* **27** 6651; doi:`10.1002/adma.201503115`.

[34] Huang W., Yin Y., and Li X.; 2018 *Appl. Phys. Rev.* **5** 041110; doi:`10.1063/1.5053426`.

[35] Huang R., Ding H.C., Liang W.I., Gao Y.C., Tang X.D., He Q., Duan C.G., Zhu Z., Chu J., Fisher C.A., *et al.*; 2014 *Adv. Funct. Mater.* **24** 793; doi:`10.1002/adfm.201301470`.

[36] Borisevich A., Ovchinnikov O.S., Chang H.J., Oxley M.P., Yu P., Seidel J., Eliseev E.A., Morozovska A.N., Ramesh R., Pennycook S.J., *et al.*; 2010 *ACS Nano* **4** 6071; doi:`10.1021/nn1011539`.

[37] Rondinelli J.M., May S.J., and Freeland J.W.; 2012 *MRS Bull.* **37** 261; doi:`10.1557/mrs.2012.49`.

[38] Kan D., Aso R., Kurata H., and Shimakawa Y.; 2014 *J. Appl. Phys.* **115**; doi:`10.1063/1.4875839`.

[39] Bhalla A.S., Guo R., and Roy R.; 2000 *Mater. Res. Innov.* **4** 3; doi:`10.1007/s100190000062`.

[40] Johnsson M. and Lemmens P.; 2007 in *Handb. Magn. Adv. Magn. Mater.*; John Wiley & Sons, Ltd, Chichester, UK; doi:`10.1002/9780470022184.hmm411`.

[41] Kaur P., Sharma K.K., Pandit R., Choudhary R.J., and Kumar R.; 2014 *Appl. Phys. Lett.* **104** 081608; doi:`10.1063/1.4866775`.

[42] von Hippel A., Breckenridge R.G., Chesley F.G., and Tisza L.; 1946 *Ind. Eng. Chem.* **38** 1097; doi:`10.1021/ie50443a009`.

[43] Petrus M.L., Schlipf J., Li C., Gujar T.P., Giesbrecht N., Müller-Buschbaum P., Thelakkat M., Bein T., Hüttner S., and Docampo P.; 2017 *Adv. Energy Mater.* **7** 1; doi:`10.1002/aenm.201700264`.

[44] Smyth D.M.; 1985 *Ann. Rev. Mater. Sci* **15** 329; doi:`10.1146/annurev.ms.15.080185.001553`.

[45] Smith D.M., Chang E.K., and Liu D.H.; 1996 *Phase Transitions* **58** 57; doi:`10.1080/01411599608242394`.

[46] Glazer A.M.; 1972 *Acta Crystallogr. Sect. B Struct. Crystallogr. Cryst. Chem.* **28** 3384; doi:`10.1107/s0567740872007976`.

[47] Howard C.J. and Stokes H.T.; 2005 *Acta Crystallogr. Sect. A Found. Crystallogr.* **61** 93; doi:`10.1107/S0108767304024493`.

[48] Glazer A.M.; 1975 *Acta Crystallogr. Sect. A* **31** 756; doi:`10.1107/S0567739475001635`.

[49] Nassau K. and Miller A.; 1988 *J. Cryst. Growth* **91** 373; doi:`10.1016/0022-0248(88)90254-0`.

[50] Koster G., Kropman B.L., Rijnders G.J.H.M., Blank D.H.A., and Rogalla H.; 1998 *Appl. Phys. Lett.* **73** 2920; doi:`10.1063/1.122630`.

[51] Kawasaki M., Ohtomo A., Arakane T., Takahashi K., Yoshimoto M., and Koinuma H.; 1996 *Appl. Surf. Sci.* **107** 102; doi:`10.1016/S0169-4332(96)00512-0`.

[52] CRYSTAL GmbH; *Resistivity of Nb doped SrTiO3*.

[53] Coey J.M.D., Venkatesan M., and Stamenov P.; 2016 *J. Phys. Condens. Matter* **28** 485001; doi:`10.1088/0953-8984/28/48/485001`.

[54] Crandles D.A., Desroches B., and Razavi F.S.; 2010 *J. Appl. Phys.* **108** 053908; doi:`10.1063/1.3481344`.

[55] Liu Z.Q., Lü W.M., Lim S.L., Qiu X.P., Bao N.N., Motapothula M., Yi J.B., Yang M., Dhar S., Venkatesan T., *et al.*; 2013 *Phys. Rev. B - Condens. Matter Mater. Phys.* **87** 3; doi:`10.1103/PhysRevB.87.220405`.

[56] Garcia M.A., Fernandez Pinel E., de la Venta J., Quesada A., Bouzas V., Fernández J.F., Romero J.J., Martín González M.S., and Costa-Krämer J.L.; 2009 *J. Appl. Phys.* **105** 013925; doi:`10.1063/1.3060808`.

[57] Abraham D.W., Frank M.M., and Guha S.; 2005 *Appl. Phys. Lett.* **87** 1; doi:`10.1063/1.2146057`.

[58] Rosa A., Tulli D., Castera P., Gutierrez A.M., Griol A., Baquero M., Vilquin B., Eltes F., Abel S., Fompeyrine J., *et al.*; 2017 *Opt. Mater. Express* **7** 4328; doi:`10.1364/OME.7.004328`.

[59] Acosta M., Novak N., Rojas V., Patel S., Vaish R., Koruza J., Rossetti G.A., and Rödel J.; 2017 *Appl. Phys. Rev.* **4**; doi:`10.1063/1.4990046`.

[60] Nowotny J. and Rekas M.; 1991 *Ceram. Int.* **17** 227; doi:`10.1016/0272-8842(91)90017-T`.

[61] Ravel B., Stern E.A., Vedrinskii R.I., and Kraizman V.; 1998 *Ferroelectrics* **206** 407; doi:`10.1080/00150199808009173`.

[62] Kwei G.H., Lawson A.C., Billinge S.J., and Cheong S.W.; 1993 *J. Phys. Chem.* **97** 2368; doi:`10.1021/j100112a043`.

[63] Li C., Cui D., Zhou Y., Lu H., Chen Z., Zhang D., and Wu F.; 1998 *Appl. Surf. Sci.* **136** 173; doi:`10.1016/S0169-4332(98)00342-0`.

[64] Cao D., Cai M.Q., Zheng Y., and Hu W.Y.; 2009 *Phys. Chem. Chem. Phys.* **11** 10934; doi:`10.1039/b908058a`.

[65] Bahoosh S.G., Trimper S., and Wesselinowa J.M.; 2011 *Phys. Status Solidi - Rapid Res. Lett.* **5** 382; doi:`10.1002/pssr.201105419`.

[66] Roginskaya Y., Tomashpol'Skiĭ Y., Venevtsev Y., Petrov V., and Zhdanov G.; 1966 *Sov. J. Exp. Theor. Phys.* **23** 47.

[67] Kiselev S.V., Ozerov R.P., and Zhdanov G.S.; 1963 *Sov. Phys.-Dokl.* **7** 742.

[68] Royen P. and Swars K.; 1957 *Angew. Chemie* **69** 779; doi:`10.1002/ange.19570692407`.

[69] Catalan G. and Scott J.F.; 2009 *Adv. Mater.* **21** 2463; doi:`10.1002/adma.200802849`.

[70] Kubel F. and Schmid H.; 1990 *Acta Crystallogr. Sect. B Struct. Sci.* **46** 698; doi:`10.1107/S0108768190006887`.

[71] Baettig P., Ederer C., and Spaldin N.A.; 2005 *Phys. Rev. B* **72** 214105; doi:`10.1103/PhysRevB.72.214105`.

[72] Neaton J.B., Ederer C., Waghmare U.V., Spaldin N.A., and Rabe K.M.; 2005 *Phys. Rev. B - Condens. Matter Mater. Phys.* **71** 014113; doi:`10.1103/PhysRevB.71.014113`.

[73] Teague J.R., Gerson R., and James W.J.; 1970 *Solid State Commun.* **8** 1973.

[74] Lu J., Günther A., Schrettle F., Mayr F., Krohns S., Lunkenheimer P., Pimenov A., Travkin V.D., Mukhin A.A., and Loidl A.; 2010 *Eur. Phys. J. B* **75** 451; doi:`10.1140/epjb/e2010-00170-x`.

[75] Dzyaloshinsky I.; 1958 *J. Phys. Chem. Solids* **4** 241; doi:`10.1016/0022-3697(58)90076-3`.

[76] Moriya T.; 1960 *Phys. Rev.* **120** 91; doi:`10.1103/PhysRev.120.91`.

[77] Ederer C. and Spaldin N.A.; 2005 *Phys. Rev. B - Condens. Matter Mater. Phys.* **71** 1; doi:`10.1103/PhysRevB.71.060401`.

[78] Zhang J.T., Lu X.M., Zhou J., Sun H., Su J., Ju C.C., Huang F.Z., and Zhu J.S.; 2012 *Appl. Phys. Lett.* **100** 242413; doi:`10.1063/1.4729555`.

[79] Popkov A.F., Davydova M.D., Zvezdin K.A., Solov'Yov S.V., and Zvezdin A.K.; 2016 *Phys. Rev. B* **93** 5; doi:`10.1103/PhysRevB.93.094435`.

[80] Sosnowska I., Peterlin-Neumaier T., and Steichele E.; 1982 *J. Phys. C Solid State Phys.* **15** 4835.

[81] Caicedo J.M., Zapata J.A., Gómez M.E., and Prieto P.; 2008 *J. Appl. Phys.* **103** 1; doi:`10.1063/1.2839276`.

[82] Popov Y.F., Kadomtseva A.M., Vorob'ev G.P., and Zvezdin A.K.; 1994 *Ferroelectrics* **162** 135; doi:`10.1080/00150199408245098`.

[83] Ruette B., Zvyagin S., Pyatakov A.P., Bush A., Li J.F., Belotelov V.I., Zvezdin A.K., and Viehland D.; 2004 *Phys. Rev. B* **69** 064114; doi:`10.1103/PhysRevB.69.064114`.

[84] Sosnowska I., Schäfer W., Kockelmann W., Andersen K., and Troyanchuk I.; 2002 *Appl. Phys. A Mater. Sci. Process.* **74** s1040; doi:`10.1007/s003390201604`.

[85] Le Bras G., Colson D., Forget A., Genand-Riondet N., Tourbot R., and Bonville P.; 2009 *Phys. Rev. B - Condens. Matter Mater. Phys.* **80** 1; doi:`10.1103/PhysRevB.80.134417`.

[86] Gabbasova Z., Kuz'min M., Zvezdin A., Dubenko I., Murashov V., Rakov D., and Krynetsky I.; 1991 *Phys. Lett. A* **158** 491; doi:`10.1016/0375-9601(91)90467-M`.

[87] Lazenka V.V., Lorenz M., Modarresi H., Brachwitz K., Schwinkendorf P., Böntgen T., Vanacken J., Ziese M., Grundmann M., and Moshchalkov V.V.; 2013 *J. Phys. D. Appl. Phys.* **46** 175006; doi:`10.1088/0022-3727/46/17/175006`.

[88] Bai F., Wang J., Wuttig M., Li J., Wang N., Pyatakov A.P., Zvezdin A.K., Cross L.E., and Viehland D.; 2005 *Appl. Phys. Lett.* **86** 1; doi:`10.1063/1.1851612`.

[89] Jiang Z.Z., Guan Z., Yang N., Xiang P.H., Qi R.J., Huang R., Yang P.X., Zhong N., and Duan C.G.; 2017 *Mater. Charact.* **131** 217; doi:`10.1016/j.matchar.2017.07.009`.

[90] Béa H., Bibes M., Barthélémy A., Bouzehouane K., Jacquet E., Khodan A., Contour J.P., Fusil S., Wyczisk F., Forget A., *et al.*; 2005 *Appl. Phys. Lett.* **87** 2; doi:`10.1063/1.2009808`.

[91] Eerenstein W.; 2005 *Science (80-.).* **307** 1203a; doi:`10.1126/science.1105422`.

[92] Go H.y., Wakiya N., Funakubo H., Satoh K., Kondo M., Cross J.S., Maruyama K., Mizutani N., and Shinozaki K.; 2007 *Jpn. J. Appl. Phys.* **46** 3491; doi:`10.1143/JJAP.46.3491`.

[93] Sando D., Barthélémy A., and Bibes M.; 2014 *J. Phys. Condens. Matter* **26** 473201; doi:`10.1088/0953-8984/26/47/473201`.

[94] Béa H., Dupé B., Fusil S., Mattana R., Jacquet E., Warot-Fonrose B., Wilhelm F., Rogalev A., Petit S., Cros V., *et al.*; 2009 *Phys. Rev. Lett.* **102** 1; doi:`10.1103/PhysRevLett.102.217603`.

[95] Jang H.W., Ortiz D., Baek S.H., Folkman C.M., Das R.R., Shafer P., Chen Y., Nelson C.T., Pan X., Ramesh R., *et al.*; 2009 *Adv. Mater.* **21** 817; doi:`10.1002/adma.200800823`.

[96] Saito K., Ulyanenkov A., Grossmann V., Ress H., Bruegemann L., Ohta H., Kurosawa T., Ueki S., and Funakubo H.; 2006 *Japanese J. Appl. Phys. Part 1-Regular Pap. Br. Commun. Rev. Pap.* **45** 7311; doi:`Doi10.1143/Jjap.45.7311`.

[97] Pabst G.W., Martin L.W., Chu Y.H., and Ramesh R.; 2007 *Appl. Phys. Lett.* **90** 1; doi:`10.1063/1.2535663`.

[98] Eerenstein W., Morrison F.D., Sher F., Prieto J.L., Attfield J.P., Scott J.F., and Mathur N.D.; 2007 *Philos. Mag. Lett.* **87** 249; doi:`10.1080/09500830601173053`.

[99] Kawae T., Tsuda H., Naganuma H., Yamada S., Kumeda M., Okamura S., and Morimoto A.; 2008 *Jpn. J. Appl. Phys.* **47** 7586; doi:`10.1143/JJAP.47.7586`.

[100] Kawae T., Terauchi Y., Tsuda H., Kumeda M., and Morimoto A.; 2009 *Appl. Phys. Lett.* **94**; doi:`10.1063/1.3098408`.

[101] Kim J.K., Kim S.S., Kim W.J., Bhalla A.S., and Guo R.; 2006 *Appl. Phys. Lett.* **88** 132901; doi:`10.1063/1.2189453`.

[102] Gao F., Qiu X.Y., Yuan Y., Xu B., Wen Y.Y., Yuan F., Lv L.Y., and Liu J.M.; 2007 *Thin Solid Films* **515** 5366; doi:`10.1016/j.tsf.2007.01.035`.

[103] Gowrishankar M., Babu D.R., and Madeswaran S.; 2016 *J. Magn. Magn. Mater.* **418** 54; doi:`10.1016/j.jmmm.2016.03.085`.

[104] Hasan M., Basith M.A., Zubair M.A., Hossain M.S., Mahbub R., Hakim M.A., and Islam M.F.; 2016 *J. Alloys Compd.* **687** 701; doi:`10.1016/j.jallcom.2016.06.171`.

[105] Singh S.K. and Ishiwara H.; 2006 *Jpn. J. Appl. Phys.* **45** 3194; doi:`10.1143/JJAP.45.3194`.

[106] Wu J., Wang J., Xiao D., and Zhu J.; 2012 *ACS Appl. Mater. Interfaces* **4** 1182; doi:`10.1021/am300236j`.

[107] Yang H., Wang Y.Q., Wang H., and Jia Q.X.; 2010 *Appl. Phys. Lett.* **96** 94; doi:`10.1063/1.3291044`.

[108] Hu Z., Li Q., Li M., Wang Q., Zhu Y., Liu X., Zhao X., Liu Y., and Dong S.; 2013 *Appl. Phys. Lett.* **102** 102901; doi:`10.1063/1.4795145`.

[109] Seidel J., Martin L.W., He Q., Zhan Q., Chu Y.H.H., Rother A., Hawkridge M.E., Maksymovych P., Yu P., Gajek M., *et al.*; 2009 *Nat. Mater.* **8** 229; doi:`10.1038/nmat2373`.

[110] Farokhipoor S. and Noheda B.; 2011 *Phys. Rev. Lett.* **107** 3; doi:`10.1103/PhysRevLett.107.127601`.

[111] Lou X.J., Yang C.X., Tang T.A., Lin Y.Y., Zhang M., and Scott J.F.; 2007 *Appl. Phys. Lett.* **90**; doi:`10.1063/1.2752724`.

[112] Singh S.K. and Ishiwara H.; 2005 *Japanese J. Appl. Physics, Part 2 Lett.* **44** 3; doi:`10.1143/JJAP.44.L734`.

[113] Chen X., Zou Y., Yuan G., Zeng M., Liu J.M., Yin J., and Liu Z.; 2013 *J. Am. Ceram. Soc.* **96** 3788; doi:`10.1111/jace.12580`.

[114] Jeon B.C., Lee D., Lee M.H., Yang S.M., Chae S.C., Song T.K., Bu S.D., Chung J.S., Yoon J.G., and Noh T.W.; 2013 *Adv. Mater.* **25** 5643; doi:`10.1002/adma.201301601`.

[115] Wu J., Fan Z., Xiao D., Zhu J., and Wang J.; 2016 *Prog. Mater. Sci.* **84** 335; doi:`10.1016/j.pmatsci.2016.09.001`.

[116] Jun Y.K., Moon W.T., Chang C.M., Kim H.S., Ryu H.S., Kim J.W., Kim K.H., and Hong S.H.; 2005 *Solid State Commun.* **135** 133; doi:`10.1016/j.ssc.2005.03.038`.

[117] Lee D., Kim M.G., Ryu S., Jang H.M., and Lee S.G.; 2005 *Appl. Phys. Lett.* **86** 1; doi:`10.1063/1.1941474`.

[118] Khomchenko V.A., Kopcewicz M., Lopes A.M., Pogorelov Y.G., Araujo J.P., Vieira J.M., and Kholkin A.L.; 2008 *J. Phys. D. Appl. Phys.* **41** 102003; doi:`10.1088/0022-3727/41/10/102003`.

[119] Hu Z., Li M., Yu B., Pei L., Liu J., Wang J., and Zhao X.; 2009 *J. Phys. D. Appl. Phys.* **42**; doi:`10.1088/0022-3727/42/18/185010`.

[120] Begum H.A., Naganuma H., Oogane M., and Ando Y.; 2011 *Materials (Basel).* **4** 1087; doi:`10.3390/ma4061087`.

[121] Lazenka V.V., Zhang G., Vanacken J., Makoed I.I., Ravinski a.F., and Moshchalkov V.V.; 2012 *J. Phys. D. Appl. Phys.* **45** 125002; doi:`10.1088/0022-3727/45/12/125002`.

[122] Heron J.T., Schlom D.G., and Ramesh R.; 2014 *Appl. Phys. Rev.* **1**; doi:`10.1063/1.4870957`.

[123] Yu P., Lee J.S., Okamoto S., Rossell M.D., Huijben M., Yang C.H., He Q., Zhang J.X., Yang S.Y., Lee M.J., *et al.*; 2010 *Phys. Rev. Lett.* **105** 1; doi:`10.1103/PhysRevLett.105.027201`.

[124] Yu P., Chu Y.H., and Ramesh R.; 2012 *Philos. Trans. R. Soc. A Math. Phys. Eng. Sci.* **370** 4856; doi:`10.1098/rsta.2012.0199`.

[125] Guo E.J., Petrie J.R., Roldan M.A., Li Q., Desautels R.D., Charlton T., Herklotz A., Nichols J., van Lierop J., Freeland J.W., *et al.*; 2017 *Adv. Mater.* **1700790** 1; doi:`10.1002/adma.201700790`.

[126] Oh Y.S., Crane S., Zheng H., Chu Y.H., Ramesh R., and Kim K.H.; 2010 *Appl. Phys. Lett.* **97** 052902; doi:`10.1063/1.3475420`.

[127] Ismailzade I.H., Ismailov R.M., Alekberov A.I., and Salaev F.M.; 1981 *Phys. Status Solidi Appl. Mater. Sci.* **68** 81.

[128] Yang S.c., Kumar A., Petkov V., and Priya S.; 2013 *J. Appl. Phys.* **113** 144101.

[129] Freitas V.F., Dias G.S., Protzek O.A., Montanher D.Z., Catellani I.B., Silva D.M., Cótica L.F., and dos Santos I.A.; 2013 *J. Adv. Ceram.* **2** 103; doi:`10.1007/s40145-013-0052-2`.

[130] Wei Y., Zhu J., Wang X.X., Jia J., and Wang X.X.; 2013 *J. Am. Ceram. Soc.* **96** 3163; doi:`10.1111/jace.12475`.

[131] Guo Y., Xiao P., Wen R., Wan Y., Zheng Q., Shi D., Lam K.H., Liu M., and Lin D.; 2015 *J. Mater. Chem. C* **3** 5811; doi:`10.1039/c5tc00507h`.

[132] Sathiya Priya A., Shameem Banu I., and Anwar S.; 2015 *Mater. Lett.* **142** 42; doi:`10.1016/j.matlet.2014.11.111`.

[133] Ueda K., Tabata H., and Kawai T.; 1999 *Appl. Phys. Lett.* **75** 555; doi:`10.1063/1.124420`.

[134] Murugavel P., Lee J.H., Jo J.Y., Sim H.Y., Chung J.S., Jo Y., and Jung M.H.; 2008 *J. Phys. Condens. Matter* **20** 415208; doi:`10.1088/0953-8984/20/41/415208`.

[135] Sharma S., Tomar M., Kumar A., Puri N.K., and Gupta V.; 2014 *Phys. B Condens. Matter* **448** 125; doi:`10.1016/j.physb.2014.03.089`.

[136] Sharma S., Tomar M., Kumar A., Puri N.K., and Gupta V.; 2015 *AIP Adv.* **5** 0; doi:`10.1063/1.4934578`.

[137] Sharma S., Tomar M., Kumar A., Puri N.K., and Gupta V.; 2015 *J. Appl. Phys.* **118** 074103; doi:`10.1063/1.4928964`.

[138] Gupta R., Chaudhary S., and Kotnala R.K.; 2015 *ACS Appl. Mater. Interfaces* **7** 8472; doi:`10.1021/am509055f`.

[139] Kotnala R.K., Gupta R., and Chaudhary S.; 2015 *Appl. Phys. Lett.* **107** 10; doi:`10.1063/1.4929729`.

[140] Ranjith R., Lüders U., Prellier W., Da Costa A., Dupont I., and Desfeux R.; 2009 *J. Magn. Magn. Mater.* **321** 1710; doi:`10.1016/j.jmmm.2009.02.116`.

[141] Ranjith R., Prellier W., Cheah J.W., Wang J., and Wu T.; 2008 *Appl. Phys. Lett.* **92** 1; doi:`10.1063/1.2937843`.

[142] Wu Y., Wan J.G., Huang C., Weng Y., Zhao S., Liu J.M., and Wang G.; 2008 *Appl. Phys. Lett.* **93** 2006; doi:`10.1063/1.3028089`.

[143] Toupet H., Shvartsman V.V., Lemarrec F., Borisov P., Kleemann W., and Karkut M.; 2008 *Integr. Ferroelectr.* **100** 165; doi:`10.1080/10584580802541023`.

[144] Ivanov M.S., Sherstyuk N.E., Mishina E.D., Sigov A.S., Mukhortov V.M., and Moshnyaga V.T.; 2012 *Ferroelectrics* **433** 158; doi:`10.1080/00150193.2012.696448`.

[145] Chen C., Lv S., Li J., Wang Z., Liang X., Li Y., Viehland D., Nakajima K., and Ikuhara Y.; 2015 *Appl. Phys. Lett.* **107** 031601; doi:`10.1063/1.4926732`.

[146] Kumar M.M., Srinivas A., Kumar G.S., and Suryanarayana S.V.; 1999 *Journal of Physics: Condensed Matter* **11** 8131; doi:`10.1088/0953-8984/11/41/315`.

[147] Lorenz M., Wagner G., Lazenka V., Schwinkendorf P., Bonholzer M., Van Bael M.J., Vantomme A., Temst K., Oeckler O., and Grundmann M.; 2016 *Materials (Basel).* **9** 44; doi:`10.3390/ma9010044`.

[148] Lorenz M., Wagner G., Lazenka V., Schwinkendorf P., Modarresi H., Van Bael M.J., Vantomme A., Temst K., Oeckler O., and Grundmann M.; 2015 *Appl. Phys. Lett.* **106** 012905; doi:`10.1063/1.4905343`.

[149] Lorenz M., Lazenka V., Schwinkendorf P., Van Bael M.J., Vantomme A., Temst K., Grundmann M., and Höche T.; 2016 *Adv. Mater. Interfaces* **3** 1500822; doi:`10.1002/admi.201500822`.

[150] Lazenka V., Lorenz M., Modarresi H., Bisht M., Rüffer R., Bonholzer M., Grundmann M., Van Bael M.J., Vantomme A., and Temst K.; 2015 *Appl. Phys. Lett.* **106** 082904; doi:`10.1063/1.4913444`.

[151] Lazenka V., Jochum J.K., Lorenz M., Modarresi H., Gunnlaugsson H.P., Grundmann M., Van Bael M.J., Temst K., and Vantomme A.; 2017 *Appl. Phys. Lett.* **110** 092902; doi:`10.1063/1.4977434`.

[152] Jochum J.K., Lorenz M., Gunnlaugsson H.P., Patzig C., Höche T., Grundmann M., Vantomme A., Temst K., Van Bael M.J., and Lazenka V.; 2018 *Nanoscale* **10** 5574; doi:`10.1039/C8NR00430G`.

[153] Lorenz M. and Ramachandra Rao M.S.; 2014 *J. Phys. D. Appl. Phys.* **47** 030301; doi:`10.1088/0022-3727/47/3/030301`.

[154] Christen H.M. and Eres G.; 2008 *J. Phys. Condens. Matter* **20** 264005; doi:`10.1088/0953-8984/20/26/264005`.

[155] Lorenz M.; 2008 in K. Ellmer, A. Klein, and B. Rech, editors, *Transparent Conduct. Zinc Oxide*; volume 104 of *Springer Series in Materials Science*; pages 303–357; Springer Berlin Heidelberg, Berlin, Heidelberg; ISBN 978-3-540-73611-0; doi:`10.1007/978-3-540-73612-7`.

[156] Singh R.K. and Narayan J.; 1990 *Phys. Rev. B* **41** 8843; doi:`10.1103/PhysRevB.41.8843`.

[157] Willmott P.R. and Huber J.R.; 2000 *Rev. Mod. Phys.* **72** 315; doi:`10.1103/RevModPhys.72.315`.

[158] Wicklein S., Sambri A., Amoruso S., Wang X., Bruzzese R., Koehl A., and Dittmann R.; 2012 *Appl. Phys. Lett.* **101** 11; doi:`10.1063/1.4754112`.

[159] Singh R.K., Bhattacharya D., and Narayan J.; 1990 *Appl. Phys. Lett.* **57** 2022; doi:`10.1063/1.104118`.

[160] Vlieg E.; 2002 *Surface Science* **500** 458; doi:`10.1016/S0039-6028(01)01541-2`.

[161] Kinoshita K., Ishibashi H., and Kobayashi T.; 1994 *Jpn. J. Appl. Phys.* **33** L417; doi:`10.1143/JJAP.33.L417`.

[162] Holý V., Pietsch U., and Baumbach T.; 1999 *High-Resolution X-Ray Scattering from Thin Films and Multilayers*; volume 149 of *Springer Tracts in Modern Physics*; Springer Berlin Heidelberg, Berlin, Heidelberg; ISBN 978-3-540-62029-7; doi:`10.1007/BFb0109385`.

[163] Nelson J.B. and Riley D.P.; 1945 *Proc. Phys. Soc.* **57** 160; doi:`10.1088/0959-5309/57/3/302`.

[164] Bartels W.J., Hornstra J., and Lobeek D.J.W.; 1986 *Acta Crystallogr. Sect. A* **42** 539; doi:`10.1107/S0108767386098768`.

[165] Spieß L., Teichert G., Schwarzer R., Behnken H., and Genzel C.; 2009 *Moderne Röntgenbeugung*; Vieweg+Teubner, Wiesbaden; ISBN 978-3-8351-0166-1; doi:`10.1007/978-3-8349-9434-9`.

[166] Yang P., Liu H., Chen Z., Chen L., and Wang J.; 2013 *ArXiv e-prints* **1311** 3382.

[167] Roesener T., Klinger V., Weuffen C., Lackner D., and Dimroth F.; 2013 *J. Cryst. Growth* **368** 21; doi:`10.1016/j.jcrysgro.2013.01.007`.

[168] Fewster P.F.; 1997 *Crit. Rev. Solid State Mater. Sci.* **22** 69; doi:`10.1080/10408439708241259`.

[169] Zabel H.; 1994 *Appl. Phys. A Solids Surfaces* **58** 159; doi:`10.1007/BF00324371`.

[170] Nečas D. and Klapetek P.; 2012 *Open Physics* **10**; doi:`10.2478/s11534-011-0096-2`.

[171] Schindelin J., Arganda-Carreras I., Frise E., Kaynig V., Longair M., Pietzsch T., Preibisch S., Rueden C., Saalfeld S., Schmid B., *et al.*; 2012 *Nat. Methods* **9** 676; doi:`10.1038/nmeth.2019`.

[172] Arlinghaus H.F.; 2011 in *Surface and Thin Film Analysis*; chapter 7, pages 115–139; Wiley-VCH Verlag GmbH & Co. KGaA, Weinheim, Germany; doi:`10.1002/9783527636921.ch7`.

[173] Hutter H.; 2011 in G. Friedbacher and H. Bubert, editors, *Surface and Thin Film Analysis*; chapter 8, pages 141–159; Wiley-VCH Verlag GmbH & Co. KGaA, Weinheim, Germany; ISBN 9783527636921; doi:`10.1002/9783527636921.ch8`.

[174] Meyer R., Waser R., Prume K., Schmitz T., and Tiedke S.; 2005 *Appl. Phys. Lett.* **86** 1; doi:`10.1063/1.1897425`.

[175] Schmitz T., Prume K., Reichenberg B., Roelofs A., Waser R., and Tiedke S.; 2004 *J. Eur. Ceram. Soc.* **24** 1145; doi:`10.1016/S0955-2219(03)00583-1`.

[176] Prume K., Schmitz T., and Tiedke S.; 2005 in R. Waser, U. Böttger, and S. Tiedke, editors, *Polar Oxides*; chapter 3, pages 53–75; Wiley-VCH Verlag GmbH

& Co. KGaA, Weinheim, FRG; ISBN 9783527405329; doi:`10.1002/3527604650.ch3`.

[177] Scott J.F.; 2008 *J. Phys. Condens. Matter* **20** 021001; doi:`10.1088/0953-8984/20/02/021001`.

[178] Foner S.; 1956 *Rev. Sci. Instrum.* **27** 548; doi:`10.1063/1.1715636`.

[179] Quantum Design; 2011; *Vibrating Sample Magnetometer (VSM) Option User 's Manual.*

[180] Rivera J.P.; 1994 *Ferroelectrics* **161** 165; doi:`10.1080/00150199408213365`.

[181] Vopson M.M., Fetisov Y.K., Caruntu G., and Srinivasan G.; 2017 *Materials (Basel).* **10** 1; doi:`10.3390/ma10080963`.

[182] Prof M.J.V.B., Prof K.T., and Jochum J.K.; 2018 *Interface Phenomena in Magnetic Nanostructures*; Phd thesis; KU Leuven.

[183] Rijnders G., Koster G., Leca V., Blank D.H.A., and Rogalla H.; 2000 *Appl. Surf. Sci.* **168** 223; doi:`10.1016/S0169-4332(00)00602-4`.

[184] Aso R., Kan D., Shimakawa Y., and Kurata H.; 2014 *Cryst. Growth Des.* **14** 2128; doi:`10.1021/cg500285m`.

[185] Aso R., Kan D., Shimakawa Y., and Kurata H.; 2013 *Sci. Rep.* **3** 1; doi:`10.1038/srep02214`.

[186] He Q., Ishikawa R., Lupini A.R., Qiao L., Moon E.J., Ovchinnikov O., May S.J., Biegalski M.D., and Borisevich A.Y.; 2015 *ACS Nano* **9** 8412; doi:`10.1021/acsnano.5b03232`.

[187] Borisevich A.Y., Chang H.J., Huijben M., Oxley M.P., Okamoto S., Niranjan M.K., Burton J.D., Tsymbal E.Y., Chu Y.H., Yu P., *et al.*; 2010 *Phys. Rev. Lett.* **105** 1; doi:`10.1103/PhysRevLett.105.087204`.

[188] Saito M., Kimoto K., Nagai T., Fukushima S., Akahoshi D., Kuwahara H., Matsui Y., and Ishizuka K.; 2009 *J. Electron Microsc. (Tokyo).* **58** 131; doi:`10.1093/jmicro/dfn023`.

[189] Ujimoto K., Yoshimura T., Ashida A., Fujimura N., Yoshimura T., Ashida A., and Fujimura N.; 2013 *Jpn. J. Appl. Phys.* **52** 045803.

[190] Dho J., Qi X., Kim H., MacManus-Driscoll J.L., and Blamire M.G.; 2006 *Adv. Mater.* **18** 1445; doi:`10.1002/adma.200502622`.

[191] Shelke V., Harshan V.N., Kotru S., and Gupta A.; 2009 *J. Appl. Phys.* **106**; doi:`10.1063/1.3254190`.

[192] Liu F., Fina I., Bertacco R., and Fontcuberta J.; 2016 *Sci. Rep.* **6** 1; doi:`10.1038/srep25028`.

[193] Zhou Y., Chan H.K., Lam C.H., and Shin F.G.; 2005 *J. Appl. Phys.* **98** 024111; doi:`10.1063/1.1984075`.

[194] Abe K., Komatsu S., Yanase N., Sano K., and Kawakubo T.; 1997 *Japanese J. Appl. Physics, Part 1 Regul. Pap. Short Notes Rev. Pap.* **36** 5846.

[195] Baek S.H. and Eom C.B.; 2012 *Philos. Trans. R. Soc. A Math. Phys. Eng. Sci.* **370** 4872; doi:`10.1098/rsta.2012.0197`.

[196] Arlt G. and Neumann H.; 1988 *Ferroelectrics* **87** 109; doi:`10.1080/00150198808201374`.

[197] Damodaran A.R., Breckenfeld E., Chen Z., Lee S., and Martin L.W.; 2014 *Adv. Mater.* **26** 6341; doi:`10.1002/adma.201400254`.

[198] Abe K., Yanase N., Yasumoto T., and Kawakubo T.; 2002 *Jpn. J. Appl. Phys.* **41** 6065; doi:`10.1143/JJAP.41.6065`.

[199] Aramaki M., Kariya K., Yoshimura T., Murakami S., and Fujimura N.; 2016 *Jpn. J. Appl. Phys.* **55** 10TA16; doi:`10.7567/JJAP.55.10TA16`.

[200] Luo Y., Li X., Chang L., Gao W., Yuan G., Yin J., and Liu Z.; 2013 *AIP Adv.* **3** 122101; doi:`10.1063/1.4840595`.

[201] Chen J., Luo Y., Ou X., Yuan G., Wang Y., Yang Y., Yin J., and Liu Z.; 2013 *J. Appl. Phys.* **113** 1; doi:`10.1063/1.4807794`.

[202] Beekman C., Siemons W., Chi M., Balke N., Howe J.Y., Ward T.Z., Maksymovych P., Budai J.D., Tischler J.Z., Xu R., *et al.*; 2016 *Adv. Funct. Mater.* **26** 5166; doi:`10.1002/adfm.201600468`.

[203] Agarwal S., Caltun O.F., and Sreenivas K.; 2012 *Solid State Commun.* **152** 1951; doi:`10.1016/j.ssc.2012.08.002`.

[204] Vidal J.V., Timopheev A.A., Kholkin A.L., and Sobolev N.A.; 2016 in I. Tiginyanu, P. Topala, and V. Ursaki, editors, *Nanostructures Thin Film. Multifunct. Appl.*; chapter 7, pages 227–265; Springer, Cham, Switzerland; 1st edition; ISBN 978-3-319-30197-6; doi:`10.1007/978-3-319-30198-3_7`.

[205] Timopheev A.A., Vidal J.V., Kholkin A.L., and Sobolev N.A.; 2013 *J. Appl. Phys.* **114** 044102; doi:`10.1063/1.4816400`.

[206] Koster G., Rijnders G., Blank D.H., and Rogalla H.; 2000 *Phys. C Supercond.* **339** 215; doi:`10.1016/S0921-4534(00)00363-4`.

[207] Béa H., Bibes M., Fusil S., Bouzehouane K., Jacquet E., Rode K., Bencok P., and Barthélémy A.; 2006 *Phys. Rev. B - Condens. Matter Mater. Phys.* **74** 3; doi:`10.1103/PhysRevB.74.020101`.

[208] Chen A.P., Khatkhatay F., Zhang W., Jacob C., Jiao L., and Wang H.; 2013 *J. Appl. Phys.* **114** 124101; doi:`10.1063/1.4821643`.

[209] Kan D. and Shimakawa Y.; 2011 *Appl. Phys. Lett.* **99** 3; doi:`10.1063/1.3628461`.

[210] Jaber N., Wolfman J., Daumont C., Négulescu B., Ruyter A., Sauvage T., Courtois B., Bouyanfif H., Longuet J., Autret-Lambert C., *et al.*; 2017 *Thin Solid Films* **634** 107; doi:`10.1016/j.tsf.2017.05.003`.

[211] Cultrera L., Zeifman M.I., and Perrone A.; 2007 *Applied Surface Science* **253** 6322; doi:`10.1016/j.apsusc.2007.01.049`.

[212] Proyer S., Stangl E., Borz M., and Bäuerle D.; 1996 *Appl. Surf. Sci.* **96-98** 668; doi:`10.1016/0169-4332(95)00540-4`.

[213] Blank D.H.A., Dekkers M., and Rijnders G.; 2014 *J. Phys. D. Appl. Phys.* **47** 034006; doi:`10.1088/0022-3727/47/3/034006`.

[214] Stamenov P. and Coey J.M.D.; 2006 *Rev. Sci. Instrum.* **77** 1; doi:`10.1063/1.2149190`.

[215] Duley W.W.; 1996 in *UV Lasers*; chapter 1, pages 1–35; Cambridge University Press; ISBN 9780521464987; doi:`10.1017/CBO9780511524134.002`.

[216] Opel M., Geprägs S., Althammer M., Brenninger T., and Gross R.; 2014 *Journal of Physics D: Applied Physics* **47** 034002; doi:`10.1088/0022-3727/47/3/034002`.

[217] Choi E.M., Fix T., Kursumovic A., Kinane C.J., Arena D., Sahonta S.L., Bi Z., Xiong J., Yan L., Lee J.S., *et al.*; 2014 *Adv. Funct. Mater.* **24** 7478; doi:`10.1002/adfm.201401464`.

[218] Paudel B., Vasiliev I., Hammouri M., Karpov D., Chen A., Lauter V., and Fohtung E.; 2019 *RSC Adv.* **9** 13033; doi:`10.1039/C9RA01503E`.

[219] Singh S., Xiong J., Chen A.P., Fitzsimmons M.R., and Jia Q.X.; 2015 *Phys. Rev. B - Condens. Matter Mater. Phys.* **92** 224405; doi:`10.1103/PhysRevB.92.224405`.

[220] Singh S., Haraldsen J.T., Xiong J., Choi E.M., Lu P., Yi D., Wen X.D., Liu J., Wang H., Bi Z., *et al.*; 2014 *Phys. Rev. Lett.* **113** 047204; doi:`10.1103/PhysRevLett.113.047204`.

[221] Khaydukov Y., Soltwedel O., and Keller T.; 2015 *Journal of large-scale research facilities JLSRF* **1** A38; doi:`10.17815/jlsrf-1-30`.

[222] Uribe-Laverde M.A., Satapathy D.K., Marozau I., Malik V.K., Das S., Sen K., Stahn J., Rühm A., Kim J.H., Keller T., *et al.*; 2013 *Physical Review B* **87** 115105; doi:`10.1103/PhysRevB.87.115105`.

[223] Burdin D.A., Ekonomov N.A., Chashin D.V., Fetisov L.Y., Fetisov Y.K., and Shamonin M.; 2017 *Materials (Basel).* **10** 1; doi:`10.3390/ma10101183`.

[224] Greve H., Woltermann E., Quenzer H.J., Wagner B., and Quandt E.; 2010 *Appl. Phys. Lett.* **96** 182501; doi:`10.1063/1.3377908`.

[225] Srinivasan G., DeVreugd C.P., Flattery C.S., Laletsin V.M., and Paddubnaya N.; 2004 *Appl. Phys. Lett.* **85** 2550; doi:`10.1063/1.1795365`.

[226] Shen Y., Gao J., Wang Y., Li J., and Viehland D.; 2012 *Appl. Phys. Lett.* **100** 1; doi:`10.1063/1.4705298`.

[227] Huijben M., Koster G., Liao Z.L., and Rijnders G.; 2017 *Appl. Phys. Rev.* **4**; doi:`10.1063/1.4985770`.

[228] Zhang Q.M., Wang H., Kim N., and Cross L.E.; 1994 *J. Appl. Phys.* **75** 454; doi:`10.1063/1.355874`.

[229] Zhu L.F., Liu Q., Zhang B.P., Cen Z.Y., Wang K., Li J.j., Bai Y., Wang X.H., and Li J.F.; 2018 *RSC Adv.* **8** 35794; doi:`10.1039/C8RA07553K`.

[230] Fang F., Xu Y.T., and Yang W.; 2012 *J. Appl. Phys.* **111** 023906; doi:`10.1063/1.3677945`.

[231] Walther T., Straube U., Köferstein R., and Ebbinghaus S.G.; 2016 *J. Mater. Chem. C* **4** 4792; doi:`10.1039/C6TC00995F`.

[232] Jia C.L., Nagarajan V., He J.Q., Houben L., Zhao T., Ramesh R., Urban K., and Waser R.; 2007 *Nat. Mater.* **6** 64; doi:`10.1038/nmat1808`.

[233] Wang W., Sun W., Zhang G., Ren F., Wang Y., You C., and Cheng Z.; 2020 *Journal of Advanced Research* **24**; doi:`10.1016/j.jare.2020.04.012`.

Own and Contributed Work

[H1] M. Lorenz, D. Hirsch, C. Patzig, H. Hochmuth, V. Lazenka, K. Temst, T. Höche, **S. Hohenberger**, H. Hochmuth, V. Lazenka, K. Temst and M. Grundmann: *Correlation of Interface Impurities and Chemical Gradients with High Magnetoelectric Coupling Strength in Multiferroic* $BiFeO_3$–$BaTiO_3$ *Superlattices*, 2017 *ACS Applied Materials and Interfaces*, **9** (22); doi:`10.1021/acsami.7b04084`.

[H2] M. Lorenz, H. Wei, F. Jung, **S. Hohenberger**, M. Grundmann, C. Patzig, S. Selle and T. Höche: *Two-dimensional Frank-van der Merwe growth of functional oxide and nitride thin film superlattices by pulsed laser deposition*, 2017 *Journal of Materials Research*, **32** (21);doi:`10.1557/jmr.2017.266`

[H3] **S. Hohenberger**, V. Lazenka, K. Temst, S. Selle, C. Patzig, T. Höche, M. Grundmann and M. Lorenz: *Effect of double layer thickness on magnetoelectric coupling in multiferroic* $BaTiO_3$-$Bi_{0.95}Gd_{0.05}FeO_3$ *multilayers*, 2018 *Journal of Physics D: Applied Physics*, **51** (18); doi:`10.1088/1361-6463/aab8c9`

[H4] **S. Hohenberger**, J. K. Jochum, M. J. Van Bael, K. Temst, C. Patzig, T. Höche, M. Grundmann and M. Lorenz: *Enhanced Magnetoelectric Coupling in* $BaTiO_3$-$BiFeO_3$ *Multilayers — An Interface Effect*, 2020 *Materials*, **13** (1)doi:`10.3390/ma13010197`

[H5] **S. Hohenberger**, V. Lazenka, S. Selle, C. Patzig, K. Temst and M. Lorenz: *Magnetoelectric Coupling in Epitaxial Multiferroic* $BiFeO_3$–$BaTiO_3$ *Composite Thin Films*, 2020 *physica status solidi (b)*, **257** (7); doi:`10.1002/pssb.201900613`

Acknowledgment

I would like to take the chance to express my thanks to everyone involved for their advice, help and work that led to the completion of this thesis:

- Prof. Michael Lorenz, who suggested the topic of this thesis and continually supported my work throughout the last years
- Prof. Marius Grundmann, for accepting me into the Semiconductor Physics Group
- Prof. Kristiaan Temst and Prof. André Vantommé of the KU Leuven for providing the lab resources for measuring ME coupling
- Dr. Vera Lazenka for building the ME setup and conducting measurements
- Dr. Johanna Jochum for operating the ME setup, helpful discussions and the opportunity to measure PNR
- Anja Heck and Birgit Wendisch for all their organizational work
- Jörg Lenzner for his help in IT matters, Helium, operating the SEM, and his efforts in building the ME setup in Leipzig
- Holger Hochmuth for maintaining the PLD system, Monika Hahn and Gabriele Ramm for preparing substrates and sintering PLD targets
- Dr. Christian Patzig and Dr. Susanne Selle for conducting TEM measurements, and Andrea Böbenroth for preparing the TEM samples
- Dr. Jens Bauer for measurement and analysis of the ToF-SIMS data
- Dr. Yury Khaydukov for his role in carrying out the PNR measurements
- Dr. Vitaly Zviagin, Dr. Daniel Splith, Georg Blanke and Poriya Rezaimanesh for patiently hunting for spelling and formatting errors and giving advice on the composition of this thesis

- Dr. Michael Bonholzer for his introductory input
- Dr. Daniel Splith, Dr. Sofie Vogt, Dr. Peter Schlupp, Max Kneiß and Tillmann Stralka for their company in the office and interesting discussions , as well as the entire Semiconductor Physics group and an overall pleasant work atmosphere
- Gabriele Benndorf for an endless supply of chocolate and laughter during coffee breaks
- my friends and family for giving me encouragement each time I felt challenged by my time as a doctorate student

I also acknowledge the collaborative research center SFB 762: Functionality of Oxide Interfaces, which provided the funding for the work on the topic presented in this thesis.

Selbstständigkeitserklärung

Hiermit erkläre ich, dass ich die von mir vorgelegte Dissertation mit dem Titel:

“Magnetoelectric Coupling in $BaTiO_3$-$BiFeO_3$ Multilayers:
Growth Optimization and Characterization”

ohne unzulässige Hilfe und ohne Benutzung anderer als der angegebenen Hilfsmittel angefertigt und dass die aus fremden Quellen direkt oder indirekt übernommenen Gedanken in der Arbeit als solche kenntlich gemacht wurden. Ich versichere, dass außer den von mir in der Dissertation genannten keine weiteren Personen bei der geistigen Herstellung der vorliegenden Arbeit beteiligt waren und ich insbesondere nicht die Hilfe eines Promotionsberaters in Anspruch genommen habe. Weiterhin erkläre ich, dass keine weiteren Personen von mir oder in meinem Auftrag weder unmittelbar noch mittelbar geldwerte Leistungen für Arbeiten erhalten haben, die im Zusammenhang mit dem Inhalt der vorgelegten Dissertation stehen. Ich versichere, dass die vorgelegte Arbeit weder im Inland noch im Ausland in gleicher oder in ähnlicher Form in einer anderen Prüfungsbehörde zum Zwecke einer Promotion oder eines anderen Prüfungsverfahrens vorgelegt und in ihrer Gesamtheit noch nicht veröffentlicht wurde. Ich erkläre, dass ich bisher keine erfolglosen Promotionsversuche unternommen habe.

Leipzig, den 01.09.2020

Stefan Hohenberger

Erratum

Folgende Änderungen und Korrekturen wurden in der vorliegenden Version der Dissertation im Vergleich zu der für das Promotionsverfahren eingereichten Version eingearbeitet:

- Der Lebenslauf wurde aus dem Dokument entfernt.
- Zusammenfassung nach §11 (4) der Promotionsordnung der Fakultät für Physik und Geowissenschaften der Universität Leipzig wurde aus dem Dokument entfernt.
- Außerdem wurde das Titelblatt gemäß den Vorgaben aktualisiert und die Seitenzahl in der Bibliographische Beschreibung angepasst.